

# Changes to Functional Biomechanics and Structure of the Haemophilic Ankle Joint

Harriet Georgina Talbott

Submitted in accordance with the requirements for the degree

of Doctor of Philosophy

The University of Leeds

School of Mechanical Engineering

May 2022

## Intellectual Property and Publications Statement

The candidate confirms that the work submitted is her own, except where work which has formed part of jointly authored publications has been included. The contribution of the candidate and the other authors to this work has been explicitly indicated below. The candidate confirms that appropriate credit has been given within the thesis where reference has been made to the work of others.

**Chapter 2:** Talbott, H.G., Wilkins, R.A., Redmond, A.C., Brockett, C.L., and Mengoni, M (2021). Morphological Variation of the Hemophilic Talus. *Clinical Anatomy*, 34(6), 941-947.

**Chapter 5:** Talbott, H, Wilkins, R, Redmond, A, Brockett, C and Mengoni, M (2022). The relationship between subchondral bone cysts and cartilage health in the Tibiotalar joint: A finite element analysis. *Clinical Biomechanics*. Available online: doi.org/10.1016/j.clinbiomech.2022.105745

Talbott, H, Wilkins, R, Redmond, A, Brockett, C, and Mengoni, M (2020). P014 / The influence of subchondral bone cysts on tissue pressures in the tibiotalar joint. *Haemophilia*, 26: 27-181

In both of these chapters the work was carried out by myself, with other authors contributing to study design and manuscript/abstract preparation.

**Chapter 6:** the biomechanical data used in this chapter was collected for previous research by R Wilkins

This copy has been supplied on the understanding that it is copyright material and that no quotation from the thesis may be published without proper acknowledgement

## Acknowledgements

I would foremost like to express my sincerest gratitude to my supervisor Dr Marlène Mengoni for her continuous support throughout my PhD. Her guidance, encouragement and knowledge have helped me through all stages of my research. She has not only encouraged me in achieving my PhD, but in preparing me for my future careers, for which I cannot thank her enough.

I would secondly like to thank my other supervisors, Dr Claire Brockett, Professor Anthony Redmond and Dr Robert Cooper, for their support and expertise throughout my PhD. I extend this thanks to Dr Richard Wilkins who provided guidance on the clinical elements of this work throughout.

I am extremely grateful for the opportunities the Institute of Medical and Biological Engineering has provided me, including the sense of community from my fellow PhD students; this camaraderie has improved my research experience immeasurably, and I feel honoured to have worked alongside such brilliant minds.

My final thanks go to my family and friends, without their support none of this would have been possible. I cannot thank them enough for being understanding when I start talking about my research!

## Abstract

Haemophilia is a rare disease that causes musculoskeletal bleeds in up to 80% of patients. These bleeds cause arthritic changes to the targeted joint; the aim of the research carried out in this thesis was to investigate the influence of these arthritic changes on the ankle joint. In order to achieve this, longitudinal morphological analysis and finite element studies were carried out on a patient cohort with haemarthropathy of the ankle.

Robust, patient specific models were generated in order to carry out novel studies into the influence of features of subchondral bone cysts, such as size, location and depth; and to develop a quasi-dynamic method of modelling patient specific haemophilic gait. The results gathered from these models highlighted the importance of patient specificity in a disease with such variable joint outcomes.

Despite a small sample size, and informational constraints, the results of the studies undertaken highlighted structural and functional changes of the haemophilic ankle, and demonstrated potential relationships between the two. Morphological analysis showed a significant flattening of the talus in the medial and lateral regions of the haemophilic ankle. Upon investigation of the link between this morphological variation and consequent joint function, a significant negative correlation between talar collapse and cartilage contact pressure, and bone stresses was found in static modelling; and through the gait cycle the regions of high contact forces related to regions of significant talar collapse.

## Table of Contents

<b>Intellectual Property and Publications Statement .....</b>	<b>ii</b>
<b>Acknowledgements .....</b>	<b>iii</b>
<b>Abstract.....</b>	<b>iv</b>
<b>Table of Figures.....</b>	<b>ix</b>
<b>Table of Tables .....</b>	<b>xv</b>
<b>Abbreviations .....</b>	<b>1</b>
<b><i>CHAPTER 1: INTRODUCTION.....</i></b>	<b>3</b>
<b>1.1 Introduction.....</b>	<b>3</b>
<b>1.2 Literature Review .....</b>	<b>6</b>
1.2.1 Haemophilia.....	6
1.2.2 Haemophilic Joint Disease.....	6
1.2.3 Anatomy and Function of the Ankle.....	15
1.2.4 Computational Methods.....	18
<b>1.3 Aims and Objectives .....</b>	<b>28</b>
<b>1.4 Patient Data .....</b>	<b>29</b>
<b><i>CHAPTER 2: MORPHOLOGY OF THE HAEMOPHILIC TROCHLEAR TALUS.....</i></b>	<b>32</b>
<b>2.1 Introduction.....</b>	<b>32</b>
<b>2.2 Data Acquisition and Method Development.....</b>	<b>33</b>
2.2.1 Haemophilic Patient Data .....	34
2.2.2 Non-Diseased Control Group Data .....	34
2.2.3 Image Data.....	34
2.2.4 Method Development .....	35
2.2.5 Ratios .....	38
<b>2.3 Verification Studies.....</b>	<b>39</b>
2.3.1 Methods .....	39
2.3.2 Results .....	41
2.3.3 Discussion.....	45
<b>2.4 Morphology of the Haemophilic Talus.....</b>	<b>48</b>
2.4.1 Methods .....	48
2.4.2 Results .....	50
2.4.3 Discussion.....	53

2.5	Conclusion .....	55
<b>CHAPTER 3: DEVELOPMENT OF PATIENT SPECIFIC ANKLE MODELS.....</b>		<b>58</b>
3.1	Introduction.....	58
3.2	Model Generation .....	59
3.3	Outcomes of Interest .....	64
3.4	Material Properties.....	64
3.4.1	Sensitivity to Inhomogeneous Bone .....	66
3.4.2	Results .....	67
3.4.3	Discussion.....	70
3.5	Mesh Convergence Study .....	71
3.5.1	Results .....	72
3.5.2	Discussion.....	74
3.6	Imaging Direction Verification.....	76
3.6.1	Methods .....	76
3.6.2	Results .....	76
3.6.3	Discussion.....	78
3.7	Verification of Image Resolution.....	79
3.7.1	Methods .....	79
3.7.2	Results .....	79
3.7.3	Discussion.....	83
3.8	MRI Sequence Type.....	84
3.8.1	Methods .....	84
3.8.2	Results .....	84
3.8.3	Discussion.....	85
3.9	Talar Cropping.....	87
3.9.1	Methods .....	87
3.9.2	Results .....	89
3.9.3	Discussion.....	90
3.10	Conclusion .....	91
<b>CHAPTER 4: CHRONOLOGICAL STUDY USING PATIENT SPECIFIC ANKLE MODELS.....</b>		<b>94</b>
4.1	Introduction.....	94
4.2	Methods.....	94
4.2.1	Material properties.....	95

4.2.2	Loading Conditions.....	95
4.2.3	Longitudinal Study Outputs.....	97
4.2.4	Coefficient of Friction Study.....	97
<b>4.3</b>	<b>Longitudinal Study Outputs .....</b>	<b>102</b>
<b>4.4</b>	<b>Discussion.....</b>	<b>105</b>
<b>4.5</b>	<b>Conclusion .....</b>	<b>106</b>
<b>CHAPTER 5: FINITE ELEMENT ANALYSIS OF SUBCHONDRAL BONE CYSTS...</b>		<b>108</b>
<b>5.1</b>	<b>Introduction.....</b>	<b>108</b>
<b>5.2</b>	<b>Methods.....</b>	<b>109</b>
5.2.1	Addition of Subchondral Bone Cysts.....	110
5.2.2	Finite Element Analysis.....	110
5.2.3	Material Properties.....	111
5.2.4	Subchondral Bone Cyst Volume.....	112
5.2.5	Cyst Depth Study.....	113
5.2.6	Statistical Testing.....	114
<b>5.3</b>	<b>Results .....</b>	<b>114</b>
5.3.1	SBC Property Sensitivity Study.....	115
5.3.2	Intact Bone vs Cystic Tissue.....	116
5.3.3	Subchondral Bone Cyst Volumes .....	118
5.3.4	Cyst Volume Study.....	120
5.3.5	Influence of SBC Location .....	124
5.3.6	Cyst Depth Study.....	124
<b>5.4</b>	<b>Discussion.....</b>	<b>128</b>
5.4.1	Impact of SBC Volume.....	130
5.4.2	Impact of SBC Location .....	132
5.4.3	Influence of Cyst Depth.....	134
5.4.4	Effect of Arthritic Stage.....	135
5.4.5	Simplifications to the Haemophilic Model .....	135
<b>5.5</b>	<b>Conclusion .....</b>	<b>137</b>
<b>CHAPTER 6: FINITE ELEMENT ANALYSIS OF GAIT IN THE HAEMOPHILIC ANKLE MODEL.....</b>		<b>139</b>
<b>6.1</b>	<b>Introduction.....</b>	<b>139</b>
<b>6.2</b>	<b>Methods.....</b>	<b>140</b>
6.2.1	Method development .....	142
6.2.2	Reduction of Range of Motion .....	144

6.2.3	Haemophilic gait.....	145
<b>6.3</b>	<b>Results .....</b>	<b>147</b>
6.3.1	Method Development .....	147
6.3.2	Reduction of Range of Motion .....	150
6.3.3	Haemophilic gait.....	152
<b>6.4</b>	<b>Discussion.....</b>	<b>157</b>
6.4.1	Reduction of Range of Motion .....	157
6.4.2	Haemophilic gait.....	158
<b>6.5</b>	<b>Conclusion .....</b>	<b>160</b>
<b>CHAPTER 7: DISCUSSION AND CONCLUSION .....</b>		<b>162</b>
<b>7.1</b>	<b>Summary.....</b>	<b>162</b>
<b>7.2</b>	<b>Implications of Morphology on Ankle Biomechanics .....</b>	<b>162</b>
<b>7.3</b>	<b>Influence of Subchondral Bone Cysts on Joint Health .....</b>	<b>163</b>
<b>7.4</b>	<b>Relationship between Altered Biomechanics and Joint Health .....</b>	<b>165</b>
<b>7.5</b>	<b>Limitations.....</b>	<b>166</b>
<b>7.6</b>	<b>Future work.....</b>	<b>167</b>
7.6.1	Morphological Analysis.....	167
7.6.2	Patient Specific Finite Element Model Generation.....	168
7.6.3	Subchondral Bone Cyst Analysis.....	169
7.6.4	Biomechanical Analysis .....	169
<b>7.7</b>	<b>Conclusion .....</b>	<b>170</b>
<b>8</b>	<b><i>Bibliography</i>.....</b>	<b>171</b>
<b>9</b>	<b><i>Appendix</i> .....</b>	<b>187</b>
<b>9.3</b>	<b>Chapter 3: Method Development .....</b>	<b>187</b>
9.3.1	Materials Sensitivity .....	187
<b>9.4</b>	<b>Chapter 4: Chronological Study .....</b>	<b>189</b>
9.4.1	Coefficient of Friction Study – No SBCs .....	189
9.4.2	Coefficient of Friction Study – SBC models .....	192
9.4.3	Longitudinal Study Outputs.....	195
<b>9.5</b>	<b>Chapter 5: Subchondral Bone Cysts .....</b>	<b>197</b>
<b>9.6</b>	<b>Chapter 6: Biomechanical Analysis.....</b>	<b>205</b>



## Table of Figures

Figure 1 Joint features and their respective haemarthropathy characteristics (adapted from Pulles et al. 2017).	8
Figure 2 Labelled diagram of the bones in the right foot, including joint names (Servier Medical Art) adapted	16
Figure 3 Motions of the foot and ankle(Cazacu and Doroftei 2015) (adapted)	16
Figure 4 3D model of the talus, reconstructed from MRI data. Medial, Anterior and Lateral view labelled (M – medial, L – lateral, A – anterior, P – posterior).	33
Figure 5 Visualisation of differences in MRI sequences on ankles (A) SPACE, (B) T1 weighted, (C) T2 weighted, (D) STIR	35
Figure 6 Sagittal MRI of the talus. Images in rows show 1) medial talus, 2) central talus, and 3) lateral talus. Column A shows the fitting of the arc to calculate Trochlear Tali Arc Length (TaAL), Trochlear Tali Length (TaL) and Talus Height (TaH). Column B shows the fitting of a circle to find Trochlear Tali Radius (TaR). Points A, B and C relate to those set out in Table 5	37
Figure 7 Measurements fitted to a 3D reconstruction of two different tali with different degrees of collapse (green – minimal flattening; red – greater degree of flattening). Showing how the measurements change with a flattened talus. With increased flattening (red): increased TaR; decreased TaL, TaAL and TaH.	39
Figure 8 Outputs of previous studies compared to the non-diseased control group. Patterns show location across the talus: medial - vertical stripe, central - diagonal stripe, lateral - horizontal stripe, location not specified - block colour. Error bars show reported or calculated standard deviation.	43
Figure 9 Change in TaR:TaALm and TaR:TaALl with time in months from the first sequence available. The average trend lines show haemophilic (red dashed) and non-diseased (green dotted) mean values from all eight ankles. The ratios are split into two categories, paediatric/adolescent (first row – paediatric data has not been included in reported stats), and adult (second row). Colour-codes relate to the age bracket the patient fell into at the first MRI sequence: grey/black – paediatric; greens/blues – adolescent; orange –adult. After approx. 40 months 1R moved from adolescent to adult.	51
Figure 10 Changes in TaAL:TaLm and TaAL:TaLl with time in months. Details as described in legend of previous figure.	52
Figure 11 Changes in TaL:TaHm and TaL:TaHl with time in months. Details as described in the legend of Figure 9.	52

Figure 12 (A) Tibial model following resampling and smoothing, (B) Tibial model, smoothed with no resampling, (C) MRI with smoothed tibial (cyan) and talar (green) masks overlaid, demonstrating volume loss when resampling is not carried out. ....	60
Figure 13 Modelling processes within ScanIP (A) segmentation – translucent mask allows underlying MR image to be seen more clearly (cysts were not included in this model while present in the tibia), (B) Smoothing, (C) Cropping, and (D) Meshing. ....	62
Figure 14 (A) material placeholders: white - bone; fuchsia and cyan - cartilage. (B) loading and boundary conditions.....	63
Figure 15 Split layered bone model, A) with translucent uniform thickness overlaying MRI image, and B) reconstructed model with 50% translucency applied to cortical talar layer.....	67
Figure 16 Violin plots comparing A) Tibial, and B) Talar cartilage contact pressures (MPa) distributions in the three ankles in both bone conditions.....	68
Figure 17 Box plots of VMS (MPa) in A) tibia, and B) talus.....	69
Figure 18 Mesh convergence for highest coefficient of friction (0.5); VMS (MPa) in the tibia and talus, and contact pressure (MPa) in the tibial and talar cartilage (quadratic, C3D10H elements).....	73
Figure 19 Mesh convergence for most frequently used coefficient of friction (0.1); VMS (MPa) in the tibia and talus, and contact pressure (MPa) in the tibial and talar cartilage (quadratic, C3D10H elements) .....	73
Figure 20 Mesh convergence for frictionless contact; VMS (MPa) in the tibia and talus, and contact pressure (MPa) in the tibial and talar cartilage (quadratic, C3D10H elements) .....	74
Figure 21 Tibia and Talus models built from (A) axial slices, (B) coronal slices, and (C) sagittal slices - no resampling, all to same degree of smoothing (anterio-medial view).....	77
Figure 22 Views of the talus generated from (A) axial, (B) coronal, and (C) sagittal projections. Same degree of smoothing on all models. Bottom row: coronal segmentation (B) shown from posterior view; axial (A) and sagittal (C) segmentations shown from anterior view .....	77
Figure 23 Morphological differences (highlighted with arrows) between the original and resampled tali, showing smoothing of some morphological features in the resampled talus - Control 11 .....	80
Figure 24 Tibial cartilage contact pressure distribution in original (left) and resampled (right) for control 1 .....	81
Figure 25 Tibial cartilage contact pressure distribution in original (left) and resampled (right) for control 7 .....	81

Figure 26 Tibial cartilage contact pressure distribution in original (left) and resampled (right) for control 11 .....	81
Figure 27 Talar cartilage contact pressure distribution in original (left) and resampled (right) for control 1 .....	82
Figure 28 Talar cartilage contact pressure distribution in original (left) and resampled (right) for control 7 .....	82
Figure 29 Talar cartilage contact pressure distribution in original (left) and resampled (right) for control 11 .....	82
Figure 30 Contact Pressure (MPa) Distribution in A) Tibial Cartilage, B) Talar Cartilage for T1 (left) and T2 (right) weighted models .....	85
Figure 31 Ankle model used to carry out cropping study A) uncropped, and B) with the greatest degree of cropping applied .....	88
Figure 32 Encastre boundary condition on uncropped talus .....	88
Figure 33 Peak (left) and mean (right) bone stresses (MPa) with cropping in the A) tibia, and B) talus .....	89
Figure 34 Changes in peak and mean contact pressure (MPa) in the tibial (left) and talar (right) cartilage with talar cropping .....	90
Figure 35 Area in contact (%) in the tibial and talar cartilage with talar cropping .....	90
Figure 36 changes in talar cartilage Contact Pressure for Ankle 1R with increasing coefficient of friction .....	98
Figure 37 changes in talar cartilage Contact Pressure (MPa) for Ankle 2R and 2L with increasing coefficient of friction .....	99
Figure 38 changes in talar cartilage Contact Pressure (MPa) for Ankle 3R with increasing coefficient of friction .....	99
Figure 39 changes in talar cartilage Contact Pressure (MPa) for Ankle 3L with increasing coefficient of friction .....	100
Figure 40 changes in talar cartilage Contact Pressure (MPa) for Ankle 4L with increasing coefficient of friction .....	100
Figure 41 changes in talar cartilage Contact Pressure (MPa) for Ankle 5R and 5L with increasing coefficient of friction .....	101
Figure 42 Change in mean VMS in the Tibia with time for each ankle .....	103

Figure 43 Change in mean VMS in the Talus with time for each ankle .....	103
Figure 44 Change in mean Cartilage Contact Pressure in the Tibial Cartilage with time for each ankle .....	104
Figure 45 Change in mean Cartilage Contact Pressure in the Talar Cartilage with time for each ankle .....	104
Figure 46 Subchondral bone cyst highlighted on T1 weighted MRI sequence (left) and T2 weighted MRI sequence (right) .....	108
Figure 47 Models generated from images, and the studies carried out from these .....	110
Figure 48 Translation of cyst segmentation on the same MRI slice. A) baseline segmentation from image; B) +0.5mm from baseline; C)+1mm from baseline; D) +1.5mm from baseline; E) +2mm from baseline; F) +2.5mm from baseline; G) +3mm from baseline. ....	113
Figure 49 Sensitivity Study results for A) peak contact pressure, B) mean contact pressure, and C) % area in contact against bulk modulus .....	115
Figure 50 Sensitivity Study results for A) peak, and B) mean VVMS against bulk modulus .....	116
Figure 51 Mean (left) and Peak (right) contact pressures in A) Tibial Cartilage, and B) Talar Cartilage for all 18 models .....	117
Figure 52 Redistribution of pressure in A) Tibial, and B) Talar cartilage for model 1R2 (see appendix for all ankles redistributions). Location of peak contact pressure circled for each cartilage component under the two conditions .....	118
Figure 53 Subchondral bone cyst volumes for tibial cysts (left) and talar cysts (right). ....	119
Figure 54 Total subchondral bone cyst volume against time for four ankles. ....	119
Figure 55 Peak contact pressure in tibial cartilage against tibial cyst volume fraction (left) and talar cyst volume fraction (right) .....	120
Figure 56 Mean contact pressure in tibial cartilage against tibial cysts volume fraction (left) and talar cyst volume fraction (right) .....	121
Figure 57 Peak contact pressure in talar cartilage against tibial cysts volume fraction (left) and talar cyst volume fraction (right) .....	121
Figure 58 Mean contact pressure in talar cartilage against tibial cysts volume fraction (left) and talar cyst volume fraction (right) .....	121
Figure 59 Peak VMS in the tibia against tibial cysts volume fraction (left) and talar cyst volume fraction (right) .....	122

Figure 60 Mean VMS in the tibia against tibial cysts volume fraction (left) and talar cyst volume fraction (right) .....	122
Figure 61 Peak VMS in the talus against tibial cysts volume fraction (left) and talar cyst volume fraction (right) .....	123
Figure 62 Mean VMS in the talus against tibial cysts volume fraction (left) and talar cyst volume fraction (right).....	123
Figure 63 Peak (left) and mean (right) VMS for both the tibia and talus with varying cyst depth.....	125
Figure 64 Peak (left) and mean (right) contact pressure for both the tibial cartilage and talar cartilage with varying cyst depth.....	125
Figure 65 Contact Pressure in the tibial cartilage in A) 1R7C with no offset; C) +1mm offset; D) +1.5mm offset; E) +2mm offset; F) +2.5mm offset; G) +3mm offset.....	127
Figure 66 Contact Pressure in the talar cartilage in A) 1R7C with no offset; C) +1mm offset; D) +1.5mm offset; E) +2mm offset; F) +2.5mm offset; G) +3mm offset .....	127
Figure 67 Foot position at heel strike, mid stance and toe off (right leg) .....	139
Figure 68 Study design for two gait studies, including models used to generate each.....	140
Figure 69 General view (left) and frontal projection (right) with coordinate system and reference point (RP) shown.....	143
Figure 70 Kinematic coupling between reference point and top surface of tibia .....	143
Figure 71 Gait data collected in shoe from haemophilic ankles, and control group average .....	146
Figure 72 Cartilage Contact Pressure (MPa) distribution before load is applied at maximum dorsiflexion. A) Load and Offload in separate time steps, and B) Ramping load in one time step....	148
Figure 73 Cartilage Contact Pressure (MPa) distribution at maximum dorsiflexion. A) Load and Offload in separate time steps, and B) Ramping load in one time step.....	148
Figure 74 Cartilage Contact Pressure (MPa) distribution after maximum dorsiflexion offload. A) Load and Offload in separate time steps, and B) Ramping load in one time step.....	148
Figure 75 Cartilage Contact Pressure (MPa) distribution before load is applied at mid stance. A) Load and Offload in separate time steps, and B) Ramping load in one time step.....	149
Figure 76 Cartilage Contact Pressure (MPa) distribution at mid stance. A) Load and Offload in separate time steps, and B) Ramping load in one time step.....	149
Figure 77 Cartilage Contact Pressure (MPa) distribution after mid stance offload. A) Load and Offload in separate time steps, and B) Ramping load in one time step.....	149

Figure 78 Cartilage Contact Pressure (MPa) distribution before load is applied at maximum plantarflexion. A) Load and Offload in separate time steps, and B) Ramping load in one time step.	150
Figure 79 Change in contact distribution at maximum dorsiflexion between (A) non-diseased, (B) 50% reduced RoM and (C) 80% reduced RoM .....	151
Figure 80 Change in contact distribution at maximum plantarflexion between (A) non-diseased, (B) 50% reduced RoM and (C) 80% reduced RoM .....	152
Figure 81 Change in contact distribution between (A) Heel Strike, (B) Flat Foot, (C) Mid Stance, (D) Heel Off and (E) Toe Off in 4L .....	153
Figure 82 Contact distribution at Heel Strike in (A) Control, (B) 3R, (C) 3L, (D) 4L, and (E) 6R ...	154
Figure 83 Contact distribution at Flat Foot in (A) Control, (B) 3R, (C) 3L, (D) 4L, and (E) 6R .....	154
Figure 84 Contact distribution at Mid Stance in (A) Control, (B) 3R, (C) 3L, (D) 4L and (E) 6R ...	155
Figure 85 Contact distribution at Heel Off in (A) Control, (B) 3R, (C) 3L, and (D) 4L .....	155
Figure 86 Contact distribution at Toe Off in (A) Control, (B) 3R, (C) 3L, (D) 4L, and (E) 6R.....	156
Figure 87 Geometry used for material sensitivity study before application to whole ankle model....	188
Figure 88 changes in tibial contact pressure (MPa) in Ankle 1R with increasing coefficient of friction .....	189
Figure 89 changes in tibial contact pressure (MPa) in Ankle 2R and 2L with increasing coefficient of friction.....	189
Figure 90 changes in tibial contact pressure (MPa) in Ankle 3R with increasing coefficient of friction .....	190
Figure 91 changes in tibial contact pressure (MPa) in Ankle 3L with increasing coefficient of friction .....	190
Figure 92 changes in tibial contact pressure (MPa) in Ankle 4L with increasing coefficient of friction .....	191
Figure 93 changes in tibial contact pressure (MPa) in Ankle 5R and 5L with increasing coefficient of friction.....	191
Figure 94 changes in contact pressure (MPa) in A) tibial cartilage, and B) talar cartilage in Ankle 1RC with increasing coefficient of friction .....	192
Figure 95 changes in contact pressure (MPa) in A) tibial cartilage, and B) talar cartilage in Ankle 2RC and 2LC with increasing coefficient of friction .....	193

Figure 96 changes in contact pressure (MPa) in A) tibial cartilage, and B) talar cartilage in Ankle 3RC with increasing coefficient of friction.....	194
Figure 97 Mean contact pressure (MPa) in the tibial cartilage plotted against morphological measurements.....	195
Figure 98 Mean contact pressure (MPa) in the talar cartilage plotted against morphological measurements.....	196
Figure 99 Change in contact distribution between (A) Heel Strike, (B) Flat Foot, (C) Mid Stance, (D) Heel Off and (E) Toe Off in non-diseased control ankle model.....	205
Figure 100 Individual gait data trials for ankle 4L, with grand mean used as input data (green markers) .....	206

## Table of Tables

Table 1 Global Self-Reported Comorbidities from 230 Young Adults (18-30 years of age) with Haemophilia (Witkop et al. 2015).....	11
Table 2 The compatible scales for progressive and additive MRI assessments of haemophilic arthropathy, where additive score is calculated from all imaging manifestations present in joint (Lundin et al. 2012) .....	14
Table 3 Information on data gathered for each patient and chapter numbers (Ch #).....	29
Table 4 Information on the chronologically sequential MRI data collected from eight of the haemophilic ankles .....	30
Table 5 Measurements taken for each image- medial, central, and lateral measurements were each denoted with m, c or l – i.e. Lateral Trochlear Tali Length = TaLl .....	36
Table 6 Ratios and their anticipated changes with talar collapse.....	38
Table 7 Error (%) between adjacent ratios across the talus for one MRI sequence per patient.....	45
Table 8 Control group and haemophilic (adult) group mean values for each ratio at the three locations (m-medial, c-central, l-lateral), and p-values from T-tests (* indicates significant differences).....	50
Table 9 Behaviour of the ratios for the 8 haemophilic ankles – Considering the expected differences from the non-diseased control, those that behaved as anticipated (from Table 6) are highlighted in green. E.g. In the central images, should the haemophilic ankle behave as anticipated: $TaR:TaALc > 0.56$ , $TaAL:TaLc < 1.15$ , and $TaL:TaHc > 4.21$ .....	51
Table 10 Cortical bone thickness for the three ankle models .....	66

Table 11 Minimum, maximum and mean VMS (MPa) in both the homogenous and split bone models for the three ankles.....	69
Table 12 Mesh convergence tests to find appropriate ratio between mesh sizes for cartilage and bone .....	71
Table 13 Mesh coarseness values sensitivity analysis .....	72
Table 14 Volumes (mm <sup>3</sup> ) of tibia and talus from the three different fields of view .....	77
Table 15 Volumes (mm <sup>3</sup> ) of the original slice thickness and resampled models for all bone and cartilage components .....	79
Table 16 Error (%) for the cartilage contact pressure outputs between the resampled and original slice resolution in the three control models.....	80
Table 17 Error (%) for the VMS outputs in the bone between the resampled and original slice resolution in the three control models.....	80
Table 18 Volumes (mm <sup>3</sup> ) from the segmentations from T1 and T2 .....	84
Table 19 Peak and Mean Results (MPa) comparing the T1 and T2 results for 3L7 .....	85
Table 20 Patient Weight and Total Force for all models .....	96
Table 21 Sensitivity Analysis Parameters for cyst material properties (ordered by increasing equivalent bulk modulus) .....	112
Table 22 Cyst Volume Fraction for each time point (left to right with disease progression).....	119
Table 23 Spearman's correlation (r <sub>s</sub> ) for total cyst volume against peak and mean stress outputs in the tibia and talus. Significant correlations marked with * .....	120
Table 24 Tibia results for Spearman's correlation (r <sub>s</sub> ) correlations for stress outputs against tibial cyst volume fractions (vol%) and talar cyst vol%. Significant correlations marked with * .....	122
Table 25 Talus results for Spearman's (r <sub>s</sub> ) correlations for stress outputs against tibial cyst volume fraction (vol%) and talar cyst vol%. Significant correlations marked with * .....	123
Table 26 Spearman's correlation (r <sub>s</sub> ) values for the cyst depth study, assessing for correlation between cyst depth and peak and mean outputs. Significant values marked with * .....	126
Table 27 Example boundary and loading condition for the rotation and loading steps, where A is displacement to make contact $\theta$ is joint angle, in radians, and F is force calculated based on patient weight. Loads in tibial axis direction follow the nodal rotation from rotation step .....	144
Table 28 Load (N) applied to gait model for each haemophilic ankle, calculated from GRF .....	147



Table 29 percentage decreases in contact pressure (peak and mean), and increases in contact area between non-diseased gait and 80% reduced RoM. Including averages calculated for each output. Those that did not behave as expected are highlighted in red .....	151
Table 30 Joint Angles (degrees) at each point simulated in the gait cycle .....	152
Table 31 Material properties from sensitivity studies carried out on simplified model.....	187
Table 32 SBC volumes, and respective tibial cartilage contact pressure redistributions.....	197
Table 33 SBC volumes, and respective talar cartilage contact pressure redistributions.....	201

## Abbreviations

2D – Two Dimensional

3D – Three Dimensional

BMD – Bone Mineral Density

BMI – Body Mass Index

CT – Computed Tomography

FE – Finite Element

FEA – Finite Element Analysis

FEM – Finite Element Modelling

GRF – Ground Reaction Force

HA – Haemarthropathy

HJHS – Haemophilia Joint Health Score

IPSG – International Prophylaxis Study Group

JA – Joint Angle

MRI – Magnetic Resonance Imaging

OA – Osteoarthritis

PwH – People with Haemophilia

RoM – Range of Motion

SBCs – Subchondral Bone Cysts

VMS – Von Mises Stress

# CHAPTER 1

## INTRODUCTION

# CHAPTER 1: INTRODUCTION

## 1.1 Introduction

Haemophilia is a genetic disorder, caused by a deficiency in coagulation factors; commonly presenting in the form of recurrent bleeds, eighty percent of which occur in the musculoskeletal system (Kasper 2008; Rodriguez-Merchan 2010). These bleeds occur most commonly in the ankle joint (Stephensen *et al.* 2009). The prevalence of ankle bleeds is a completely different picture to osteoarthritis (OA), where the prevalence in the ankle (3.4%) (Paget *et al.* 2021) is considerably lower than the prevalence in the knee (12.2%) and the hip (7.4%) (Quintana *et al.* 2008). Around 70-80% of OA in the ankle is post traumatic (Paget *et al.* 2021), this may be more directly related to the high tendency for bleeds in the ankles, as these are hypothesised to relate to high intra-articular stresses (Buckwalter and Saltzman 1999) or trauma.

Treatment for haemophilia can cost upwards of \$500,000 per year; around 90% of these costs are associated with clotting factor replacement (Zhou *et al.* 2015). This treatment is not a cure, rather a bleed management strategy, meaning these are lifelong associated costs. Despite clotting factor replacement, bleeds still occur (Kempton 2021) and initiate consequent joint damage.

Repeated joint haemorrhages initiate joint degeneration known as haemarthropathy (HA). HA has commonalities with both rheumatoid- and osteo- arthritis (Blobel *et al.* 2015; Roosendaal *et al.* 1999). It has been seen that there is a progressive nature to HA, with evidence that even a small number of bleeds can trigger irreversible joint damage (Rodriguez-Merchan 2012). This is worsened by the loading of the joints when a bleed has occurred (van Meegeren *et al.* 2013).

Patient specific Finite Element Analysis (FEA) can be used to better understand the influence of this joint loading, and potential interventions to alleviate this. Previously published models, on non-haemophilic cohorts, have considered interventions commonly used in patients with ankle HA, such as arthroplasty, or orthotic design. Implementing such models on the ankles of people with haemophilia (PwH), would allow for the joint stresses to be considered following the intervention, without any risk of inducing a joint bleed.

The most commonly known, and widely used tool for assessing haemarthritic changes is the Haemophilia Joint Health Score (HJHS), which is a clinical measure of joint health and used to monitor joint changes from paediatrics through to adults. However, the HJHS is not validated in adults, only in under 18s (Feldman *et al.* 2011). Three versions of the HJHS exist, the latest (version 2.1) assesses swelling (0-3), duration of swelling (0-1), muscle atrophy (0-2), crepitus on motion (0-2), flexion loss (0-3), extension loss (0-3), joint pain (0-2) and strength (0-4). This score is used for ankles, knees and elbows, as well as a global gait score (0-4). Each joint is scored between 0-20, with a higher score indicating worse joint health (Kuijlaars *et al.* 2020). The total HJHS score is from 0 to 124 points, as it is all six joints (two ankles, two knees, two elbows), plus the global gait score. This scoring system is not sensitive to early stages of HA, or for detecting structural changes.

A second assessment of joint health is the International Prophylaxis Study Group (IPSG) MRI scoring system; MRI data is routinely collected in haemophilic patients to assess these structural changes that HJHS is not sensitive to. Multiple studies have found no correlation between the two scores, with highly abnormal MRI findings over a wide spectrum of clinical scores (Manco-Johnson *et al.* 2007). This finding suggest that imaging abnormalities may have limited bearing on clinical joint status, which may be driven at least in part by individual pain perception and functional mobility, rather than a true reflection on joint health.

The biological response of the tissues in the joint space – synovium and cartilage – have been widely researched with regards to their role in the disease pathogenesis. The wider story regarding the implications of these changes on joint health is however inconclusive. It is believed that there are non-haematological factors that also influence the progression towards HA (McCarthy *et al.* 2015) due to the fact that treatment of haemophilia has been optimised, yet the clinical goals of zero bleeds and no consequent joint damage is not being realised.

This unmet clinical need is particularly applicable to the ankle joint, as it is unclear why bleeds target this specific joint at a higher rate than the knee and elbow. No clear answer can be found in the haematological aspects of the disease, hence the importance of investigating non-haematological factors, such as joint stresses. In a survey of clinicians in the haemophilia community, a wide range of potential factors influencing the development of HA in the ankle were seen. In particular, 94% (29/31) believed the specific foot and ankle biomechanics were key to the disease progression (McCarthy *et al.* 2015); this was the greatest consensus on the perceived importance in the survey. This may be due to the growing appreciation for the fact that minor alterations to – or imbalances in – biomechanics can predispose the general

population to injury or joint damage; a phenomenon that is exacerbated in unhealthy tissue (Millar 2003).

The key features of HA present in various medical imaging modalities; this is taken advantage of in a clinical setting, where medical imaging is used to diagnose, stage, and track disease progression. The medical images are not utilised in prognosis, as the disease progression varies between individuals; clinicians believe there are over 40 non-haematological factors that influence the musculoskeletal response to intraarticular bleeds (McCarthy *et al.* 2015). The non-haematological factor to be investigated in this computational study is the influence of the morphology on the disease response, through the joint stresses incurred in the ankle.

## 1.2 Literature Review

### 1.2.1 Haemophilia

Haemophilia is a sex-linked genetic disorder, resulting in a deficiency of plasma factor coagulant activity. There are multiple bleeding disorders that fall under the umbrella term Haemophilia. The incidence of Haemophilia A, caused by factor VIII deficiency, is highest at approximately one in every 5,000 male births. Haemophilia B is around one quarter of that. It is estimated that approximately 1.1 million men globally suffer some form of haemophilia (Iorio *et al.* 2019).

These deficiencies or dysfunctions of clotting factors cause people with haemophilia (PwH) to suffer internal bleeds, or slow but persistent bleeds if there are lacerations to the skin. Eighty percent of internal haemorrhages occur in the musculoskeletal system, with the other 20% taking place in the central nervous system and other organ systems (Kasper 2008; Rodriguez-Merchan 2010).

Symptoms of haemophilia commonly present in the early years, with joint haemorrhages to the ankle occurring from as young as 24 months, in line with early ambulation in the child (Rodriguez-Merchan 2012; Rodriguez-Merchan 2006). Given the young age haemorrhages initiate in patients, it is often difficult to control the outcome of bleeds. The bleeds are often unpredictable and recur in short spaces of time (Kasper 2008). The main aim of musculoskeletal treatments is to slow the progression of HA by protecting the joints from mechanical stresses. Key ways of achieving this are: weight management (Wong *et al.* 2011); orthotics (Brouwer *et al.* 2014; Kasper 2008); physical therapy (Pulles *et al.* 2017); strengthening of supporting muscles, and modification of sporting activities (Seuser *et al.* 2007); and in some cases joint distraction (van Valburg *et al.* 1999; Xu, Zhu and Xu 2017).

Treatment for haemophilia comes in the form of clotting factor infusions, and can be either preventative, or on-demand depending on disease severity. In prophylaxis, a preventative treatment type, regular infusions aim to achieve zero bleeds. On-demand treatment is used in less severe haemophilia, and is used following an episode of prolonged bleeding. Neither treatment is 100% successful at achieving zero bleeds, with musculoskeletal bleeds this can lead to joint health complications.

### 1.2.2 Haemophilic Joint Disease

Around 90% of individuals with severe haemophilia, who experience musculoskeletal bleeds, go on to suffer chronic degenerative changes in at least one major joint by the second or third

decade of life (Rodriguez-Merchan 2010). PwH can have recurrent bleeds in multiple joints; the joint is defined clinically as a target joint when four or more bleed recurrences affect the same joint in a six-month time period (Engl, Patrone and Abbuehl 2016; Geraghty 2012). The annual bleed rate of people with severe haemophilia using on-demand treatment has been investigated; these bleed rates vary widely from mean values ranging from 9 to 18 (Perrin *et al.* 1996; Van Den Berg *et al.* 2001), to median values as high as 44 bleeds per year (Valentino *et al.* 2012).

These bleed rates relate to spontaneous acute haemorrhages; an acute bleed is the most common bleed type, defined as “bleeds with loss of clinical function, pain and/or swelling requiring more than one infusion of clotting factor” (Den Uijl *et al.* 2011), and is most closely associated with degenerative changes within a joint. However, chronic microbleeds can also occur, and have been investigated for their detrimental effect. In a previous clinical study (van Meegeren *et al.* 2013) joint damage was observed in PwH in the absence of reported acute bleeds. The reaction to the subclinical bleeds was less than that induced by clinically evident bleeds (where the total volume of blood the joints were exposed to was similar) there was evidence of biological reactions in both bleed types (van Meegeren *et al.* 2013).

Animal models have shown that a single joint haemorrhage can result in lasting adverse changes in chondrocyte activity and cartilage matrix integrity (Rodriguez-Merchan 2010), which in turn infers, depending on the mechanism of damage, that it could only take one bleed to initiate joint degeneration.

Mechanical factors are hypothesised to also be important in the onset of haemarthrosis, due to the more frequent occurrence of bleeds into the legs than the arms, and the predisposition to joint bleeds on the dominant side (Madhok, York and Sturrock 1991; Hooiveld *et al.* 2003).

This has led to investigations regarding the influence of loading after this blood exposure; where it has been seen that it is blood exposure in combination with loading that results in progressive degenerative joint damage (Hooiveld *et al.* 2004; Rodriguez-Merchan 2012). Due to the implications of these bleeds on cartilage matrix turnover and integrity, and cartilage’s incapacity for intrinsic repair, the loading of cartilage is therefore key to disease initiation (Rodriguez-Merchan 2012).

A consensus has not been reached on the order in which HA occurs, though it is understood to be multifactorial, with changes occurring in the synovium, bone, cartilage, and blood vessels (Knobe and Berntorp 2011). There is a known biological response of the synovium to the iron in the blood, which induces an inflammatory response (Gomperts *et al.* 2017; Knobe and



Berntorp 2011; Rodriguez-Merchan 2010; Rodriguez-Merchan 2006; Roosendaal and Lafeber 2006). This inflammation has a subsequent implication on the cartilage, due to the increased pressure within the joint (Gomperts *et al.* 2017), which has been linked to cartilage loss (Anderson *et al.* 2011b). The cartilage degeneration results not only from the synovial dependent mechanism, but also independent mechanisms – there is a direct, harmful influence from haemosiderin depositions. Haemosiderin is the iron-storage complex within blood; the exposure of cartilage to iron not only causes extra-cellular matrix degeneration, but also apoptosis of the chondrocytes responsible for the matrix synthesis (Pulles *et al.* 2017). It can be seen in Figure 1 that the reactions of the synovium, cartilage and bone are all interlinked. The implication then is that the progression of the arthritic changes will elicit a response in all components of the joint. Whereas in osteoarthritis (OA), it is the fully eroded cartilage surface, and supervening secondary osteoarthritic changes (Madhok *et al.* 1988) where subchondral bone is exposed, that allow the joint to tend towards sclerosis and collapse.

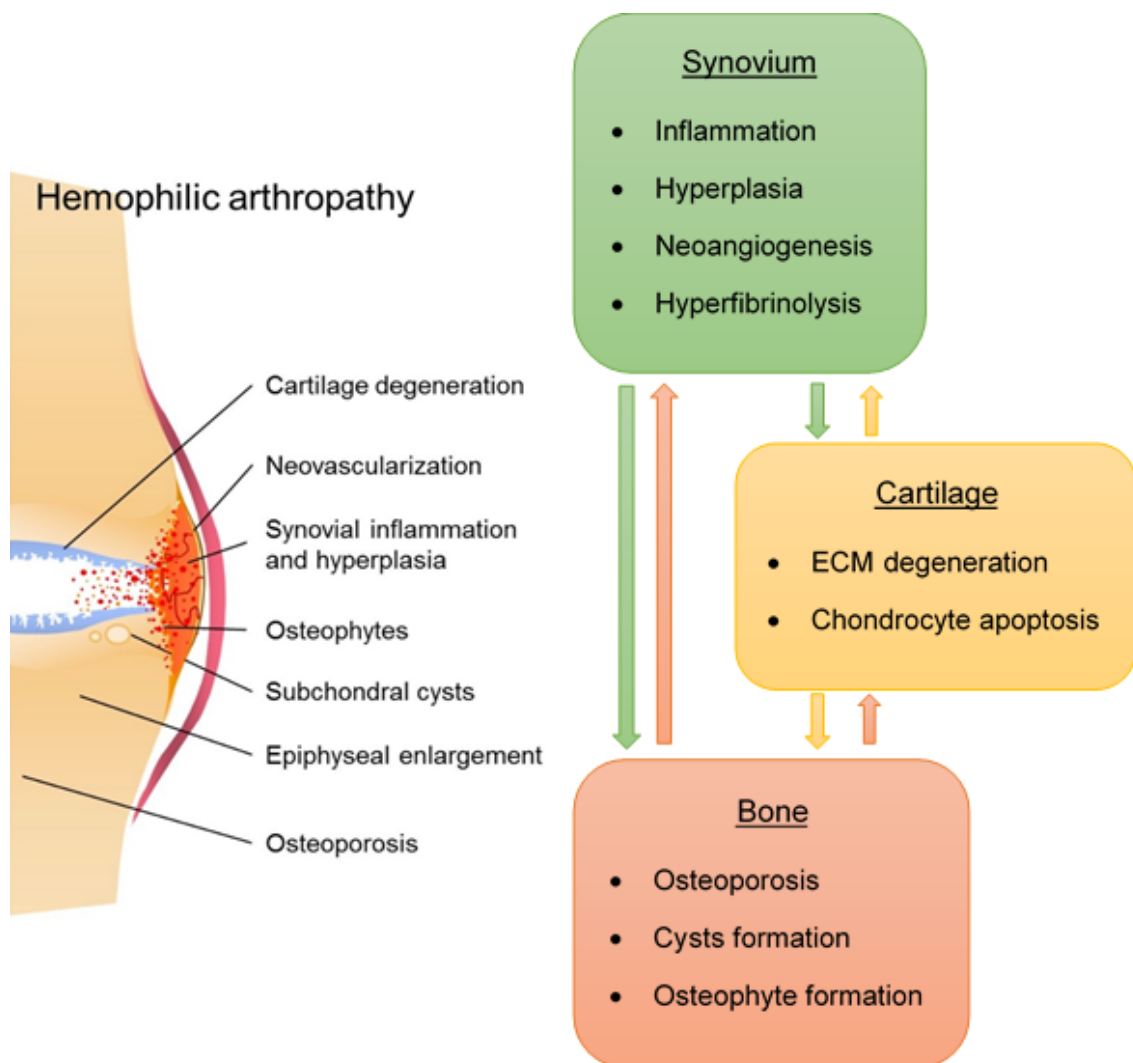


Figure 1 Joint features and their respective haemarthropathy characteristics (adapted from Pulles *et al.* 2017).

The pathogenesis of haemophilic joint damage is unclear, and still not fully understood (Madhok *et al.* 1988; Roosendaal *et al.* 1999; Roosendaal and Lafeber 2006). A consensus on the role of intra-articular bleeds on the propagation of damage has been reached (Roosendaal *et al.* 1999), however, the order in which the key degenerative changes occur is uncertain.

Some groups argue that the long-lasting damage to the cartilage is independent of synovial changes (van Meegeren *et al.* 2013), with arthritic changes in the absence of inflammatory changes (Madhok *et al.* 1988). While others have found evidence that the cartilage changes are amplified by the inflammatory response of the synovium (Roosendaal *et al.* 1999). A third suggestion is that the inflammatory response of synovitis is a key aspect in the onset of HA (Knobe and Berntorp 2011; Rodriguez-Merchan 2006; Roosendaal and Lafeber 2006).

The combination of characteristics of both rheumatoid- and osteo-arthritis (Roosendaal *et al.* 1999; Blobel *et al.* 2015) would uphold the increased rate of degeneration seen with HA in clinical practice (Jansen *et al.* 2008).

Haemosiderin depositions are commonly reported in the synovial fluid, however, have also been found to occur in cartilage (Jansen *et al.* 2009; Lafeber, Miossec and Valentino 2008; Valentino and Hakobyan 2006; van Vulpen, Holstein and Martinoli 2018). The deposition of iron in the synovium is hypothesised to be part of the onset of the cartilage loss and bone surface erosion also identified in the IPSTG MRI scoring system. In haemochromatosis, joint destruction is caused by iron overload, with a reduced bone quality linked to an increase in osteoclast activity.

The iron depositions from the blood directly impacts the tissues in the joint space (Pulles *et al.* 2017), with preclinical studies demonstrating detrimental effects of iron on all components of the joint (synovial inflammation, chondrocyte death, and impaired osteoblast function) (van Vulpen, Holstein and Martinoli 2018). In haemophilia, iron depositions in cartilage is believed to play an important role in direct and continued cartilage toxicity and destruction, which is likely to be directly linked with the progression to HA (von Drygalski *et al.* 2019). The consequent changes to mechanical properties in these tissues, have however, not yet been ascertained.

The changes that occur at bone level occur due to a disturbed equilibrium in bone resorption and formation; this leads to a decrease in bone mineral density (BMD) and osteoporosis (Kempton, Antonucci and Rodriguez-Merchan 2015; Wallny *et al.* 2007). This damage is largely considered to only occur at the late stages of disease progression. However, murine

studies have demonstrated excessive bone remodelling as early as two weeks after joint bleeds were induced (Lau *et al.* 2014; Sørensen *et al.* 2016).

The negative biological response in bone would correspond with the osteoporotic bone quality reported in literature (Kempton, Antoniucci and Rodriguez-Merchan 2015; Kovacs 2008; Wallny *et al.* 2007; Goldscheitter *et al.* 2021). MRI studies have found haemosiderin depositions present in between the bone and the cartilage (von Drygalski *et al.* 2019), which may influence the bone biology as seen in haemochromatosis.

It is still disputed whether the bone changes are directly or indirectly linked to the bleeds; there are strong similarities between the bone changes in haemophilic arthritis, and other forms of arthritis. Peak BMD is primarily determined by genetic factors with contributions from general health, nutrition, physical activity, concurrent illnesses and medication during growth; hence, it is unsurprising that BMD is less in PwH than in the general population.

It has been shown in accelerometer studies that movement behaviour is altered in PwH (Timmer *et al.* 2018). The adaptation appears to relate to the severity of haemophilia, with adults with severe haemophilia taking part in less walking and running activities, while those with mild or moderate haemophilia adapting their activity to a lesser extent. Therefore, the decrease in BMD could be linked with this disuse of the joint; fear and/or pain related decline in physical activity (Gringeri, Ewenstein and Reininger 2014); or avoidance of weight bearing physical activity during periods of haemorrhage and recovery (Kovacs 2008) as per clinical guidance.

Alongside the difference in BMD in PwH, it has also been reported that joint inflammation in the growing years stimulates excess growth at the ends of the long bones, which can lend itself to limb-length discrepancies, and morphological abnormalities at the ends of bones.

Talar collapse is also seen in approximately half of patients, and has previously been linked to avascular necrosis (Macnicol and Ludlam 1999), low BMD (Steinhorn and Vahlensieck 2000), and osteopenia in children with haemophilia (Kovacs 2008). This talar collapse rarely presents alone, often presenting at the same time as sclerosis and joint space narrowing; the exact mechanism of collapse are unconfirmed, as they are likely influenced by numerous factors, which happen concurrently to produce varying outcomes.

These morphological changes to the bone can in turn propagate further cartilage damage through malalignment, and heightened contact pressures, demonstrating how highly linked the changes in the three joint components are.

### 1.2.2.1 Consequences of Haemophilic Joint Disease

The majority of incidences of haemophilia are present at birth, this causes the affected individual to suffer recurrent bleeds from a young age, as well as experiencing comorbidities (Table 1) in the early years. As the mortality rate of haemophilia has decreased in recent years with improved treatment options, these comorbidities have become increasingly long term.

Table 1 Global Self-Reported Comorbidities from 230 Young Adults (18-30 years of age) with Haemophilia (Witkop *et al.* 2015)

Comorbidity	Related to haemophilia, %	Unrelated to haemophilia, %	Any, %
Arthritis	40	2	42
Chronic Pain	27	6	33
Viral Infections	21	9	27
Psychological/psychiatric	26	26	43
Cardiovascular conditions	7	15	19
Metabolic conditions	7	13	20

The percentages are all self-reported, so may not accurately represent the true percentages, for example, the self-reported incidences of arthritis are 40%, while literature quotes around 90%. Imaging manifestations, especially in the early stages of HA, are not always in line with the symptoms presented by a patient. Patient joint health scores using the World Federation of Haemophilia physical examination score have also shown insensitivity to the early stages of HA (Lambert *et al.* 2014).

The prevalence of patient reported arthritis increases with age (60% in PwH over 40 years of age), which demonstrates the progressive problematic nature of this comorbidity. This, along with pain, was seen to regularly interfere with daily activities in 86% of respondents (Witkop *et al.* 2015). Although chronic pain was reported at a much lower rate, these comorbidities cause PwH to modify (Lobet *et al.* 2012) or not participate in activities (Timmer *et al.* 2018).

HA can be extremely debilitating; pain, loss of mobility, deformities, and disuse atrophy of adjacent muscles regularly coincide with disease progression. The most common deformities affecting the ankle are: fixed plantar flexion due to degeneration of the anterior part of the ankle; varus hindfoot due to malalignment of the subtalar joint; and valgus rotations of the ankle due to differential overgrowth of the distal tibial epiphysis during adolescence (Rodriguez-Merchan 1996; Rodriguez-Merchan 2006) or progressive arthropathy during

maturity (Rodriguez-Merchan 2006). These deformities are initially correctable, however, eventually become fixed. Morphological variations will alter the biomechanics of the ankle, magnifying the stresses transmitted to the joint. This in turn may be a risk factor for development and progression of joint disease (Tümer *et al.* 2016), given compromised tissues do not respond to forces in the same way healthy tissues do (Millar 2003).

Gait analysis also suggests that PwH adapt their walking strategy in order to alleviate pain (Lobet *et al.* 2012), or where range of motion (RoM) is reduced, they may walk slower than non-diseased peers in order to mediate joint load reduction (Mundermann *et al.* 2004) and maintain metabolic power in the normal physiological range (Walters and Mulroy 1999).

This adaptation to activity in PwH, however, could be detrimental due to the relationship between a sedentary lifestyle and high body mass index (BMI); it has been seen that overweight and obesity rates within haemophilia are similar to – and in certain subsets even higher than – those of the general population (Wong *et al.* 2011). Obesity increases the risk of arthritis and musculoskeletal pain (Felson *et al.* 1987; Pottie *et al.* 2006), and has been linked to impaired quality of life and premature mortality (Kahan *et al.* 2017).

As with many diseases, the early identification of joint disease is vital to initiate, or modify, treatment in order to prevent progressive joint damage. Hence more sensitive and precise methods are required in order to detect worsening joint disease in the absence of clinical impairment, and detect more subtle differences in disease pathogenesis, including differences in outcomes of treatment (Lambert *et al.* 2014; Lobet *et al.* 2017).

#### *1.2.2.2 Manifestations in Medical Imaging*

Imaging techniques are used to diagnose and stage HA. Both two dimensional (2D), and three dimensional (3D) methods are used in clinical practice. A combination of X-Ray, Ultrasound, Magnetic Resonance Imaging (MRI), and Computed Tomography (CT) are used to assess joint health in PwH. CT is considered the gold standard for imaging dense structures such as bone, while MRI is more appropriate for soft tissues.

Only MRI can assess all structures of a joint, including cartilage, ligaments, muscle, cortical and trabecular bone, bone marrow and synovium (Hayashi, Roemer and Guermazi 2016). It is therefore the most sensitive (Cross, Vaidya and Fotiadis 2013; Den Uijl *et al.* 2011; Zukotynski *et al.* 2007) and complete (Cross, Vaidya and Fotiadis 2013) option for the detection and

diagnosis of HA. When utilising conventional radiography, or CT, cartilage is not visualised well; this in turn makes MRI sequences more suitable given the traditional view that articular cartilage is the central feature of degenerative joint disease, and primary target for intervention and measurement (Roemer *et al.* 2014). 3D imaging such as MRI is advantageous over 2D imaging due to its ability to clearly demonstrate the extent, shape, and exact location of features in any slice (Cohen *et al.* 2015). When considering the complex anatomy of the ankle – where there is a significant amount of structural overlap – this means that manifestations can be associated with a specific morphological feature.

The IPSSG have created an MRI assessment scale using the six main imaging manifestations of HA. The scale is based on the predicted pathogenesis of HA starting with synovial changes, then progressing to cartilage and bone changes. The MRI scale was introduced in order to improve early diagnosis in both haemophilia A and haemophilia B (Lundin *et al.* 2012), as the joint changes are similar in their clinical presentation and image findings (Jaganathan, Gamanagatti and Goyal 2011).

The changes within the bone are categorised as surface erosion, or subchondral bone cysts in that order; however, it is still much debated in which order these bone manifestations occur (Jelbert, Vaidya and Fotiadis 2009). Subchondral bone cysts (SBCs) and haemophilic pseudotumours are varieties of bone tumours that occur as complications of haemophilia. Pseudotumours are rare, occurring in less than 2% of individuals with haemophilia A or B (Purkait *et al.* 2014). SBCs are a much more common presentation. In adults, both types of tumour occur most commonly in the pelvis and long bones of the lower extremities, whereas the hands and feet are more often affected in children (Geyskens *et al.* 2004; Mittal *et al.* 2011; Purkait *et al.* 2014).

Table 2 The compatible scales for progressive and additive MRI assessments of haemophilic arthropathy, where additive score is calculated from all imaging manifestations present in joint (Lundin *et al.* 2012)

	Progressive Scale	Additive Scale
<i>Effusion / Haemarthrosis</i>		
Small	(1)	
Moderate	(2)	
Large	(3)	
<i>Synovial Hypertrophy</i>		
Small	(4)	(1)
Moderate	(5)	(2)
Large	(6)	(3)
<i>Haemosiderin</i>		
		(1)
Small	(4)	
Moderate	(5)	
Large	(6)	
<i>Changes of subchondral bone or joint margins</i>		
Any surface erosion	(7)	(1)
Any surface erosion in at least two bones		(1)
Half or more of the articular surface eroded in at least one bone	(8)	(1)
Half or more of the articular surface eroded in at least two bones		(1)
At least one subchondral cyst	(7)	(1)
More than one subchondral cyst	(8)	(1)
Subchondral cysts in at least two bones		(1)
Multiple subchondral cysts in each of at least two bones		(1)
<i>Cartilage Loss</i>		
Any loss of joint cartilage height	(9)	(1)
Any loss of joint cartilage height in at least two bones		(1)
Any loss of joint cartilage height involving more than one-third of the joint surface in at least one bone		(1)
Any loss of joint cartilage height involving more than one-third of the joint surface in at least two bones		(1)
Full-thickness loss of joint cartilage in at least some area in at least one bone	(10)	(1)
Full-thickness loss of joint cartilage in at least some area in at least two bones		(1)
Full-thickness loss of joint cartilage involves at least one-third of the joint surface in at least one bone		(1)
Full-thickness loss of joint cartilage involves at least one-third of the joint surface in at least two bones		(1)

The correlation between MRI scores and lifetime number of bleeds is weak (Den Uijl *et al.* 2011; Manco-Johnson *et al.* 2007). High MRI scores have been associated with joints with no clinically evident bleeds, while other joints with more than 10 clinically evident bleeds have not shown any signs of joint damage (Manco-Johnson *et al.* 2007). These findings do not devalue the use of MRI scoring, but show the variability in joint degeneration between patients,

and supports the hypothesis that joint damage can be initiated without clinically evident bleeds (van Meegeren *et al.* 2013).

When considering the correlation between joint scoring systems (HJHS and IPSPG MRI scores) and relaxation times is strongly negative (von Drygalski *et al.* 2019); whereas, in non-haemophilic populations, elevated T2 signal intensity has been considered to represent irreversible damage to the extracellular matrix – meaning there would be a positive correlation between T2 relaxation and joint status (Mosher and Dardzinski 2004). These results contradict one another; this may be due to the iron accumulations found in cartilage, which would decrease the T2 relaxation time. These findings suggest it is reasonable to assume that haemarthritic cartilage would not behave in the same way as osteoarthritic cartilage, as this iron loading would likely have some impact on behaviour. To date there is no knowledge about the extent of iron accumulation in cartilage of haemophilic joints in relation to joint status, function or dynamics of joint deterioration (von Drygalski *et al.* 2019). It is likely that the biological response to iron deposited in cartilage, similar to the synovium, will play an important role in the direct and continued toxicity, and consequent progression to HA; however, in order to relate this information to the disease stage, additional imaging sequences – where iron deposits in cartilage can be visualised – and a clear relationship between the T2 signal intensity and cartilage property would need to be identified.

### 1.2.3 Anatomy and Function of the Ankle

The ankle is prone to the complications of HA due to its complexities. The rearfoot is made up of two joints, the talocrural joint and the subtalar joint. These joints consist of four main bones (Figure 2). The articulating surfaces of the tibia, fibula, talus and calcaneus all influence the RoM in dorsiflexion/plantarflexion, pronation/supination, and inversion/eversion (Figure 3) (O'brien and Freund 2002), as well as the distribution of forces from the body onto the ground. When ‘the Ankle’ is referred to throughout this thesis, it is discussing the talocrural joint, which is also known as the ‘True Ankle Joint’.



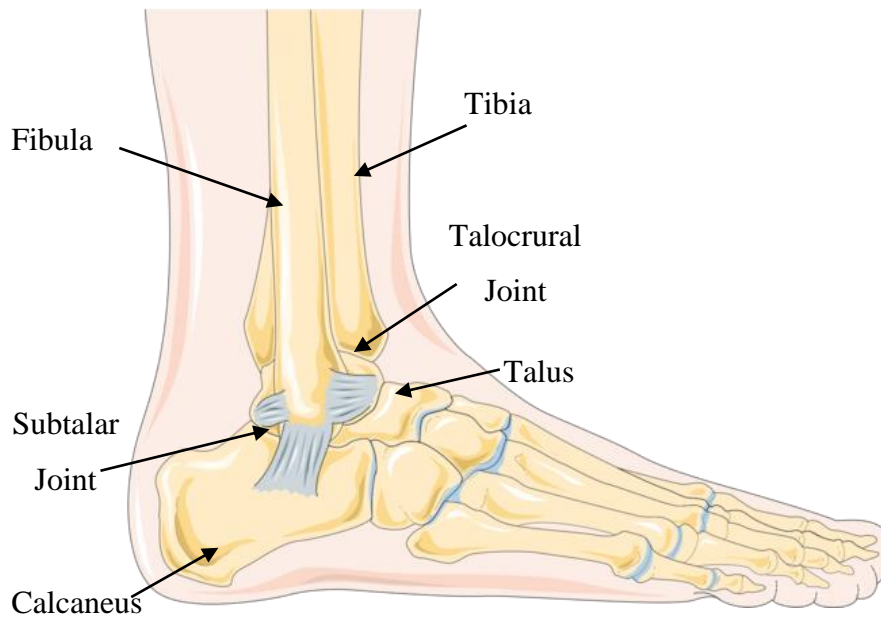


Figure 2 Labelled diagram of the bones in the right foot, including joint names (Servier Medical Art) adapted

The bones of the foot assume adult shape by the age of 6-8 (Jaffe and Laitman 1982), with little morphological variation in the talus from the age of three (Nakai *et al.* 2000). Male bone maturity in the foot, including the calcaneus but not the rest of the ankle, was found to occur around 12.5 years (Whitaker *et al.* 2002). However, it has previously been seen that the calcaneus is commonly the last to be fully formed (Donatelli 1996). Ossification of the bones in the rearfoot – i.e. the ankle – reaches completion around the age of 20 in males; however, the tibia, fibula and talus all tend to be fully formed between the age of 17 and 18 (Donatelli 1996).

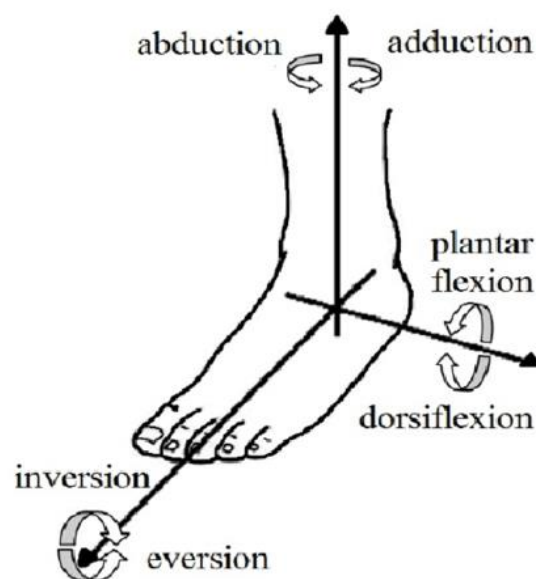


Figure 3 Motions of the foot and ankle (Cazacu and Doroftei 2015) (adapted)

Normal geometry of the articulating surfaces is important to the maintenance of joint health, and consequent normal biomechanics. Abnormalities in the joint congruity – such as malalignment, arthrodesis, or tilting – may alter the gait and hence the forces being transmitted through the foot and ankle.

The surfaces of the articulating geometries of the ankle have a thin layer (~1-2mm) of articular cartilage coating them (Saltzman *et al.* 2005; Sugimoto *et al.* 2005), and the entire structure is encapsulated by a fibrous capsule, which is attached just beyond the articular margins except anteriorly and inferiorly, where it attaches to the neck of the talus (O'Brien and Freund 2002). Within the joint space is the synovial fluid, which lubricates the joint in order to eliminate frictional forces. The principal function of articular cartilage is to provide a smooth, lubricated surface for articulation and to facilitate the transmission of loads with a low frictional coefficient (Fox, Bedi and Rodeo 2009).

Cartilage is a resilient structure that is both strong and flexible (Lees and Partington 2016). Healthy cartilage demonstrates little to no evidence of damage or degenerative change – with a unique ability to withstand high cyclic loads – however, when damaged, cartilage has limited capacity for intrinsic healing and repair (Buckwalter and Mankin 1998; Robinson and Keith 2015) because it is devoid of blood vessels, lymphatics, and nerves; and is subject to a harsh biochemical environment (Fox, Bedi and Rodeo 2009). Once articular cartilage is damaged, full recovery of its structure, function, and biomechanical properties is unlikely and is usually a step toward progression to osteoarthritis (Buckwalter and Mankin 1998; Robinson and Keith 2015).

Adult articular cartilage has both a fluid and a solid phase; possesses different mechanical properties depending on the direction; and the stress-strain relationship of cartilage is dependent on the strain rate or changes if either stress or strain is kept constant. These mechanical properties allow cartilage to protect the bone it surrounds, however also enable damage to the cartilage when abnormal biomechanical forces are applied. These forces can arise from a multitude of issues which place abnormal stresses on the articular surface (Merkely, Ackermann and Lattermann 2018).

There are differences in tissue characteristics between juvenile and adult joints. These differences lead to an altered susceptibility to injury with age. Articular cartilage is particularly susceptible to injury in adolescents; the immature tissues of the ankle are susceptible to

additional mechanism of injury, including: axial loading, rotational torques, and angular stress (Outerbridge, Trepman and Micheli 2002).

The subtalar joint and talocrural joint (Figure 2) work in unison to provide the required conformity of the whole joint. Because of the concurrent function of two complex anatomies, the ankle is the most frequently injured weight-bearing joint (Robinson and Keith 2015). Efficient repetitive transfer of forces in a cyclical manner reduces the likelihood of joint damage. To allow for this, the ankle joint does not simply act as a hinge, nor is its primary axis fixed, but changes direction and position throughout the range of ankle motion (Robinson and Keith 2015), behaving predominantly as a rolling joint.

The rearfoot takes the greatest proportion of the force due to bodyweight during neutral ground standing, to the extent that forefoot and midfoot forces have been deemed negligible in Finite Element Models (Cheung and Zhang 2005; Taha *et al.* 2016). The main function of the forefoot is for balance purposes, with force transmission carried out by the bones and soft tissues of the foot and ankle.

#### 1.2.4 Computational Methods

Computational methods can be used to analyse complex systems, predicted numerically using mathematical models. They allow for predictions of the behaviour of a system under varying conditions, and can be used where experimental methods are not viable.

##### 1.2.4.1 Shape Analysis

The study of anatomical shape has become a central focus of medical image analysis. Morphological analysis has been developed to describe variations in the bones. Image measurements, and statistical shape models (SSM) have both been used for the purpose of assessing shape differences between healthy subjects, and in comparison with those affected by a specific disease. Given the importance of normal morphology on joint biomechanics, understanding of morphological differences can provide clinical insights, ultimately improving diagnostics and treatment (Zhang and Golland 2016).

Statistical shape models have been used to characterise shape variation in the cervical spine (Bredbenner *et al.* 2014), lumbar spine (Hollenbeck *et al.* 2018), knee (Bowes *et al.* 2015; Clouthier *et al.* 2019; Haverkamp *et al.* 2011), pelvis (Meller and Kalender 2004), femur (Doherty *et al.* 2008; Bryan *et al.* 2010; Nicolella and Bredbenner 2012; Sarkalkan, Weinans

and Zadpoor 2014), scapula (Casier *et al.* 2018), sacrum (Wagner *et al.* 2014), and ankle (Tümer *et al.* 2016; Lenz *et al.* 2021; Melinska *et al.* 2017). Given its statistical aspects, a large number of specimen is required to derive such models.

Morphological analysis has also been widely used to assess the ankle, with both 2D (Fessy, Carret and Bejui 1997; Stagni *et al.* 2005; Kwon *et al.* 2014) and 3D (Hayes, Tochigi and Saltzman 2006; Kuo *et al.* 2014; Claassen *et al.* 2019; Liu *et al.* 2020) analysis carried out to assess the differences based on age, sex, ethnicity and body composition.

Previously, the morphological changes in the hip have been linked to finite element model outputs (Sarkalkan, Weinans and Zadpoor 2014), where the distributions of stresses and strains have been investigated in both physiological and pathological conditions.

#### 1.2.4.2 Finite Element Modelling

Finite Element Analysis (FEA) is a numerical technique, used to solve problems described by partial differential equations. Finite Element Modelling (FEM) has numerous applications within engineering, including but not limited to structural analysis. This has been taken advantage of in orthopaedic biomechanics since 1972, when the concept was introduced by Brekelmans *et al.* (Huiskes and Chao 1983). The 1983 review by Huiskes and Chao discussed the early applications of this computational technique, which have only grown more advanced with the capabilities of technology.

FEM intends to discretise the structure into small elements with simple shapes. This discretisation process creates a mesh, with integration points where the numerical analysis is carried out. When meshing a three-dimensional model, there are two main types of elements: tetrahedral elements (4 faces, 4 vertices) and hexahedral elements (6 faces, 8 vertices) (Midas NFX). Hexahedral meshes have been seen to give better results when compared to tetrahedral meshes and are hence preferred (Ruffoni and van Lenthe 2017), however most complex geometries cannot be automatically meshed with hexahedral elements. The mesh used is a key consideration in the accuracy of model outputs.

Mathematical modelling that existed prior to FEA, was not suitable for the highly irregular properties of bone. Theoretical results for stresses and strains in orthopaedics would vary greatly from the experimental; whereas, more recent FEA results closely resemble the *in vivo* or *in vitro* results. Despite this improvement, the potential for errors is still large, due to the complexity of FEA and the uncertainties associated to models. Generating appropriate results requires every effort to be made to simulate the subject to a suitable degree of accuracy,

especially in clinical applications (Morales-Orcajo, Bayod and Barbosa de Las Casas 2016). The validity of a model is of equal importance; where the precision can be assessed relatively easily, validation of a model can be challenging or sometimes impossible (Ruffoni and van Lenthe 2017).

Verification is the process of determining that a model implementation accurately represents the conceptual description and solution to the model (Anderson, Ellis and Weiss 2007). While validation is the process of determining the degree to which a model is an accurate representation of the real world from the perspective of the intended use of the model (Schwer 2007). Both verification and validation are required as a model can be verified yet not produce results meaningful to the real world. Validation models are required to ensure the observation is representative of the problem being modelled. Assessing model results against the gold standard experimental technique is the preferred validation method, however this is not always possible. Hence two approaches can be taken to validate a model: either experimental validation or model-to-model validation (Niu *et al.* 2013). Experimental validation can also apply to validating a model using previously published data (Ramlee, Kadir and Harun 2013).

MRI or CT have been used separately and in combination to produce the geometry in patient-specific FE models. Medical findings from MRI and CT have regularly been contrasted; however, how the outputs of these models differ does not appear to have been investigated in literature. Given bone is more appropriately modelled by CT, and cartilage by MRI; due to them being the respective gold standards for obtaining geometry, it would be expected the outputs of models generated from the two would not be the same.

The accuracy of patient specific geometry is influenced by the images used; the slice thickness, slice gap, and voxel size all influence the model geometry. The values for these that may be clinically acceptable for diagnosis, prognosis and follow up, may not be appropriate for 3D modelling techniques.

Patient specific FE models, refer not only to this specific geometry, but also material properties, and loading conditions of individual patients used in simulations (Poelert *et al.* 2012). The loading conditions in FEA should reflect what is being simulated; in orthopaedic modelling this can vary greatly in complexity, as there are numerous anatomical features that could be included in the analysis. Simulations can also be quasi-static, or dynamic, to represent the joint in a range of scenarios. Geometrical accuracy aids the correct transfer of loads within an FE

model, and enhances FE model outputs, especially when the motion of the joint is the concern of the simulation (Chawla, Mukherjee and Sharma 2005).

The material properties should reflect tissue properties as accurately as possible. Bone is regularly modelled as isotropic and homogenous (Niu *et al.* 2013; Ramlee, Kadir and Harun 2013) when it is known that bone has two differing structures, cortical and trabecular, which both have different mechanical properties. The trabecular tissue, found in both the distal tibia and the entire talus, is porous in nature, with a plate and rod structure. This structure means that assuming isotropic behaviour is a simplification.

The elastic modulus for cortical tissue range from 14.3-21.1 GPa, and trabecular tissue range between 1-20 GPa (González-Carbonell *et al.* 2015). Not only does the cortical bone layer have very different properties to the trabecular bone, but the distribution of these material properties is also not homogenous (Poelert *et al.* 2012). To best represent this, material properties calibrated from the Hounsfield Units from CT scans have been used (Helgason *et al.* 2008; Taddei *et al.* 2006; Zannoni, Mantovani and Viceconti 1999).

Tissue properties are seen to have considerable variability based on sex, ethnicity, degeneration, measurer and experimental conditions (Li *et al.* 2007; Niu *et al.* 2013). Hence, it is likely that no current experimental value correctly represents the haemophilic cohort. Literature regularly cites data collected from cadaveric cohorts, from donors who may not be age matched with juvenile PwH. Cohorts also regularly represent both sexes, however, with variability in tissue properties based on this, male tissue properties would be more appropriate in HA. The changes in tissue properties with disease progression will also be impactful (Morales-Orcajo, Bayod and Barbosa de Las Casas 2016). Therefore, a patient specific model would require the material properties to account for the exact stage of the disease. This may not be feasible, hence knowledge of how material properties impact model outputs is necessary to justify any simplifications solicited.

These factors, in combination with the complexities due to the nature of bones structure, cause difficulties in appropriate representation in finite element models.

Tissue composition changes between joints, which reflects in the mechanical properties; hence data collected from other joints in the human body, or collected from other species would be less appropriate than ankle data. 7.3 GPa is the most commonly used elastic modulus for homogenous bone in foot and ankle FEA (Antunes *et al.* 2011; Cheung and Nigg 2008; Hsu *et al.* 2008; Nakamura, Crowninshield and Cooper 1981; Wang *et al.* 2018; Ozen, Sayman and Havitcioglu 2013). When the cortical and trabecular bone are modelled separately, a range of

values have been used. These have been calculated from density values (Bouguecha *et al.* 2011; Mondal and Ghosh 2019a; Mondal and Ghosh 2019b; Sopher *et al.* 2017), or based off experimental data (Miller *et al.* 2004; Bing *et al.* 2021). Using a homogenous elastic modulus of 7.3 GPa (Cheung and Zhang 2005), and Poisson's Ratio of 0.3 would be assuming that the characteristics of the bone being modelled are the same as that in the literature. Model outputs are highly sensitive to the input properties (Poelert *et al.* 2012).

Cartilage is a complex biological material to model, as it can experience nonlinear behaviour; including hyper-elasticity (large deformations) and viscoelasticity (time dependent nature). When modelling joints on the macroscale, the cartilage properties are regularly simplified to isotropic linear elastic materials due to their relatively low computational cost. Under short term or instantaneous loading, this simplification has been deemed to give appropriate results based on the idea that under short term loading the fluid does not have the chance to flow in the cartilage (Clift 1992). This simplification has primarily been carried out on whole joint models, where the focus of the outputs is not within the cartilage, as it has been seen that models do not lose accuracy due to the influence of cartilage on the outputs being negligible compared to other tissues (Morales-Orcajo, Bayod and Barbosa de Las Casas 2016).

It is known, however, that cartilage undergoes large deformations, has a non-linear stress strain definition in compression (Oloyede, Flachsmann and Broom 1992), and behaves as an incompressible elastic solid (Pierce *et al.* 2009). For these reasons, a hyper-elastic material model is a more appropriate representation of cartilage properties, without overengineering to include the anisotropic and biphasic nature of cartilage to these models. It is reported the most appropriate hyper-elastic model to represent the properties of cartilage is Mooney-Rivlin (Li *et al.* 2007; Ramlee, Kadir and Harun 2013).

#### **1.2.4.2.1 Simplifications in Finite Element Modelling**

Informational constraints often mean that simplifications are often required for FEM, however, simplifications may also be required due to computational limitations. This is the case when modelling complex biological structures; clinical applications of FEM tend to simplify the 'least important' element of the model to ensure the computational costs are not too high for the intended output of the simulation.

It is important not to over simplify a model, or make simplifications to important aspects of a model. For example, idealised geometries can lead to poor estimations of contact stresses within a model (Cooper *et al.* 2018). As there is a relationship between unusual geometry and abnormal loading patterns (Gregory *et al.* 2007), which in turn influence contact pressures, and

joint stresses (Anderson *et al.* 2011b; Li *et al.* 2008) it is important that geometry and loading conditions are not over-simplified as this could be influential to result outputs. Idealised or simplified geometries may be a useful tool in verifying material properties used in the final model; given material properties have a large impact on the FE results (Trabelsi, Milgrom and Yosibash 2014). There are six main aspects of FEM to ensure accuracy (Behforootan *et al.* 2017) when modelling the foot for clinical applications: geometry reconstruction, foot function, material properties, loading conditions, meshing, and validation.

In order to evaluate the influence of each of these simplifications, sensitivity testing is used. This is a method of ensuring an FE model is robust; assessing the influence of different values of an independent variable on the model output, this is necessary when there are multiple independent variables that could impact the output. This is important in FEA where these independent variables may not be consistent across all models due to the complex nature of modelling biological tissues.

With time constraints it may not be possible to sensitivity test every element, however sensitivity testing may in turn reduce computational costs and time to run a simulation, should simplifications be feasible. Such sensitivity studies have demonstrated the influence of idealised geometry in orthopaedic simulations (Anderson *et al.* 2010; Beck *et al.* 2005; Cooper *et al.* 2018), others have shown that the orthotropic nature of bone does not influence models on the macro scale (Baca *et al.* 2008; Peng *et al.* 2006). Therefore idealised material properties are more justifiable than idealised geometry as a simplification.

Simplifications to the material properties may be required for a number of reasons. There are multiple tissues found in the joint space, models may opt to neglect or simplify them, should their computational cost outweigh their benefit to the model. It is recognised that bone is an orthotropic material; with a specific spatial orientation and an anisotropic mechanical response (Morales-Orcajo, Bayod and Barbosa de Las Casas 2016). However, this would be computationally expensive to model in the macroscale. Studies have investigated the influence of this aspect of the material property (Baca *et al.* 2008; Peng *et al.* 2006). Results indicated that macroscale FE models were not sensitive to the orthotropic nature of bone, and assuming isotropy to reduce computational costs is justified. Orthotropic modelling significantly increases the model complexity, as it is necessary to know nine independent elastic constants and the spatial orientation of the principal axes of orthotropy (Baca *et al.* 2008).



Alongside the simplifications to homogenous, isotropic bone properties, articular cartilage is commonly simplified in FEM. Articular cartilage is a complex element of a joint geometry, and it is often necessary to simplify it to achieve a model that produces an output. FE models may simplify the cartilage properties (Cheung *et al.* 2005; Ramlee, Kadir and Harun 2013; Tao *et al.* 2009), model simplified cartilage geometry (Camacho *et al.* 2002; Mondal and Ghosh 2017; Ramlee, Kadir and Harun 2013), or neglect to include the cartilage completely (Iaquinto and Wayne 2010; Qiu *et al.* 2011).

As the cartilage is not visible in CT, and may be unclear in MRI, it is often generated by extruding the bone geometry by the average thickness of cartilage for that joint (Camacho *et al.* 2002; Mondal and Ghosh 2017; Ramlee, Kadir and Harun 2013). This simplification may be appropriate when modelling a healthy joint, but would be an oversimplification when considering arthritic joint changes involving cartilage loss, or cartilage defects. This is due to the findings when comparing irregular cartilage thickness to smoothed articular cartilage; where smoothed cartilage surfaces produced underestimations of joint contact pressures and more evenly distributed patterns of contact (Anderson *et al.* 2010).

Synovial fluid is largely excluded from orthopaedic FE models, due to the additional model complexity, which for many applications is unnecessary. There are three other main functions of the synovial fluid, of these the most important being to reduce friction by lubricating the joint. This fact means most models replicate these conditions by assuming the contact between the geometries to be frictionless or with a low friction coefficient.

The influence of including synovial fluid has been demonstrated, with qualitative changes to stress distribution, and quantitative changes to maximum principal stresses (19.8 Nmm<sup>-2</sup> reduction) (Hamid *et al.* 2016). This simulation modelled the synovial fluid as water, where as it is a much more viscous, non-Newtonian fluid. Synovial fluid is in fact dilatant, meaning its viscosity increases with shear force. These properties, Hamid *et al.* hypothesised, would cause an even greater reduction in maximum principal stresses.

Alongside simplifications to model geometry and material properties, simplifications to loading and boundary conditions are often made in orthopaedic FE modelling. This may reflect unknowns in the exact loading of a joint, or soft tissue constraints; or it may relate to not being able to represent these highly complex conditions.

Incorrect bony alignment will influence the loading patterns in the joint (Hamid *et al.* 2016) therefore it is important to have a correctly aligned joint to apply the loading and boundary

conditions to. In later stages of HA the ankle tends to plantar flexion (Rodriguez-Merchan 1996; Rodriguez-Merchan 2006) hence the typically non weight-bearing MR or CT images may require realignment to represent as best as possible the ankle loaded as in neutral standing. The method for representing loading conditions will depend on the geometries modelled; soft tissues, tendons and ligaments are all influential on the force distribution through the foot and ankle (Camacho *et al.* 2002; Mondal and Ghosh 2017; Ramlee, Kadir and Harun 2013). Therefore, it is important that the constraints, when they are removed from FE models due to their computational cost, reflect how these would cause the joint to behave in the joint.

All models require some form of simplification so that the computational costs do not outweigh the benefits of the simulation. It is important, however, to consider whether oversimplification is occurring, which would influence the model results. Verification and validation are key in assessing this, aiding in appropriate modelling decisions being made.

#### **1.2.4.2.2 Finite Element Modelling in the Foot and Ankle**

Utilising FEM in the foot and ankle is relatively complex due to the intricate geometry, and the complex loading; with muscle force, soft tissues, ligaments and osseous material properties all impacting the load transfer and stress distributions. Due to this, research modelling the foot and ankle is relatively sparse compared to other anatomical locations.

There has been an advance in the description of the ankle and hindfoot mechanics both *in vivo* and *in vitro*, yet the development of relevant mathematical models has not corresponded to this, and many results are still unsatisfactory (Leardini *et al.* 1999). The complexity of the ankle anatomy is both a positive and a negative when considering FE modelling; developing a good finite element model of an ankle joint is both challenging and time consuming (Ramlee, Kadir and Harun 2013) yet could harbour results that would potentially be impossible to gather by any other means. Outcomes such as internal stresses and displacements which would be otherwise impossible to measure *in vivo* can however be predicted via this technique (Ramlee, Kadir and Harun 2013).

The isolated forces through the ankle joint are predicted based on the current assumption that the influence of the forefoot and midfoot on load transfer is negligible in normal locomotion of a healthy foot-ankle-complex. Despite this, the force through the ankle joint is not the whole ground reaction force. Assuming neutral bipedal standing, it is cited that the force transmitted through the Achilles' tendon is approximately 50% of the force applied on the foot during

balanced standing (Cheung and Zhang 2005). Those models that incorporate the entire foot and ankle, including soft tissues, assume the force on the joint interface to be half of the force exerted by the bodyweight of the subject (Cheung and Zhang 2005; Taha *et al.* 2016). In their static simulation, Taha *et al.* noted that peak plantar pressure occurs in the heel of their whole foot model, which included all the soft tissues. This observation correlates with the assumption that the forces distributed in the forefoot may be negligible in the modelling situation of the ankle joint.

Correctly representing these loading conditions in a joint model, rather than whole foot model, may require some assumptions to be made. This is due to the 33 joints influencing the biomechanics of the foot and ankle, and the vast number of articulations distributing forces (Barton, Lintz and Winson 2011). Modelling the ankle joint alone would influence the model outcome prior to any other simplifications due to model constraints. The integrity of muscles and tendons in the ankle model would also impact the load experienced directly by the joint, which is assumed to be 25% of the total weight in a non-diseased subject (Cheung and Zhang 2005).

There are informational constraints when modelling the foot and ankle; material properties, even in non-diseased ankle models, are commonly simplified. Bone material properties (Cheung *et al.* 2005; Gefen 2001; Tao *et al.* 2009; Yu *et al.* 2007; Ozen, Sayman and Havitcioglu 2013), ligament properties for the 37 ligaments associated with the ankle joint (Cheung *et al.* 2005; Dai *et al.* 2006; Tao *et al.* 2009), and cartilage material properties (Cheung *et al.* 2005; Tao *et al.* 2009) have all been simplified. In some models cartilage has not even been included (Iaquinto and Wayne 2010; Qiu *et al.* 2011). These informational constraints are commonly seen in biological modelling, due to the changes in tissue properties with age, anatomical location, and disease.

Disease complicates FEM material properties further, as different stages of degeneration will influence these. Changes to the bone in OA include thickening of the subchondral bone plate, increased stiffness, increased bone mineral density and content, and alterations in the trabecular structure and size of the bone (Gregory *et al.* 2007). These will alter both the material properties, and proliferation of bone.

Ensuring that the FE model is appropriate for the application when developing a foot and ankle model is key due to the potential clinical application. The model must have an acceptable degree of accuracy for clinical applications. Simplifications to material properties tend to occur

when there is a wider scope to the modelling. Previous FEM of the foot and ankle has not, considered the influence of disease, however focusses more on footwear design (Yu *et al.* 2007), orthotics (Cheung and Zhang 2005) or orthopaedic implants (Miller *et al.* 2004; Mondal and Ghosh 2019a; Mondal and Ghosh 2019b; Sopher *et al.* 2017; Wang *et al.* 2018).

The techniques used in these studies are transferrable to a diseased ankle model, as considerations such as joint alignment and force transfer are applicable in both the foot form alterations due to orthotics and due to disease. Computational modelling of degenerative disease progression would be highly susceptible to informational constraints.

### 1.3 Aims and Objectives

From the literature reviewed, it was clear that there were changes to both the structure and the function of the haemophilic ankle. However, how these related to each other has not yet been considered. The benefits, and limitations, of computational modelling were also highlighted; the aim of this thesis was therefore, to consider both changes to the morphology and joint stresses in the talocrural joint with progressive haemarthropathy in order to ascertain if there is a relationship between the two. Understanding how morphology relates to walking range of motion, as a biomechanical function, is also a key consideration for this investigation.

To achieve this aim, there were multiple objectives:

- 1) Assess the morphology of the haemophilic talus, and how this differs from non-diseased tali.
- 2) Generate static patient specific finite element model of the talocrural joint.
- 3) Carry out quasi-dynamic modelling using subject specific gait, linking the adapted gait to the changing morphology within the ankle.
- 4) Assess haemarthritic specific features such as subchondral bone cysts, to understand their influence on joint health.

This thesis is divided into seven chapters: Chapter 2 considers the morphological analysis carried out; Chapter 3 shows the methods developed to create a robust patient specific model from clinical MRI; and Chapter 4 uses the method developed in Chapter 3 to consider the patient specific models over time, relating these findings to the subject specific morphology. Chapters 5 and 6 use a subset of these patient specific models, to first look at the influence of subchondral bone cysts in the five ankles with these present (Chapter 5), and then understand the influence of the adapted gait in people with haemophilia (PwH) (Chapter 6). Chapter 7 discusses the relationship between these bodies of work, and the potential future directions for this research.

## 1.4 Patient Data

For this thesis, anonymised patient data for six PwH was collected in line with local ethical approval (MEEC 18-022 and MEEC 20-008) (Table 3). Patients with chronologically sequential MRI data (N=5) were identified by clinicians based on the selection criteria of one or both ankles being target joints of recurrent musculoskeletal bleeds, with no bias to left or right ankles. MRI data is routinely collected in clinical practice for PwH in Leeds Teaching Hospitals NHS Trust when there are suspected joint changes, and images are consented for anonymised use in research. A total of nine ankles were collected as three patients had image data for both ankles.

Under MEEC 18-022, a total of 39 haemophilic MRI sequences were collected, details of these can be seen in Table 4. All ankle MRI sequences were collected using the same non-weightbearing (supine) setup. A naming protocol was set up in order to easily determine the patient, ankle side, and chronology. Three patients had bilateral presentation, hence this information was included in the naming protocol, despite it not being considered of importance in the results. For those models where a subchondral bone cyst (SBC) region was included (as detailed in Chapter 5), this was noted by adding a C to the end of the name. For example, Patient 1's first MRI is named 1R1, as their affected ankle is the right ankle; the corresponding SBC model is named 1R1C.

*Table 3 Information on data gathered for each patient and chapter numbers (Ch #)*

<b>Model</b>	<b>1R</b>	<b>2R</b>	<b>2L</b>	<b>3R</b>	<b>3L</b>	<b>4L</b>	<b>5R</b>	<b>5L</b>	<b>6R</b>
<b>Number of MRI</b>	7	3	4	8	7	3	4	2	1
<b>Total timescale (months)</b>	112	28	48	114	90	72	24	6	N/A
<b>MRI included in morphology statistics (Ch 2)</b>	7	3	4	4	4	3	3	2	0
<b>Subchondral Bone Cysts (Ch 5)</b>	Y	Y	Y	Y	N	N	N	N	Y
<b>Biomechanical Data (Ch 6)</b>	N	N	N	Y	Y	Y	N	N	Y

The date of birth and patient weight were included, which allowed patients to be categorised (paediatric/adolescent/adult), and subject specific loading conditions to be modelled. The patient group varies widely from 7.5 years to 45 years of age.

Clinicians shared the closest known patient weight to the date of scan for each MRI sequence. This was used to estimate patient specific forces for the static loading condition, in Chapter 3, and quasi-dynamic loading through the gait cycle in Chapter 6. Patient weight is regularly recorded for factor replacement therapy, as this is done on patient weight, hence it was available retrospective data.

*Table 4 Information on the chronologically sequential MRI data collected from eight of the haemophilic ankles*

<b>Number of scans per ankle</b>	$\bar{x}$ =4.67, mode = median = 4, Range = 2 – 8
<b>Total imaging time frame (months)</b>	$\bar{x}$ =61.75, median=60 (6-114)
<b>Age at first scan (years)</b>	$\bar{x}$ = 16.6, mode=median=15 (7.5 – 39)
<b>Time between scans (months)</b>	$\bar{x}$ =16.5, mode=6, median=11.5 (4 – 43)
<b>Side of Body</b>	Left = 4; Right = 4
<b>Frequency of sequence type</b>	T1= 30, T2= 7, STIR=1

MEEC 18-022 also covered MRI data for a sex-matched non-diseased control group. The sex and MRI data of this control group were collected from a pre-existing research data set (Arnold *et al.* 2020).

Biomechanical data was collected as part of an intervention study (LASERHAEM), local ethics MEEC 20-008 permitted use of this data in this thesis. This data was collected for four of the nine haemophilic ankles (Table 3). Due to the biomechanical data capture being delayed by two years (due to the ongoing Covid-19 situation), two ankles had been fused between final imaging timepoint and the intervention study. A final patient opted out of participating in the gait study for reasons relating to the Covid-19 pandemic.

Alongside the original patient cohort, in-shoe gait data was also collected for a non-diseased (not sex matched) control group, and a sixth PwH. The sixth PwH did not have long term image data to be included in any other aspects of this research, therefore their data was used in Chapter 6 alone, to give a total of four ankles with patient specific gait.

# CHAPTER 2

## MORPHOLOGY OF THE HAEMOPHILIC TROCHLEAR TALUS



# CHAPTER 2: MORPHOLOGY OF THE HAEMOPHILIC TROCHLEAR TALUS

## 2.1 Introduction

The morphology of the healthy talus has previously been studied to investigate the influence of age, sex, ethnicity and body composition on morphology, with findings that each of these factors have some influence on talar morphology. This morphological analysis has also been used clinically to aid the improvement of orthopaedic implants.

Morphological measurements have been carried out on both 2D radiographs (Fessy, Carret and Bejui 1997; Stagni *et al.* 2005; Kwon *et al.* 2014) and 3D CT images (Hayes, Tochigi and Saltzman 2006; Kuo *et al.* 2014; Claassen *et al.* 2019; Liu *et al.* 2020). CT is considered the gold standard in morphological measurement due to the improved definition of the bone boundary. However, these are very rarely collected routinely in clinic due to the radiation exposure. A key factor of this work therefore was to understand if routinely collected MRI are an appropriate medium from which to take morphological measurements.

Clinically, a flattening of the haemophilic talus has been observed, and the quantification of this may aid in understanding the influence of morphological changes on disease progression. Talar flattening is not one of the six main imaging presentations used to diagnose and stage HA (Lundin *et al.* 2012). These imaging presentations also do not directly consider the clinically observed morphological changes described as angulation (Jelbert, Vaidya and Fotiadis 2009) or talar tilt; talar tilt is caused by a morphological variation in the tibia, where relative undergrowth of the lateral side of the tibial epiphysis can lead to a pronated foot (Hacking and Dixon 2018). These morphological changes, involving the articulating region between the tibia and the talus have been identified, but not quantified, and it has not been asserted if these are universal changes across the haemophilic population.

The morphology of the talus varies across the medial-lateral axis of the talus (Figure 4 - Anterior View), hence it is important to assess the implication of disease across the width of the talar dome. Non-uniform morphological differences between non-diseased and haemophilic tali may implicate mechanical factors that influence disease progression.

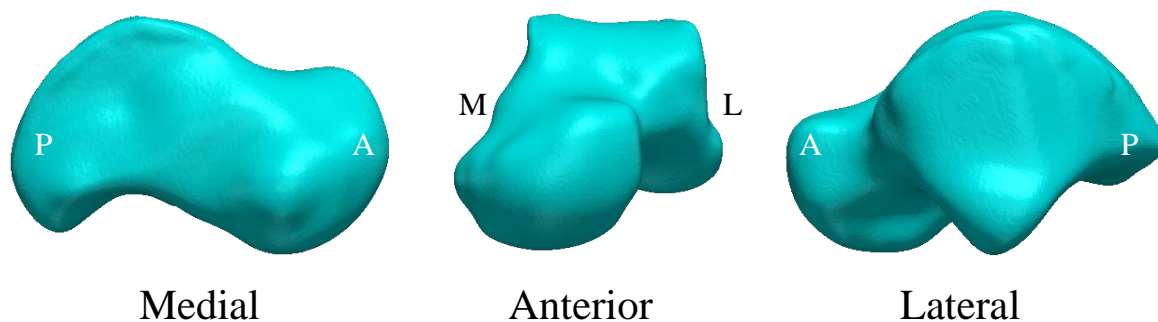


Figure 4 3D model of the talus, reconstructed from MRI data. Medial, Anterior and Lateral view labelled (M – medial, L – lateral, A – anterior, P – posterior).

Both the degree of change, and location of change across the talar dome are unknown. It is also unknown if either of these are common across the haemophilia population, or if each haemophilic talus experiences morphological changes differently. If the haemophilic talus does follow a morphological trend as HA progresses, it would suggest that simple measurements could be made quickly and easily in order to aid in assessing the progression of the joint disease quantitatively.

The aim of the work presented in this chapter was to ascertain if there is a quantifiable morphological variation in the haemophilic trochlear talus. In order to carry this out, a verification study on the use of MR images for morphological measurement was carried out against CT and radiographic measurements. Morphological measurements taken from MRI of haemophilic tali, and non-diseased control tali, could then be contrasted to assess their differences and the changes through time.

## 2.2 Data Acquisition and Method Development

In order to carry out a morphological analysis, image data had to be acquired for the haemophilic patient group and non-diseased control group. A total of 47 MRI sequences were acquired across the two groups. As the morphology differs across the talar width, measurements were taken for three sagittal projections across the talus: medial, central and lateral. A total of 141 images were measured – 3x11 control, and 3x36 haemophilic. The process of slice selection, and measurement were both manual and unblinded.

### 2.2.1 Haemophilic Patient Data

For the purpose of adult classification, sequences from patients under the age of 13 have been excluded from the analysis (Table 3) – allowing all statistics to be classified as adult, for best comparison with the fully adult non-diseased control group. Due to this, of the 36 MRI sequences, five were excluded from statistical analysis as they fell under the paediatric classification.

### 2.2.2 Non-Diseased Control Group Data

A sex-matched non-diseased control group was gathered from pre-existing MRI data (Arnold *et al.* 2020) with consent for use in research, this data was collected at a single time point, so there was only one MRI per control ankle. All adult male MRI data from the midfoot study was assessed by a radiologist to confirm it was free of joint disease before being anonymised for use in this study.

Sex matching was considered a key factor in the control group selection criteria, based on literature indicating that there is no significant difference in morphology between the right and left talus (Liu *et al.* 2020) but sex does influence measurements (Kuo *et al.* 2014; Liu *et al.* 2020).

Only MR images were shared, with no additional patient information such as variables that might influence bone morphology (age, height or weight) available for the 12 non-diseased male ankles. Only 11 were included in the control group, as one control ankle did not have the entire talus visible in the sagittal projection.

### 2.2.3 Image Data

The MRI sequences collected in clinic for the patient group consist of both T1 and T2 weighted scans, as well as Short Tau Inversion Recovery (STIR) sequences in some instances (Figure 5). It was intended to use T1 weighted sequences for all patient image data due to it more closely resembling the control group sequence type. However, this was not possible due to the compromised quality of some sequences. Blurring and motion artefacts were the primary reasons sequences could not be used.

1R varied most from the desired method, with four T2 weighted sequences and the STIR sequence used alongside two T1 weighted sequences. 2L and 3R had one and two T2 weighted sequences respectively, while there was no divergence from the intended sequence type in 2R, 3L, 4L, 5R or 5L.

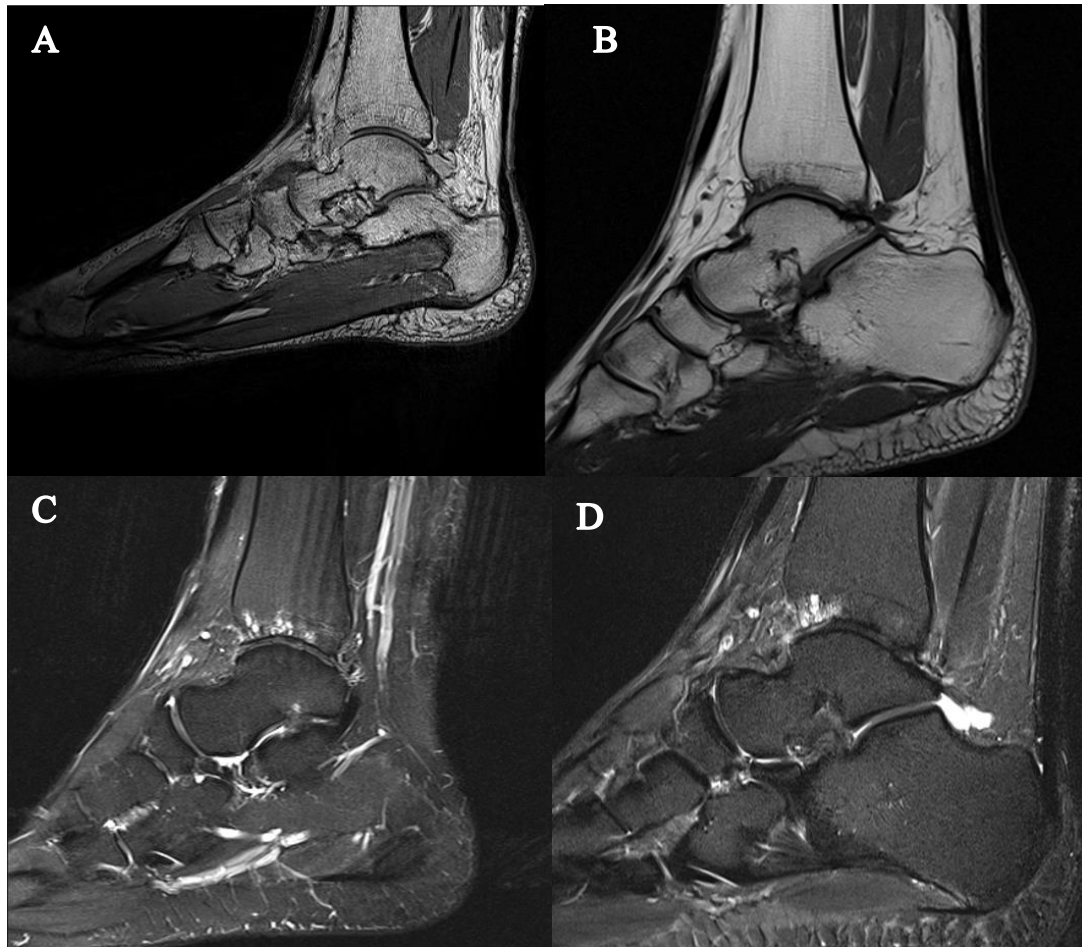


Figure 5 Visualisation of differences in MRI sequences on ankles (A) SPACE, (B) T1 weighted, (C) T2 weighted, (D) STIR

The sequences previously collected for the 11 ankles used in the control group were 3D turbo spin sequences (SPACE). The T1 and T2 sequences for the control group did not have full coverage of the talus, hence could not be used.

All sequences had the same in plane resolution (0.5357 mm), however the control group data was collected for research, and therefore had a smaller slice thickness (0.5 mm) than the clinical MRI for the haemophilic cohort (~3.3 mm).

#### 2.2.4 Method Development

Given that the main variation in talar morphology was expected to present in the trochlear talus, where there is articulation with the tibia, this highlighted a region of interest from which to take the measurements. The three locations across the talus were selected based on being the most medial, and most lateral slices with articular cartilage present, and the central slice of talus. For example, if the talus was covered by 11 slices, the central image would be the sixth slice with talar geometry present.

Four measurements (Table 5) were taken from each image using ImageJ (1.52v) (Rasband 1997-2018; Schneider, Rasband and Eliceiri 2012). The measurements were selected based off the ability to verify them against literature. However, it was also important that they may indicate morphological changes, such as trochlear talar flattening.

*Table 5 Measurements taken for each image- medial, central, and lateral measurements were each denoted with m, c or l – i.e. Lateral Trochlear Tali Length = TaLl*

<b>TaAL</b>	<i>Trochlear Tali Arc Length</i>		Distance between the most anterior (A), posterior (B) and proximal (C) points in the trochlear tali
<b>TaH</b>	<i>Talar Height</i>		Height of the trochlear tali, calculated as the distance between point C and the AB line
<b>TaL</b>	<i>Trochlear Tali Length</i>		Distance between most anterior (A) and posterior (B) points in the trochlear tali. The AB line is the shortest possible distance between these two points
<b>TaR</b>	<i>Trochlear Tali Radius</i>		Radius of a circle fitted to the talar dome

The measurements taken from each image are depicted and labelled in Figure 6. It can be seen how these differed slightly across the talus, however, the tools used were consistent across all sequences. For TaH and TaL, the straight-line tool was used and measurement feature to determine the length of each of these. To measure the TaR a circle was fitted to the curve of the talar dome; this did not always fit to the entire talar dome – but was overlaid to be the best fit – then the radius was measured.

Initially, two approaches were taken to measuring TaAL on the control group images. The first approach traced a freehand line over the talar arc. However, this was not repeatable, and when contrasted with the second method consistently overestimated TaAL. The second method involved using the Bezier Curve tool, where a curve (with multiple sections where required) was fitted to the talar dome and then measured directly using the measurement tool.

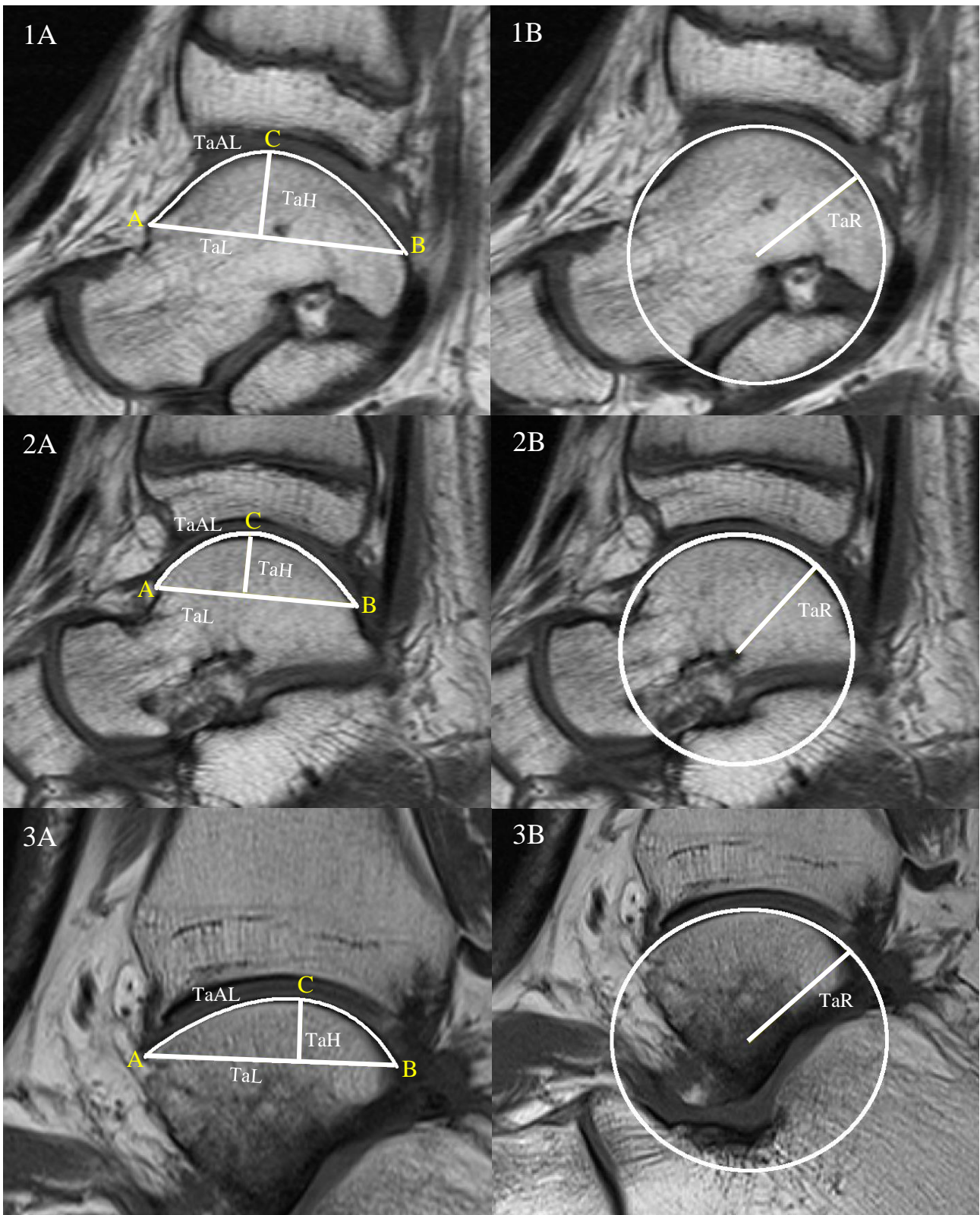


Figure 6 Sagittal MRI of the talus. Images in rows show 1) medial talus, 2) central talus, and 3) lateral talus. Column A shows the fitting of the arc to calculate Trochlear Tali Arc Length (TaAL), Trochlear Tali Length (TaL) and Talus Height (TaH). Column B shows the fitting of a circle to find Trochlear Tali Radius (TaR). Points A, B and C relate to those set out in Table 5.

### 2.2.5 Ratios

It is known that age and body composition can have small influences on bone geometries (Kuo *et al.* 2014; Liu *et al.* 2020). Given the large range in age (13-45yo), and mass (45.7-117kg) of the adult haemophilic group, it was anticipated these may influence the measurements. Height could also influence body composition and is highly likely to vary amongst the patients. Ethnicity was another unknown from the patient data which has been seen to influence measurements (Fessy, Carret and Bejui 1997; Stagni *et al.* 2005; Hayes, Tochigi and Saltzman 2006; Kuo *et al.* 2014; Kwon *et al.* 2014; Claassen *et al.* 2019; Liu *et al.* 2020), and would be relevant due to the global prevalence of haemophilia (Stonebraker *et al.* 2010).

The MRI data was collected over a number of years for some patients, and given the age ranges, it was likely that growth would occur. The aim of the ratios generated was to account for the influences age and body composition may have on adult bone geometries, meaning that the focus of the results would be on the morphological change of interest. The use of ratios would also potentially reduce the natural variability across the patient group and non-diseased control group due to non-disease-related factors such as height, weight, and age, which differ across the patient group.

Three ratios were developed in order to quantify talar collapse, should it occur in the haemophilic patient group: TaR:TaAL, TaAL:TaL, and TaL:TaH. These ratios were identified due to the measurements anticipated changes with talar collapse (Table 6).

*Table 6 Ratios and their anticipated changes with talar collapse*

Ratio	TaR:TaAL	TaAL:TaL	TaL:TaH
Expected Change With Collapse	↑	↓	↑
Expected Measurement Behaviour	TaR increase TaAL decrease	TaAL decrease TaL unchanged	TaL unchanged TaH decrease

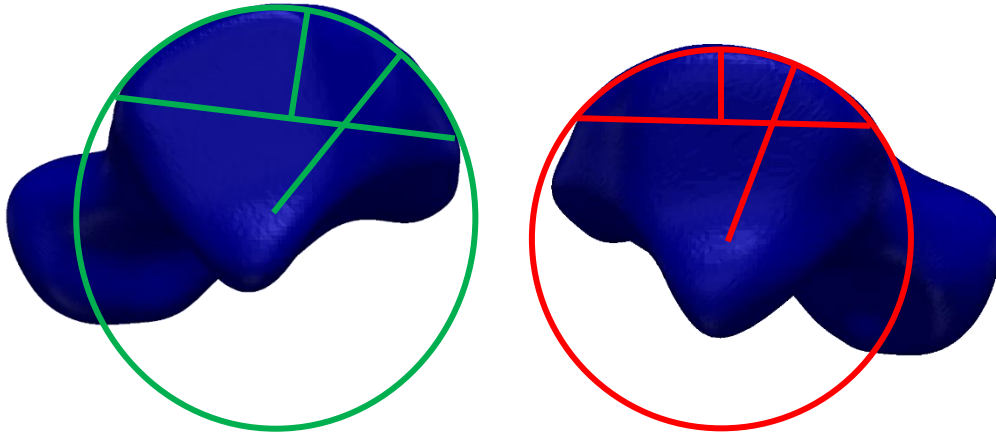


Figure 7 Measurements fitted to a 3D reconstruction of two different tali with different degrees of collapse (green – minimal flattening; red – greater degree of flattening). Showing how the measurements change with a flattened talus. With increased flattening (red): increased TaR; decreased TaL, TaAL and TaH.

In order to fully understand the morphological changes with haemophilia, it is best to assess the behaviour of all three ratios. For example, the increase in TaL:TaH was expected to be driven by a decrease in TaH with disease, while TaAL:TaL was expected to decrease due to TaAL driving the ratio. With TaR driving TaR:TaAL, all measurements are anticipated to have some involvement in disease progression; their percentage changes relative to non-diseased may aid in understanding what this may mean for the diseased morphology of the talar dome.

## 2.3 Verification Studies

The aim of this work was to verify the use of MRI sequences for morphological measurements, to gain confidence that this imaging type was appropriate for comparing haemophilic measurement to a matched control group.

### 2.3.1 Methods

Given the novel approach to taking morphological measurements of bone from clinical MR images, verification of the methods was needed to ensure this was appropriate for a comparison between the haemophilic and non-diseased groups.

#### 2.3.1.1 Verification of taking measurements from MRI

In order to validate the approach taken to the measurements from MRI, the data was compared to measurements from previous studies carrying out talocrural measurements from radiographs (Fessy, Carret and Bejui 1997; Stagni *et al.* 2005; Kwon *et al.* 2014) or CT images (Kuo *et al.* 2014; Claassen *et al.* 2019; Liu *et al.* 2020). These imaging modes would be deemed more



appropriate for measurements of the bone due to the clearer definition of bone boundaries. However, MR imaging is carried out as part of the clinical assessment of haemophilia patients in the Leeds Teaching Hospitals NHS Trust following incidences such as major bleeds to a target joint. As this is the imaging modality readily available, the measurements must be verified against the gold standard imaging technique.

The six previous studies either considered the sexes separately (Claassen *et al.* 2019; Kuo *et al.* 2014; Liu *et al.* 2020), or together (Fessy, Carret and Bejui 1997; Kwon *et al.* 2014; Stagni *et al.* 2005). Sample sizes range from 36 (Stagni *et al.* 2005) to 100 (Kwon *et al.* 2014) ankles. These were non-diseased cohorts with primary aims mostly considering sex, or population differences.

The data collected in these studies were used to verify the methods for each of the four measurements. The difference between the control group measurements and each of the six studies was assessed using two-tailed Student's T-Tests (statistical significance set at 0.05). Where data was reported for the separate sexes, the comparison was made against the male data. This was done for all available measurements, except TaR results presented in one study (Claassen *et al.* 2019) as this did not agree with previous studies. For the studies where measurements were taken at multiple locations, these were all assessed with respect to the same locations. However, for the four studies that only reported one mean value for the whole talus, this was compared directly to the largest of the three values for the control group. This approach was taken due to the assumption that the measurements from radiographs would be the maximum, owing to the projection nature of this imaging modality.

### *2.3.1.2 Error Evaluations (Measurement repeatability and MRI slice location)*

In order to check for repeatability of defining the regions to be measured, the measurements were repeated three times on a subset of MRI sequences at the three locations. This was done for images from both groups in case differences in the two groups made one more susceptible to errors. The error was then calculated in these to ensure this would not influence findings.

To assess the measurement variation due to the location of the MRI slice across the width of the talus, measurements were taken in adjacent slices for one sequence per haemophilic ankle (N= 8). The four measurements were taken on each slice, and the three ratios generated. The

sequence selected was the first included in the statistics, i.e. the first adult ankle, as it was unknown if the implication would be different in the paediatric tali.

In order to calculate the percentage error, two adjacent ratios were used in the formula:

$\frac{R_1 - R_2}{R_2} \times 100$  where  $R_1$  is the more lateral of the two ratios, and  $R_2$  is the more medial ratio. All

results were rounded to one decimal place for Table 7.

The image selection protocol initially used defined the best slices for measurements to be taken from based on the assumption that the sequences covered the same portion of the talus. The medial and lateral images were selected as the first and last images in the sequence with articular cartilage present; beyond these images, there was either no further talar bone present, or the talus clearly did not articulate with any other part of the ankle joint, hence would not be expected to have great morphological changes, should articulation be the driving force of disease progression as hypothesised. These were similar regions to those selected in previous studies – as close as possible given slice thickness limitation (Kuo *et al.* 2014; Claassen *et al.* 2019). It was found that this slice selection in those medial and lateral regions was not the most appropriate method due to a number of sequences covering the medial malleolus and the articular surface of the lateral process of the talus. These marginal slices gave unreasonable measurements, and ratios that did not follow the trend of adjacent slices due to the change in talar morphology in these regions. Careful slice selection ensured these regions were excluded from measurements.

The portion of the MRI sequences that covered the talus ranged from 8 to 11 images. It was assessed whether the side of the body (left or right), or the number of slices across the talus influenced the outputs. Whether the ratio changed more between adjacent slices, or the same location in the MRI sequence for the patient was used to determine how much the change seen with time might be influenced by slice location across the talus.

## 2.3.2 Results

### 2.3.2.1 Verification of taking measurements from MRI

The means and standard deviations reported in literature and calculated from the non-diseased control can be seen in Figure 8. Five of the studies reported TaH, while only three studies reported results for each of the other three measurements.

TaR measured in this work showed no statistically significant difference against the measurements derived from CT or radiograph ( $p$  values between 0.06 and 0.88 for location-

specific comparison (Kuo *et al.* 2014), and 0.82 for comparison of maximum value (Stagni *et al.* 2005)). The difference in central TaR measurement taken by Kuo *et al.* was close to the significance threshold ( $p = 0.06$ ). Kuo *et al.* carried out their measurements on 3D reconstructions of the talus, where smoothing may potentially influence their findings.

Mixed outcomes were found for TaH, where the measurement showed no difference to four values ( $p$  values of 0.13 (Liu *et al.* 2020), 0.33 (Kwon *et al.* 2014), 0.35 (Fessy, Carret and Bejui 1997) and 0.82 (Kuo *et al.* 2014), comparison of the maximum value only) but yielded statistically significant differences with the fifth, which was much greater than the previous studies ( $p = 0.006$  (Claassen *et al.* 2019)).

Significant differences were found for TaL in two of the three studies ( $p = 0.015$  (Stagni *et al.* 2005) and 0.010 (Liu *et al.* 2020)), the third showing no difference ( $p = 0.32$  (Fessy, Carret and Bejui 1997)). The group in this study however was not sex matched with the control group, as the results reported were for both male and female subjects; while the studies reporting only male measurements rejected the null hypothesis that the two studies were the same.

TaAL had results both across the talus, and for a maximum values. Both medial TaAL results showed significant differences ( $p < 0.001$  (Kuo *et al.* 2014; Claassen *et al.* 2019)). While the central TaAL measurements showed no significant difference from the literature ( $p = 0.39$  (Claassen *et al.* 2019)) and mixed outcomes were obtained for the lateral TaAL measurements ( $p = 0.15$  (Kuo *et al.* 2014) and  $p = 0.005$  (Claassen *et al.* 2019)). The maximum value showed a significant difference ( $p < 0.001$  (Kwon *et al.* 2014)).

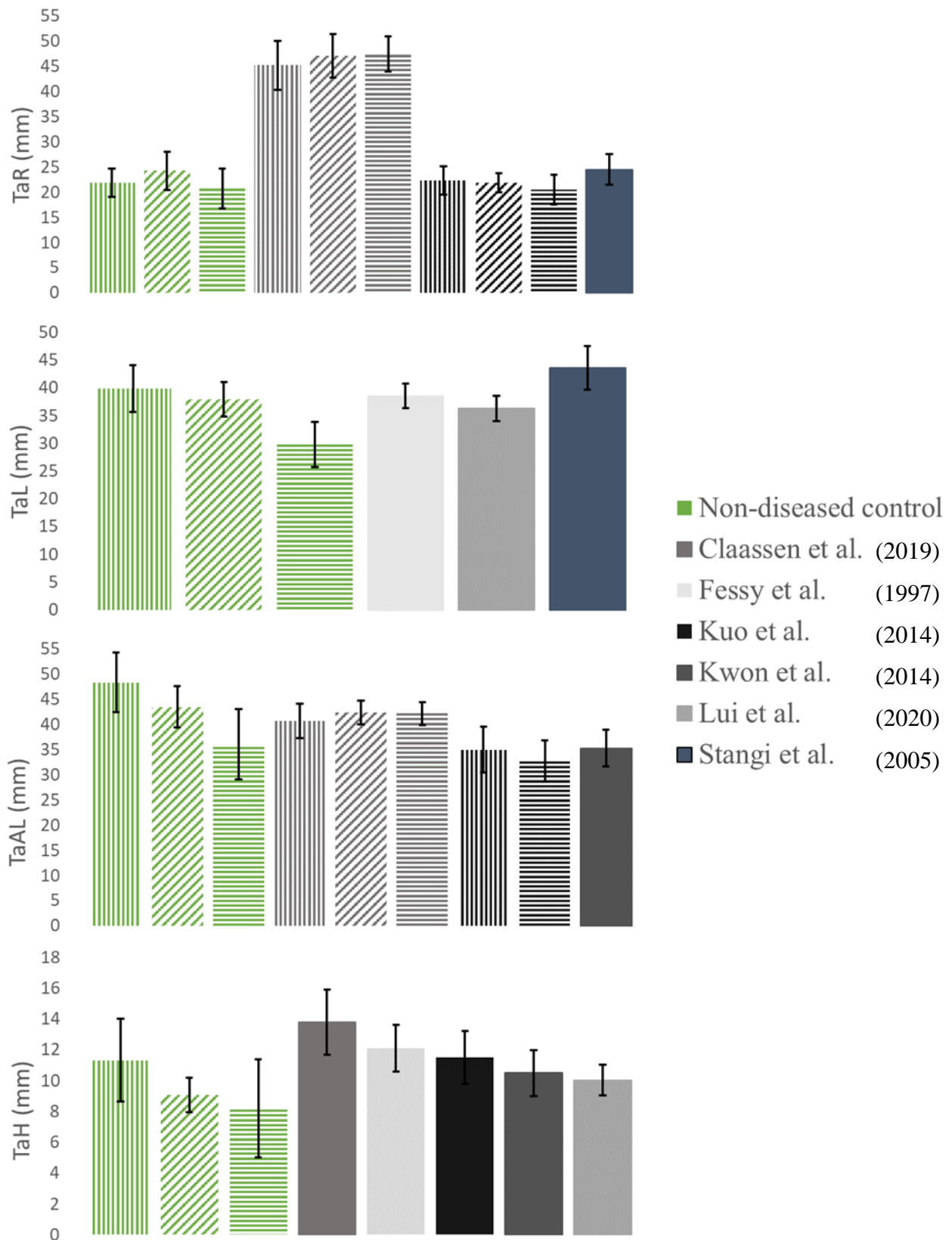


Figure 8 Outputs of previous studies compared to the non-diseased control group. Patterns show location across the talus: medial - vertical stripe, central - diagonal stripe, lateral - horizontal stripe, location not specified - block colour. Error bars show reported or calculated standard deviation.

### 2.3.2.2 Error Evaluations (*Measurement repeatability and MRI slice location*)

The TaAL measurements taken using the freehand line tool gave varied, and often large errors ( $\bar{x} = 5.95\%$ , S.D = 8.49, range = 0.46 – 43.76 %) and when contrasted to the Bezier curve tool were always an overestimation.

Another potential source for error was the selection of locations A and B (Figure 6), as many of the tali did not have clear landmarks to define these. To assess for this, measurements were repeated on three separate occasions for the subset of eight sequences. These repeated measurements were predominantly within a 1% relative difference across the three iterations. With the largest margin of error between two repeats being 5%.

The percentage difference between ratios measured on adjacent slices gave a range of outcomes amongst the eight sequences measured (Table 7); the largest difference between adjacent slices occurred in TaR:TaAL, with values ranging between 1.45% and 103% ( $\bar{x} = 15.5\%$ ), while TaL:TaH ranged from 0.5% to 78.4% ( $\bar{x} = 12.9\%$ ). The percentage differences between adjacent slices were much smaller in TaAL:TaL, with values ranging from 0.1% to 15% ( $\bar{x} = 3.4\%$ ).

Table 7 Error (%) between adjacent ratios across the talus for one MRI sequence per patient

		<b>Medial</b> <span style="font-size: 1.2em;">→</span> <b>Lateral</b>									
<b>1R</b>	TaR:TaAL	-7.6	7.9	-25.0	-1.7	11.9	-20.3	2.5	-0.2	-4.8	
	TaAL:TaL	3.3	-2.6	-1.1	2.7	-0.5	6.5	-1.3	-0.6	4.4	
	TaL:TaH	7.9	-9.0	4.2	-9.0	3.1	-13.7	-7.0	2.9	-7.4	
<b>2R</b>	TaR:TaAL	39.2	-29.4	-5.2	14.7	15.6	-17.1	-20.5			
	TaAL:TaL	-4.3	7.6	2.8	-6.0	-1.1	3.2	5.4			
	TaL:TaH	17.2	-19.3	-3.7	33.3	-12.3	-7.8	-20.5			
<b>2L</b>	TaR:TaAL	-34.3	-10.5	4.9	1.9	-15.6	20	65			
	TaAL:TaL	9.1	0.4	-0.4	-2.0	10.6	-3.6	0.1			
	TaL:TaH	-41.1	-10.3	6.3	2.3	-25.1	9.9	1.5			
<b>3R</b>	TaR:TaAL	-10.1	-3.9	-2.6	-2.6	-0.3	-9.2	9.7	-5.8	-1.5	
	TaAL:TaL	3.1	1.7	4.1	-1.8	-1.4	5.1	-4.4	0.3	-0.6	
	TaL:TaH	-8.3	-12.3	-7.3	8.4	1.4	-8.8	12.7	-4.1	2.6	
<b>3L</b>	TaR:TaAL	32.1	-30.2	-12.5	33.9	-8.1	-12.4	-9.9	19.7	32.5	1.6
	TaAL:TaL	1.8	6.9	2.2	0.6	0.7	-2.2	1.9	-3.1	0.3	-6.6
	TaL:TaH	-3.2	-23.9	-8.5	-4.3	-0.5	9.6	-6.9	1.9	13.4	72.5
<b>4L</b>	TaR:TaAL	-25.5	-14.0	15.0	-14.1	-9.6	5.0	-6.1	-3.6	54.5	
	TaAL:TaL	3.6	3.7	-3.3	3.8	-2.0	1.5	1.0	4.6	-6.2	
	TaL:TaH	-32.6	-5.3	9.7	-8.6	-0.6	3.1	-9.8	-11.4	42.3	
<b>5R</b>	TaR:TaAL	-24.5	-4.1	6.7	3.2	9.7	-6.8	-9.7	9.1	14.9	34.2
	TaAL:TaL	15.0	2.1	-2.5	-1.3	-1.3	3.5	5.3	-5.6	-6.9	-6.0
	TaL:TaH	-43.7	-4.0	6.8	-1.4	8.8	-7.5	-11.8	8.2	36.7	21.0
<b>5L</b>	TaR:TaAL	40.8	-15.6	2.0	19.3	-4.5	-3.8	-8.6	4.5	-11.2	103.3
	TaAL:TaL	-2.1	11.9	-0.8	-3.3	3.0	-0.5	-0.1	-0.9	2.0	-9.1
	TaL:TaH	-2.5	-33.7	12.7	4.7	-8.3	3.4	-2.9	5.4	-3.0	78.4

### 2.3.3 Discussion

#### 2.3.3.1 Verification of taking measurements from MRI

MRI is not the most appropriate imaging modality for measuring the bone boundaries (Hayashi, Roemer and Guermazi 2016), however, is the best medium for assessing arthropathic changes in HA (Lundin *et al.* 2012) and is the imaging modality of choice in clinical practice. In order to confirm the capacity of MRI for assessing morphological changes it was verified against CT

scans and radiographs. Four of the studies reported the measurements for both sexes separately, allowing for like-for-like comparison with the non-diseased control group (Stagni *et al.* 2005; Kuo *et al.* 2014; Claassen *et al.* 2019; Liu *et al.* 2020), the remaining two studies reported their population as a whole (Fessy, Carret and Bejui 1997; Kwon *et al.* 2014). Two studies using CT imaging took measurements across the talus in the sagittal projection, reporting medial, central and lateral values for all measurements except TaH (Kuo *et al.* 2014; Claassen *et al.* 2019). This method was not possible for the three studies carried out on radiographs, which reported the mean of the maximum value per measurement (Fessy, Carret and Bejui 1997; Stagni *et al.* 2005; Kwon *et al.* 2014). The final study was carried out on 3D models of each talus, generated from CT images, where the mean values were calculated from the maximum measurement for each talus (Liu *et al.* 2020).

Comparisons were made against all available measurements from the six studies in order to best identify any issues with the software and techniques used for the MRI derived morphological measurements.

As the difference was assessed for the direct measurements, it was anticipated that different age ranges and body compositions may impact the verification. Some groups were better matched (by sex, and method), hence closer equivalence was expected for these. The influence of ethnicity on talar morphology has been noted (Liu *et al.* 2020), however, as this was an unknown for all members of the non-diseased control group, this means it was unknown whether there were any studies with good like-for-like comparison.

The measurements taken in the previous six studies did not allow for the ratios to be directly compared to literature. Missing measurements meant that only two of the studies could generate a ratio for TaL:TaH (Fessy, Carret and Bejui 1997; Liu *et al.* 2020), one for TaR:TaL (Stagni *et al.* 2005), and none for TaAL:TaL due to a lack of TaL measurements in the majority of studies. It is also not certain that in the radiograph studies the maximum values would have occurred at the same point on the talus, which would make ratios invalid.

Comparing MRI derived measures against CT and radiograph measures, no differences were found in the trochlear tali radius values, however, some differences were found in the linear measures of talus height, trochlear talus arc length and trochlear talus length. This could potentially relate to linear measurements being prone to a magnification effect, especially in X-ray derived measures, which will differ across the four studies used for comparison (Stagni *et al.* 2005; Kuo *et al.* 2014; Claassen *et al.* 2019; Liu *et al.* 2020).

Where measurements were reported across the talus, the central measurement was seen to differ considerably less from the non-diseased control when compared to the medial and lateral measurements (Claassen *et al.* 2019), this was confirmed by the significant differences seen in the medial and lateral measurements, while there was no significance in the central measurements. Trochlear tali length (TaL) and talus height (TaH) were only reported as maximum values in literature, hence it is unclear whether this represents a magnification effect, or due to the location of these maximum values not mapping exactly onto one of the three locations measured in the non-diseased control group. Kuo *et al.* (2014) did not report a central measurement for trochlear tali arc length (TaAL) to confirm whether it is the definition of bone boundaries in MRI which makes this a more difficult measurement to take, or whether it is the effect of discrepancies in slice location at the medial and lateral extremes.

These differences could also be explained by the higher sampling frequencies in the CT studies, as it was seen in the verification across the talus there were sudden changes in the ratios between adjacent slices at the medial and lateral extremes. This indicated a potential error in the subjective manner of selecting the slices to capture the data from – where higher sampling frequencies gave slice thicknesses of 0.625 mm and 1.5 mm for Kuo *et al.* and Claassen *et al.* respectively. For the haemophilic group, the precision of these CT studies could not be matched, as the slice thickness for each sequence was in the region of 3 mm.

The sensitivity to measurement location, alongside the potential differences that may occur due to the range of software and methods used for taking the measurements (Mys *et al.* 2021), highlight the importance of confirmation against multiple studies with differing approaches to measurement. A check for this was carried out, to assess the differences between the results reported in literature. This showed the difference between MRI measurements and CT or radiographic measurements ( $\bar{x}$  =3.13 mm; 0.17-13.3 mm) were not larger than the difference between CT and radiographic measurements from the literature ( $\bar{x}$  =4.61 mm; 1.48-9.50 mm). This information confirmed that measurements can be taken from MRI to evaluate trochlear talar morphology with the same level of confidence as those taken from CT or radiographs. It is likely that the difference in some measurements between MRI and CT or radiographs is as much due to the difference in patient groups as it is in imaging techniques used for the measurements.



### 2.3.3.2 *Error Evaluations (Measurement repeatability and MRI slice location)*

The measurement repeatability confirmed that the Bezier curve tool was the appropriate tool to carry out the TaAL measurement, and that as long as care is taken in identifying the trochlear tali then there should be minimal human error associated with taking the measurements. However, the literature verification indicated the potential error surrounding the subjective manner of selecting the slice to capture the data from, which was confirmed in the measurements across the talus.

It is not possible to avoid these discrepancies in the haemophilic group, due to the imaging protocol used clinically. The slice thicknesses ranged between 1.5-3.6 mm, with the most common protocol giving a slice thickness of 3.3 mm. This limits the number of images to choose from (8 to 11 slices per talus), creating a natural variability. The verification was carried out on the haemophilic group, rather than non-diseased control due to the larger slice thickness in the haemophilic group, meaning there was potential for larger discrepancies between neighbouring slices.

The highest percentage errors appeared to occur in the medial and lateral extremes of the ankles where the articular surfaces for the medial malleolus and the articular surface of the lateral process were covered in the sequences. The sequences for 5R and 5L covered these, and saw the largest percentage changes between the most medial and most lateral slices and their respective neighbours. Highlighting the need for careful slice selection.

The error evaluations demonstrated there are still some areas of uncertainty in these measures, with up to 5% human error in landmark selection for carrying out the measurements, and up to a 103% error in the calculated ratios when considering slice selection. Though the averages were much lower than this, it could still influence the comparisons between ankles, and between timepoints, but the methods have been refined where possible to negate these errors.

## 2.4 Morphology of the Haemophilic Talus

### 2.4.1 Methods

The comparison between non-diseased and haemophilic ankles can be broken down to three levels: whole haemophilic average against the non-diseased group average; individual haemophilic ankle average compared with non-diseased average; and changes within each individual haemophilic ankle with time.

The measurements taken from the images were collated in Microsoft Excel (Office 365) and organised into location across the talus, and grouped by individual haemophilic ankles. The

three ratios were calculated using formulas in excel removing any potential further human error. These results were used to make the comparisons to answer the question whether the haemophilic group differed from the non-diseased group, and if this occurred, how they differed, and whether these followed a trend with time.

To achieve this, statistical testing was carried out on the ratios for the control and patient groups to assess the significance of the difference between the two groups. 15 patient images were excluded from the haemophilia statistics (3x 5 MRI sequences), as the patient was still classified as paediatric for those sequences. As mentioned previously, whether these ratios should be the same in paediatric population is unknown, hence they have been excluded from the statistical analysis.

The matched control group was selected to diminish the effect of the body composition factors attributing to morphological variation, and should be completely negated by the use of ratios when comparing the two groups.

Statistical analysis was carried out to assess the normality of the data for all measurements and ratios. It is necessary to know if data is normally distributed when carrying out statistical analysis, hence, Shapiro-Wilk tests were carried out. Following these, equality of variance between the non-diseased control and haemophilic groups was assessed using Levene Tests. The equality of variance between the control group and the haemophilia group were important in choosing the appropriate T-Test to use, either Student's T-Tests, or Welch's T-Tests. These T-Tests were used to investigate the difference between the two groups (statistical significance set at 0.05).

The Shapiro-Wilk Test showed that all of the control group measurements and ratios, at all three locations, were normally distributed. For the haemophilic group,  $TaAL:TaLc$  and  $TaL:TaHl$  were not normally distributed.

The Levene test showed that some of the T-Test's should be carried out assuming unequal variance (Welch's T-Tests), as there were significant differences between the variances of the control and the haemophilic group. These were:  $TaR:TaALm$ ,  $TaL:TaHm$ ,  $TaAL:TaLc$  and  $TaL:TaHc$ . The remaining five were carried out assuming equal variance between the two groups (Student's T-Tests). T-Tests can provide  $p$  values for both one- and two-tailed tests, however, one-tailed tests were carried out as the hypothesis being tested was that the value for the control group should be greater than the haemophilic group in each instance.

## 2.4.2 Results

### 2.4.2.1 Haemophilic vs. Non-Diseased Ankles

When comparing the haemophilic group to the non-diseased control group, ratios behaved consistently, with flattening in the medial and lateral trochlear talus: greater values for both TaR:TaAL and TaL:TaH in the haemophilic group, and TaAL:TaL smaller (Table 8). The differences between the haemophilic and non-diseased groups were found to be statistically significant in all ratios in the medial talus, and two of the three ratios in the lateral talus, but not in the central talus.

Table 8 Control group and haemophilic (adult) group mean values for each ratio at the three locations (*m*-medial, *c*-central, *l*-lateral), and *p*-values from T-tests (\* indicates significant differences)

	TaR:TaAL			TaAL:TaL			TaL:TaH		
	<i>m</i> *	<i>c</i>	<i>l</i>	<i>m</i> *	<i>c</i>	<i>l</i> *	<i>m</i> *	<i>c</i>	<i>l</i> *
<b>Non-diseased</b>	0.46	0.56	0.59	1.21	1.15	1.20	3.64	4.21	4.01
<b>Haemophilia</b>	0.55	0.53	0.61	1.14	1.17	1.14	4.5	4.1	4.75
<b><i>p</i>-values</b>	0.003	0.22	0.31	0.001	0.08	0.004	0.002	0.28	0.05

Where the differences were significant between the groups the ratios behaved as expected with a flattening of the talus. The magnitude of differences however, did vary between the ratios. Where the greatest differences occurred, in the medial talus, TaR:TaAL<sub>*m*</sub> increased by 20.7% and TaL:TaH<sub>*m*</sub> increased by 23.5%, while TaAL:TaL<sub>*m*</sub> only decreased by 5.9%. The lateral talus also experienced collapse, with results indicating this is to a lesser degree: TaR:TaAL<sub>*l*</sub>=3.4% increase; TaAL:TaL<sub>*l*</sub>=5.5% decrease; and TaL:TaH<sub>*l*</sub>=18.4% increase. The smallest relative difference with disease occurred in the central talus, with the direction of these not indicating collapse: 4.6% decrease in TaR:TaAL<sub>*c*</sub>. TaAL:TaL<sub>*c*</sub>=2.0% increase, and TaL:TaH<sub>*c*</sub>=2.7% decrease with haemophilia.

### 2.4.2.2 Trends within Haemophilic Ankles

The eight ankles each responded to haemophilia differently, with averages of adult sequences measurements per ankle (Table 9) being variable between ankles.

Given the data in Table 9 represents a range of timescales, Figure 9-Figure 11 were generated to show the ratios at each timepoint, at each location across the talus. These results take into account the period of disease that the MRI is captured over – plotted as number of months from first MRI scan. Paediatric data has been plotted in these figures; it can be seen these results that

the morphology is less stable in these than in adulthood (4L – all images, 1R – month 39 to 112). There is no clear pattern of morphological response to HA in paediatrics or adolescents, with responses even differing between paired ankles.

Table 9 Behaviour of the ratios for the 8 haemophilic ankles – Considering the expected differences from the non-diseased control, those that behaved as anticipated (from Table 6) are highlighted in green. E.g. In the central images, should the haemophilic ankle behave as anticipated:  $TaR:TaALc > 0.56$ ,  $TaAL:TaLc < 1.15$ , and  $TaL:TaHc > 4.21$

		1R	2R	2L	3R	3L	4L	5R	5L
<b>TaR:TaAL</b>	<i>m</i>	<b>0.66</b>	0.44	<b>0.6</b>	<b>0.68</b>	0.43	<b>0.64</b>	0.42	0.36
	<i>c</i>	<b>0.57</b>	<b>0.62</b>	<b>0.61</b>	0.54	0.45	0.53	0.46	0.41
	<i>l</i>	<b>0.69</b>	0.55	<b>0.77</b>	0.54	0.55	<b>0.6</b>	0.58	0.45
<b>TaAL:TaL</b>	<i>m</i>	<b>1.12</b>	<b>1.13</b>	<b>1.08</b>	<b>1.09</b>	1.2	<b>1.1</b>	1.2	1.29
	<i>c</i>	<b>1.13</b>	<b>1.13</b>	<b>1.12</b>	1.16	1.23	1.15	1.23	1.26
	<i>l</i>	<b>1.11</b>	<b>1.14</b>	<b>1.05</b>	1.16	<b>1.14</b>	1.2	<b>1.13</b>	1.24
<b>TaL:TaH</b>	<i>m</i>	<b>4.74</b>	<b>4.36</b>	<b>5.32</b>	<b>5.79</b>	3.3	<b>5.35</b>	3.47	2.86
	<i>c</i>	<b>4.76</b>	<b>4.35</b>	<b>4.55</b>	<b>4.27</b>	3.24	<b>4.39</b>	3.3	3.08
	<i>l</i>	<b>5.52</b>	<b>4.52</b>	<b>6.79</b>	3.98	4.05	3.99	<b>4.35</b>	3.35

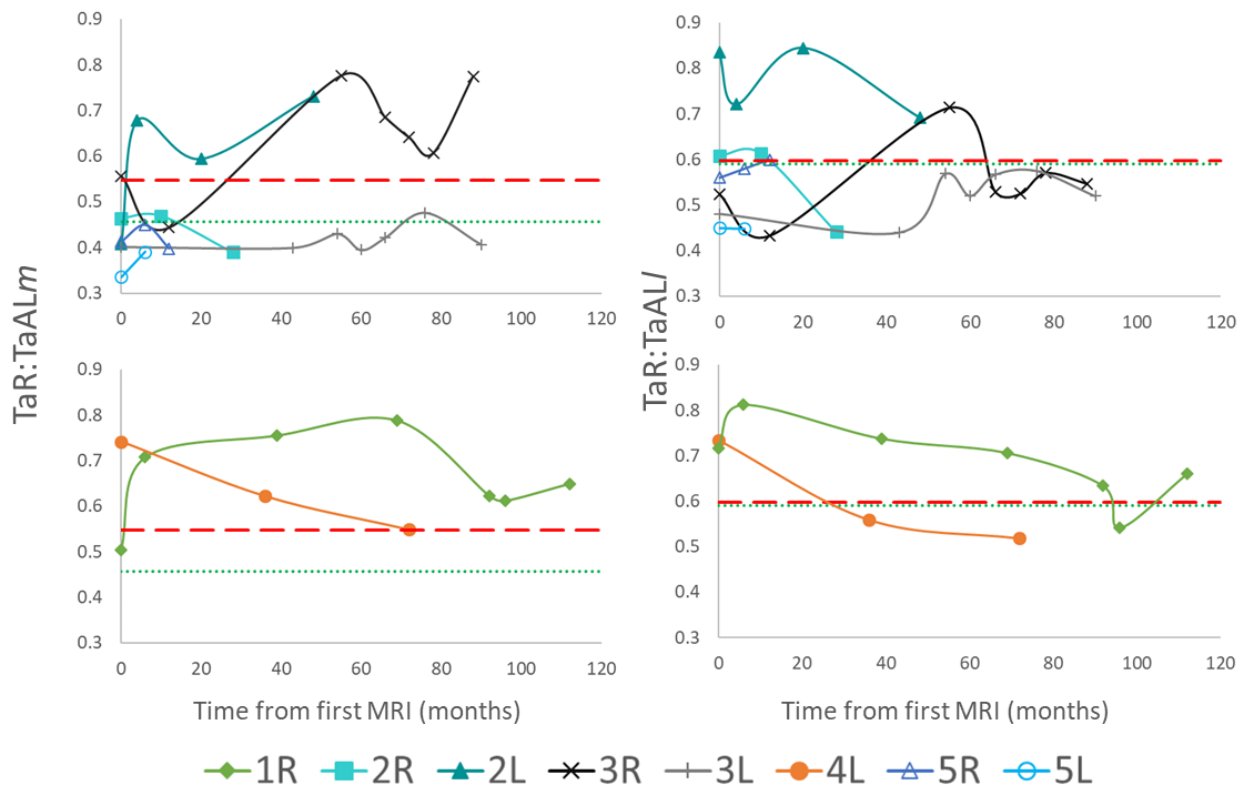


Figure 9 Change in  $TaR:TaALm$  and  $TaR:TaALl$  with time in months from the first sequence available. The average trend lines show haemophilic (red dashed) and non-diseased (green dotted) mean values from all eight ankles. The ratios are split into two categories, paediatric/adolescent (first row – paediatric data has not been included in reported stats), and adult (second row). Colour-codes relate to the age bracket the patient fell into at the first MRI sequence: grey/black – paediatric; greens/blues – adolescent; orange – adult. After approx. 40 months 1R moved from adolescent to adult.

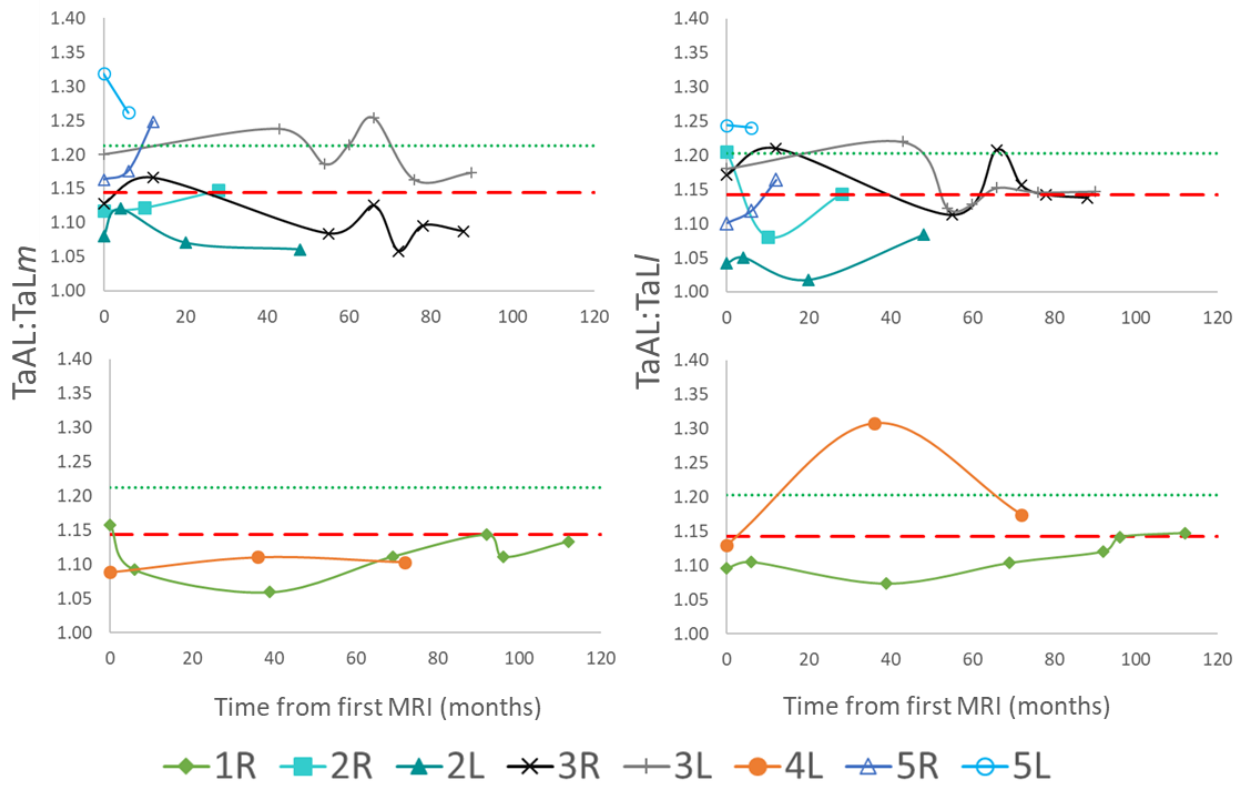


Figure 10 Changes in TaAL:TaLm and TaAL:TaLl with time in months. Details as described in legend of previous figure.

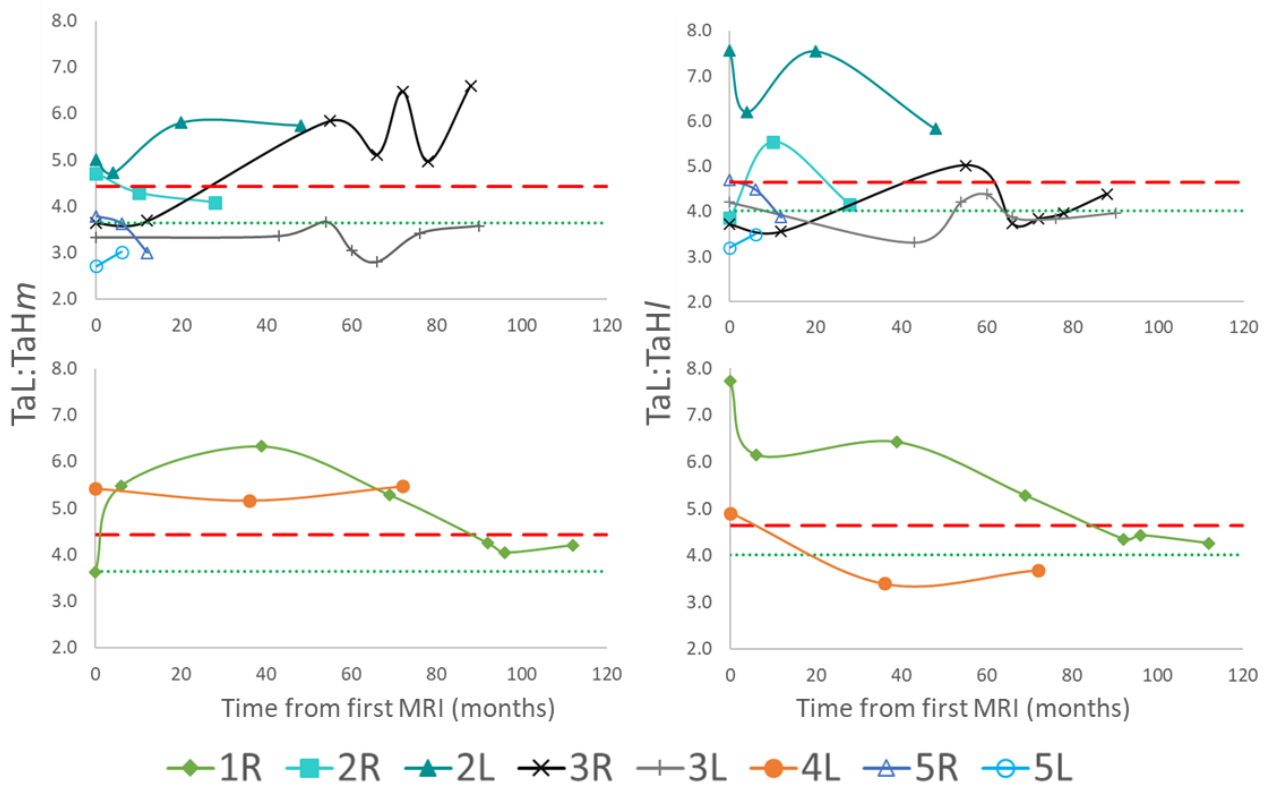


Figure 11 Changes in TaL:TaHm and TaL:TaHl with time in months. Details as described in the legend of Figure 9.

### 2.4.3 Discussion

The aim of this work was to investigate the influence of HA on talar morphology with disease progression by considering the differences between haemophilic and non-haemophilic groups, as well as the progressive nature of morphological changes with time. The ratios generated for each MRI sequence confirmed there was a non-uniform geometric change to the trochlear talus with disease; these changes were however non-linear with time in all haemophilic ankles.

#### 2.4.3.1 *Haemophilic vs. Non-Diseased Ankles*

It was anticipated that haemophilic ratios would differ from the non-diseased, as non-uniform flattening of the talar dome has been observed clinically in the haemophilic population (Macnicol and Ludlam 1999; Jelbert, Vaidya and Fotiadis 2009). The behaviour of the four measurements is important in understanding how the ratios should change with flattening, however due to the patient range should not be relied upon individually to see differences in the two groups. Larger values of TaR are expected with a flatter talus, while TaAL and TaH should decrease. How TaL changes is undetermined, and depends on the mechanism of morphological changes and whether the collapse causes osteophytes to be included in this measurement. It is possible that this value could increase, decrease, or remain relatively unchanged depending on the cause of this morphological change; whether it is a redistribution of the bone, or a biological attack to remove bone. This is an area for future investigation when considering bone mechanobiology in the presence of blood.

The behaviour of the measurements is important when considering whether they drive the ratio. TaR did not behave as hypothesised, as TaR was expected to drive change in TaR:TaAL, the reliability of using this measurement alone to indicate morphological changes is unclear. Both values are seen to move in the same direction, giving smaller than anticipated differences with disease. TaAL tending towards TaL appeared to most reliably demonstrate talar flattening of the three ratios, however the suggestion remains that the ratios should be used in combination.

The results appear to clearly indicate more highly affected regions of the talus. The non-uniform morphological change may be partly involved in the angulation phenomenon which has previously been accounted for by tibial morphology (Hacking and Dixon 2018). However, as both extremes are seen to be influenced not just the lateral side, this may be an unrelated morphological variation.

#### *2.4.3.2 Trends within Haemophilic Ankles*

The individual response to the haemophilic changes is also important, with commonalities and differences key in understanding the manifestation and development of the disease. HA is progressive and how these ratios changes with time could aid in understanding where in the staging this morphological change should fit – with rapid early changes leading to a different conclusion to slow linear progression.

With clear differences between the haemophilic and non-diseased groups in the medial and lateral regions of the talus, the influence of disease on individual ankles was considered. This investigation would have been strengthened by the HJHS outcomes, and whether there was any relationship between this and the individual joint outcomes. It was seen from the individual ankle's averages that morphological changes were unique to each ankle. It was also determined the effect on morphology with time was non-linear, and inconsistent across the eight ankles, even those in the three patients with bilateral presentation. Progressive flattening of the talar dome over time was not seen in all eight ankles.

However, it is clear that trochlear talar flattening can easily be quantified from clinical MRI, and the range in these morphological changes highlight the need to assess each ankle individually. If these values were being used to assess degree of disease progression, comparison against mean values of either a non-diseased or haemophilic groups may be insufficient, and longitudinal assessment of an individual would be preferable.

Changes in morphology were inconsistent across the eight ankles, and not all tended towards collapse. The same degree of change would not be expected, as the period of disease differs for each patient range from 6 to 112 months. It would not be representative to normalise the data with respect to time, as the point at which arthropathic changes occur appear to differ for each patient, and each target joint is likely to have a different annual bleed rate.

Some care must be taken in considering the progressive changes shown in Figure 9-Figure 11 due to the errors relating to the slice selection; this could translate to slice location when comparing timepoints in ankles. It cannot be guaranteed that the slices cover the same geometry in each sequence. These errors could explain some of the non-linear nature of the changes; to further understand this, measurements for all MRI sequences across the talus could be made for one ankle – such as 3R – to see if this accounts for the variability in the final four sequences.

It was not anticipated to see the same changes for all eight ankles due to different timescales the images were captured over. However, should morphological changes be progressive with haemophilic arthropathy, the ratios should follow the trends expected when comparing results to non-diseased ankles. Considering the changes seen in Figure 9-Figure 11 the progressive nature of the disease is not seen, especially not in the paediatric and adolescent cases. The results for these age groups are much less stable, with pairs of ankles from the same patient, hence same body composition, age and ethnicity, showing different trends. These differences must relate to the haemophilic response within the joint, however cannot be connected to the annual bleed rate, or HJHS as this information is not available – though could potentially explain the instability in joint morphology.

Only the older adult patient experienced a linear flattening with time, at which point it may be more reasonable that disease management and degenerative change have stabilised. This could also explain why this patient has only three sets of images over a six year period, as the images are collected following acute bleeds, conversely, those with greater numbers of bleeds in a shorter time frame may expect greater instability in response to blood in the joint.

Flattening occurred in some regions of the talus in the majority of the ankles as disease progressed; while growth or no change occurred in others. The differing response across the talus, at the same time point, could reflect the mechanism of the morphological change. Suggesting that there is a redistribution of bone with the morphological change, not just total bone loss causing uniform talar collapse. This would need to be confirmed in a larger cohort, however if it is seen in a larger population, would highlight the importance of investigating the mechanism of morphological change in future work.

## 2.5 Conclusion

The results presented in this chapter indicate that MRI is an adequate substitute for CT or radiographs as a medium for morphological measurements when evaluating talar morphology. The study is limited by being unblinded, meaning it was known both whether the ankle was from the haemophilic cohort, or the non-diseased cohort, and also which haemophilic ankle and timepoint was being measured. Although it was not seen, this does create some potential for bias in the results.



The results contrast non-diseased ankles, and those with a clinical history of musculoskeletal bleeds. They highlight there are unique morphological changes in each haemophilic ankles, and on the whole the haemophilic talus is likely flatter than a sex matched non-diseased talus. This study indicated that TaAL:TaL best indicated the morphological change in the talus, however would be best used in combination with TaL:TaH. TaR:TaAL could be used to support these ratios, however, as TaR did not follow the expected trend it may not be reliable for all haemophilic tali.

The flattening indicated by these ratios did not appear to progress with time as anticipated, and in paediatrics and adolescents morphological change is highly unstable. From this it is concluded it is unreasonable to extrapolate results beyond the time period imaged, or suggest that these results would be relevant to all haemophilic ankles.

The results imply a flattening of the talus which is non-uniform, with a greater influence of the disease on the medial and lateral margins of the talus, and insignificant changes in the centre. This flattening does not progress linearly with the disease – especially in younger patients. Each ankle has an individual response to disease progression, even in those patients with bilateral presentation. The unique morphological response to haemophilic arthropathy makes it impossible to judge a patient's response and give a prognosis off any of the trends seen in these results. With additional information such as HJHS for each ankle, a clearer correlation between the trends in the ratios could potentially be found. This is however unavailable data, hence, a similar approach will be taken with the outcomes of Finite Element Models in later chapters. Linking these morphological changes (Figure 9-Figure 11) to the contact pressure areas from Finite Element Models in Chapter 4 of this thesis will aid in understanding how the joint congruity changes with morphological changes.

# CHAPTER 3

## DEVELOPMENT OF PATIENT SPECIFIC ANKLE MODELS

# CHAPTER 3: DEVELOPMENT OF PATIENT SPECIFIC ANKLE MODELS

## 3.1 Introduction

The ankle is the most commonly affected joint for musculoskeletal bleeds due to haemophilia; this is hypothesised to be due to high intra-articular stresses (Buckwalter and Saltzman 1999) which ankles are susceptible to in everyday activities. These recurrent intra-articular bleeds have been seen to cause effusion, synovial hypertrophy, haemosiderin depositions, changes to the subchondral bone/joint margins, and cartilage loss and consequent joint space narrowing (Lundin *et al.* 2012). Osteoporosis has also been linked to HA (Kempton, Antonucci and Rodriguez-Merchan 2015; Kovacs 2008; Wallny *et al.* 2007; Bos *et al.* 2021), and osteophyte formation is reported to be similar in nature to osteoarthritic changes. Epiphyseal enlargement has also been noted in PwH when bleeds occur prior to epiphyseal fusion, although the consequence of this is little understood.

The aim of the model development is to create patient specific models from MR image data, to include as many disease features as necessary to assess the disease pathogenesis of HA. The purpose of the models is to analyse the stresses and contact pressures occurring within the ankle joint. These outputs are of interest due to the evidence of weight bearing influencing disease progression (Hooiveld *et al.* 2003), and treatment for HA focussing on decreasing bleed instances by reducing intra-articular pressures.

Patient specific finite element models exist to varying degrees in the literature, as was described in Chapter 1. The nature of the morphology and interactions in the ankle joint mean these can have a range of complexities, prior to taking into account the additional haemophilic manifestations.

It is vital to show that the methods to build these patient specific models are robust, and do not influence the outcomes of the investigations. There are three primary methods to demonstrating a model is robust; verification, validation, and sensitivity studies. These processes are key to Finite Element (FE) Models producing realistic models, with results meaningful to the real world, given the sensitivity of Finite Element Analysis (FEA) to modelling inputs.

In order to develop a robust FE model from clinical MRI, six sensitivity studies were undertaken, highlighting the key considerations when developing a patient specific ankle model.

The fact retrospective clinical MRI data is being used, rather than research protocols, introduces the need to assess whether the models generated are influenced by the variables in the MRI data. Therefore, six sensitivity studies were carried out on small subsets of MRI data – ranging between one to three MRI sequences per study – in order to ascertain how these may influence outcomes of the segmentation specific ankle models.

The Sensitivity to Inhomogeneous Bone (Section 3.4.1), was carried out on three MRI scans from three different PwH, while the Verification of Image Resolution (Section 3.7) was carried out on three of the eleven non-diseased control ankles. The remaining studies were carried out on one ankle at one timepoint, with the Mesh Convergence Study (Section 3.5), Imaging Direction Verification (Section 3.6), and Talar Cropping Study (Section 3.9) all using one ankle model, while MRI Sequence Type (Section 3.8) considered both T1 and T2 sequences at the same timepoint.

## 3.2 Model Generation

Models were generated from the same MRI sequences used for the morphological measurements work package in Chapter 2; ensuring that any connections made between morphology and finite element outputs were not influenced by differing sequence types.

Manual segmentation of the tibia, talus, cartilage components and cysts was carried out in Simpleware ScanIP (version P-2019, Synopsis Inc., Mountain View, California). Each MRI sequence was resampled, from the original slice thickness of 3.3 mm. Initially, this step was not included, however this caused a staircase artefact, which was over-smoothed if additional iterations of smoothing were carried out to remove this artefact (Figure 12). As neither of these options are appropriate, each image was resampled to 0.5357 mm slice thicknesses.

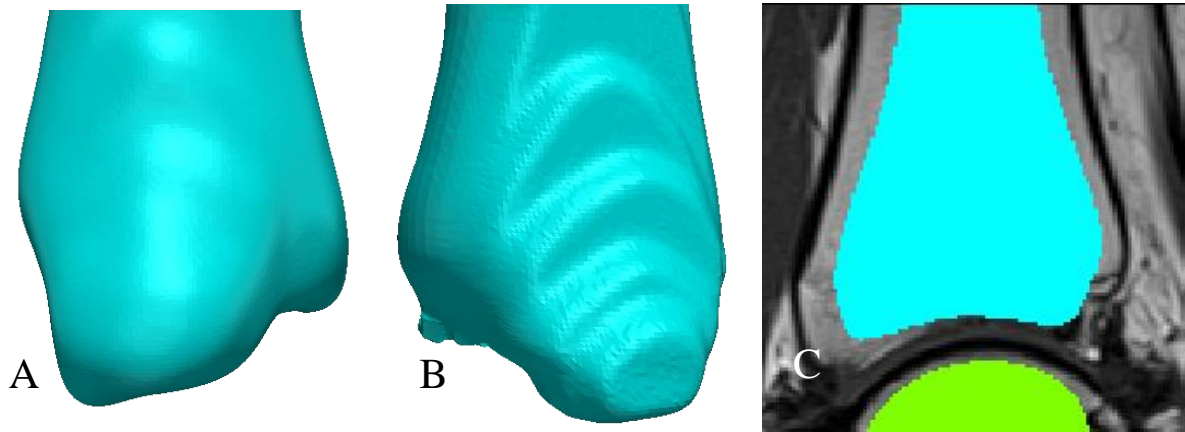


Figure 12 (A) Tibial model following resampling and smoothing, (B) Tibial model, smoothed with no resampling, (C) MRI with smoothed tibial (cyan) and talar (green) masks overlaid, demonstrating volume loss when resampling isn't carried out.

Resampling produced multiple copies of each MRI slice; these copies were segmented simultaneously, reducing variability from manually repeating the same mask on multiple slices. These masks produced a 3D volume that then need to be processed to produce a smoothed model (Figure 12A). The postprocessing varied depending on the volume, the Recursive Gaussian smoothing filter was used for all components; however, greater smoothing was needed in the tibia and the talus, and additional dilation to increase the cartilage thickness by one pixel before smoothing. Because smoothing can substantially influence FE-predicted contact stresses, with up to 30% reduction in peak contact stress (Li *et al.* 2008) the same degree of smoothing was used for each model to ensure this was not influencing comparisons made between models.

Figure 13 shows the model generation processes carried out in ScanIP for the tibia, talus, and their respective cartilages. In order for these models to not have severe errors within Abaqus CAE (Abaqus 2017, Dassault Systèmes, Vélizy-Villacoublay, FR), it was important to ensure there were no gaps between the cartilage and bone layers, and no overlap between the tibial and talar cartilage components where the contact is defined. Cartilage overlap was removed by carrying out a Boolean subtraction.

Following the segmentation and smoothing processes (A and B in Figure 13) each model was cropped to a similar tibial length, as some MR images had a much larger field of view and therefore the tibia was significantly longer. The cropping of both the tibia and talus gave flat surface onto which the loading and boundary conditions would be applied in Abaqus. The

decision to crop the talus rather than also investigate the talocalcaneal interaction was made based on the observation that the primary changes in HA in the ankle is within the talocrural joint (Pasta *et al.* 2008). Some tali had to be cropped to a greater degree due to irregular geometries causing sharp edges or small disconnected regions at the talar head. Due to this, a sensitivity study is reported in Section 3.9 to confirm this was not influential to results.

In a small number of models, realignment had to be carried out at this stage of the process to align the bones in a neutral standing position (approx. 90 degree angle between the foot and the tibia (Stufkens *et al.* 2011)). This was carried out prior to cropping to achieve these flat surfaces for the loading in Abaqus, the alignment was manipulated by rotating the tibial component by specified angles until the joint was in a neutral position. This was only carried out for models that were in a highly flexed or extended position.

An FE model was generated from the segmentation of the bones and cartilage (Figure 13D). Information relevant to the Abaqus stage of the process can be set up at this point, including: mesh generation, material properties, contacts, and node sets. This information is all exported to Abaqus with the geometry. +FE free meshing was used with multiple values of coarseness in the tetrahedral mesh – with the tibia having the coarsest mesh, and the talar cartilage the least coarse. A mesh convergence study was carried out (Section 3.5) to ensure an appropriate density was being used in the modelling, to strike the balance between computational cost, and model accuracy.

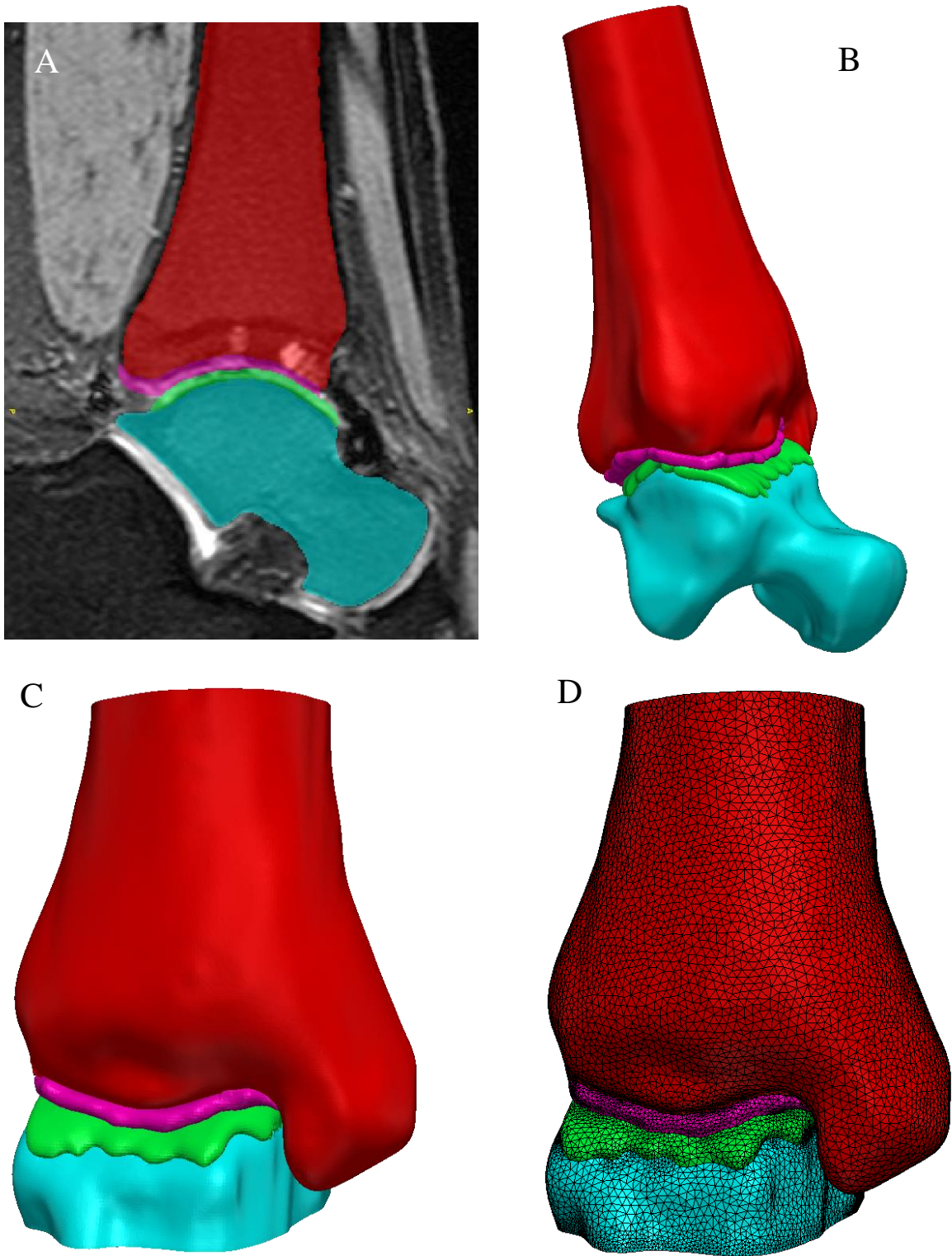


*Figure 13 Modelling processes within ScanIP (A) segmentation – translucent mask allows underlying MR image to be seen more clearly (cysts were not included in this model while present in the tibia), (B) Smoothing, (C) Cropping, and (D) Meshing.*

Placeholders were put in for the material properties of each tissues, for these to later be defined in Abaqus. Contact was defined between the two cartilage components, and surfaces defined for each component. It was ensured that the node sets on the cropped top surface of the tibia, and the bottom surface of the talus were defined, for the application of the loading and boundary conditions after the export of the model.

In Abaqus, the material properties, contact properties, loading conditions and boundary conditions were all defined (Figure 14). Loading was patient specific, and represented patient bodyweight at neutral still standing. Encastre boundary conditions, which allow no translation or rotation in any direction were applied to the cropped bottom surface of the talus. This was applied to each node, and was maintained for the duration of the simulation. In order to initiate contact, a vertical displacement was applied; this differed depending on the model, ranging from  $1 \times 10^{-6}$  mm to 0.5 mm. No other translational or rotational boundary conditions were applied to the tibia in the contact step. This displacement was then deactivated for when the load was applied, meaning there were no translational or rotational boundary conditions applied to the tibia in this step. This vertical load was applied as a force distributed between the nodes on the top surface of the tibia, and was calculated based on patient mass.

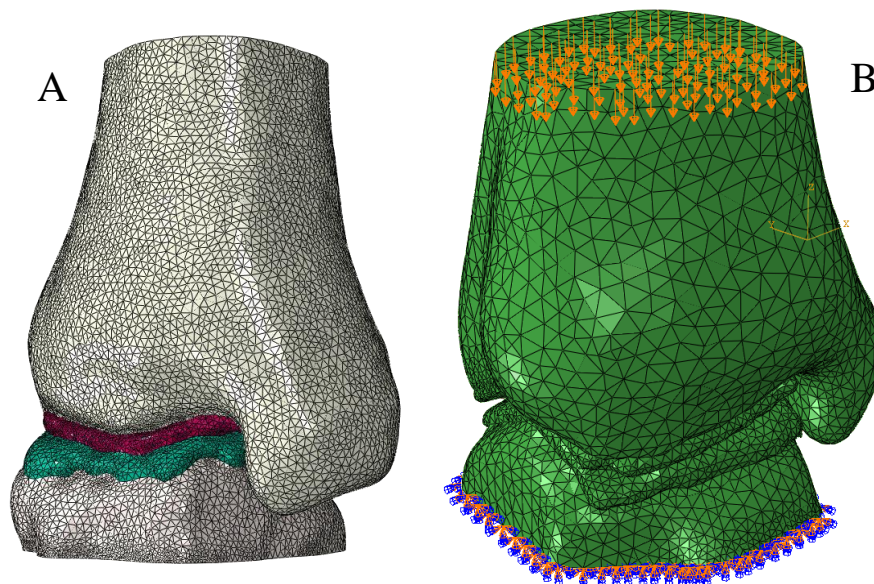


Figure 14 (A) material placeholders: white - bone; fuchsia and cyan - cartilage. (B) loading and boundary conditions

The properties of the contact defined between the two cartilage components in ScanIP were edited in Abaqus. Surface to surface discretisation was used with finite sliding, and adjustment



to remove any possible overclosure between the contact surfaces. The normal and tangential contact properties were defined for the entire simulation; a coefficient of friction of 0.1 was intended for use, being on the higher end of the values reported for literature. A full sensitivity to these properties carried out on 54 of the models is discussed in Chapter 4.

### 3.3 Outcomes of Interest

Results analysis was carried out separately in each bone and cartilage component. The results analysed for the sensitivity analysis were contact pressure, and how this contact was distributed, on the cartilage surface, and Von Mises stress (VMS) in the bone. Peak and mean values were reported for all outputs, and contact distribution was quantified as a % of cartilage surface area.

Cartilage contact pressure was selected as the metric of interest due to both qualitative and quantitative links with arthritic changes in post-traumatic OA (Anderson *et al.* 2011a; Anderson *et al.* 2011b; Li *et al.* 2008). Qualitatively, the distribution of this is of interest, given abnormal contact distributions may propagate cartilage destruction; the pressure values can also be quantified, and related to the destructive nature of overloading cartilage. Both highlighting potential detriment to joint health.

A similar approach was considered when selecting VMS as an output; localised elevated VMS values previously being linked to microfractures and subchondral bone cyst (SBC) growth (Dürr *et al.* 2004). As SBCs occur in HA, and VMS is not unsuitable due to the homogenous bone properties, this was selected as the key output of interest. Three other stresses were all also reported due to their links with disease progression in non-haemophilic joint damage: Shear stress (Tresca), compressive stress (Minimum Principal Stress), and tensile stress (Maximum Principal Stress).

### 3.4 Material Properties

Due to the unknown properties of haemophilic bone, the intention was to use simplified material properties to represent the bone and the cartilage. This involved modelling the bone as a homogenous, isotropic material. This is a simplification, as the cortical and trabecular structures of bone have different mechanical properties due to their structures and organisation responding to loading.

These simplified properties would not represent the osteoporotic quality of bone caused by haemarthrosis (Kempton, Antonucci and Rodriguez-Merchan 2015; Kovacs 2008; Wallny *et*

*al.* 2007), which would likely have a reduced stiffness. This in turn would be reflected in the stresses experienced in the bone.

In order to assess the sensitivity to these simplified properties, an analysis on the material properties was carried out. Both the influence of different cartilage properties found in literature, and the simplification to bone homogeneity were investigated independently. Prior to implementation on full ankle models, a simplified geometry of two curved components was used to carry out comparisons of 20 different combinations of materials for the bone and cartilage based on literature (See Appendix). The ‘bone’ components were partitioned to assign different materials to the cortical and trabecular regions in four of these tests. The impact of increasing and reducing the homogenous bone Youngs Modulus was assessed, as 7.3 GPa frequently used in literature (Ozen, Sayman and Havitcioglu 2013) is likely too high for the osteoporotic bone reported in haemophilia.

Both homogenous bone properties, and separate properties for cortical and trabecular bone were considered. As well as both linear elastic and different hyper-elastic models for the cartilage. There are multiple hyper-elastic material models used to model cartilage; three are most commonly referenced (Mooney-Rivlin, Neo Hooke and Yeoh), these were all considered in the sensitivity analysis (see Appendix). It has been shown that the material constants vary across joints and between individuals, hence the properties tested in the sensitivity analysis were ascertained from ankle models (Miller *et al.* 2004; Cheung and Zhang 2005; Butz *et al.* 2011; Niu *et al.* 2013; Ramlee, Kadir and Harun 2013; Klekiel and Będziński 2015; Ozen, Sayman and Havitcioglu 2013). The Mooney-Rivlin model is believed to better represent the nature of cartilage (Li *et al.* 2007; Ramlee, Kadir and Harun 2013) hence the selection for use in all 38 models. The properties used were from non-diseased ankle models; as a relationship between mechanical properties and tissue composition has been seen (Kiviranta *et al.* 2006), the values used are unlikely to represent the haemarthritic condition.

This testing allowed for a range of scenarios to be considered, however the simplification to the geometry influenced the results. Therefore, the separate bone properties for cortical and trabecular (Miller *et al.* 2004) were implemented on three full ankle models generated using the methods described in Section 0. For these three ankle models, the homogenous comparator was modelled with a Young’s Modulus ( $E$ ) of 7.3 GPa, of a Poisson’s ratio ( $\nu$ ) of 0.3. The cartilage in both the homogenous and split-bone instances was modelled as a hyper-elastic

material with Mooney-Rivlin properties with two coefficients defined:  $C_{10}= 4.5$  MPa and  $C_{01}=0.66$  MPa. The cartilage was assumed to be completely incompressible ( $D_1 = 0$ ).

### 3.4.1 Sensitivity to Inhomogeneous Bone

In order to create a split bone model, the cortical bone thickness was measured at five locations in the tibia, and three in the talus, on the central MRI slice, and averaged. This was repeated for the three ankle models (Table 10). This measurement process was carried out as the thickness is seen to vary dependent on the location, however, for the purpose of this study manual segmentation of the cortical and trabecular bone would have been a highly time consuming process. Taking cortical bone measurement from MRI is still an estimate, due to the unclear bone boundary definitions, however, all three were in good agreement with literature values, and agreed with the finding that the talar cortical bone is thinner than the tibial cortical layer (Tsegai *et al.* 2017).

Table 10 Cortical bone thickness for the three ankle models

<i>Model Number</i>	<i>Ankle</i>	<i>Cortical Thickness (mm)</i>	
		<i>Tibia</i>	<i>Talus</i>
1	Patient 1, Right	0.6	0.4
2	Patient 3, Left	0.7	0.35
3	Patient 4, Left	0.7	0.35

In order to assure the total bone volume was unchanged, the tibial mask was duplicated in Simpleware ScanIP (Synopsis, 2019) and the erode feature used to shrink the duplicate mask by the cortical thickness (Table 10) to create a second trabecular bone mask, which was deducted from the cortical mask using a Boolean operation. These masks (Figure 15A) were then used to generate segmentation specific FE models using the method described in Section 0.

The differences between the homogenous and split bone models was assessed for all outputs of interest in both the bone and cartilage. A 2-sample Kolmogorov-Smirnov test was carried out (significance level 0.05) to compare the distributions in the contact pressures and bone stresses between the two models in each ankle.

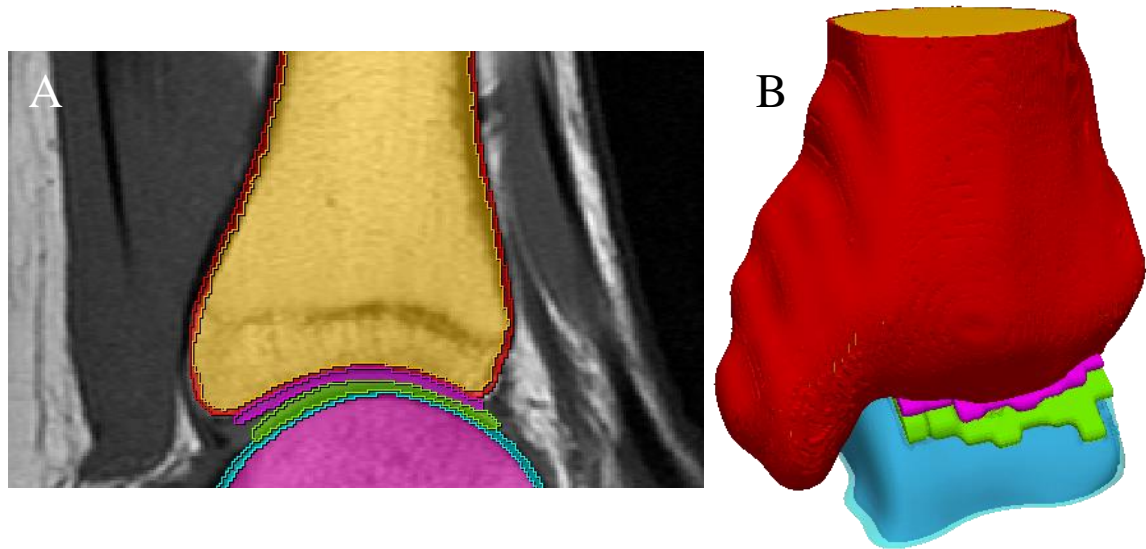


Figure 15 Split layered bone model, A) with translucent uniform thickness overlaying MRI image, and B) reconstructed model with 50% translucency applied to cortical talar layer

### 3.4.2 Results

The contact pressures and bone stresses were influenced by the splitting of the bone; with both the distribution in the histogram of values in the contact pressures (Figure 16), and VMS (Figure 17) influenced by the change in bone properties.

Statistical testing showed that there were significant differences between the layered bone and homogenous model distribution of results; this was the case for the contact pressure in both the tibial and talar cartilage ( $p < 0.0001$ ), and the VMS in both the tibia and talus ( $p < 0.0001$ ).

The violin plots in Figure 16 show how these distributions varied between cases in both the tibial and talar cartilage. The violin plots for the VMS can be found in the Appendix, however less clearly demonstrate the distribution due to the large peak stresses (Table 11).

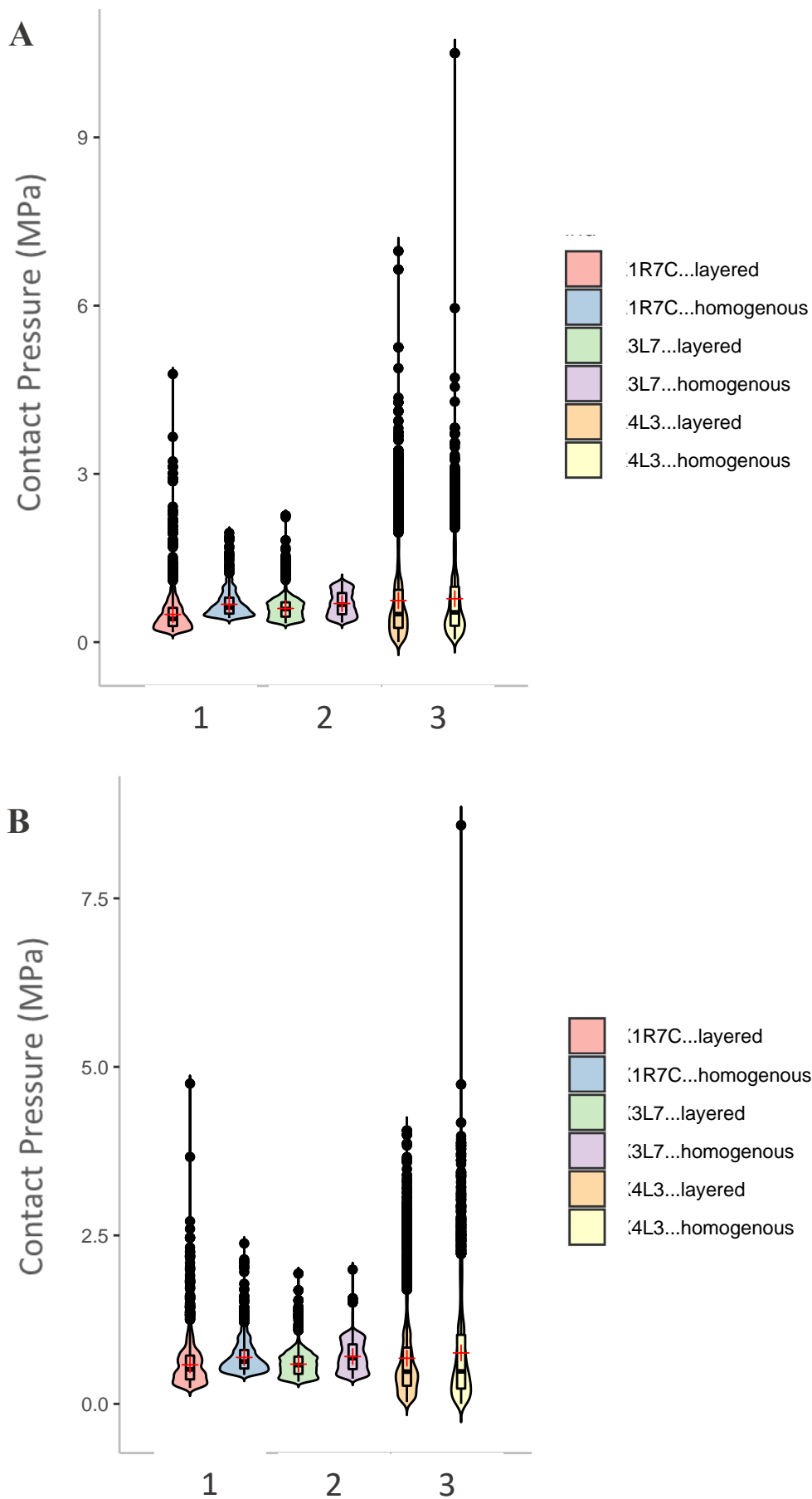


Figure 16 Violin plots comparing A) Tibial, and B) Talar cartilage contact pressures (MPa) distributions in the three ankles in both bone conditions

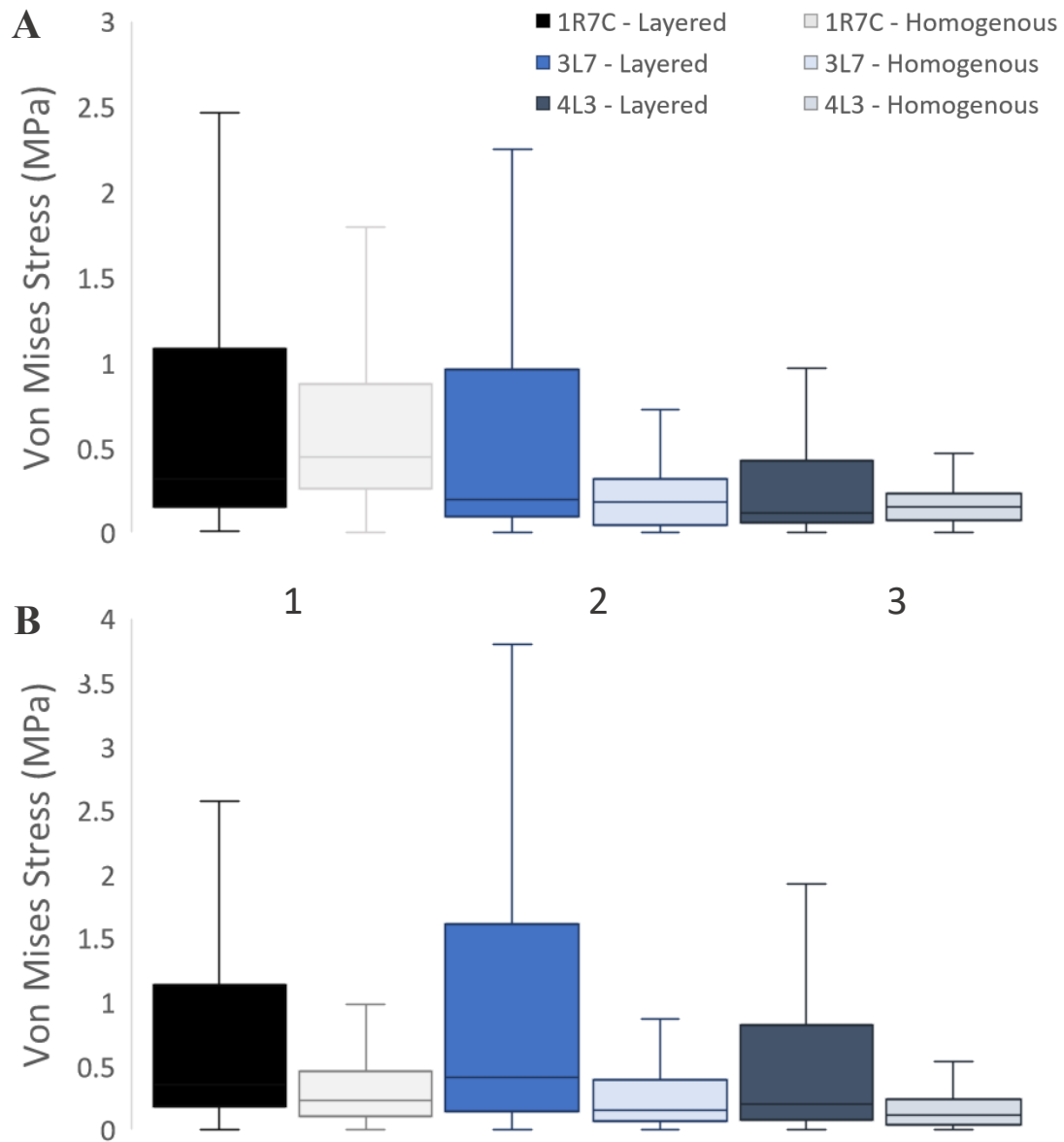


Figure 17 Box plots of VMS (MPa) in A) tibia, and B) talus

Table 11 Minimum, maximum and mean VMS (MPa) in both the homogenous and split bone models for the three ankles

		1		2		3	
		<i>split</i>	<i>homogenous</i>	<i>split</i>	<i>homogenous</i>	<i>split</i>	<i>homogenous</i>
<b>Tibia</b>	min	6.86E-03	2.11E-03	1.82E-03	1.34E-03	9.02E-04	1.07E-04
	max	222.711	47.492	20.744	7.351	12.266	9.023
	mean	1.077	0.858	0.676	0.226	0.390	0.209
<b>Talus</b>	min	7.88E-03	1.01E-04	4.50E-03	1.19E-03	4.01E-03	2.74E-04
	max	17.142	34.396	16.691	6.128	15.177	3.493
	mean	0.848	0.373	0.928	0.262	0.568	0.178

### 3.4.3 Discussion

The true properties of haemarthritic bone and cartilage are unknown, hence all properties considered in the sensitivity analysis are likely to be over-simplifications. While the biological influence of blood on bone and cartilage is understood, the implication of these on the respective mechanical properties is still unknown. It is likely that the osteoporotic tendencies in HA would lower the Young's Modulus of the bone, but whether this occurs, and to what extent would be patient specific. The presence of haemosiderin depositions in the synovium would likely change the contact properties between the cartilage layers, and have unknown implication on the mechanical properties of cartilage.

The properties considered in the cartilage were all taken from literature reporting on healthy ankle cartilage, while arthritic properties would better suit the model application. Given these are not widely available, and would again differ in HA, this was taken as a limitation of the model. In order to represent the arthritic condition, a higher coefficient of friction was used to define the interaction between the two cartilage components.

Sensitivity studies are key in understanding how these simplifications to the materials used influence model outputs. The assumption of homogeneity is seen to influence the results, with significant differences in the distribution of the data, between the layered and homogenous bone models for both bone and cartilage results in all three ankles. The difference in peak bone outputs was especially clear in the comparison for model 1, this almost five-fold increase in peak stress is most likely due to an oddly shaped element in the mesh between the cortical bone and cystic regions.

Peak values are highly sensitive to the mesh used, not just the material differences, hence the difference in the peaks was anticipated as the thin layer of cortical bone would influence the meshes in each comparison. However, the mean values should be less sensitive to this, and therefore the differences seen should be driven by the differing bone properties. These means were seen to increase in the bone stresses in the layered bone models, while there were minimal differences in the cartilage contact pressures (Table 11). We cannot take the values from these models to be the exact values experienced by each patient, however, trends in how these change with time or under haemarthritic conditions can still be considered as this variable is maintained throughout all models.

The data from this sensitivity analysis led to the conclusion that it is unlikely to be possible to experimentally validate any bone stresses experienced within the ankle joint using simplified bone material properties. However, these properties are an appropriate substitute when considering the influence on cartilage health.

### 3.5 Mesh Convergence Study

The second sensitivity study was a mesh convergence study, which considered the meshing strategy, and mesh refinement for one model, at three coefficients of friction (0.5, 0.1 and frictionless). Multiple contact properties were assessed to ensure the results were relevant to more than one modelling strategy.

An appropriate relationship between the edge lengths in the cartilage and in the bone components was sought (Table 12). It was anticipated that large jumps in element edge lengths between parts in the models could cause some issues with convergence due to oddly shaped elements at the boundaries.

Table 12 Mesh convergence tests to find appropriate ratio between mesh sizes for cartilage and bone

Test Number	Mesh Measurements		Edge length ratio	Number of Elements
	Cartilage	Bone		
1	1 mm	2 mm	1:2	121,235
2	1 mm	3 mm	1:3	97,409
3	0.5 mm	2 mm	1:4	408,360
4	0.25 mm	2 mm	1:8	1,880,393
5	2 mm	2 mm	1:1	66,572
6	0.5 mm	3 mm	1:6	384,333
7	0.25 mm	1 mm	1:4	2,108,772
8	0.5 mm	1 mm	1:2	632,646
9	1 mm	1 mm	1:1	358,781

Once the appropriate edge length ratios was found, this was converted to coarseness values to generate the first mesh. The coarseness values can be seen in Table 13, and the ratio between these was kept in line in all bar Test1\_coarse. The start point (Test 1) was both increased and decreased in density, however, meshes finer than 40% of the coarseness values (Test1\_0.4) were too computationally expensive to simulate. Both linear (C3D4) and quadratic (C3D10H) elements were considered at three different coefficients of friction, however none of the linear meshes converged before Test1\_0.4, hence only quadratic mesh results are reported. Convergence was checked for mean VMS, and mean contact pressures, as these are used throughout the chronological study in Chapter 4.



Table 13 Mesh coarseness values sensitivity analysis

Sensitivity Name	Number of Nodes		Number of Elements
	Linear	Quadratic	
<i>Test1_coarse</i>	8,602	56,563	34,212
<i>Test1_1.25</i>	12,526	83,188	50,909
<i>Test1_1.2</i>	13,162	87,603	53,729
<i>Test1</i>	16,309	109,587	67,965
<i>Test1_0.9</i>	17,849	120,173	74,718
<i>Test1_0.8</i>	21,572	146,098	91,531
<i>Test1_0.7</i>	25,946	176,390	111,120
<i>Test1_0.6</i>	33,623	230,477	146,981
<i>Test1_0.5</i>	42,575	292,534	187,091
<i>Test1_0.4</i>	63,397	440,466	285,167
<i>Test1_0.2</i>	205,468	1,469,664	986,954
<i>Test1_0.1</i>	481,587	3,503,891	2,400,697
<i>Test1_0</i>	5,916,400	46,914,774	36,825,177

### 3.5.1 Results

The edge length study showed that the difference between the bone components and cartilage components should be less than 1 mm. Test 3 and Test 4, which had finer cartilage meshes produced no better results than Test 1. The least appropriate tests were those with differences over 2 mm between the cartilage mesh edge length, and bone mesh edge length (Test 2 and Test 6); confirming that large jumps in edge length should be avoided.

Using this information the edge lengths from Test 1 were then used to carry out the convergence seen in Figure 18 to Figure 20. The percentage error between the selected mesh density (Test1\_0.7) and the finest mesh (Test1\_0.4) was calculated for each output for the coefficients of friction (cf): 0.5 and 0.1. The largest error was in the tibial VMS (7% for both cf), the talar VMS had a 4% error for both (cf), while all contact pressures were within 2% (range: 0.02% to 1.6%).

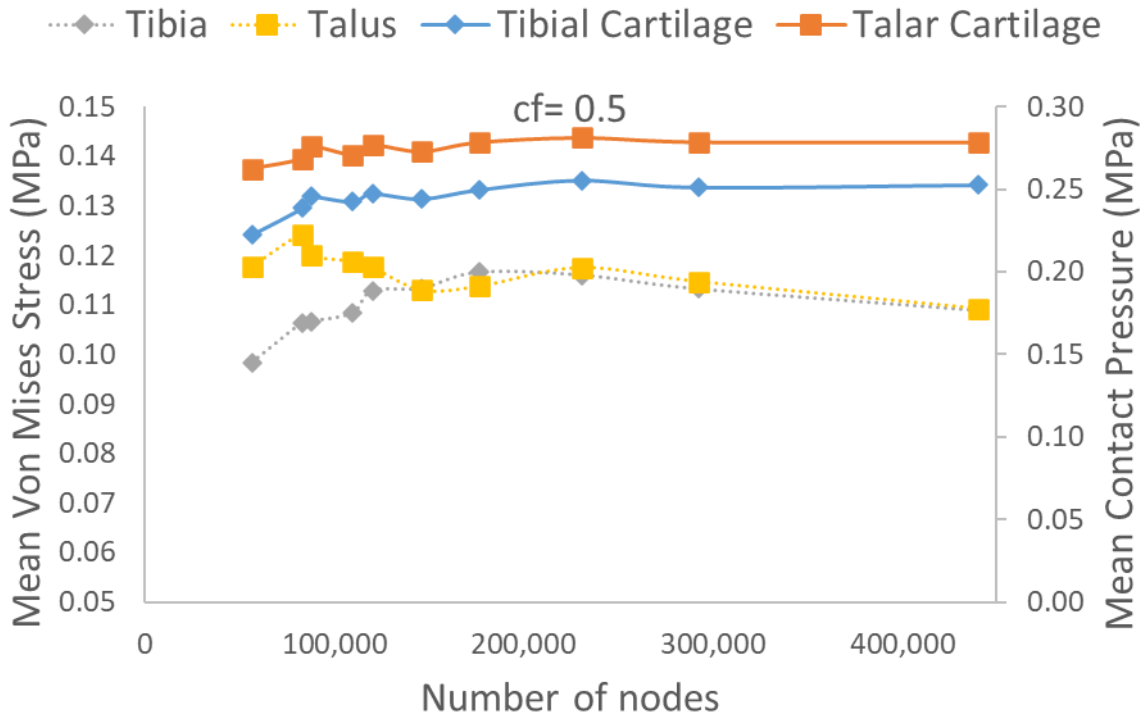


Figure 18 Mesh convergence for highest coefficient of friction (0.5); VMS (MPa) in the tibia and talus, and contact pressure (MPa) in the tibial and talar cartilage (quadratic, C3D10H elements)

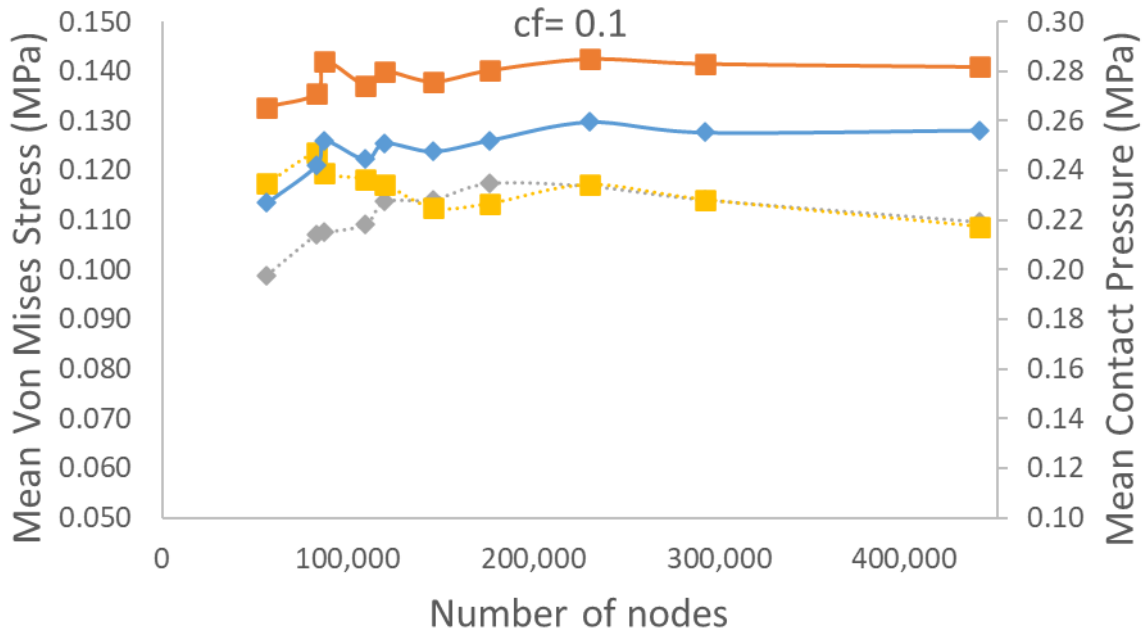


Figure 19 Mesh convergence for most frequently used coefficient of friction (0.1); VMS (MPa) in the tibia and talus, and contact pressure (MPa) in the tibial and talar cartilage (quadratic, C3D10H elements)

The frictionless contact (Figure 20) was less reliable in the mesh convergence, and did not allow for errors to be calculated, as the model only completed 83% of the load step for the

finest mesh (Test1\_0.4), likely due to the high peak contact pressure that the frictionless model was tending towards. However, this was not of concern due to the frictionless contact not being used in the chronological analysis considered in Chapter 4.

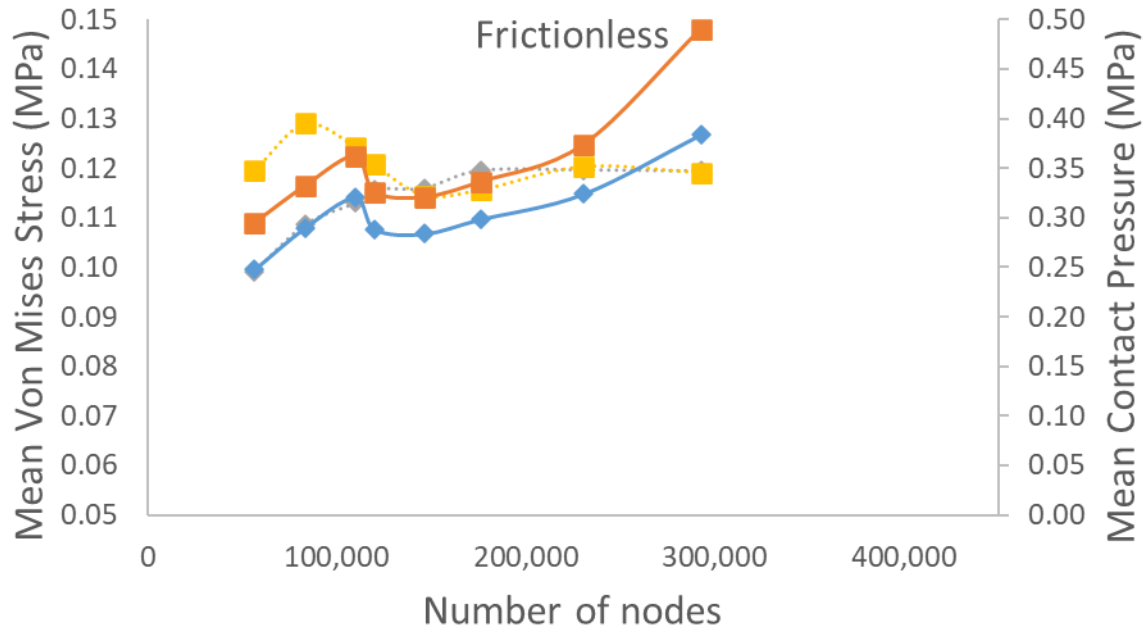


Figure 20 Mesh convergence for frictionless contact; VMS (MPa) in the tibia and talus, and contact pressure (MPa) in the tibial and talar cartilage (quadratic, C3D10H elements)

### 3.5.2 Discussion

Mesh convergence is a key aspect of FEM, as results can be highly dependent on mesh quality. The density and shape of the elements both play a role in model outputs, as does the order of the mesh, which dictates the number of nodes per element.

Meshes should converge for all outputs of interest, in all regions of interest, hence checks were also carried out for compressive, tensile and shear stress in the tibia and talus. Contact properties are a key consideration, hence showing the mesh is converged for the coefficients of friction used in the chronological study is important. This mesh convergence confirmed the assumption that contact pressures may be more highly influenced by coefficient of friction, hence will be used as the output of interest in the coefficient of friction sensitivity analysis (Chapter 4).

The mean values were used, as peak stresses tend to relate to oddly shaped elements, or stress concentrations can occur around fixed nodes, that are not representative of true stresses experienced in the joint. The fixation and loading of nodes is important to the correct

displacements of the structure during loading; without fixation, the model would move infinitely through space rather than converging. However, these unrealistic peak stresses should be ignored as they are likely a side-effect of the boundary conditions applied.

It was found, when assessing the meshing strategy, that the different versions of ScanIP (2018 and 2019) produced different meshes. Therefore it was ensured all models were meshed using the 2019 version of ScanIP, as this was the version the convergence study meshes were generated in.

The coarseness values determined by the mesh sensitivity were then applied to the 38 models used to investigate the disease presentations. It was ensured these mesh densities maintained the same maximum edge length value as the converged mesh. Convergence appeared to begin just before 200,000 nodes (Test1\_0.7), therefore, the edge length values were extracted from this mesh. Although edge lengths could be shorted than this, this increased the computational expense unnecessarily. These edge lengths gave residual errors up to 7% in the tibial von mises stress, however, these related to differences of only 8Pa which is relatively small when considering its influence on the comparison between models.

### 3.6 Imaging Direction Verification

In the standard clinical assessment of the ankle joint within Leeds Teaching Hospitals NHS Trust, three imaging directions are collected: Sagittal, Coronal and Axial. The sagittal projection is recommended in literature to best capture the morphology of the talus when using 2D MRI. It was also the projection utilised for the morphological measurements as it best demonstrated talar collapse. However, a simple sensitivity study was carried out to demonstrate the suitability of this projection.

#### 3.6.1 Methods

Utilising the segmentation methods described in Section 0, including isotropic resampling, one MRI sequence was used to generate 3D models for the three different imaging directions. Segmentation was only carried out for the tibia and talus, as the cartilage components were not clearly visible in the axial projection. The difference in the three volumes, and the morphological features of the talus were assessed. As no cartilage could be segmented in the axial view, it was not possible to carry out any finite element analysis verification, however, the clear differences between the imaging directions meant that only a qualitative assessment was needed to support the use of the sagittal projection.

#### 3.6.2 Results

The features of both bones were influenced by the imaging direction, the lack of cartilage definition in the axial view made it the least appropriate for finite element modelling of the ankle. The cartilage definition was less clear in the coronal projection, compared to the sagittal projection, making it more challenging to capture accurate cartilage geometry in the coronal view.

Although there were some volumetric differences (Table 14), the morphology is where the influence was more clear. Some differences were seen in the tibia (Figure 21), however the greatest variation was found in the talus (Figure 22). The talus generated in the axial view did not demonstrate the classic saddle shape, with the slice thickness clearly causing this feature to be missed. It was seen in the coronal view that additional bony features were captured in the posterior talus (bottom central model, Figure 22).

Table 14 Volumes ( $\text{mm}^3$ ) of tibia and talus from the three different fields of view

	<i>Axial</i>	<i>Coronal</i>	<i>Sagittal</i>
<i>Tibia</i>	51,673	59,124	56,567
<i>Talus</i>	26,711	27,485	30,265

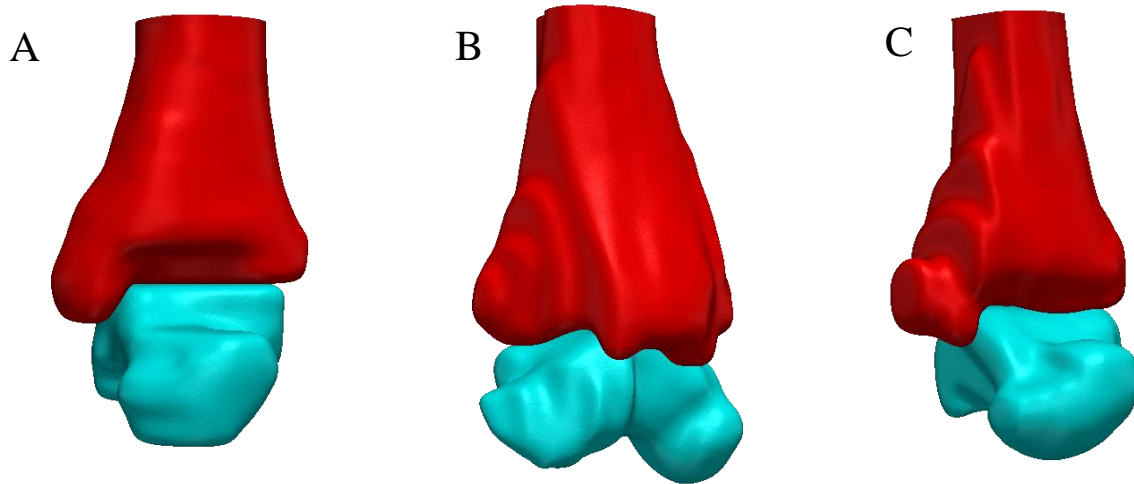


Figure 21 Tibia and Talus models built from (A) axial slices, (B) coronal slices, and (C) sagittal slices - no resampling, all to same degree of smoothing (anterio-medial view)

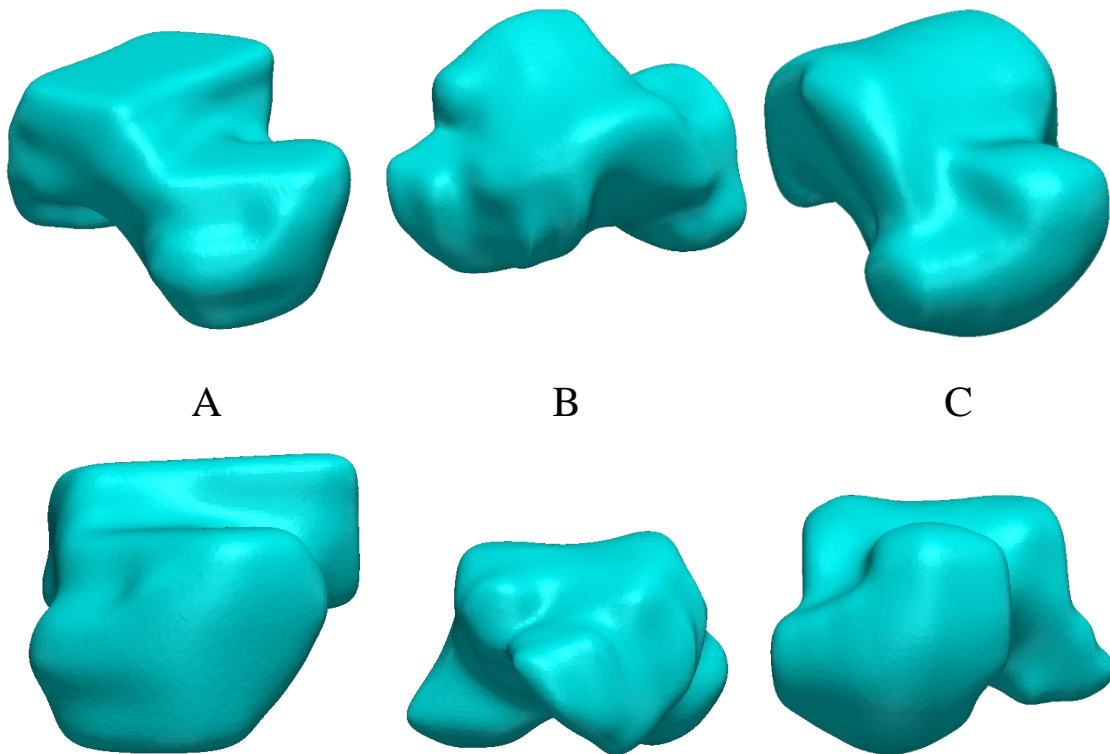


Figure 22 Views of the talus generated from (A) axial, (B) coronal, and (C) sagittal projections. Same degree of smoothing on all models. Bottom row: coronal segmentation (B) shown from posterior view; axial (A) and sagittal (C) segmentations shown from anterior view

### 3.6.3 Discussion

The MRI sequences collected clinically are clinical 2D sequences, which differ from 3D sequences preferred for research and modelling purposes. The segmentation of these 2D slices would differ depending on the imaging direction they are taken from, while in 3D they should generate the same volume. For this reason, it was assessed how these volumes from 2D differed, and which was the least, and most appropriate for generating the ankle joint geometries.

The least appropriate imaging direction for generating a model of the talus is the axial view, as the classic saddle shape to the trochlear talus is missing, and the articular cartilage of the talocrural joint was missing. The coronal view more clearly showed the geometry of the articulating surfaces, however, there were additional bony features on the talus, which were potentially segmentations of surrounding soft tissues. Therefore, the sagittal view was selected, as it most clearly showed the geometry across the talus, and allowed for clear definition of the articular cartilage, where the surrounding soft tissue was more clearly defined and therefore not misinterpreted as bone.

### 3.7 Verification of Image Resolution

The clinical MRI used for this study is a relatively low resolution when compared with those previously used to build finite element models; the purpose of this sub study was to investigate the impact of using these lower resolution images on the morphology and consequent FEA outputs. This was possible, given that higher resolution MRI, collected for clinical research were available from the control group (Chapter 2).

#### 3.7.1 Methods

MRI data for three non-diseased control was processed in ScanIP, with two models created for each control ankle: original slice thickness (0.5 mm), and resampled slice thickness (0.5357 mm). In order to create the resampled slice thickness, the original high resolution images were down sampled to the most common slice thickness found in the clinical MRI (3.3 mm), then resampled to the same resolution used for the patient specific ankle models (0.5357 mm). These two sets of images were segmented, giving two models per ankle with the difference between these models being their slice resolution. These models were compared for their geometry and volumetric differences, and consequent finite element model outputs.

#### 3.7.2 Results

There were small volumetric differences between the two image resolutions in both bone and cartilage components (Table 15); though the morphological differences were more important (Figure 23). The differences between the original and resampled morphology had a consequent influence on the cartilage contact pressures (Table 16), and VMS (Table 17). The resampling has a different influence on the three models, however, error in the peak values had the greatest variation.

Table 15 Volumes ( $\text{mm}^3$ ) of the original slice thickness and resampled models for all bone and cartilage components

	<b>Control 1</b>		<b>Control 7</b>		<b>Control 11</b>	
	<i>original</i>	<i>resampled</i>	<i>original</i>	<i>resampled</i>	<i>original</i>	<i>resampled</i>
<b>Tibia</b>	55,783	55,204	61,999	60,338	53,339	52,894
<b>Talus</b>	35,893	33,886	48,016	46,552	40,704	39,477
<b>Tibial Cartilage</b>	1,174	1,315	1,214	1,489	933	1,182
<b>Talar Cartilage</b>	1,249	1,344	1,576	1,685	1,496	1,266



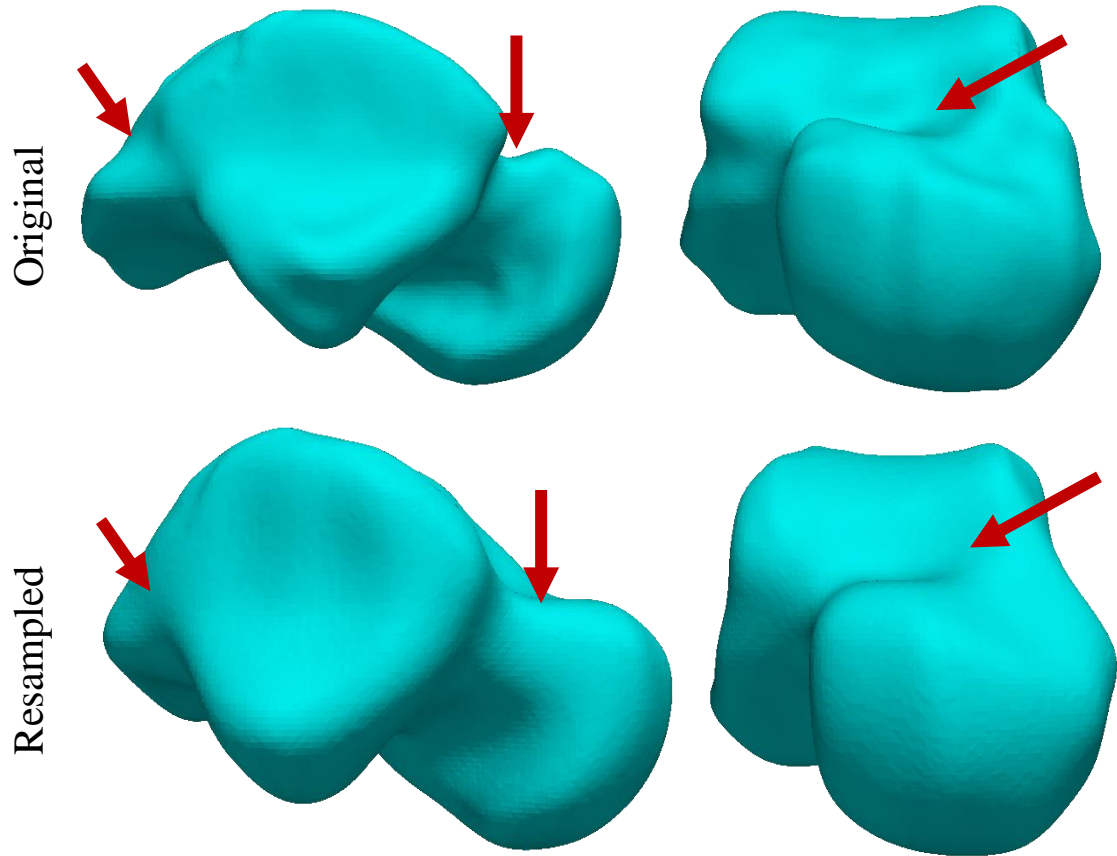


Figure 23 Morphological differences (highlighted with arrows) between the original and resampled tali, showing smoothing of some morphological features in the resampled talus - Control 11

Table 16 Error (%) for the cartilage contact pressure outputs between the resampled and original slice resolution in the three control models

		Control 1	Control 7	Control 11
<b>Tibial</b>	<i>Peak</i>	24.4	20.5	15.1
<b>Cartilage</b>	<i>Mean</i>	0.94	5.5	23.6
<b>Talar</b>	<i>Peak</i>	12.2	3.1	42.9
<b>Cartilage</b>	<i>Mean</i>	2.7	3.9	28.4

Table 17 Error (%) for the VMS outputs in the bone between the resampled and original slice resolution in the three control models

		Control 1	Control 7	Control 11
<b>Tibia</b>	<i>Peak</i>	12.6	41.8	33.2
	<i>Mean</i>	2.1	2.8	1.8
<b>Talus</b>	<i>Peak</i>	33.7	4.4	53.1
	<i>Mean</i>	11.3	7.9	22.0

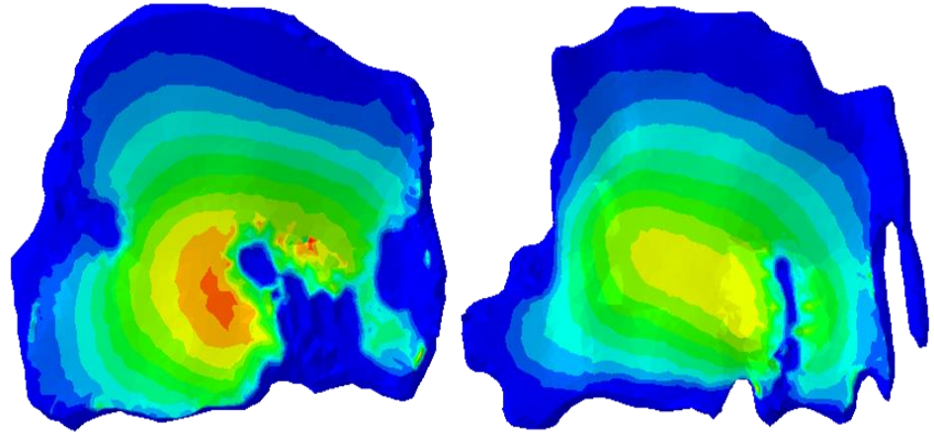
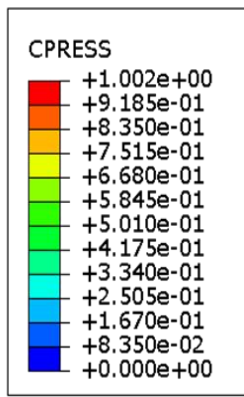


Figure 24 Tibial cartilage contact pressure distribution in original (left) and resampled (right) for control 1

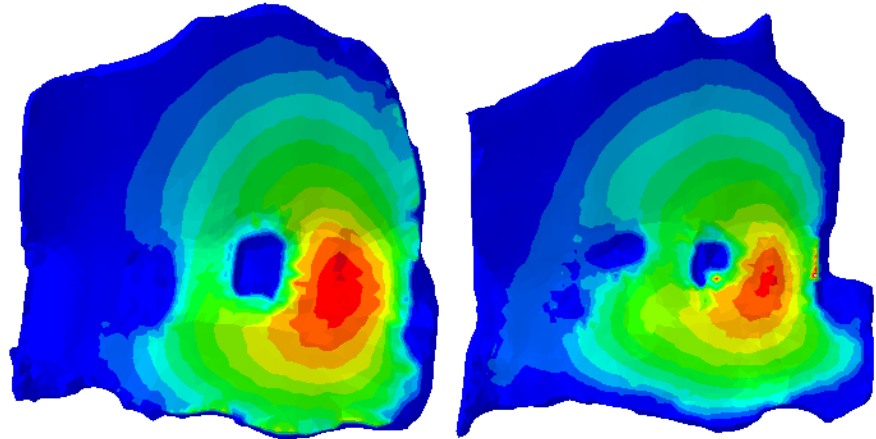
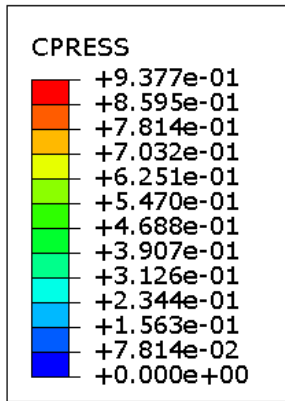


Figure 25 Tibial cartilage contact pressure distribution in original (left) and resampled (right) for control 7

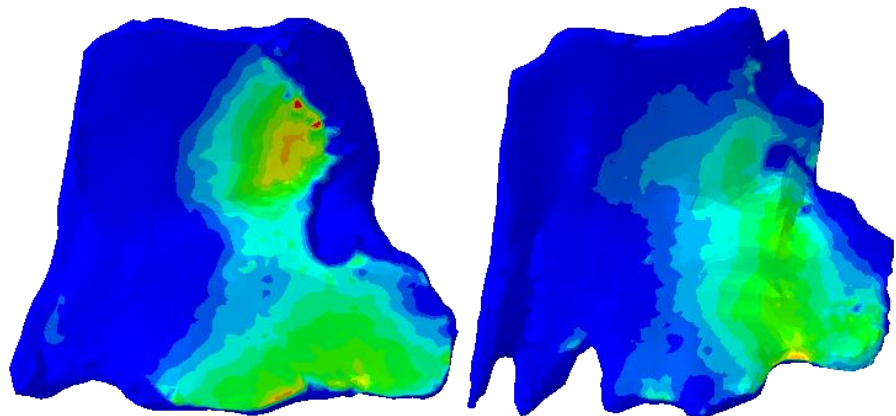
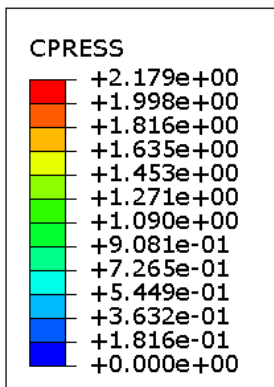


Figure 26 Tibial cartilage contact pressure distribution in original (left) and resampled (right) for control 11

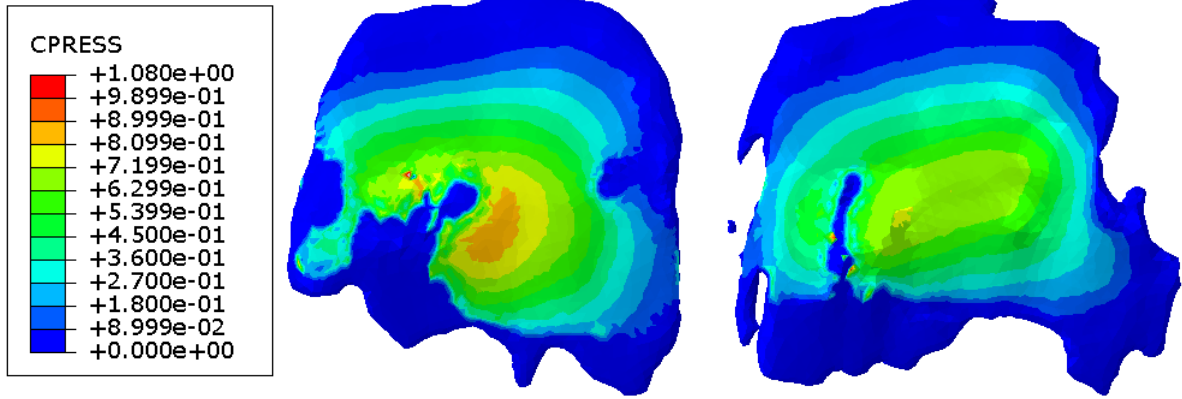


Figure 27 Talar cartilage contact pressure distribution in original (left) and resampled (right) for control 1

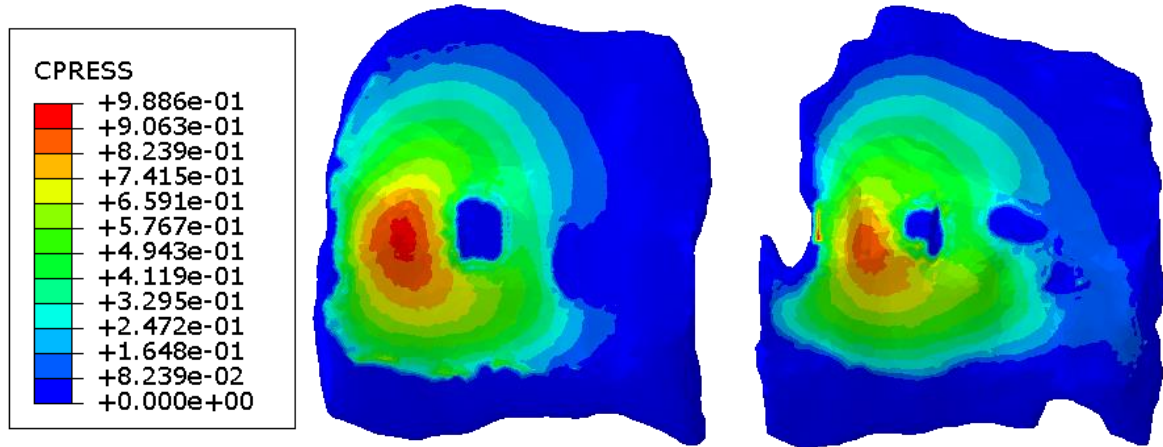


Figure 28 Talar cartilage contact pressure distribution in original (left) and resampled (right) for control 7

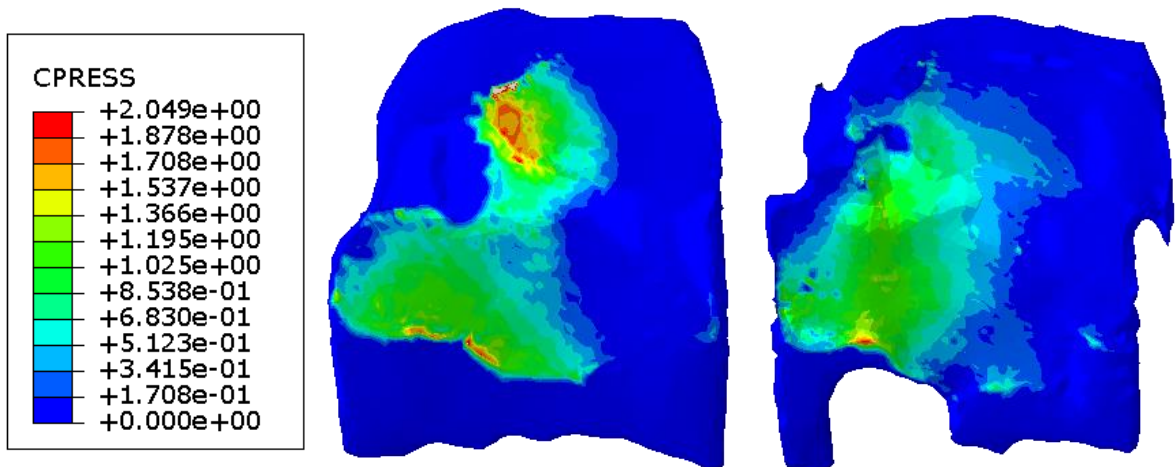


Figure 29 Talar cartilage contact pressure distribution in original (left) and resampled (right) for control 11

### 3.7.3 Discussion

The resampling of the higher resolution models showed that the slice resolution influences the geometry created, as the larger slice thicknesses resampled will create several repeats of the same slice. This helps with the smoothing processes, however has the same missing portions of geometry as the 3.3 mm slice thickness.

This difference was especially obvious in the cartilage of control 1 and control 11, though could also be seen in the bone geometry in smoothing out small additional bony features. As these were less prevalent in the articulating surfaces of the bone than the cartilage, the focus of the qualitative impact was on the cartilage.

The peaks in contact pressures influenced the mean values, therefore it was considered how this was represented in the contact distribution. The contact distribution was largely similar; it could be seen that the resampling smoothed over areas causing the peaks in contact pressure. Where the peak contact pressure was higher in the resampled case (control 7), this appeared to relate to small stress concentrations, as there were larger areas of higher contact pressures in the original case.

These findings show there will be some inaccuracies in the geometry of both the bone and the cartilage, however this is a limitation of using clinical MRI to build finite element models. This does not have a large impact on the numerical results though, so it should be taken that the resampled models give appropriate enough results for us to consider in the analysis. More importantly, the resampled models do still represent the segmentation specific geometry for patient differences to be noted. Each resampled geometry, and its consequent contact distribution, most closely resembles its original counterpart rather than either of the other controls, however some accuracy in the representation of the geometry is lost.

### 3.8 MRI Sequence Type

In different MRI sequence types, the bone and soft tissues present differently. For the purpose of this study, it was attempted to maintain the use of one sequence type (T1), however, this was not possible in some cases due to movement artefacts within images. Hence 7 models (out of a total 38) were generated using T2 scans. In order to understand the difference in modelling outcomes this may cause, one model was generated from both the T1 and T2 scans at the same timepoint and contrasted to ensure the sequence type used did not influence the FE model outputs.

#### 3.8.1 Methods

The 3D volumes from T1 and T2 were both generated for one ankle at one timepoint (3L7); this was selected due to having clear MRI for both sequence types. The volumes for the bones and cartilage were measured in ScanIP, and the same degree of cropping applied to both models. Segmentation specific meshes were then generated and exported to Abaqus, where the same neutral standing loading scenario was applied to both models. The FE outputs in both the bone and cartilage were considered to determine how this may impact the results of the models that could not be generated from T1 images.

#### 3.8.2 Results

The volumes from the two MRI sequences had some differences, with the closest volumes between the two sequence types found in the talus (Table 18). Despite the cartilage generated from the T1 images having the lower total volume, both the tibial and talar cartilage generated from T2 had holes in it (Figure 30) caused by cartilage not being clearly present on the MRI. This in turn would have some influence on the contact pressures and distributions (Table 19).

Table 18 Volumes ( $\text{mm}^3$ ) from the segmentations from T1 and T2

	<b><i>T1</i></b>	<b><i>T2</i></b>	<b><i>% difference</i></b>
<b><i>Tibia</i></b>	54,751	51,646	5.7
<b><i>Talus</i></b>	33,321	33,757	1.3
<b><i>Tibial Cartilage</i></b>	999	1,182	18.3
<b><i>Talar Cartilage</i></b>	973	1,148	18.0

Table 19 Peak and Mean Results (MPa) comparing the T1 and T2 results for 3L7

		<i>Mean</i>		<i>%</i>	<i>Peak</i>		<i>%</i>
		T1	T2	<i>difference</i>	T1	T2	<i>difference</i>
<b><i>Cartilage Contact Pressure</i></b>	Tibial	0.4257	0.3900	8.4	1.102	3.249	183.6
	Talar	0.4602	0.3995	13.2	1.992	3.202	60.7
<b><i>Von Mises Stress</i></b>	Tibia	0.2258	0.2581	14.3	7.351	6.231	15.2
	Talus	0.2616	0.2529	3.3	6.128	3.116	49.2

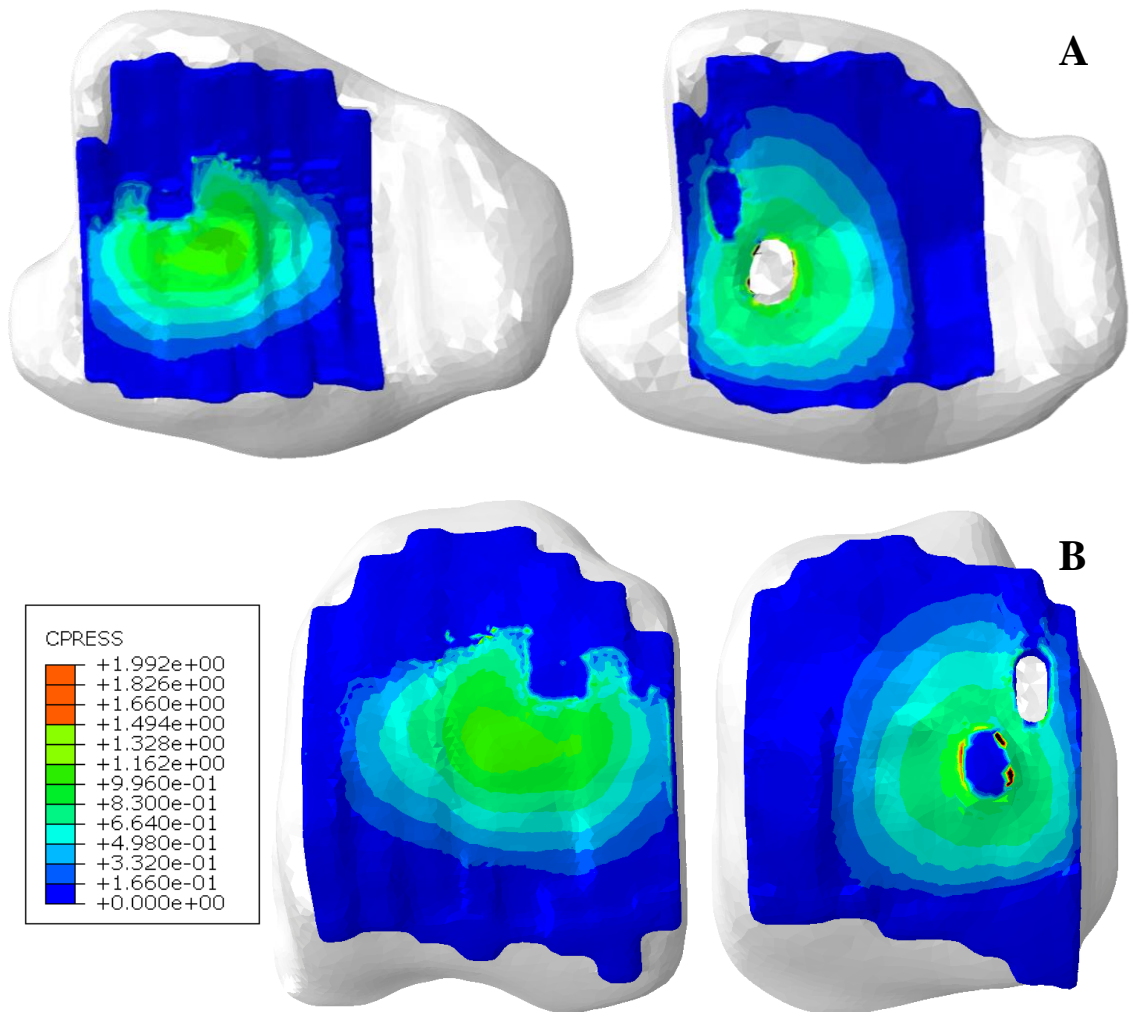


Figure 30 Contact Pressure (MPa) Distribution in A) Tibial Cartilage, B) Talar Cartilage for T1 (left) and T2 (right) weighted models

### 3.8.3 Discussion

In T1 and T2 imaging, the signal intensity of soft tissues and bone vary. T1 weighted images are best for visualising morphology and surfaces of bone, while T2 weighted images are better for differentiating between soft tissue properties.

In T1 images there are lower signal intensities for cartilage, hence it may not be clear where there are missing cartilage regions, while in T2 the slightly higher signal intensity would make this differentiation easier.

For this reason, it is possible that the cartilage modelled using the T1 sequences may be overly simplified; however, as the morphology of the bone is a key disease feature in consideration in this work, it was deemed more appropriate to try and maintain the T1 imaging type.

The holes in the articular cartilage of the T2 weighted model increases the localised contact pressures, and influences the contact distribution. However, the average contact pressures were actually reduced in this T2 model due to the volume of the cartilage being increased in this model. This highlights the importance of having correct cartilage thickness, and including cartilage defects in models where they are present, as both of these are influential on the outcomes of the peak and mean contact pressures. In the longitudinal study presented in Chapter 4, all cartilage is segmentation specific; therefore, any morphological features such as holes or thickness irregularities were maintained whether modelled from T1 or T2 MRI.

Peak values should not be the sole consideration when drawing conclusions from studies such as this, as these values closely relate to the meshing of the model. Hence, the comparisons between the means in the contact pressures and bone stresses are of more interest. The increased cartilage volumes caused a subsequent reduction in average contact pressures; a decrease in bone stresses was also seen with the increased tibial volume in T1. The volumes in the talus were very similar between the two models, on the whole, this gave very similar mean stresses for the outputs of interest with the exception of the tensile stress. The average tensile stress was 4 times higher in the model generated from T1 than that of the model generated from T2.

The fact that both T1 and T2 are both used in the 38 models is not of concern, as their influence on the results is minimal compared to other variables, however it should be taken as a limitation that the two sequence types are better for representing bone and cartilage respectively. Both bone and cartilage geometry are of interest in HA, hence it would be preferred to use imaging that clearly defines both. A combination of the gold standard for modelling of bone would be use of CT imaging, with T2 imaging for cartilage, as a method to mediate this. However, this study shows the results from the two MRI sequence types are equivalent enough for the purpose of these comparisons.

### 3.9 Talar Cropping

The focus of the patient specific modelling is on the interaction between the tibia and the talus, and does not relate to the subtalar geometry. As part of this, the talus in each model was cropped to create a regular surface for the boundary constraints. This fixation against all displacement and rotation represents the constraints due to the surrounding soft tissue and bone geometries. Within the 38 models, differing degrees of talar cropping were required due to the differing geometries in the talar head and neck. Sharp edges or disconnected regions of bone occurred in some models when a consistent degree of cropping was used. Sharp edges caused odd shaped elements, which in turn can cause excessive stresses, especially in regions where the boundary conditions are applied, as these fixation points can cause unrealistic peak stresses.

Due to these limitations, the degree of cropping ranged from 40 to 70 pixels across the 38 models. As large volumes of talus are being cropped in this range, a sensitivity analysis was run to ensure the model results were not highly influenced by the degree of dropping. If there was a relationship between the degree of cropping and the model outputs, comparisons could then only be made between models with the same degree of talar cropping.

#### 3.9.1 Methods

One ankle model was used to carry out the sensitivity analysis. The sensitivity analysis was only carried out on the talus, as the tibial cropping was much less variable within the 38 models. The talus was modelled uncropped (Figure 31A), following this four models were generated from cropping ten pixel increments up to the 40 pixel baseline used in the bulk of the modelling. This was carried out to understand what the influence might have been if less cropping was carried out. Then a further seven models were generated from cropping in five pixel increments up to 75 pixels (Figure 31B). This was done to go beyond the 70 pixels used as the most cropping within the patient specific ankle models, but was the limit before the crop would have reached the articulating regions.



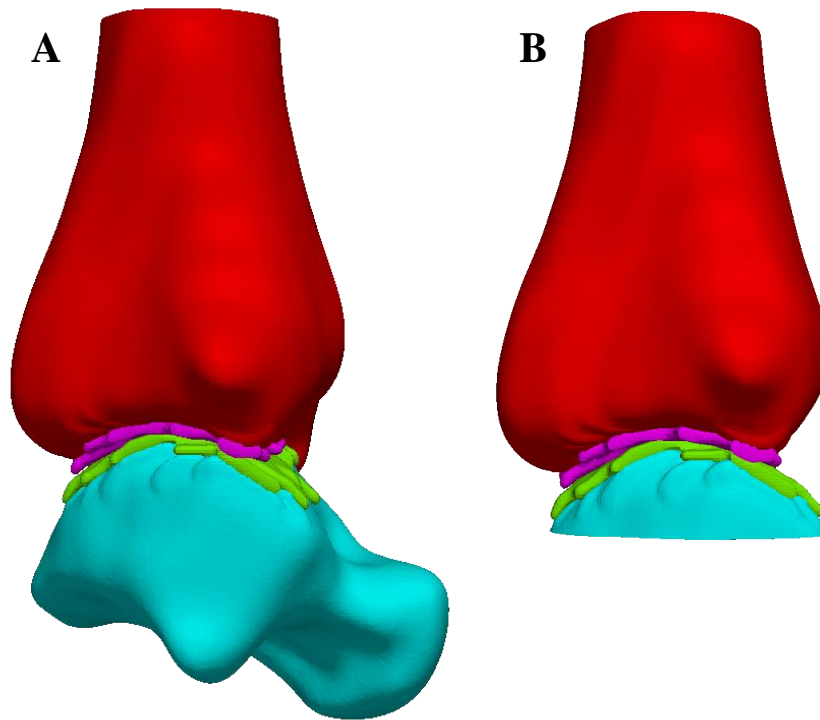


*Figure 31 Ankle model used to carry out cropping study A) uncropped, and B) with the greatest degree of cropping applied*

For each crop, the flat bottom surface of the talus was used for the boundary conditions. On the one uncropped model, a set was generated for the bottom surface of the talus for the Encastre boundary condition to be applied to (Figure 32).

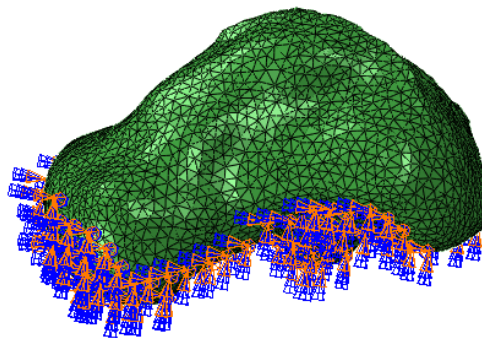


*Figure 32 Encastre boundary condition on uncropped talus*

Contact pressures, area in contact, and all bone stresses were considered in the sensitivity study. Although it was hypothesised the influence would be focussed on the talus, as this was the region the changes were occurring, the changes to both bones were considered. The peak and mean stresses were calculated from all nodes during the cropping study, including those where boundary conditions were applied. This would give the worst case scenario, as peaks caused

by localised stresses at boundary conditions were included. These regions were not included in the outputs considered in the longitudinal study, but they were potentially an important consideration in this study, with peaks due to odd shaped elements at the crop being a factor of interest.

### 3.9.2 Results

These degrees of cropping gave talar volumes ranging from 32,831 mm<sup>3</sup> uncropped, to 6,597 mm<sup>3</sup> with the greatest degree of cropping; this gave a difference of 26,234 mm<sup>3</sup> between the first and last of the twelve models. However, this 75 pixel crop was one of two models that did not converge. The other, 40 pixels, means there is a 15 pixel jump in the results in Figure 33 to Figure 35.

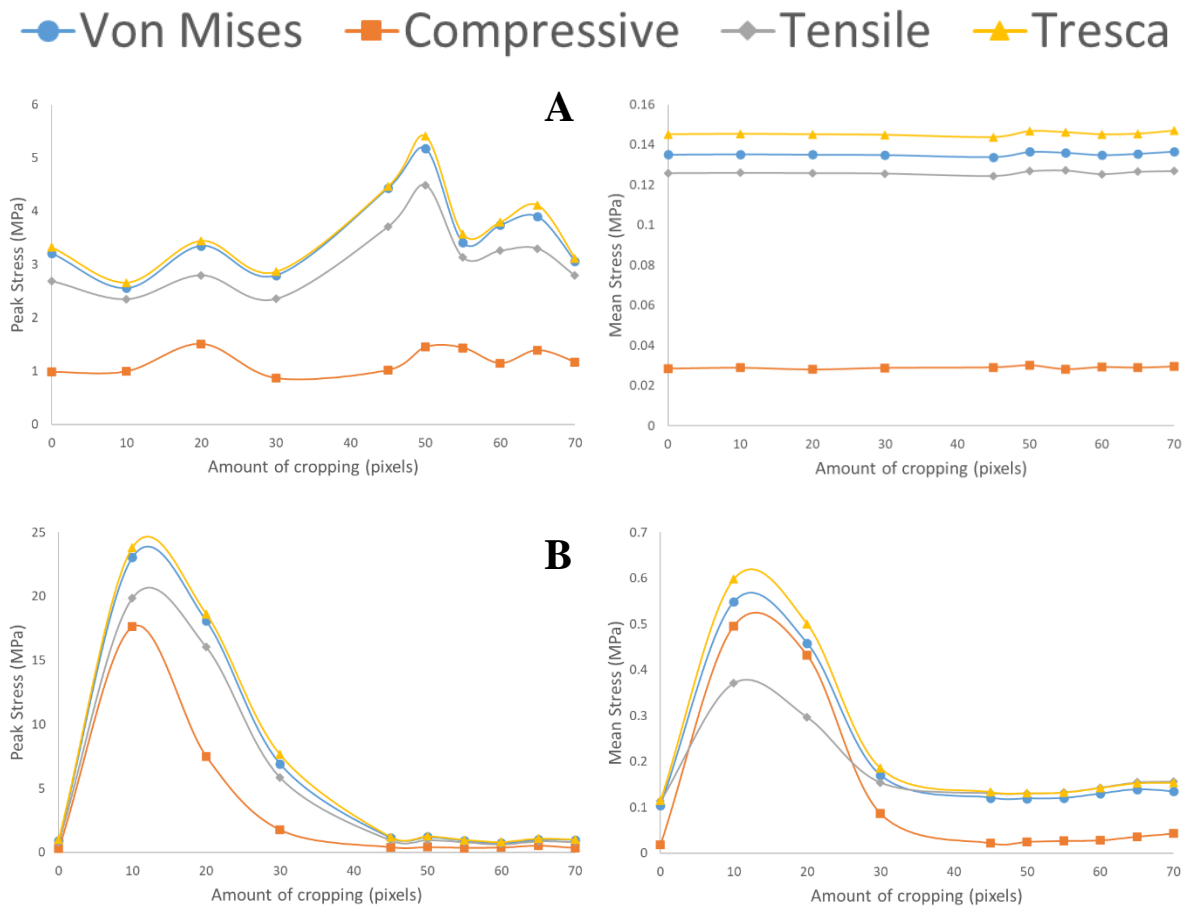


Figure 33 Peak (left) and mean (right) bone stresses (MPa) with cropping in the A) tibia, and B) talus

The mean bone stresses, which should be less influenced by the mesh applied, showed the talus was more strongly influenced by the tibia as was expected. The percentage error between the 70 pixel crop and the uncropped was within 3.5% for all mean outputs in the tibia, while the

talus was higher at up to 57% error in the compressive stress. The difference between the amounts of cropping (45 to 70 pixels) used within the patient specific model was less than 10% for all outputs.

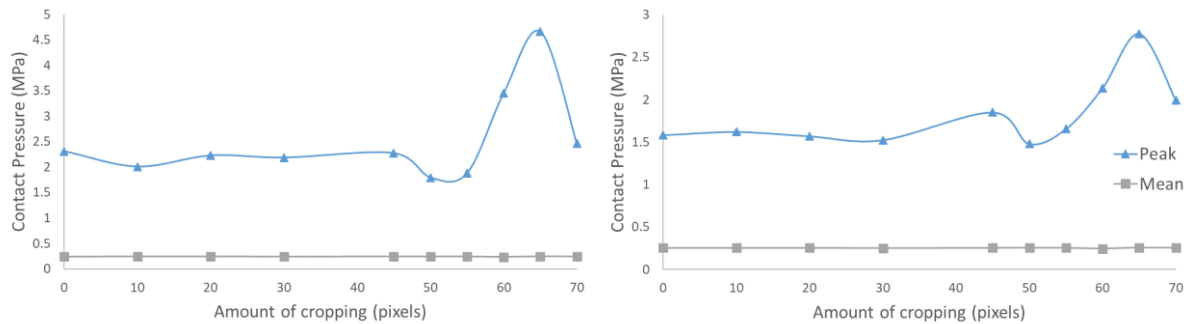


Figure 34 Changes in peak and mean contact pressure (MPa) in the tibial (left) and talar (right) cartilage with talar cropping

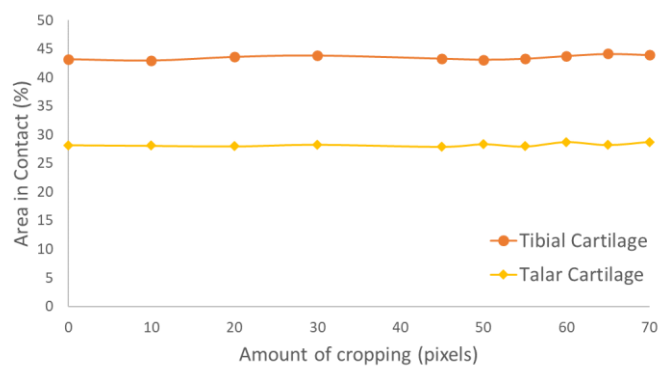


Figure 35 Area in contact (%) in the tibial and talar cartilage with talar cropping

The error in the peak talar contact pressure was high (20%), while lower errors (6%) were found in the tibial contact pressures. The mean contact pressures however were not influenced by the degree of cropping, with both experiencing less than 1% error. The contact areas were also unchanged with cropping (less than 2% error in both).

### 3.9.3 Discussion

Ensuring the decision to crop the talus was not influential to the results was a key sensitivity study for this model. It was anticipated that the area of higher stresses would be in the articulating regions, hence if cropping was applied that the mean stresses would increase.

There was a large volumetric difference in the talus between the uncropped and most cropped models; the results of this sensitivity study did not show the extreme response to this difference

in volume due to cropping that was anticipated. It agreed with the hypothesis to a small degree, as the mean stress in the talus did slightly increase with each crop in the 45 to 70 pixel range. However, the results also showed this range was the most appropriate for talar cropping, with large peaks seen for the 10 to 30 pixel crops in the talus. However, the peak and mean stresses returned to around the same value as the uncropped model beyond the 40 pixel crop. This confirmed the need to avoid sharp geometries, which were seen in the 20 pixel crop, justifying the choice to use a range of crops rather than just one for all 38 models.

It is however important to not crop beyond the upper bound used in this study, as this would reach the articulating region. As these models will also be used in quasi-dynamic models (Chapter 6), it is important to not reach the articulating cartilage, as this would impede data collection through the gait cycle.

As with the majority of the sensitivity analyses, this study has shown the peak values should not be taken at face value for the 38 models as they are more highly sensitive to the conditions being modelled. It is reasonable to suggest the combination of model simplifications would mean this model would not be validated against real world values, but gives a reasonable comparison between the models within the study.

### 3.10 Conclusion

This work has highlighted some of the limitations of models generated from clinical MRI; there are morphological uncertainties in the 3D volumes due to the slice thickness, which cannot be fully compensated for in the resampling of images. There is also an informational constraint on bone properties. These uncertainties would benefit from higher resolution CT imaging, to enable the use of greyscale based material properties, the gold standard imaging modality to generate orthopaedic finite element models. The sensitivity to inhomogeneous bone highlighted the homogenous bone properties adopted may cause an underestimation of both cartilage and bone outputs.

Despite this finding, and the informational constraints, these sensitivity studies show the patient specific ankle models generated from MRI can be used for inter-subject comparisons. The sensitivity studies and verifications have investigated the assumptions that have not been consistent across the 38 ankle models. It highlights there are still sources of uncertainty, especially when comparing models generated from T1 with those generated from T2, however these are in small percentages. In general, the sensitivity studies reflect differences to the magnitude of Pa, while inter-subject differences can be in the order of MPa. Care should be

taken when comparing stress distributions between models, however, this could be a valuable tool for considering the same geometry under different conditions.

The development of this modelling protocol for a patient specific ankle model now allows the haemophilic ankles to be compared and contrasted over the duration of the imaging; this will give potential insight into the disease progression with time. These models do not give validated quantifiable results, however do describe changes and trends with the haemophilic condition. Giving information that did not previously exist. Additional information would be required to validate these models, ensuring the methods give meaningful real world results. This has previous been carried out for CT based models of the ankle joint (Anderson *et al.* 2007). There would be two potential routes to validate models built from MRI; an experimental validation utilising models built from MRI of cadaveric ankles, or a verification against previously validated methods, where MRI could be verified against CT. The latter was planned for inclusion in this thesis, however the ability to acquire clinical imaging of cadaveric ankles was impacted by the Covid-19 situation. These limitations to this modelling are acknowledged, however, do not devalue the additional information haemophilic ankle models can provide without these methods. This is especially valuable as a basis understanding changes in the joint due to haemarthritic manifestations such as subchondral bone cysts and altered gait.

# CHAPTER 4

## CHRONOLOGICAL STUDY USING PATIENT SPECIFIC ANKLE MODELS

# CHAPTER 4: CHRONOLOGICAL STUDY USING PATIENT SPECIFIC ANKLE MODELS

## 4.1 Introduction

Given the progressive, life-long, nature of this disease, with end stage arthritis as early as the third decade of life (Rodriguez-Merchan 2010), it is important to consider this through a chronologically sequential analysis of joint health. As the talar morphology was assessed in this way, it would be possible to link these FE outputs to the morphological changes with time. The combination of these two methods would help better understand the role of the morphology in the progression of the arthropathy.

MRI is routinely collected in the clinical care of PwH. It was shown in Chapter 3 that a robust FE model can be built from these clinical MRI. There were some limitations to the models due to informational constraints, however, they allow for qualitative and quantitative analysis of the internal stresses of the ankle joint. Quantifications have not been validated, hence cannot be taken as the true stresses experienced within the joints, but the modelling approach allows comparisons between models and patients to be made. Concentrating on these differences still improves understanding of the arthropathic changes with time.

The same MRI sequences as used in Chapter 2 (Table 3) were used to build subject specific models, utilising the method developed in Chapter 3, where the geometry and loading conditions are specific to each timepoint. These models were utilised in two studies in this chapter: the first was a sensitivity study carried out on all models investigating the influence of coefficient of friction; the second was a longitudinal analysis, which was undertaken with the aim of further understanding the role that disease progression plays in cartilage contact mechanics and bone stresses. As part of this longitudinal analysis, the outputs of these models can be contrasted with the findings of Chapter 2, to provide valuable insight into the role morphological changes could play in disease progression.

## 4.2 Methods

The processes developed in Chapter 3 were used to generate a total of 38 initial models from these ankles. Each model included patient specific geometry of the tibia, talus, tibial cartilage and talar cartilage.

Based on the method developed, all models were generated from the sagittal projection. However, as not all T1 sequences were appropriate, due to motion artefacts, and given the results of the sensitivity analysis on sequence type in Chapter 3, it was acceptable to build 30 of the models from T1 sequences, and the remaining eight from T2 (1R1, 1R3, 1R4, 1R7, 2L2, 3R1, 3R3) or Short Tau Inversion Recovery (STIR) (1R5). These three sequence types are all appropriate for the purpose of model generation. Despite STIR being a variation of a T1 sequence, the fat suppression means it more closely resembles a T2 image. It was not possible to carry out a verification of the use of STIR in the same way as it was for T1 and T2 in Chapter 3, however, this resemblance means it is likely that the same findings stand: it may impact volume, but not results.

#### 4.2.1 Material properties

For the purpose of the chronological study, the assumption of homogenous, linear elastic bone was maintained. The Young's Modulus ( $E$ ) was simplified to 7.3 GPa based on healthy ankle literature (Cheung and Zhang 2005), and assigned a Poisson's ratio ( $\nu$ ) of 0.3. The cartilage was modelled as a hyper-elastic material with Mooney-Rivlin model with two coefficients defined:  $C_{10}=4.5$  MPa and  $C_{01}=0.66$  MPa. The cartilage was assumed to be completely incompressible, meaning there is no volumetric change in the simulation.

#### 4.2.2 Loading Conditions

The mass of PwH is regularly recorded, as their factor replacement is based on their mass. Therefore it was known at each imaging instance, allowing for patient specific loading for the time of imaging; for two MRI sequences weight was not measured on the day of imaging, therefore, estimations were made from the closest known weight measurement.

Based off previous FE assumptions, it was taken to be that each ankle joint takes 25% of the total bodyweight in neutral bipedal standing (Cheung and Zhang 2005). Using  $F = \frac{mg}{4}$  gave the total forces in Table 20.



Table 20 Patient Weight and Total Force for all models

<i>Model Number</i>	<i>Weight (kg)</i>	<i>Total Force (N)</i>
<i>1R1</i>	92	225.63
<i>1R2</i>	99	242.80
<i>1R3 and 1R4</i>	102	250.16
<i>1R5 and 1R6</i>	114	279.59
<i>1R7</i>	117	286.94
<i>2L1</i>	52	127.53
<i>2L2</i>	54	132.44
<i>2R1 and 2L3</i>	59.6	146.17
<i>2R2</i>	63.6	155.98
<i>2R3 and 2L4</i>	80.5	197.43
<i>3R1</i>	24.1	59.11
<i>3R2 and 3L1</i>	29.3	71.86
<i>3R3 and 3L2</i>	48	117.72
<i>3R4 and 3L3</i>	60	147.15
<i>3R5 and 3L4</i>	68	166.77
<i>3R6 and 3L5</i>	65.5	160.64
<i>3R7 and 3L6</i>	65	159.41
<i>3R8</i>	72	176.58
<i>3L7</i>	75	183.94
<i>4L1</i>	70	170.45
<i>4L2</i>	70.5	172.9
<i>4L3</i>	68.6	168.24
<i>5R1 and 5L1</i>	47.5	112.08
<i>5R2 and 5L2</i>	50.5	123.85
<i>5R3</i>	52	127.53
<i>5R4</i>	61	149.60

### 4.2.3 Longitudinal Study Outputs

The outputs in bone and cartilage were considered over the duration of imaging to see how these varied with time; VMS is reported for the bone, and contact pressure reported for the cartilage. The mean values were reported, as stress concentrations due to irregularities in the mesh may cause the peaks which do not reflect the true condition of the joint.

In order to ascertain if there was a relationship between the longitudinal outputs and the morphological measurements in Chapter 2; TaAL:TaL was used as this most reliably represented the flattening of the talus. Pearson's correlation was calculated to a significance of 0.05 for both the bone and cartilage outputs. As the measurements were taken at three locations across the talus, the correlation was calculated for each of these three relationships, giving a total of 12 correlations: three tibial, three talar, and six in total for the two cartilage components.

### 4.2.4 Coefficient of Friction Study

Based on FEA literature, it was intended to use a coefficient of friction of 0.1 for all models in the longitudinal study. This coefficient of friction is an assumption, and would vary depending on disease progression, hence the uncertainty around this value needed to be assessed.

The sensitivity studies carried out in Chapter 3 were carried out on a small sample of ankles, and, when considering the influence of coefficient of friction, it was seen there were large differences between models. For this reason, the original 36 models were simulated through the different coefficients of friction. This was carried out prior to the final mesh refinement, however, using the edge length ratio from the first step in the mesh convergence.

Eight different simulations were run for each model using different coefficient of friction values (0.5 to frictionless). This range of values represent those used in literature for both healthy and diseased cartilage models. The consideration of coefficient of friction was an important feature due to this being unknown for HA, and is likely to vary with disease progression. Current findings from a pin-on-plate study suggest coefficients of friction in the range of 0.01 to 0.05 (Sharrock *et al.* 2022), hence multiple evaluations within this range. However, this was expanded upon to cover the ranges reported in FEA of healthy cartilage (0.1 to frictionless) plus additional higher coefficients of friction which would imply a greater surface roughness in diseased cartilage.

The cartilage contact pressure was considered as the output of interest, following the finding that this was the more sensitive to the frictional properties in the mesh sensitivity analysis in

Chapter 3. The peak tibial and talar cartilage pressures were measured for each model at each coefficient of friction.

#### 4.2.4.1 Results

With a decrease in coefficient of friction, there tended to be an increase in peak contact pressures. The magnitude of this difference depended on the model. For example large increases with coefficients of friction lower than 0.1 were seen in 1R3 (Figure 36), 2R1 and 2R3 (Figure 37), while 1R6 (Figure 36) demonstrated no real change. Peak contact pressures even decreased in some models (2L4) as coefficients of friction were decreased. For the majority of models, minimal difference were seen between coefficients of friction of 0.1 and 0.5, those that differed from this are highlighted in red on Figure 36 and Figure 38. Results for tibial cartilage can be seen in the appendix.

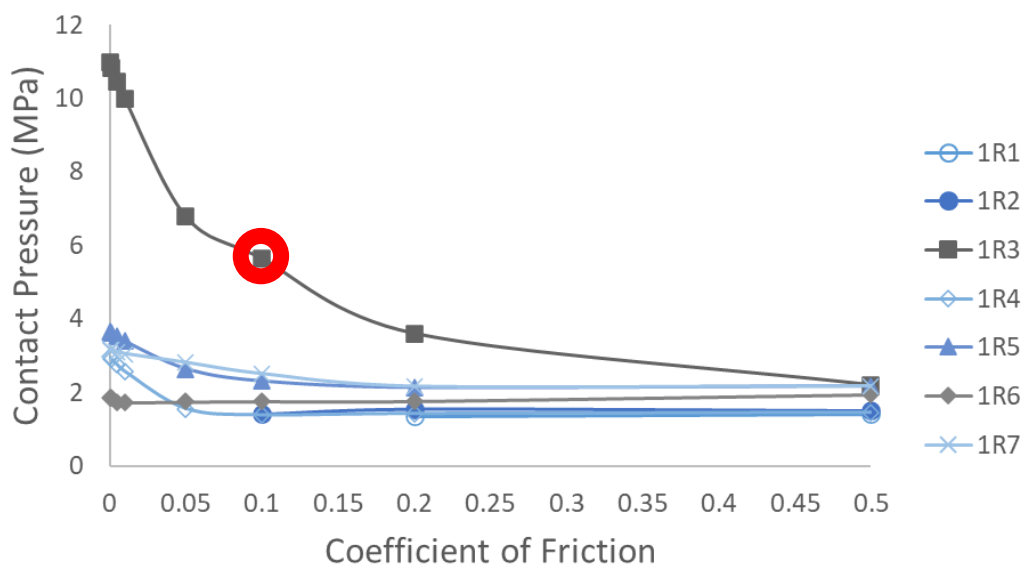


Figure 36 changes in talar cartilage Contact Pressure for Ankle 1R with increasing coefficient of friction

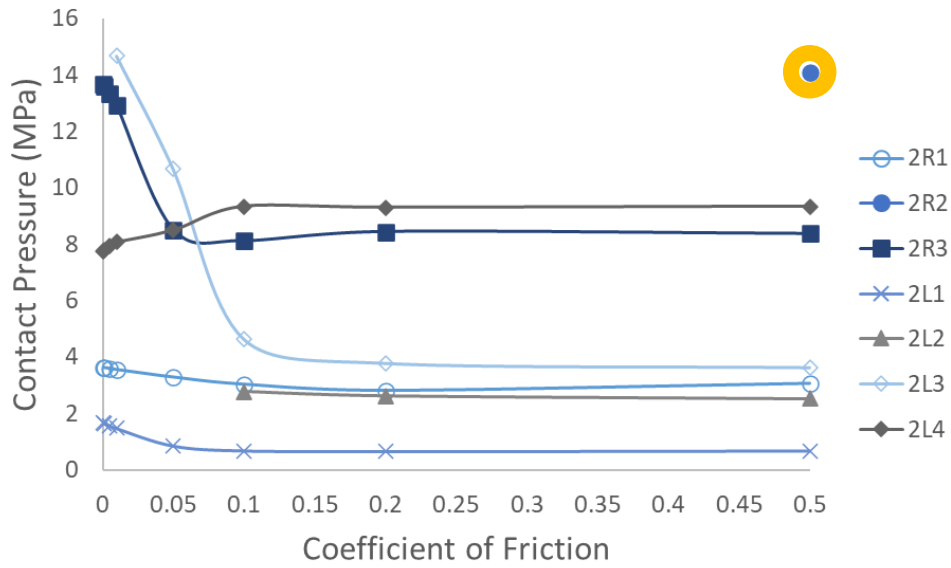


Figure 37 changes in talar cartilage Contact Pressure (MPa) for Ankle 2R and 2L with increasing coefficient of friction

While a small number of models, such as 2L4 and 3R4, required the highest coefficient of friction value of 0.5 in order for the simulation to complete; these are highlighted in orange on Figure 37 and Figure 38.

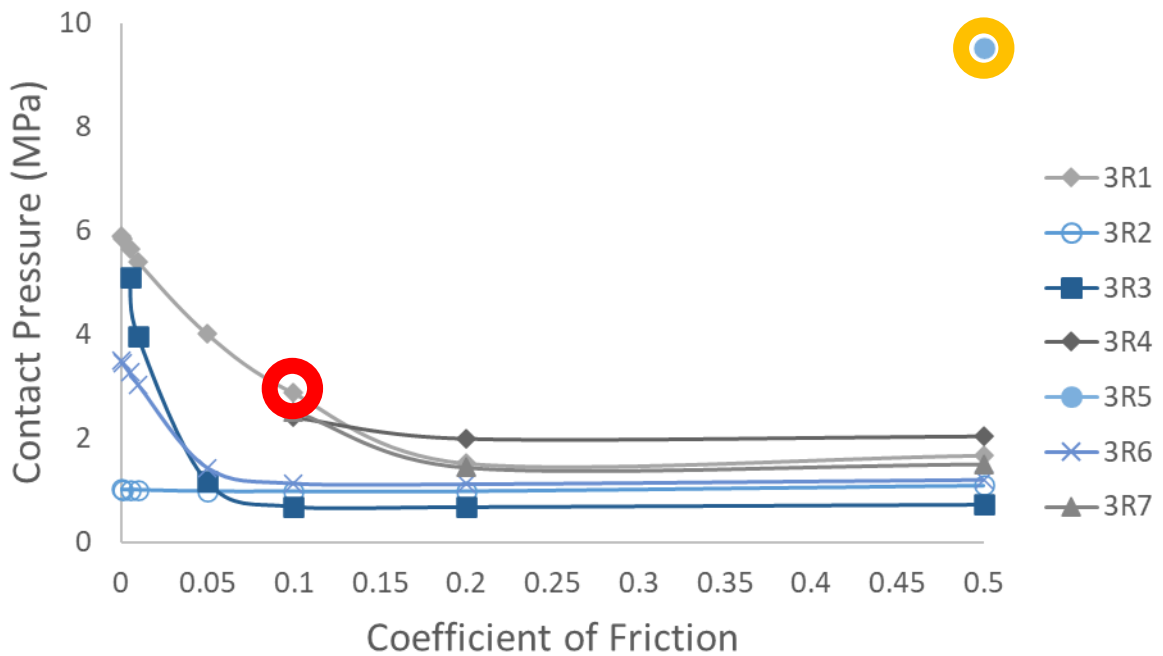


Figure 38 changes in talar cartilage Contact Pressure (MPa) for Ankle 3R with increasing coefficient of friction

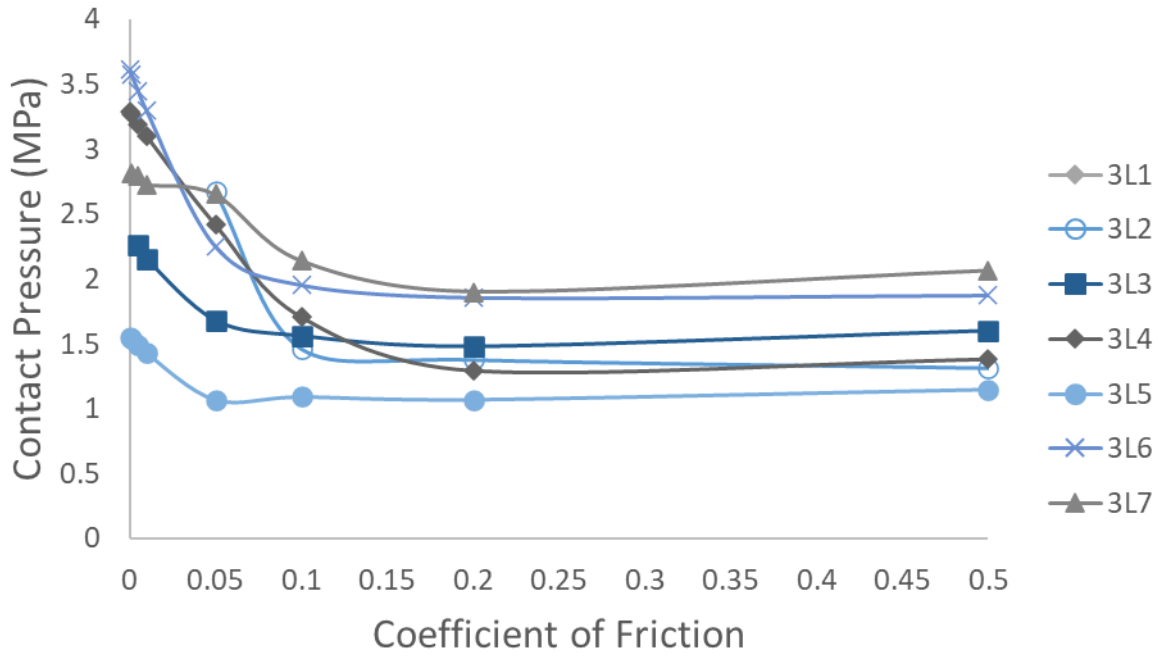


Figure 39 changes in talar cartilage Contact Pressure (MPa) for Ankle 3L with increasing coefficient of friction

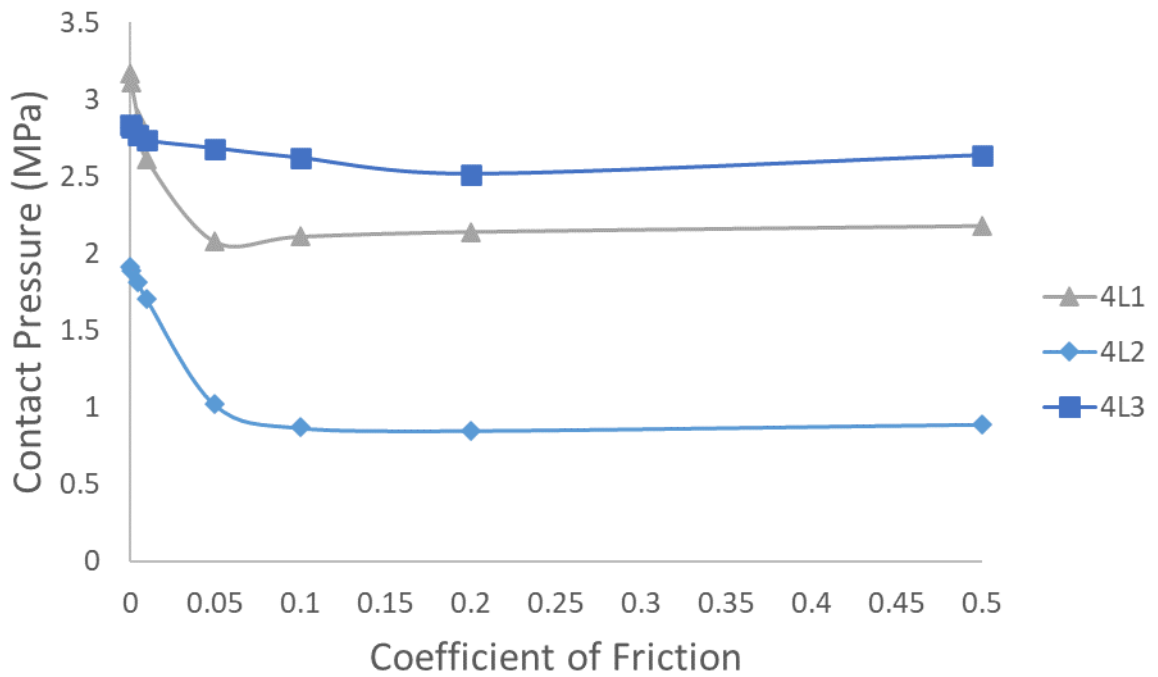


Figure 40 changes in talar cartilage Contact Pressure (MPa) for Ankle 4L with increasing coefficient of friction

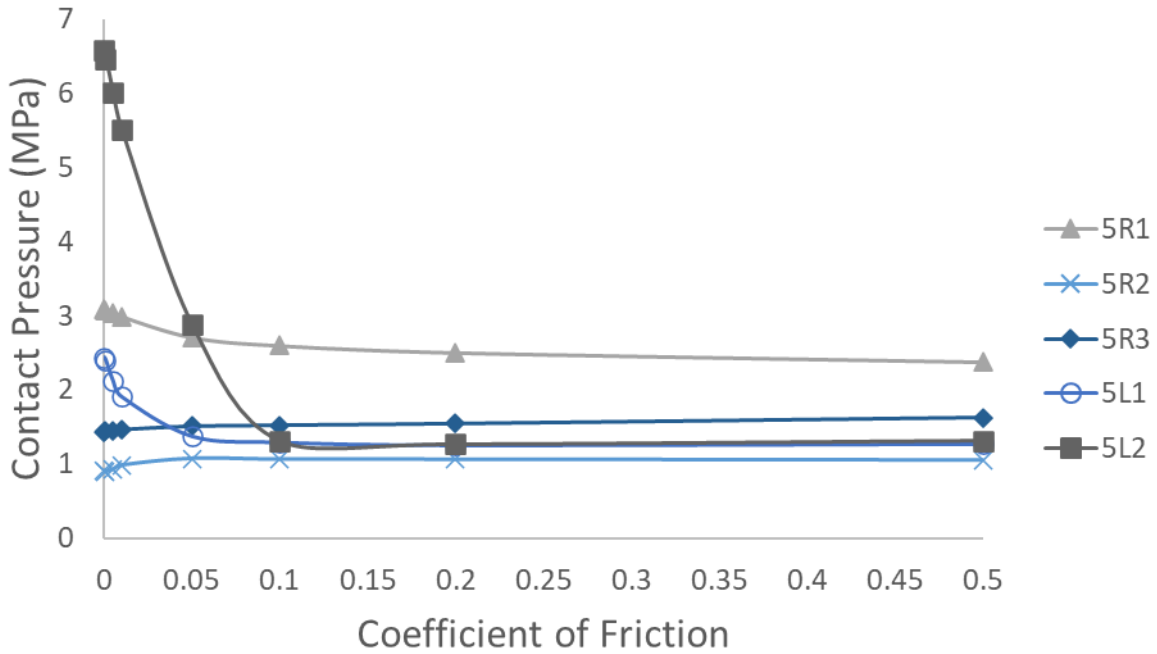


Figure 41 changes in talar cartilage Contact Pressure (MPa) for Ankle 5R and 5L with increasing coefficient of friction

#### 4.2.4.2 Discussion

The results of the coefficient of friction assessment suggests that the models in the chronological study may be an underestimation should the coefficient of friction of haemarthritic cartilage be in the range of 0.01 to 0.05 as currently suggested (Sharrock *et al.* 2022). The synovium was not included in these models, and instead was represented through the frictional properties. The higher end of the range of coefficients of friction reported in literature (0.1) was used for the chronological assessment, as synovial hypertrophy has hypothesised to increase this value. It has been seen that the synovium contributes to the stress distribution, and reduction of stresses in the ankle models (Hamid *et al.* 2016), hence, should this have been included the behaviour of the model may have differed.

A coefficient of friction of 0.1 is deemed to be an appropriate representation of arthritic cartilage interactions in FEA; a small number of the models in the chronological study did not converge at that coefficient of friction, and required the highest value of 0.5 in order for the simulation to complete. However, the findings of the coefficient of friction study suggest this is not an issue, with only four of the 54 models having any significant change between 0.1 and 0.5 coefficients of friction.

The sensitivity to coefficient of friction was assessed before the MRI sequences used to build 3R8, and 5R4 were gathered. However, the conclusions were strong enough to warrant not running these additional models at different coefficients of friction.

### 4.3 Longitudinal Study Outputs

The 38 ankle models allowed for longitudinal assessment of the eight ankles, which could be linked to the morphological analysis in Chapter 2, without considering the influence of any additional disease presentations.

Two of the 38 models (3R1 and 3R5) did not converge to 100% of the load step following the mesh convergence, and were therefore excluded from the chronological assessment. 3R5 was one of the models in the coefficient of friction study that did not simulated at any coefficient of friction below 0.5. 3R1 however converged at all cf in the coefficient of friction study, yet only achieved 68% of the load step in the longitudinal assessment model; the errors occurred due to a small area of high localised stresses – the impingement this appeared to relate to could not be counteracted without other errors occurring in the model.

Figure 42 and Figure 43 show the variability in VMS over time. The key is the same as that used in Chapter 2, with the colours representing age at first scan. The change in stresses in the bones with time is unique to each ankle, and did not appear to relate to the age categorisation. There were significant negative correlations between the mean VMS in the tibia and the medial ( $r = -0.341$ ;  $p = 0.042$ ) and central ( $r = -0.537$ ;  $p = 0.001$ ) TaAL:TaL measurements taken in Chapter 2. The correlation with the lateral measurements was non-significant ( $r = -0.299$ ;  $p = 0.076$ ).

The correlation between the mean VMS in the talus and the TaAL:TaL measurements taken in Chapter 2 was significantly negative for the central measurements ( $r = -0.437$ ;  $p = 0.008$ ), but non-significant for both the medial ( $r = -0.219$ ;  $p = 0.198$ ) and lateral ( $r = -0.157$ ;  $p = 0.362$ ) measurements.

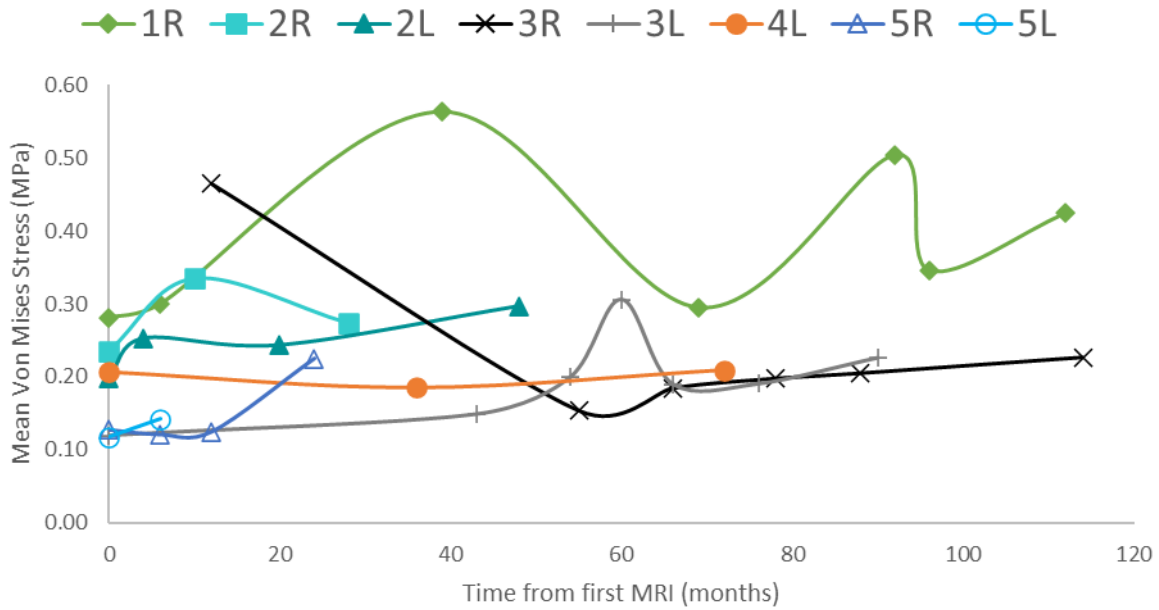


Figure 42 Change in mean VMS in the Tibia with time for each ankle

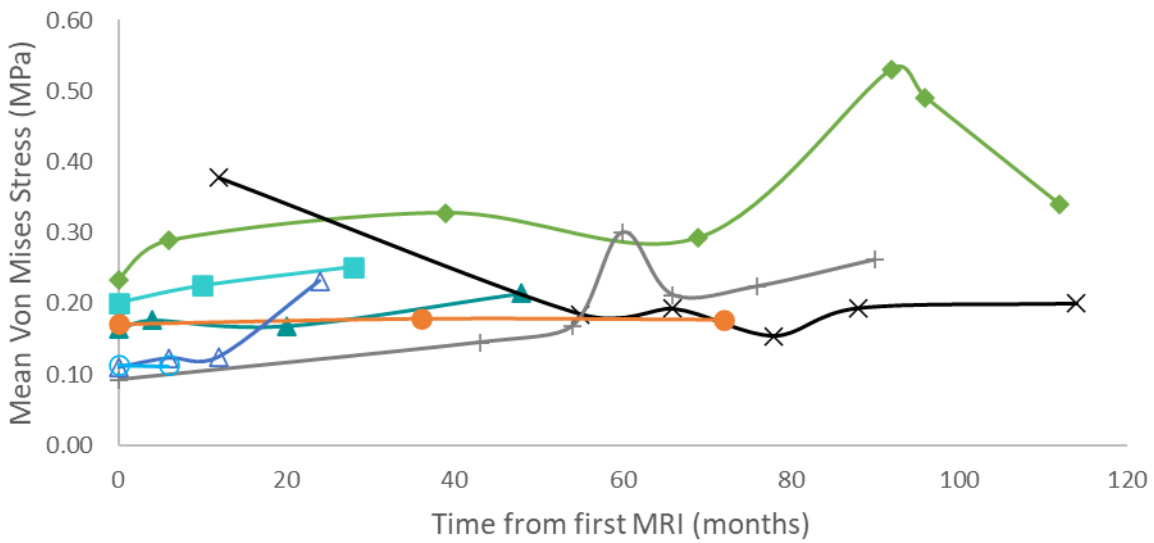


Figure 43 Change in mean VMS in the Talus with time for each ankle

There were significant negative correlations between the mean contact pressure in the tibial cartilage and the medial ( $r = -0.413$ ;  $p = 0.012$ ) and central ( $r = -0.432$ ;  $p = 0.009$ ) TaAL:TaL measurements taken in Chapter 2. The correlation with the lateral measurements was non-significant ( $r = -0.150$ ;  $p = 0.381$ ). The same relationships were seen in the talar cartilage:  $r = -0.397$ ;  $p = 0.017$ ;  $r = -0.384$ ;  $p = 0.021$ ; and  $r = -0.118$ ;  $p = 0.493$  for the medial, central and lateral measurements respectively.



This demonstrated some relationship between local morphology and global cartilage contact pressures; the same assessment was not made for the area in contact, as the morphological analysis was in specific regions of the talus, it would only be relevant if the assessment was in these three regions. The contact distributions can be seen in Table 32 and Table 33 in the Appendix.

Figure 44 to Figure 45 show the mean contact pressure in the tibial and talar cartilage with time, with the same trends appearing to occur in both cartilage components, with differing magnitudes. Figure 97 and Figure 98 in the appendix show these results against the TaAL:TaL results across the talus.

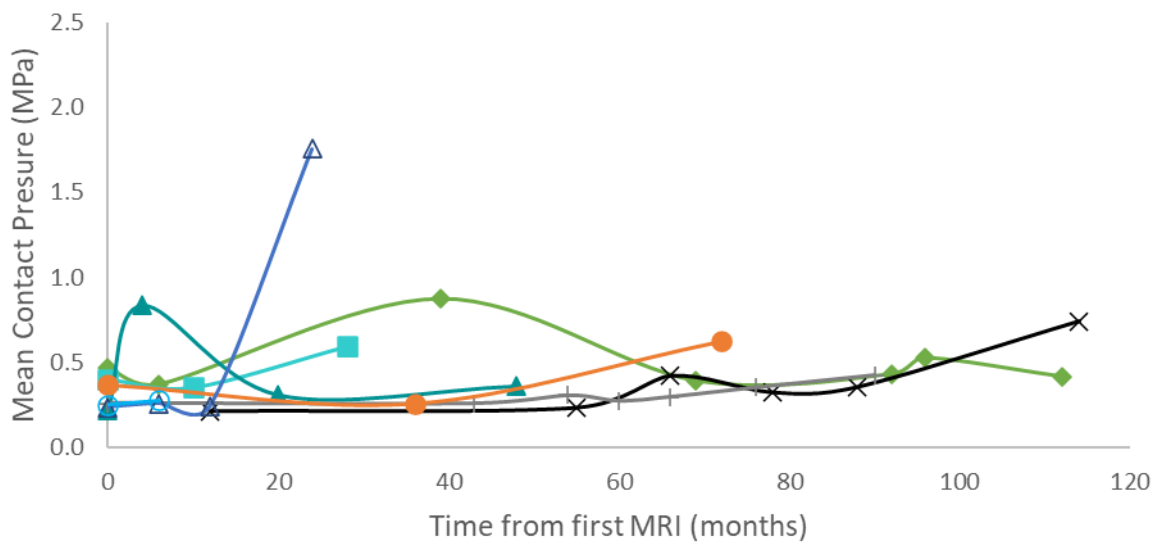


Figure 44 Change in mean Cartilage Contact Pressure in the Tibial Cartilage with time for each ankle

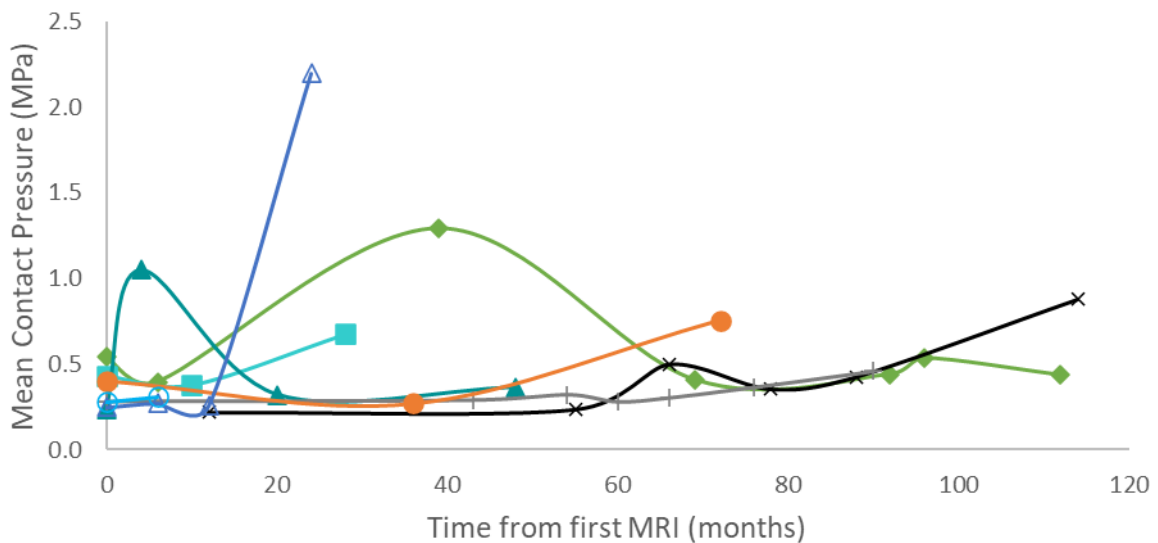


Figure 45 Change in mean Cartilage Contact Pressure in the Talar Cartilage with time for each ankle

#### 4.4 Discussion

Despite the efforts to develop a robust methodology in Chapter 3, there were two results missing from the longitudinal analysis in this chapter ankle. In spite of these missing results, the processes followed allowed for the comparison of the remaining 36 models for inter- and intra- subject comparisons over time. These models also form a basis for the models used in Chapter 5 and Chapter 6, where further haemarthritic manifestations have been considered.

These models show variable change with time. The difference between these models being the morphology and the weight of the patient. The differences are also seen in those paired due to bilateral presentation (Patient 2, 3 and 5), where weight is no longer a factor.

The sensitivity tests carried out in both Chapter 3, and the coefficient of friction study in this chapter, show that the inter-subject comparisons should not be influenced by these variables. There will be some relative error (<7%) due to differing mesh qualities depending on the morphology, though this is a much lower magnitude than the relative differences between models. It was also shown that the variables such as coefficient of friction, and degree of talar cropping should not create the variability seen in Figure 42 to Figure 45.

When considering the changes in VMS and contact pressures with time independently, it appears that there is no clear progressive change. However, when taking the morphology into account there was an apparent link between the flatness of the talus and both the bone and cartilage outputs. It was hypothesised that the talar collapse would have an implication on the contact distribution, with changes to the geometries of the articulating surfaces. However, how this might reflect in the magnitude of the contact pressures was unclear.

The influence on the magnitude of these contact pressures was of interest, as it is anticipated that elevated localised contact stresses initiate a biological response that leads to cartilage degeneration (Anderson *et al.* 2011b), hence an understanding of these with time, and talar morphology is of interest.

Both the morphological changes, and finite element outputs, were non-linear in their changes with time with some significant negative correlations between outputs and talar flattening. As the same MRI were used to generate these models as were used for the measurements, it was considered reasonable to directly ascertain a relationship. However, there was a complexity with contrasting 2D measurements at multiple locations across the joint, with the mean of the entire 3D model output. Therefore, the relationship was considered at the three regions across the talus.

It was of interest that different correlations were found in the medial and lateral regions, as they largely experienced the same morphological changes in each ankle. TaAL:TaL, which was used for the correlation in this chapter, was significantly flattened in both the medial and lateral regions of the talus, but not in the central talus. Whereas, the correlation between TaAL:TaL and the FE outputs was more repeatably significant in the central results.

On the whole, the results suggest that the talar collapse measured from TaAL:TaL, which was deemed the most reliable in Chapter 2, increase both the contact pressure and VMS experienced across the ankle joint. In turn, this suggests the talar collapse does not compensate for joint pressures, and is not a biological response intended to improve joint health. However, these conclusions are being drawn from a set of models where 19 are simplified to exclude subchondral bone cysts, hence further work is required to fully understand the true progressive changes to joint stresses and contact pressures.

#### 4.5 Conclusion

These models are the first to longitudinally assess haemarthritic ankles, investigating the potential link between morphological changes in the haemophilic ankle and joint damage. It was shown that the changes in joint stresses and contact pressures are highly variable with time, and a potential link between the morphology and joint stresses in HA was ascertained. The negative correlation between joint stresses and contact pressures and talar collapse indicate the collapse of the talus in HA may be detrimental to joint health, should this be linked to the onset of further joint bleeds, and cartilage and bone damage.

However, these models do not include potentially influential haemarthritic features; for better understanding of this progressive nature, additional haemarthritic features should be considered in the models.

# CHAPTER 5

## FINITE ELEMENT ANALYSIS OF SUBCHONDRAL BONE CYSTS

# CHAPTER 5: FINITE ELEMENT ANALYSIS OF SUBCHONDRAL BONE CYSTS

## 5.1 Introduction

Due to the commonalities with HA, many of the disease presentations discussed in Chapter 1 occur in one or both of osteo- and rheumatoid arthritis; these, however, might have a differing effect in HA due to the presence of blood in the joint. These presentations can occur concurrently or alone (Lundin *et al.* 2012), complicating their individual influence on joint health. Without extensive experimental testing on the influence of the presence of blood on all components of the joint, or their intersectional impact on biomechanical properties, it is not yet possible to accurately represent haemophilic tissues in FE models.

However, some haemophilic presentations can be considered without the need for this additional information; one such presentation is SBCs. SBCs are fluid-filled space found within the bone, these can range in size and shape, and can clearly be visualised in MR Images due to their contrast with the surrounding bone (Figure 46).

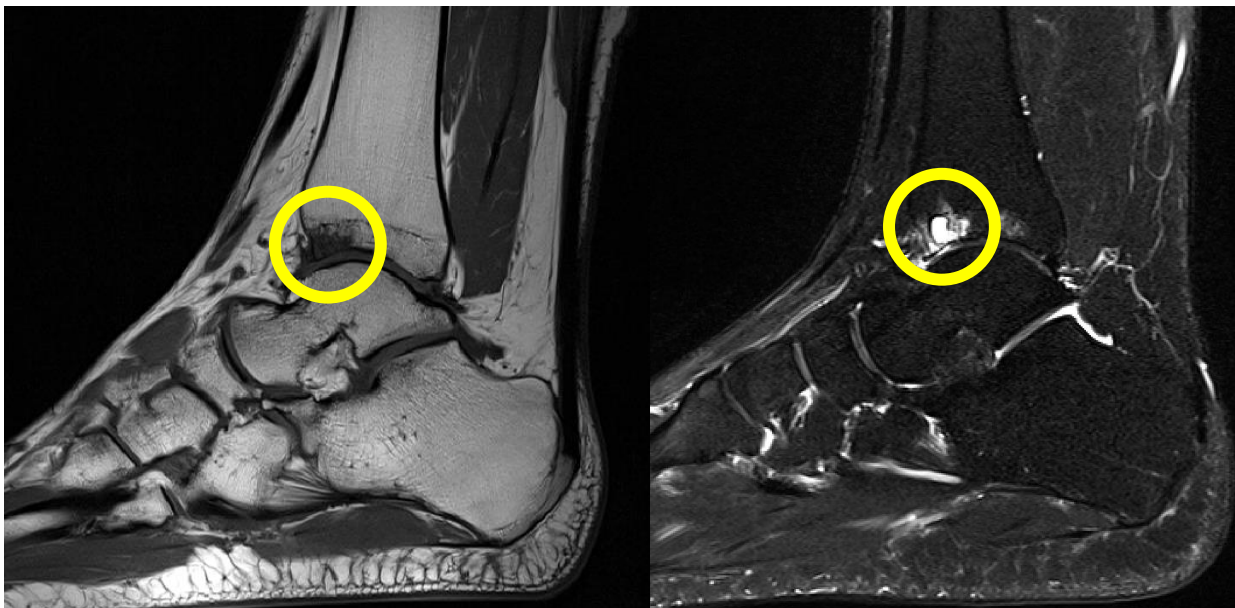


Figure 46 Subchondral bone cyst highlighted on T1 weighted MRI sequence (left) and T2 weighted MRI sequence (right)

The contrast is due to the fluid present in the SBCs, which, in T1 imaging causes low signal intensity and presents as shadows within the bone, while in T2 the high signal intensity fluid causes presents as bright spots. They have been noted to have a wall like structure around the

fluid filled space (Woods 1961), these two regions can be represented with different material properties in FE analysis (Anwar *et al.* 2020).

In adults, SBCs occur most commonly in the pelvis and long bones of the lower extremities, whereas the hands and feet are more often affected in children (Geyskens *et al.* 2004; Mittal *et al.* 2011; Purkait *et al.* 2014).

The aim of this chapter was to consider SBCs as a key disease feature, to understand their potential influence on joint health in HA. This was possible to undertake in this patient cohort, as four the ankles had one or more MRI sequences with SBCs present in one or more bone of the tibiotalar joint. A total of 18 MRI sequences had cystic tissue; each SBC varied in shape and volume, as well as depth, and the bone(s) they presented in. This gave four variables to consider when studying the SBCs, where the influence of each was considered individually as a sub-study in this chapter. These were each considered as patient specific measures, with an additional parametric study into cyst depth. Throughout the chapter it is noted whether each SBC occurs in the tibia or the talus, this variable is referred to as cyst 'location'. These variables, and their influence on the FE metrics, may guide to the influence of SBCs on joint health in HA.

## 5.2 Methods

The prevalence of SBCs within the haemophilic group made computational analysis of their influence possible to investigate. Four ankles had SBCs present in one or more bone, at a minimum of two time points. The shape, volume, depth, and location of the SBCs all varied, allowing for a number of factors to be assessed in the study. Figure 47 demonstrates how each of the MRI sequences (N=18) were utilised to create patient specific models to investigate the influence of volume and location of SBCs on the ankle joint. One of these MRI sequences was also used to generate 6 new models, which were used to understand the influence of cyst depth.

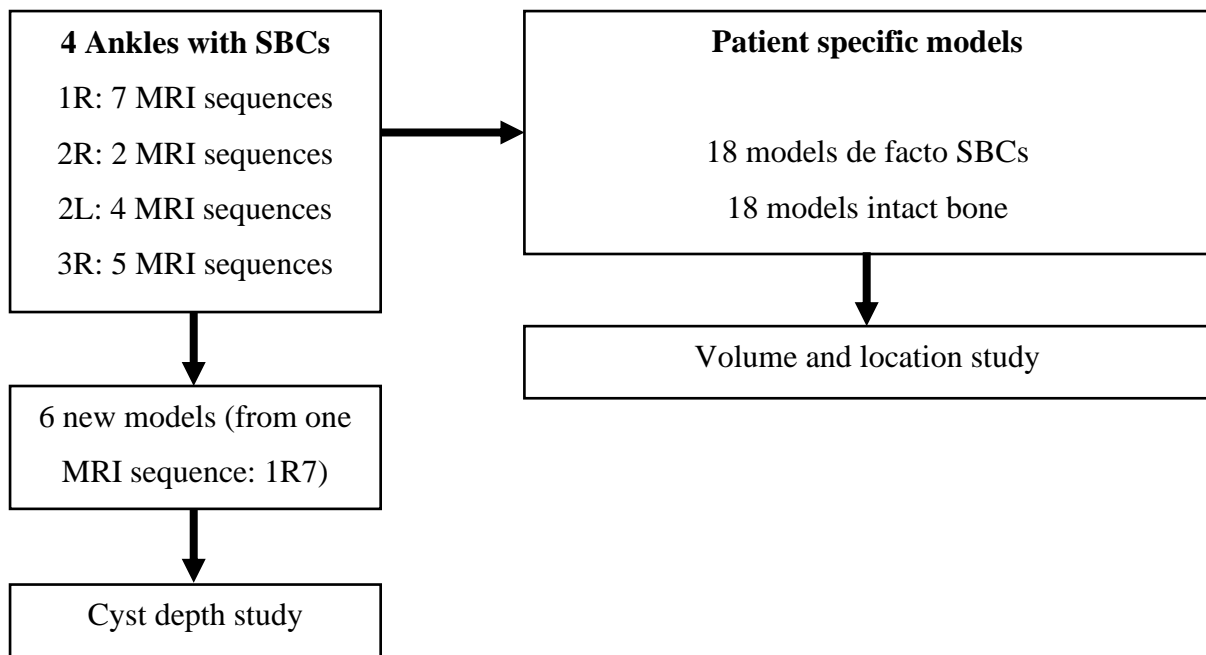


Figure 47 Models generated from images, and the studies carried out from these

### 5.2.1 Addition of Subchondral Bone Cysts

In order to investigate the influence of SBCs, two cyst conditions were modelled: cysts defined as intact bone (as described in Chapter 3), and as de facto cystic tissue.

To create the 18 models including the cystic tissue, segmentations of the bones and cartilage were copied from the original models generated for Chapter 4. The SBCs were created from the underlying MRI sequences using Simpleware-ScanIP P-2019.09 (Synopsis). The cystic masses were segmented using a thresholding feature to only capture cystic regions. Depending on the model, either T1 or T2 weighted MRI sequences (Figure 46) were used, the value of this threshold varied depending on this. This cystic segmentation was then subtracted from the surrounding bone segmentation using a Boolean operation.

Segmentation specific FE meshes were then generated using the same method described in Chapter 3, with the relevant additional properties for the cyst. This process allowed for the like-for-like models (e.g. 1R1 and 1R1C) to only differ in the cyst conditions.

### 5.2.2 Finite Element Analysis

The segmentation specific meshes for the cystic tissue condition were imported into Abaqus. The same neutral still standing loads were applied as the intact bone model, in the manner described in previous chapters. The boundary conditions, contact properties and element types all remained the same for a like for like comparison between the 18 instances.

The same degree of cropping was applied to the SBC model as its respective intact bone model, so that this was not a variable in the comparison.

The sensitivity analysis regarding the frictional properties of cartilage, was carried out as described in Chapter four on the SBC models, to ensure the outcomes were not different with the addition of SBCs to the model. The results of this analysis can be found in the Appendix.

The outputs of the Finite Element Analysis were both qualitative and quantitative; the peak and mean values for contact pressure and VMS were of interest. VMS stress was chosen as the stress output of choice due to it being a potential indicator of stress fractures, which have previously been linked to SBCs (Dürr *et al.* 2004). These allowed for the localised and wider influence of cysts to be evaluated. Qualitative analysis of the contact pressure was also conducted to evaluate the pressure distribution between the two cystic conditions.

### 5.2.3 Material Properties

The bone and cartilage material properties were maintained from Chapter 4 – where the bone was simplified to be homogenous ( $E= 7.3$  GPa,  $\nu= 0.3$ ), and the cartilage was modelled as an incompressible Mooney-Rivlin material (coefficients:  $C_{10}= 4.5$  MPa,  $C_{01}=0.66$  MPa). These were maintained so that the main sensitivity test was the cystic properties. With little known about the composition of the fluid in a SBC, the consequent mechanical properties are also unknown. Computational modelling of SBCs that has previously been carried out have no experimental values associated with the material properties, with the justification that it is appropriate to model these with a Youngs' modulus that is negligible compared to the surrounding tissues (Frazer, Santschi and Fischer 2017; McErlain *et al.* 2011); or with a bulk modulus equivalent to water (Norton, Santschi and Fischer 2022).

With this assumption in mind, and separate values not being considered for the lumen and cyst wall, the cystic tissue was modelled with a Youngs' modulus of 1 MPa (value approximated as 10 times greater than the lumen Youngs' modulus, but  $1/10^{\text{th}}$  of the cyst wall Young's' modulus) (Sarrafpour *et al.* 2019), and a Poisson's Ratio of 0.49.

#### 5.2.3.1 SBC Property Sensitivity Study

Given the values from literature for SBC properties are not derived from mechanical data, and involve large assumptions about the behaviour of the SBCs, a sensitivity analysis (Table 21) was carried out to investigate the influence of the Youngs' modulus and Poisson's Ratio on the VMS, contact pressure, and area in contact. One-Sample T-Tests were carried out to see how



the result from the material properties used across the de facto cystic models varied from the averages across all sensitivity tests. This sensitivity study was carried out on one model, with cystic volumes present in the tibia. A Bonferroni correction of 14 was applied, giving an adjusted significance of 0.0036.

*Table 21 Sensitivity Analysis Parameters for cyst material properties (ordered by increasing equivalent bulk modulus)*

<b>Youngs' Modulus (MPa)</b>	<b>Poisson's Ratio</b>	<b>Bulk modulus (MPa)</b>
1	0.45	3.3
1	0.49	16.7
1	0.499	166.7
1.32	0.499	220
132	0.45	440
1	0.4999	1,666.7
13.2	0.499	2,200
132	0.49	2,200
660	0.45	2200
200	0.49	3,333.3
1000	0.45	3,333.3
660	0.49	11,000
132	0.499	22,000

#### 5.2.4 Subchondral Bone Cyst Volume

SBC volumes were assessed in Simpleware-ScanIP P-2019.09 (Synopsis). The total volume, and where relevant, the individual tibial and talar cyst volumes were recorded. There were 14 tibial cystic volumes, and 10 talar cyst volumes (Figure 53).

The individual cyst volumes were further broken down into volume fraction of the surrounding bone component using  $\frac{\text{cyst volume}}{\text{bone volume}} \times 100$  for the tibial and talar cysts separately (Table 22).

The volume fraction was calculated, as it was possible the significance of cyst volume may relate more closely to this, due to differing bone volumes due to patient growth with time. Bone volume changes were expected due to the age of the patient group at the time of cyst development (12 – 17 years). The least bone volume change may be expected in 1R, which was adolescent and matured to adulthood around 40 months, so it was not expected there would be much growth in this time. However 2R and 2L were adolescent for the duration so may

experience some growth, and the greatest bone volume changes were expected in 3R as the patient was paediatric.

### 5.2.5 Cyst Depth Study

Due to the nature of the image based models, the three main variables of the cysts: volume; shape; and location were taken into consideration concurrently. Hence, a consequent study was carried out on one ankle model (1R7) to alter the depth of the same volume and shaped cyst. The maximum recorded depth was 3.9mm ( $\bar{x}$  = 0.55 mm, S = 0.90 mm), with the tibial cysts tending to be closer to the surface ( $\bar{x}$ = 0.29 mm, S = 0.24 mm) than those in the talus ( $\bar{x}$ = 0.89mm, S = 1.29 mm). Only one cyst depth was above the 3 mm depth, hence this was used as the upper limit in the cyst depth investigation.

To increase the distance between the cysts and the bone-cartilage boundary, translations of +0.5 mm, +1 mm, +1.5 mm, +2 mm, +2.5 mm and +3 mm along the vertical axis of the tibia were all applied to copies of the cyst segmentation in ScanIP and subtracted, using a Boolean operation from copies of the tibia model. Figure 48 shows the resultant seven models (A-G) on the same sagittal slice, where A is the baseline image based segmentation, and B-G are the translations ranging from 0.5 to 3mm in 0.5mm increments. This tibial cyst model was used for a greater range of offsets, as the talar cyst models would not have allowed for this range.

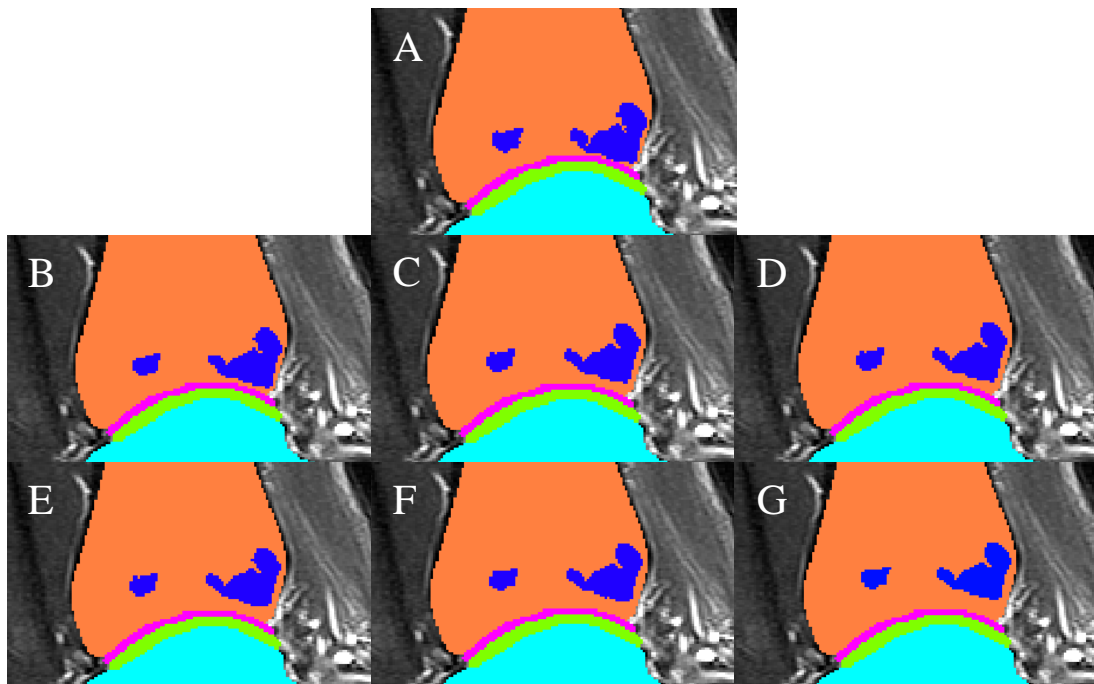


Figure 48 Translation of cyst segmentation on the same MRI slice. A) baseline segmentation from image; B) +0.5mm from baseline; C) +1mm from baseline; D) +1.5mm from baseline; E) +2mm from baseline; F) +2.5mm from baseline; G) +3mm from baseline.

The change in peak and mean values for both VMS and contact pressure were contrasted in the models, and the qualitative changes in contact pressure also assessed, as to whether the cyst depth may indicate why the qualitative change in the original models differed.

### 5.2.6 Statistical Testing

Statistical testing was carried out using IBM SPSS Statistic (version 25) to 1) calculate the significance of the differences between the two cystic conditions; 2) calculate the correlation between cyst volume and outputs; 3) calculate the correlation between cyst depth and outputs. All eighteen models were included in the statistics, including the one paediatric model (3R3). To calculate the significance of the differences between the two cystic conditions, non-parametric testing was used. This testing type was used as Shapiro Wilks testing showed most of the data was not normally distributed (only mean compressive stress in the intact bone group, and peak tensile stress in the cystic group were normally distributed). The alphas value was adjusted using a Bonferroni correction, to give a significance level of 0.0083 for the bone outputs, and 0.025 for the cartilage outputs.

For the correlations – relating to volume, location, and depth – Spearman’s rank was used over Pearson’s correlation, due to the graphs not clearly showing linearity. In the volume study, all 18 model’s outputs were contrasted against their respective total volumes, then the 14 tibial volume fractions were checked against all outputs for the models with tibial cysts, and the 10 talar volume fractions against all outputs for the models with talar cysts. The significance of the correlation was set to 0.05. A similar approach was taken in the cyst location study, with the correlations assessed between the percentage differences between the two cyst conditions and the cyst location for both bones. These statistical tests, in all four instances, were carried out on both the peak and mean outputs.

## 5.3 Results

Both qualitative and quantitative results were gathered from the eighteen models. The following sections cover the main comparisons of interest; 1) between the two cystic conditions: intact bone, and cystic tissue; 2) changes against cystic volume, and cystic volume fraction; 3) relationship with cyst location; and 4) the effect of depth as an independent variable, in order to ascertain if depth alone had any significant impact on outputs.

### 5.3.1 SBC Property Sensitivity Study

The one-Sample T-Tests showed that some outputs were more sensitive to the SBC property than others. Significant differences ( $p < 0.0001$ ) were found for the peak contact pressures (Figure 49A), while the differences were non-significant for mean contact pressures ( $p = 0.215$  and  $0.152$  in the tibial and talar cartilage respectively) (Figure 49B). There were significant differences in the contact area ( $p < 0.0001$ ), but when evaluating the percentage error for the contact areas, this was only 2.3% in the tibial contact area, and 1.8% in the talar cartilage.

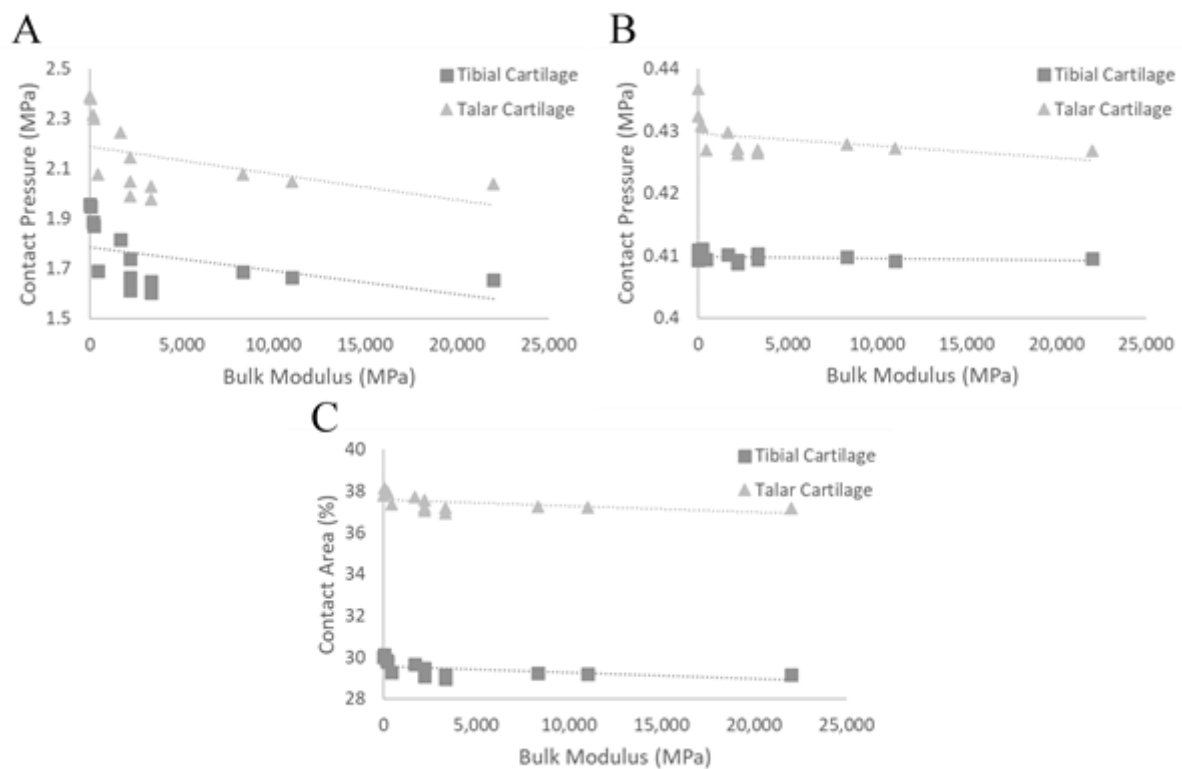


Figure 49 Sensitivity Study results for A) peak contact pressure, B) mean contact pressure, and C) % area in contact against bulk modulus

The stress outputs in the bone (Figure 50) were much more sensitive to the properties of the cyst, with significant differences in both peak ( $p < 0.0001$ ) and mean ( $p < 0.001$ ) stresses in the tibia and talus; with percentage errors in the bone outputs ranging from 2.99% to 29.14%. The localised effect was seen with these errors being greater in the tibia, where the SBC volume was present.

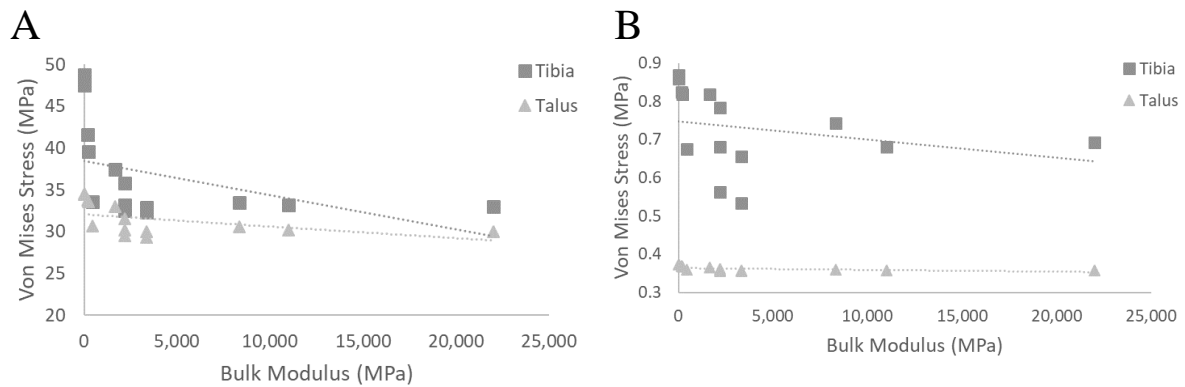


Figure 50 Sensitivity Study results for A) peak, and B) mean VVMS against bulk modulus

### 5.3.2 Intact Bone vs Cystic Tissue

The non-parametric testing used to assess whether the difference between the outputs in the intact bone, and cystic tissue groups was significant. The differences between the mean contact pressures in the cartilage were not significant in either the tibial or talar cartilage ( $p = 0.349$ ), the differences between the peak contact pressures was significant ( $p = 0.0004$ ) in the tibial cartilage, but not in the talar cartilage ( $p = 0.170$ ). In both the tibia and talus, all mean and peak outputs were significantly different between the two cystic conditions ( $p = 0.0002$  to  $0.001$ ); however, the sensitivity study (Section 5.3.1) highlighted the bone outputs are highly sensitive to the SBC properties used in the model. For this reason, the significance of the differences in bone outputs may relate to the de facto cystic property used in this study. This finding was not the case for the cartilage properties, therefore the differences between the intact bone and cystic tissue were only considered in the cartilage.

As the differences in the mean contact pressure were not significantly different between the de facto and intact groups, it was assessed if there was a redistribution effect (Figure 52). A non-parametric test was also used to assess whether there was a more localised effect. This was done by assessing the significance of the difference in the mean tibial cartilage contact pressure in the 14 models with tibial cysts ( $p = 0.300$ ), and the significance of the difference in the mean talar cartilage contact pressure in the 10 models with talar cysts ( $p = 0.374$ ). These were repeated for the peak values, where the tibial values were no longer significant due to the Bonferroni correction ( $p = 0.048$ ), and the talar values were again insignificant ( $p = 0.953$ ).

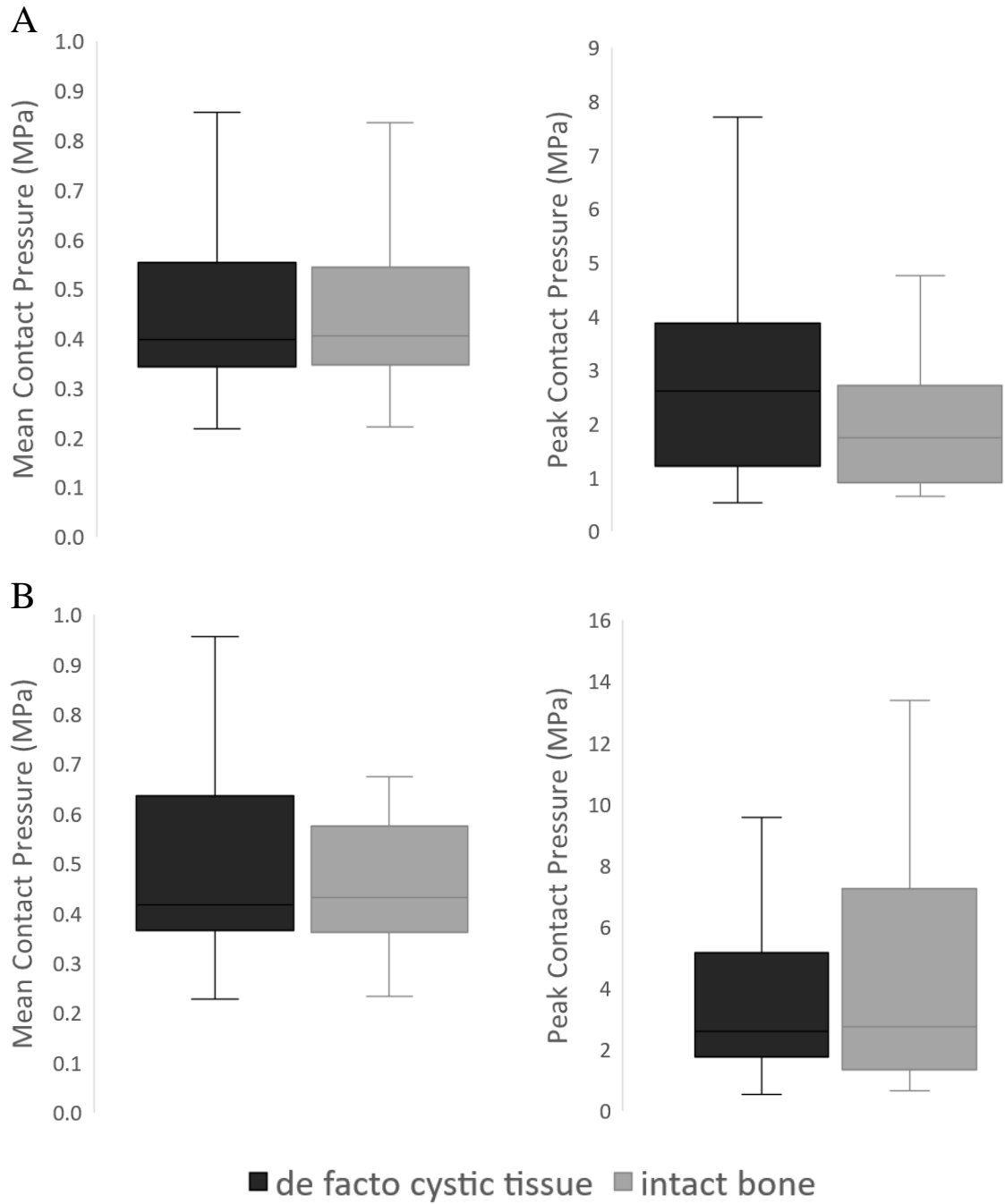


Figure 51 Mean (left) and Peak (right) contact pressures in A) Tibial Cartilage, and B) Talar Cartilage for all 18 models

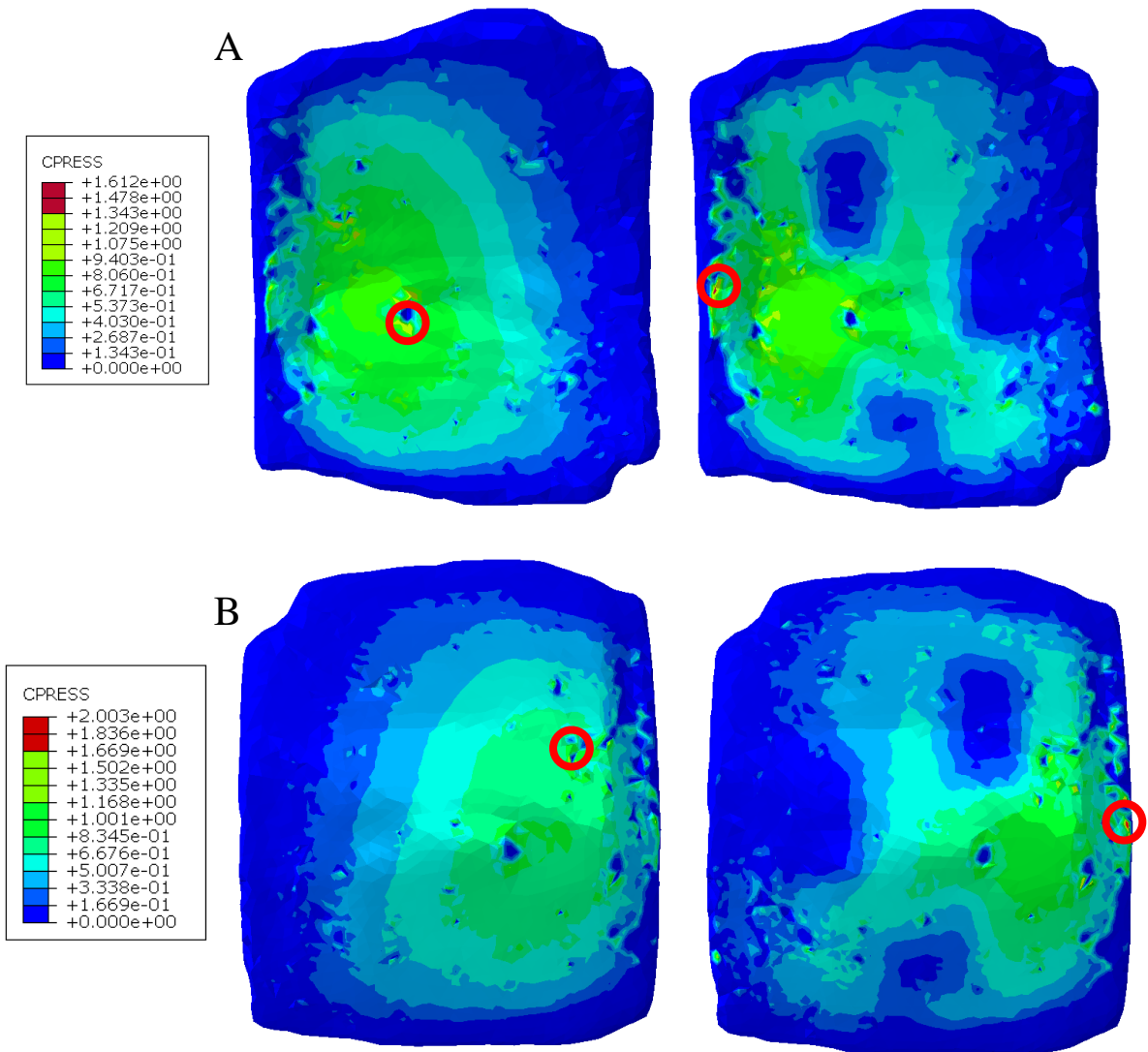


Figure 52 Redistribution of pressure in A) Tibial, and B) Talar cartilage for model 1R2 (see appendix for all ankles redistributions). Location of peak contact pressure circled for each cartilage component under the two conditions

Despite there not being significant differences between the mean outputs in both the tibial and talar cartilage, Figure 52 demonstrates a redistribution of pressure in both. This redistribution occurred in both cartilage components despite there only being tibial SBCs in 1R. The areas where pressure are reduced appear to align with one another.

### 5.3.3 Subchondral Bone Cyst Volumes

It can be seen in Figure 53 that Ankle 1 only had tibial cysts; 2R developed a small volume of tibial cyst after 28 months, while in 2L and 3R the cyst growth both propagated from the tibia.

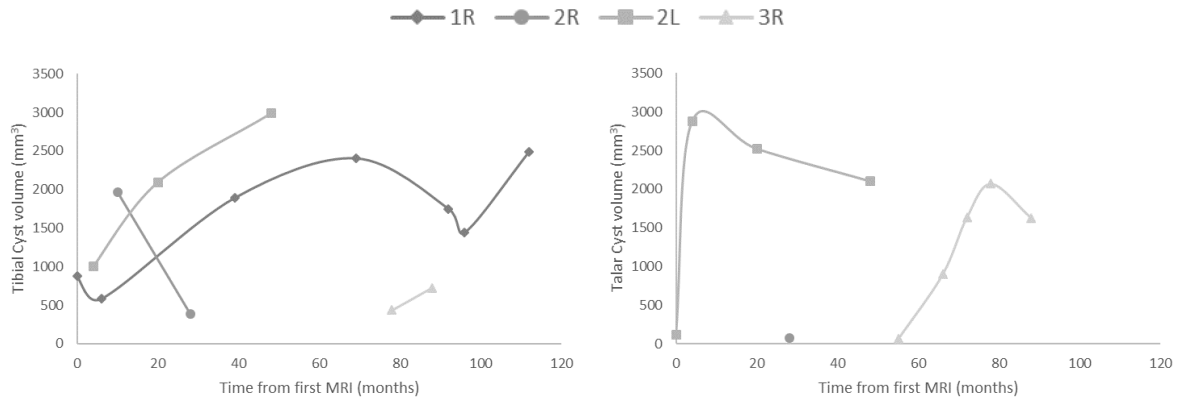


Figure 53 Subchondral bone cyst volumes for tibial cysts (left) and talar cysts (right).

Both the total cyst volume of Figure 54 and the cyst volume fractions (Table 22) were used in the correlations between cyst volume and stress outputs in Section 5.3.4.

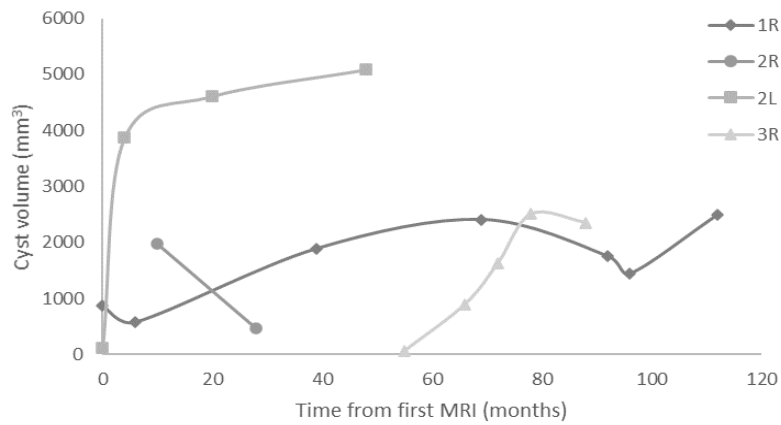


Figure 54 Total subchondral bone cyst volume against time for four ankles.

Table 22 Cyst Volume Fraction for each time point (left to right with disease progression)

		Cyst Volume (% surrounding bone)						
1R	Tibia	1.84	1.43	4.71	4.94	5.23	3.69	6.34
	Talus	8.59	1.16					
2R	Tibia		0.86					
	Talus		2.97	7.51	10.53			
2L	Tibia	0.80	22.03	18.39	13.59			
	Talus					1.14	2.12	
3R	Tibia					10.78	10.59	
	Talus	0.49	8.37	16.63	10.78	10.59		



### 5.3.4 Cyst Volume Study

No correlation with the total cyst volume was found for the peak and mean contact pressures in the tibial cartilage ( $r_s = 0.084$  and  $0.053$  respectively). The same was found for the peak and mean contact pressures in the talar cartilage ( $r_s = 0.057$  and  $0.024$  respectively).

Unlike in the results of the addition of SBCs, the influence of the de facto material properties are not the driving factor in the relationships between SBC properties and bone outputs. Therefore, bone outputs can be considered in the volume, location and depth studies. The correlation between SBC volume and the bone outputs were much more strongly positive. All outputs in the talus were significant, while in the tibia the mean values had significant positive correlations, and the peak values had positive, but non-significant correlations (Table 23).

Table 23 Spearman's correlation ( $r_s$ ) for total cyst volume against peak and mean stress outputs in the tibia and talus. Significant correlations marked with \*

	Von Mises Stress		Shear Stress		Compressive Stress		Tensile Stress	
	Peak	Mean	Peak	Mean	Peak	Mean	Peak	Mean
<b>Tibia</b>	0.233	0.639*	0.356	0.635*	0.395	0.585*	0.187	0.701*
<b>Talus</b>	0.798*	0.744*	0.794*	0.744*	0.767*	0.732*	0.705*	0.651*

#### 5.3.4.1 Tibial Cartilage

The peak and mean contact pressure showed positive but non-significant correlations with the talar cyst volume ( $r_s = 0.406$  and  $0.430$  respectively). The same contact pressure values showed negative but non-significant correlations with the tibial cyst volumes ( $r_s = -0.257$  and  $-0.138$  respectively).

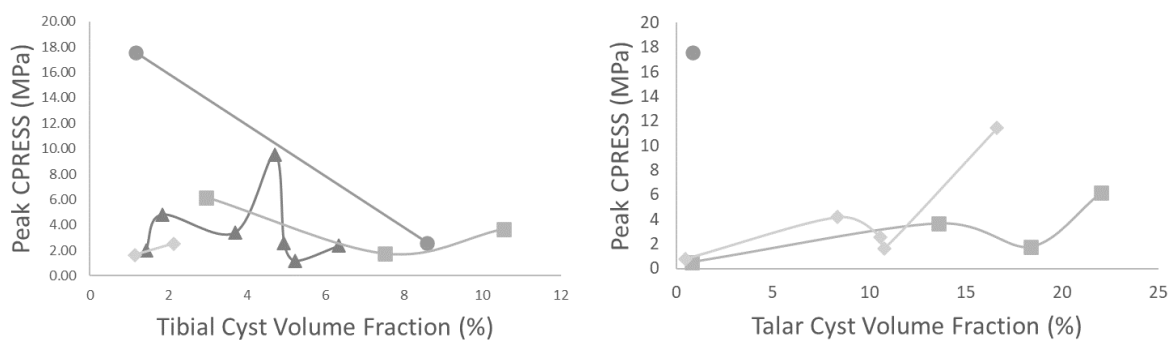


Figure 55 Peak contact pressure in tibial cartilage against tibial cyst volume fraction (left) and talar cyst volume fraction (right)

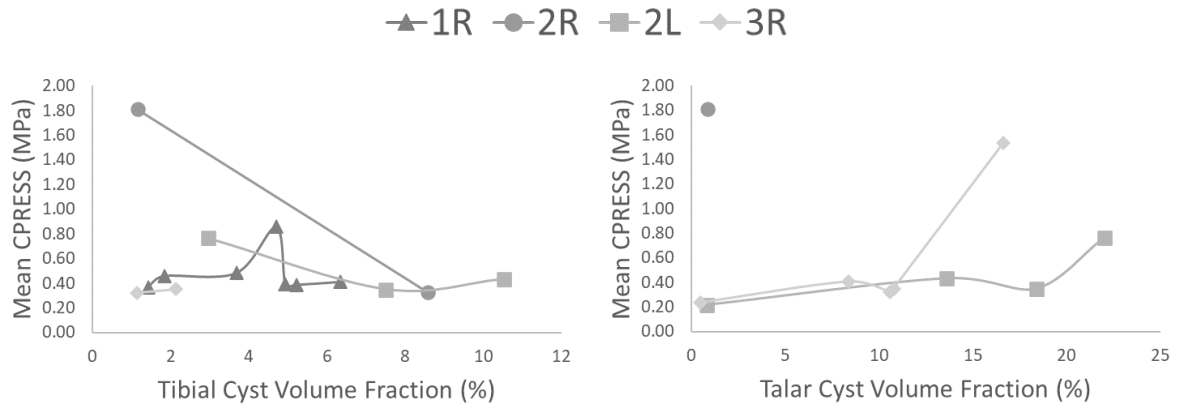


Figure 56 Mean contact pressure in tibial cartilage against tibial cysts volume fraction (left) and talar cyst volume fraction (right)

### 5.3.4.2 Talar Cartilage

Similar correlations to the tibial cartilage were seen, the peak and mean contact pressure again showing positive but non-significant correlations with the talar cyst volume ( $r_s = 0.394$  for both). The same contact pressure values showed negative but non-significant correlations with the tibial cyst volumes ( $r_s = -0.108$  and  $-0.143$  respectively).

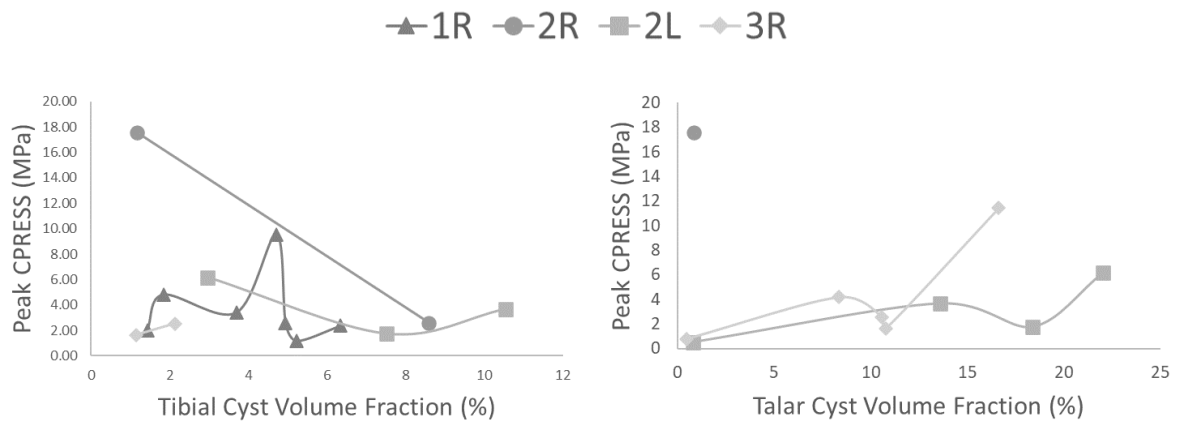


Figure 57 Peak contact pressure in talar cartilage against tibial cysts volume fraction (left) and talar cyst volume

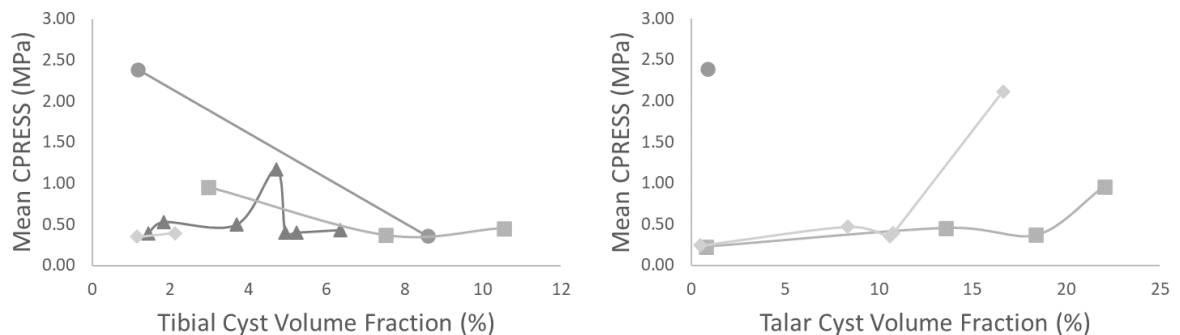


Figure 58 Mean contact pressure in talar cartilage against tibial cysts volume fraction (left) and talar cyst volume fraction (right)

### 5.3.4.3 Tibia

When considering the cyst volume fractions, rather than total cyst volume, both the peak and mean values were reduced to non-significant correlations. All were positive, except the correlation between the peak tensile stress and the tibial cyst volume fraction. These correlations all showed a less strong relationship than with the total cyst volume shown in Table 23.

Table 24 Tibia results for Spearman's correlation ( $r_s$ ) correlations for stress outputs against tibial cyst volume fractions (vol%) and talar cyst vol%. Significant correlations marked with \*

	Von Mises Stress		Shear Stress		Compressive Stress		Tensile Stress	
	Peak	Mean	Peak	Mean	Peak	Mean	Peak	Mean
	<b>Tibial Cyst vol%</b>	0.002	0.530	0.099	0.516	0.169	0.437	-0.240
<b>Talar Cyst vol%</b>	0.491	0.600	0.491	0.600	0.552	0.539	0.309	0.479

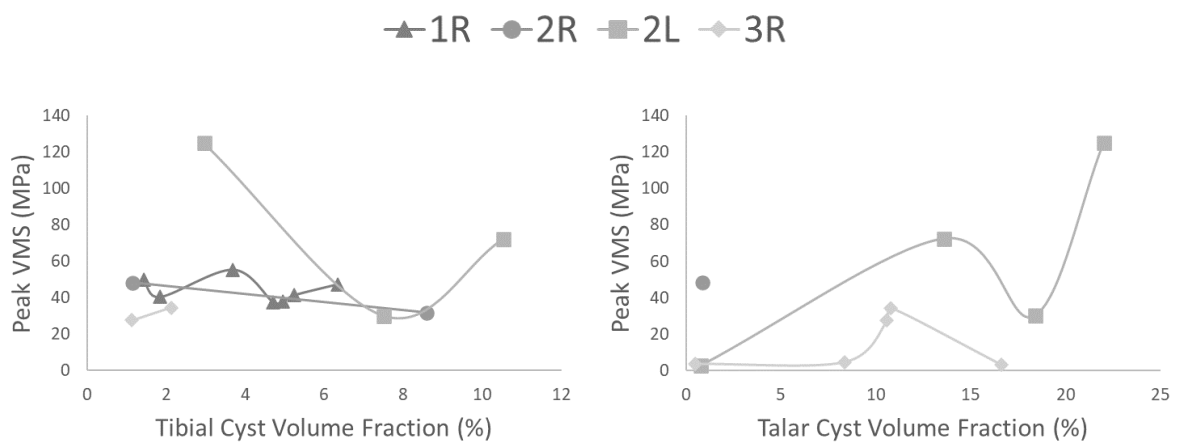


Figure 59 Peak VMS in the tibia against tibial cysts volume fraction (left) and talar cyst volume fraction (right)

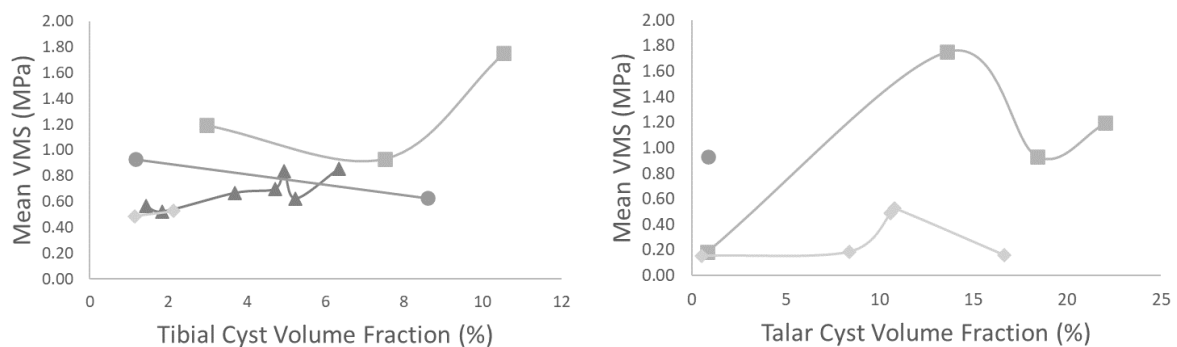


Figure 60 Mean VMS in the tibia against tibial cysts volume fraction (left) and talar cyst volume fraction (right)

### 5.3.4.4 Talus

The correlations for the peak and mean values between the talar outputs and the tibial cyst volume fraction are all positive but non-significant. The relationship between the outputs and the talar cyst volume fractions were all significant positive correlations.

Table 25 Talus results for Spearman's ( $r_s$ ) correlations for stress outputs against tibial cyst volume fraction (vol%) and talar cyst vol%. Significant correlations marked with \*

	Von Mises Stress		Shear Stress		Compressive Stress		Tensile Stress	
	Peak	Mean	Peak	Mean	Peak	Mean	Peak	Mean
<b>Tibial Cyst vol%</b>	0.336	0.327	0.301	0.327	0.319	0.284	0.415	0.495
<b>Talar Cyst vol%</b>	0.745*	0.745*	0.782*	0.745*	0.709*	0.770*	0.673*	0.685*

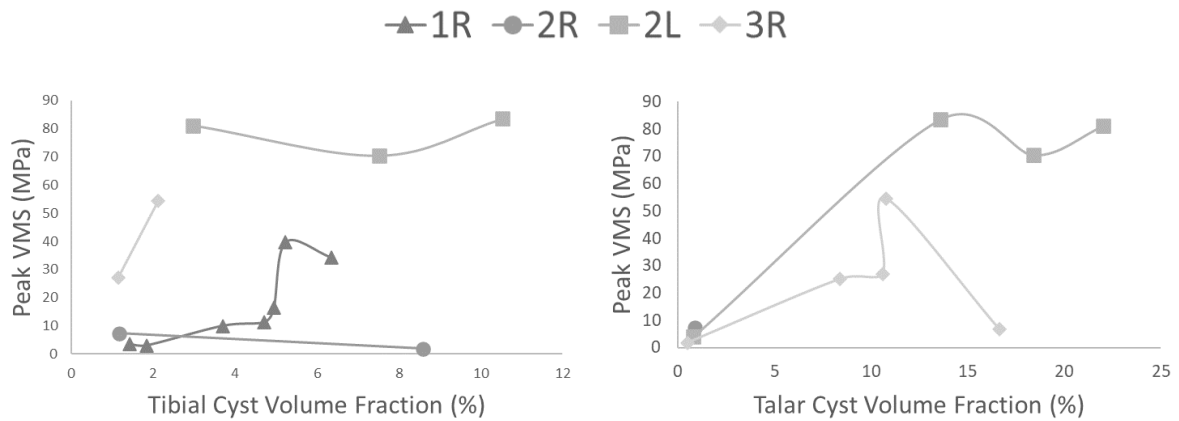


Figure 61 Peak VMS in the talus against tibial cysts volume fraction (left) and talar cyst volume fraction (right)

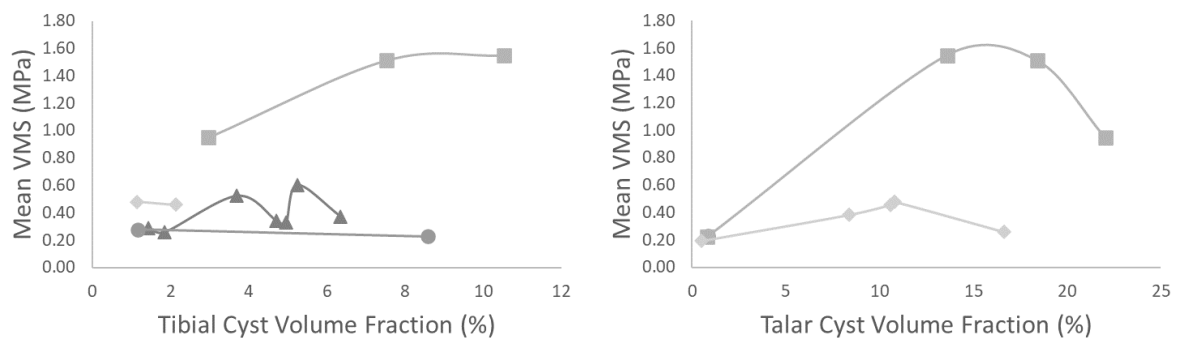


Figure 62 Mean VMS in the talus against tibial cysts volume fraction (left) and talar cyst volume fraction (right)

### 5.3.5 Influence of SBC Location

One model with tibial cyst only ( $583\text{mm}^3$ ), a model with talar cyst only ( $896\text{mm}^3$ ), and a model with cysts in both ( $460\text{mm}^3$  total –  $386\text{mm}^3$  tibial cyst,  $74\text{mm}^3$  talar cyst) were contrasted for the peak tibial and talar changes.

Percentage changes for both the peak and mean values in the tibial and talar stresses quantified the difference between the three cyst locations. From previous results, the greatest changes were expected to be localised to the bone the cyst was located in. The greatest change (706%) in peak tibial stresses occurred in the model with cysts in both bones, the increase caused by tibial cysts alone was still high (566%), while talar cysts caused a much smaller increase (6%). Peak talar stresses did not follow exactly the same trend; in the model with talar cysts alone, the percentage change was the greatest (759%), while in the model with cysts in both bones the talar stresses increased by 132%, in the tibial cyst model the increase was the smallest (10%). The change in the model with cysts in both bones likely reflects the small cyst volume ( $74\text{mm}^3$ ) in the talus, however can be seen that an amplification is caused by cysts in both bones.

The mean values followed the same trends on the whole, with significantly reduced percentage change values. Mean tibial stresses increased by 240%, 0.16% and 90% respectively with the tibial cysts, talar cyst, and cysts in both bones. While the mean talar stress decreased by 1% with the tibial cysts, the mean talar stresses increased by 99% with the talar cysts, and 10% when cysts were present in both bones.

### 5.3.6 Cyst Depth Study

The correlation between the measured minimum SBC depths and the model outputs were calculated, and showed insignificant weak negative correlations between the talar cyst depths and the peak and mean contact pressures in both cartilage components (-0.217 to -0.280). The correlation between the talar cyst depths and the VMS in both bones was also insignificant; the peak and mean tibial stresses had no correlation (0.056 and -0.093 respectively) while the peak and mean talar stresses were weakly negative (-0.354 and -0.391 respectively). There were insignificant positive correlations with the peak and mean contact pressures in both cartilage components (0.235 to 0.471). Considering the VMS and how these correlate with the tibial cyst depths, the peak and mean VMS in the talus were insignificant and negative (-0.203 and -0.380 respectively); in the tibia the peak VMS had no correlation (0.055), and the mean VMS was positive, but again insignificant (0.382).

In models where the SBC depth was varied parametrically, the peak contact pressure was seen to vary with the cyst offset to a greater degree in the talar cartilage, however, the mean value was minimally effected in both. The addition of cysts on the whole does not significantly influence the mean values, therefore the influence on redistribution was also investigated qualitatively (Figure 65 and Figure 66).

When varying the depth of the cyst, the +0.5mm offset only converged to 65% of the loading step, from this it gave a peak output in the tibia of 26.7MPa, and in the talus of 5.7MPa. Should it be assumed these were increasing linearly with the load, these would be expected to be approximately 41MPa, and 8.8MPa respectively, which fall within the expected range for this study (Figure 63).

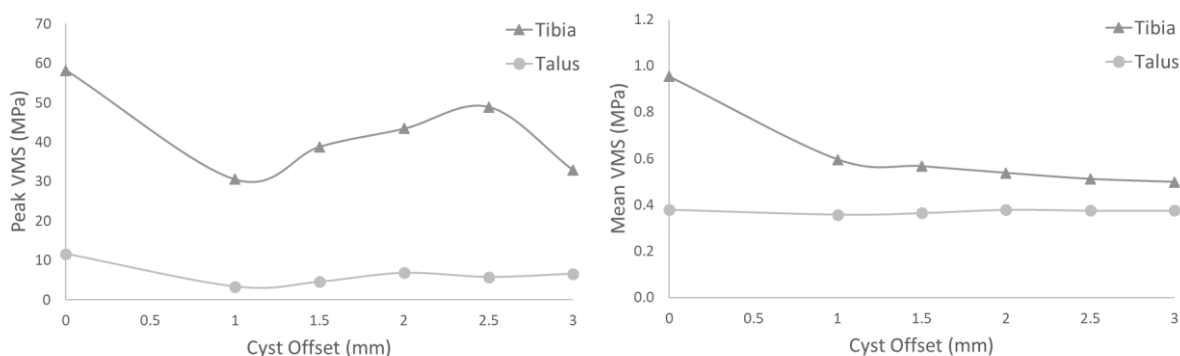


Figure 63 Peak (left) and mean (right) VMS for both the tibia and talus with varying cyst depth

The cartilage pressure values calculated from the 65% convergence also fell within the predicted range, with 3.8MPa calculated in the tibial cartilage at 100% and 4.9MPa in the talar cartilage (Figure 64).

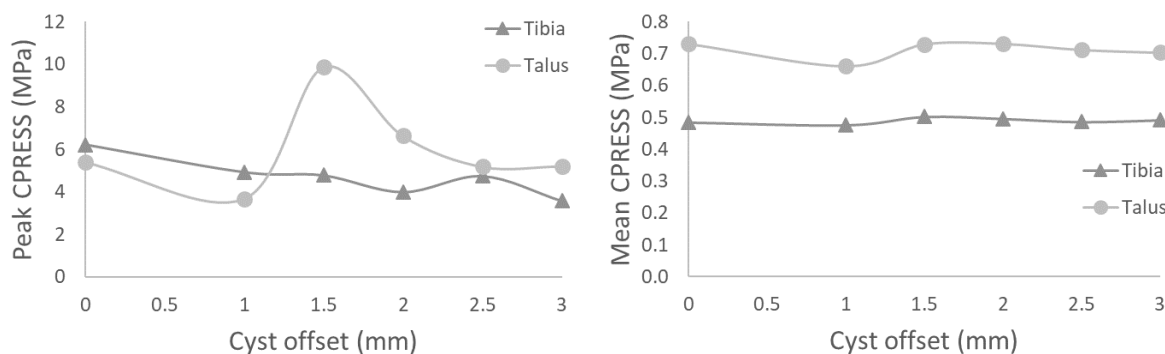


Figure 64 Peak (left) and mean (right) contact pressure for both the tibial cartilage and talar cartilage with varying cyst depth

Spearman’s correlation ( $r_s$ ) demonstrated significant correlations between SBC depth and the tibial outputs (Table 26), which was anticipated based on previous findings, due to the fact this was carried out on an ankle with only tibial cysts.

Table 26 Spearman's correlation ( $r_s$ ) values for the cyst depth study, assessing for correlation between cyst depth and peak and mean outputs. Significant values marked with \*

	<b>Tibial Cartilage</b>		<b>Talar Cartilage</b>		<b>Tibia</b>		<b>Talus</b>	
	Contact Pressure		Contact Pressure		Von Mises Stress		Von Mises Stress	
	<i>Peak</i>	<i>Mean</i>	<i>Peak</i>	<i>Mean</i>	<i>Peak</i>	<i>Mean</i>	<i>Peak</i>	<i>Mean</i>
<b><math>r_s</math></b>	-0.943*	0.429	-0.086	-0.290	-0.200	-1*	-0.029	-0.058

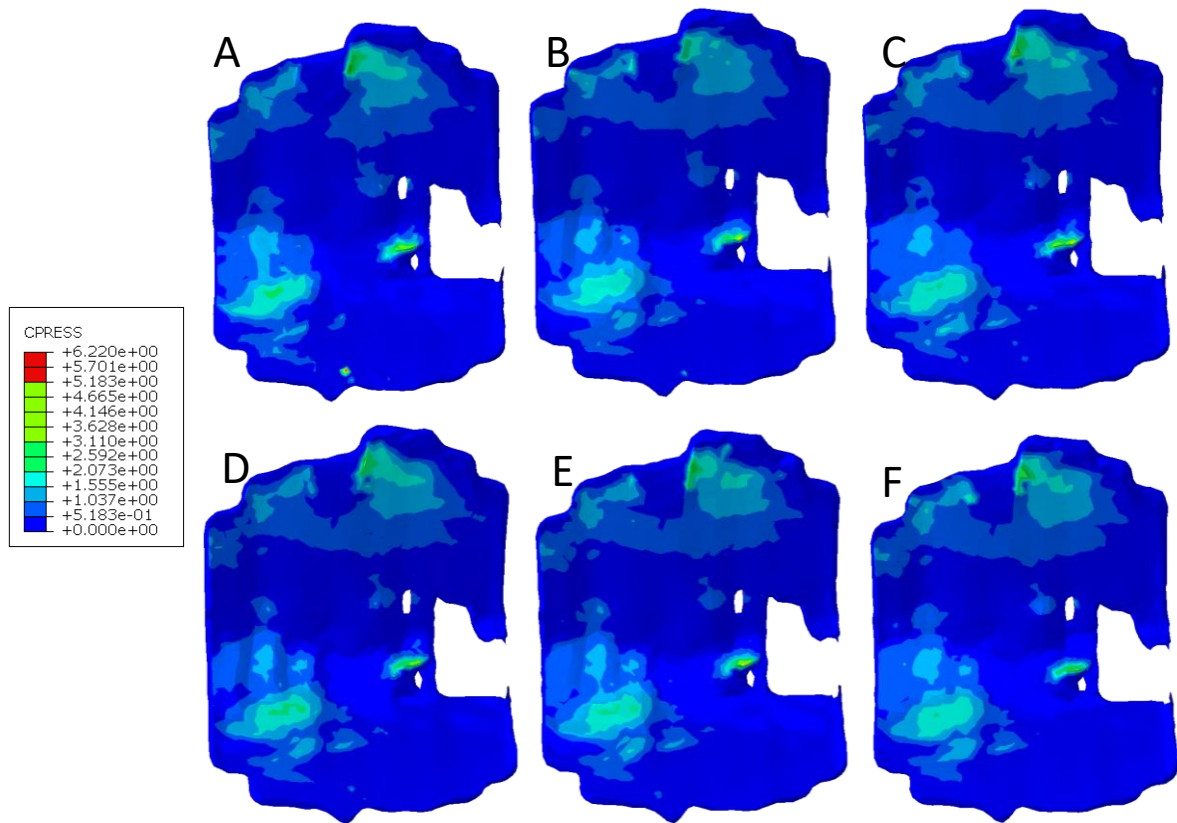


Figure 65 Contact Pressure in the tibial cartilage in A) 1R7C with no offset; C) +1mm offset; D) +1.5mm offset; E) +2mm offset; F) +2.5mm offset; G) +3mm offset.

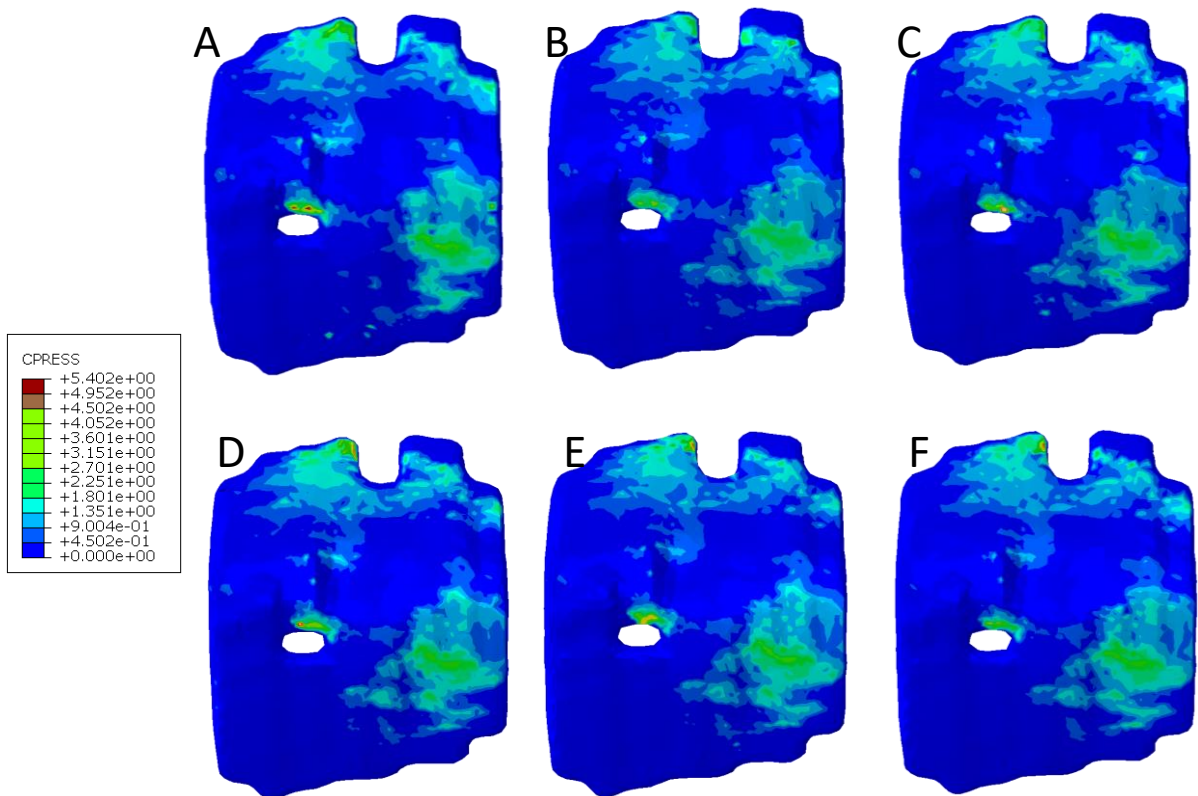


Figure 66 Contact Pressure in the talar cartilage in A) 1R7C with no offset; C) +1mm offset; D) +1.5mm offset; E) +2mm offset; F) +2.5mm offset; G) +3mm offset



## 5.4 Discussion

The use of MRI data in people with haemophilia to diagnose and stage haemarthritic changes makes it the perfect tool to quantify the implications of the main presentations. The nature of the patient specific models generated in Chapter 4 included any geometric changes to the bone or cartilage with the image specific segmentations produced. The imaging presentations of haemophilia made it possible to carry out the study in this Chapter, where the influence of SBCs on joint health are considered in depth.

Despite the prevalence in osteoarthritis (Audrey, Abd Razak and Andrew 2014; Buckland 2010), rheumatoid arthritis (Rennell *et al.* 1977), and HA (Lundin *et al.* 2012), very few studies have been carried out surrounding the impact of SBCs. Those that have been carried out contain large simplifications to the study. The representation of SBCs in FE analysis varies in literature, with 2D (Dürr *et al.* 2004) and 3D (Anwar *et al.* 2020; Frazer, Santschi and Fischer 2017) analysis carried out. The material used to represent the fluid that fills the space has not yet been characterised, however its elastic properties are assumed to be significantly smaller than the surrounding bone (Frazer, Santschi and Fischer 2017). Other representations have split the cyst into a cyst wall and cyst lumen, where the lumen is assumed to behave as a hydrogel with a Young's Modulus of 0.1 MPa (Sarrafpour *et al.* 2019). These previous SBC studies have not indicated if or how the presence of blood – should it enter the SBCs – would affect the mechanical properties due to the focus of the research being on OA (Anwar *et al.* 2020; Dürr *et al.* 2004), oral cysts (Sarrafpour *et al.* 2019), or equine studies (Frazer, Santschi and Fischer 2017).

Previous studies have all involved the simplification of the geometry as well as the properties of the cyst. The geometry in these previous studies has been simplified to a sphere (3D) or circle (2D). These would be appropriate in a number of cases, as it is found that approximately half of all SBCs are spherical, while the remainder are classified as irregular in shape (Reilingh *et al.* 2013). However, upon observing the 18 MRIs with SBCs in this study, all were irregular. The simplification to spherical therefore is not justifiable in image-based modelling given the ability to segment the cystic regions from the MRI sequences, enabling patient specific cysts to be included in the model. Patient specific cysts can also be modelled using CT, however the contrast in Hounsfield Units in CT is not as strong as between signal intensities in either MRI sequence used. The nature of the clinical MRIs, with slice thicknesses of approximately 3mm,

means that some assumptions are being made surrounding the shape and volume, however this method is still an improvement on simplifications to spherical cystic bodies.

The first consideration was the difference in the model outputs contrasted between the two conditions, this allowed the general implication of SBCs on joint health to be understood before investigating whether there was an important relationship with factors such as volume, location, or depth. These comparisons were carried out in both the cartilage and bone components.

Cartilage results highlighted there was not a large influence on the magnitude of cartilage pressure with the presence of SBCs, but there is a redistribution effect seen the majority of cartilage components (further examples in the appendix). The nature of some previous studies have not allowed the effect on cartilage to be considered. The 2D (Dürr *et al.* 2004) and dental (Sarrafpour *et al.* 2019) studies did not have the articular cartilage to consider; the equine study could have been used for a comparison, however the redistribution of stress was not evaluated (Frazer, Santschi and Fischer 2017). The one study that did consider the redistribution did so in the shear stress of the articular cartilage in the knee, finding increased values in close proximity to the SBC, and significant increases in the mean values with the inclusion of larger cyst volumes or multiple smaller cysts (Anwar *et al.* 2020). This did not agree with the findings in the four ankles in this study, each seeing reduced pressures in the area surrounding the SBCs. Cartilage loss tends to occur in areas of higher pressure, with increased wear seen in weight-bearing areas of a joint. Significantly increased contact pressures with SBC inclusion would have been of concern, given the irreversible nature of damage with disease tissue. However, in these haemophilic cases there were no significant increases in pressures, thus, it is not possible to discern if the presence of SBCs can be directly linked with cartilage degeneration as was concluded in the knee OA study (Anwar *et al.* 2020). Further investigation would be needed to understand how the redistribution of pressure may impact cartilage health.

In patients with osteochondral lesions, elevated cartilage pressures have been linked to pain, whether this connection could be made in haemophilia would depend on the availability of clinically reported pain; these scores could then also be correlated to the peak and mean contact pressures to assess if there is a relationship with SBC presence, volume, depth or location.

The stresses experienced in the bone would be of interest due to the relationship between the mechanical stresses and the microscopic morphology of bone (Martin and Burr 1989), where bone remodelling is triggered by increased stresses and strains within the bone. In healthy bone,

this remodelling either sustains the mechanical properties or increases bone strength. In diseased bone such as that in haemophilic joint disease these stresses are likely to cause an imbalance in the bone remodelling and reduced bone quality due to the increased osteoclast activity and impaired osteoblast function.

As the sensitivity study showed that the bone outputs were highly sensitive to the material properties assigned to the SBC, the true values for bone stresses cannot be ascertained without use of characterised material properties. However, the relationship with the characteristics of the SBCs, such as volume and location may still be relevant, as the correlation was calculated using the same arbitrary values for all SBCs.

Previous studies have found a tendency to elevated stresses in the bone adjacent to the SBCs (Anwar *et al.* 2020; McErlain *et al.* 2011). Largely, these studies have just considered VMS values (Anwar *et al.* 2020; McErlain *et al.* 2011) due to the hypothesis that they can be an indicator of stress fractures (Dürr *et al.* 2004). Some took into consideration the same stress outputs as this thesis: compressive, tensile, shear and Von Mises (Frazer, Santschi and Fischer 2017); the results were mixed, with the responses to their three cyst conditions different in each output. They considered percentage change in the peak outputs between normal and the cystic conditions; with results suggesting some correlation between SBC volume and outputs, however the nature of this relationship differed for each of the four stress outputs.

In the bone outputs, it was seen there was significant differences between the de facto and intact bone outputs; these increases in both peak and mean bone stresses appeared to relate to relate, initially, to cyst volume. For example, in Ankle 2R, there was only a relatively small talar cyst volume compared to the tibial cyst volume, which was reflected in the talar bone outputs. However, as the tibial cyst volume fraction decreased, the difference between the two conditions in 2R3 (relative to 2R2) increased. This appeared to be confirmed in both 2L and 3R by qualitative assessment of the results, hence the quantitative investigation into whether the presence of SBCs in bone bones amplifies the effect.

#### 5.4.1 Impact of SBC Volume

As there were a wide range of SBC volumes within the 18 MRI sequences, and when first comparing the de facto and intact models there appeared to be a relationship between the SBC volume and the stress outputs, the correlation was assessed. In the previous studies, where volume was an independent variable, it was seen to correlate (Anwar *et al.* 2020; Frazer, Santschi and Fischer 2017). However, in this study, due to the patient specific nature of the

segmentations it was not a completely independent variable. Maintaining the patient specific shape of the cyst was key to understanding the influence of the disease however; therefore, it is a known confounding factor that shape, depth and volume will all vary when the correlation is only being calculated for volume.

With the surrounding bone volumes also changing in this study, which was not the case for the correlations made in the previous studies, this was accounted for by also considering bone volume fractions for both the bone and cartilage outputs.

#### *5.4.1.1 Changes in Cartilage Contact Pressure*

A strong correlation between cartilage contact pressure and SBC volume was not expected, given the non-significant difference between the models with and without cystic tissue. The total SBC volume in each model, gave the weakest correlation with the peak and mean contact pressures in both cartilage components (0.024 to 0.084). This opposes the findings in the knee study (Anwar *et al.* 2020) . Better understanding of the relationship between SBC volume and contact pressure could be gained by treating the SBC volume as an independent variable, as has been varied out in studies considering bone stresses. However, this is more complex when considering irregular shape cysts, as volume directly influences the shape of the SBC if using a dilating or extruding method to shrink or grow the SBC.

To further the understanding of the contact redistribution, a qualitative analysis could be correlated to the SBC volume. This however, would be complex due to SBCs being present in both bones in 10 of the 18 models, as it was seen that the redistribution occurred in both cartilage components when the SBC was only present in one bone. The volume may also not be the best variable to use for this, as some SBCs had larger areas close to the bone cartilage interface, while others projected deeper into the bone. Therefore it may be area of the SBC closest to the cartilage that is more directly linked to the changes in contact pressure.

Knowledge of whether there was a relationship with either area or volume, alongside the impact of irregular contact areas on cartilage health would aid in answering whether a direct link could be made in haemarthritic ankles between the SBCs and cartilage degeneration.

#### *5.4.1.2 Changes in Bone Stresses*

Despite not being able to consider the difference between the cystic and non-cystic conditions, it was of interest whether any of the outputs were influenced by the total cyst volume, or the volume fraction within the bone. The previous SBC studies have not calculated correlations

between SBC volume and outputs, however, from the results of studies considering multiple cyst conditions it appeared there was a relationship between volume and the magnitude of stress values (Anwar *et al.* 2020; Frazer, Santschi and Fischer 2017). This relationship was confirmed for the ankle models using Spearman's correlation, where a significant positive correlation was seen between the total cyst volume and the mean stresses in both bones, and the peak stresses in the talus. While there was only a weak positive correlation with the peak tibial stresses. Pearson's correlation was also carried out to assess for linearity of the correlation, the stronger correlation values for this test suggests the relationship may be linear.

With this strong indication that there was a relationship between SBC volume and stress values, it was then investigated how the cyst volume fraction might be. Somewhat against the hypothesis, this gave weaker correlations for most outputs, with only significant positive correlations for the relationship between talar cyst volume fractions and the peak and mean talar outputs. However, the amplified stress values when cysts are present in both bones, may explain this finding, as the total volume takes into consideration both cyst volumes, while the volume fraction doesn't take this into account, and the relationship may be stronger when considering these. This would strengthen the argument that total volume is important when considering bone stresses, but the presence of cysts in both bone is increasingly detrimental to bone health.

#### 5.4.2 Impact of SBC Location

As the SBC volume alone could not account for the differences between the outcomes in the 18 SBC models, the impact of the location was then considered. This had previously been unaccounted for in literature, however, given the range of locations in the haemarthritic ankle, it was a logical consideration.

##### 5.4.2.1 Changes in Cartilage Contact Pressure

The relationship between contact pressure and any SBC variable has thus far been insignificant; therefore, it was unsurprising that the relationship between volume fractions and contact pressure, used to assess the impact of SBC location, also gave insignificant correlations. They were however a mix of positive and negative correlations depending on the bone the bone the SBCs were located in. Talar cyst volumes showed weak, but positive, correlations (0.394 to 0.430) for peak and mean values in both cartilage components, while tibial cyst volumes had weak negative correlations (-0.108 to -0.337) for the mean and peak values in both the tibial

and talar cartilage. These should not be taken at face value to look for trends, however, given the number of joints that had both tibial and talar cysts. So instead of suggesting that tibial cysts relieve cartilage contact pressures, their effect may not be as dominant due to their smaller bone volume fractions.

#### 5.4.2.2 *Changes in Bone Stresses*

The multiple cyst conditions investigated in previous studies (Anwar *et al.* 2020; Frazer, Santschi and Fischer 2017) did not consider differing cyst locations; however, the presence of SBCs in either the tibia, talus, or both bones in the 18 image based models, makes them of interest in this study. The cyst location was defined by which of the bones the SBCs were present in; it was of interest as to if this related to the degree of influence. It was expected that there would be a localised effect, as was witnessed in previous studies (Anwar *et al.* 2020; McErlain *et al.* 2011), however the wider effect on the joint is unknown.

The direct impact of SBC location is difficult to determine exactly, however, those models with cysts in both bone compartments appeared to have larger stress values when comparing with similar volumes in just one bone. This was identified by comparing the cysts with intact bone to see the difference between the two scenarios. This was done for VMS, as the four outputs in this study followed the same trends on the whole – unlike those of Frazer *et al.* (2017). Initially the peak values were investigated, however, it is likely the peak values are influenced by the mesh generated when the cyst was added, and may be linked more to the geometry, hence the comparison was also made for the mean values.

From the elevation levels seen in the three models in Section 5.3.5. it can be seen the largest implications are localised to the bone the SBCs are in confirming the findings of previous studies regarding elevated localised pressures; however, the presence of cysts in both bone compartments is likely the most detrimental to joint health – even when there is only a small cystic volume in the second bone. The correlation between cyst volumes and percentage changes were assessed, and were largely positive, which agreed with the amplified effect seen with greater cystic volumes in both bones; for example one joint had a total cyst volume of 3,870 mm<sup>3</sup> (tibial cyst: 998 mm<sup>3</sup>; talar cyst: 2,873 mm<sup>3</sup>), where the increase in stresses were vastly increased. The peak stresses in the tibia and talus increased by 1718% and 3552% respectively, while the mean stresses also increased by 372% in the tibia, and 437% in the talus.

The elevated stresses in both components of the bone is likely to explain how the SBCs propagate from one bone to another, should the elevated VMS be linked to stress fractures in bone, which were seen to cause SBC formation (Dürr *et al.* 2004). However, more than this, it is likely to explain why there is reduced bone quality surrounding SBCs, as has been seen through clinical imaging. These elevated localised bone stresses causing damage to bone with disrupted remodelling. What remains to be understood is what happens to this bone in the situations where the SBCs repair and shrink, as is seen in some of these cases, but also within the wider haemarthritic community.

### 5.4.3 Influence of Cyst Depth

As with differing locations, depth has also not been considered as an independent variable in previous studies. Unlike cyst volume, this study allowed it to be considered as a true independent variable, to ascertain how this may explain potential differences between the outcomes of the 18 models. The SBC depth was seen to vary for each model, including the different cysts within each model. Cystic regions were either fully embedded within the bone or touching the surface of the bone. 24 cyst depths were measured to calculate the average depths; 18 of those 24 measurements were less than 0.5mm from the bone cartilage boundary. Before assessing the cyst depth using the offset study, the correlation between the minimum depths and the contact pressure and VMS was calculated. There were no significant correlations between cyst depth and outputs in either bone or cartilage. As these results were potentially biased by the factors such as shape and volume, or whether there were SBCs present in both bones, it was decided that carrying out a cyst offset study may better answer whether there was a relationship between cyst depths and outputs. One model, where all other factors were consistent, except cyst depth, would best isolate this as a factor. A model with just tibial cysts (1R7) was selected, however repeating this test with an ankle with only talar cysts would help ascertain if the negative correlation seen previously is driven by the range of cyst volumes. The findings in this cyst offset study confirm the importance of depth, highlighting the potential amplified effect of SBCs closer to the bone cartilage boundary. This would need confirming in a talar study of a similar nature, but if the relationship is as seen in the tibial offset study, all results imply that larger cystic volumes close to the talar surface would be the greatest risk to joint health. This knowledge is of importance given the proximity of most SBCs to the bone cartilage boundary, with very few lying more than 0.5mm from the cartilage.

#### 5.4.4 Effect of Arthritic Stage

The four ankles containing SBCs are each at a different arthritic stage, due to both disease timelines and patient ages (12 to 26 years). It has been reported that the effect of the blood on the articulation can be specific to the maturity of the joint. With mature joints particularly influenced in the cartilage components, while immature joints may see greater changes in the bone especially linked with hypertrophy of the epiphyseal growth plates and significant structural deficiencies (Rodriguez-Merchan 1996). Due to the fact the patient group with SBCs have not yet reached bone maturity (between the age of 17 and 18 for the tibiotalar joint (Donatelli 1996)), or only reach bone maturity over the course of imaging, it was important to consider the implication in both bone and cartilage. However, bone is especially of interest given the fact that bone biology is heightened before bone maturity. This is potentially the reason that SBCs are more commonly found in paediatric and juvenile patients, and may mean there is an increased response to stresses induced by cysts in these joints.

#### 5.4.5 Simplifications to the Haemophilic Model

It is acknowledged that the models discussed in this Chapter are not without their limitations, however, even with these simplifications we are given new important information regarding the implications of SBCs on haemophilic joint health. They do however not yet provide the independent influence of volume and shape, as was given in the parametric test carried out for depth; as volume and shape cannot be independent of one another in segmentation specific SBCs. The application of the method described in this chapter to larger sample sizes however, the significance of these relationships may be more reliably ascertained.

These models do not claim to answer questions surrounding all six of the presentations of haemophilic joint disease, as so little is still known about the relationship between tissue health and features such as effusion, synovial hypertrophy and haemosiderin depositions; therefore these were not included. Therefore the models reflect osteoarthritic conditions more closely, and do not take into consideration the inflammatory effects of the rheumatic presentations within HA. SBCs are presentations in both late stage osteo- and rheumatoid- arthritis, however have only been considered in FE models with relation to osteoarthritis, hence how these may be translated into a rheumatic model is also unexplored. The previous osteoarthritic FE models also contain simplifications, as the materials are selected based on the cysts behaving as a mechanical void, rather than reflecting true known material properties of cystic tissue. Though,



this would also likely change should blood enter the cystic regions and a biological reaction between the iron occur here in the same way it does in the cartilage and synovium.

The sensitivity study into SBC properties has shown how influential these properties are, hence the importance in fully characterising these materials for any application; with, or without the presence of blood if the implication of SBCs on bone health is being considered. The SBC properties are not the only simplification when it comes to tissue properties; the bone quality in PwH is known to be compromised due to a disturbed equilibrium in bone resorption and formation – with increased osteoclast activity and impaired osteoblast function. A direct relationship between factor VIII deficiency and augmented bone resorption has also been demonstrated in a murine model (Rodriguez-Merchan and Valentino 2019). Bone changes are considered to only occur in later stages of the disease pathogenesis, as it is still largely unknown how the joint damage proliferates to the bone, with dispute whether it is a direct or indirect effect of the bleeds. Excessive bone remodelling was witnessed within two weeks of the induced joint bleeds in animal studies (Lau *et al.* 2014; Sørensen *et al.* 2016), indicating some form of direct effect. Disease presentations that may not be directly linked to bleeds include the low bone mineral density found in people with haemophilia. This may more closely relate to a decline in physical activity or joint loading which relates to pain or fear (Gringeri, Ewenstein and Reininger 2014) or the offloading of the joint in acute bleeds or recovery periods (Kovacs 2008).

Previous studies have related altered bone mineral density to the presence of SBCs (Burnett *et al.* 2019), which supports the idea of the increased bone stresses disrupting the turnover matrix and reducing the quality of the bone. How this would then factor back into the model to create a more accurate representation of the bone immediately surrounding the SBC would be an interesting factor to take into account; unfortunately, there is not the appropriate imaging to look at surrounding bone quality and to properly reflect the different bone properties. However, the elevated localised bone pressures are still hypothesised to be disruptive to this turnover matrix.

Simplifications to material properties were already made in Chapter 4, without taking into account the above details relating to deterioration of bone health with disease progression – and how this would influence the material properties used in a model. It is acknowledged these simplifications could alter the outputs of models, especially in the localised region where SBCs have their highest influence on bone stresses. Cortical and trabecular bone have different

properties, as discussed in Chapter 3, however, there has not yet been a published investigation into the mechanical properties of bone in haemophilia. As such, there is not sufficient information to capture the bone quality accurately in FE models. Therefore the assumption is that the localised, and global effect on bone stresses would reflect the change in mechanical properties with HA. There would also likely be a range of material properties across each ankle, these would vary with the patient's disease progression, and hence it would be necessary to have CT as well as MRI in order to accurately represent this.

## 5.5 Conclusion

This study has shown that there are multiple factors in SBCs that can influence the surrounding joint health. Any amount of cystic volume elevates the stresses in the surrounding bone, which, in an already diseased joint could be detrimental to joint health and link with the osteoporotic quality bone seen in PwH. The volume, depth and location of these cysts all then factor in when considering the degree of detriment due to the relationships with each individually. Intersectional behaviour of these could only worsen the outcome on the surrounding joint. For example, large, shallow SBCs in both bones are likely to cause the highest bone stresses, and hence joint damage.

The findings in this chapter highlight it is necessary that SBCs are included in subject specific finite element models using contact pressure, and pressure distributions as a joint health metric due to their redistribution effect. As there are potential relationships with all factors such as size, shape and depth, it is best practice to ensure these are segmentation specific SBCs.

The relationship between the presence of SBCs and cartilage health is still unclear; it does not appear to be a direct relationship, however, the redistribution of pressure with no significant changes in contact pressure values is an interesting outcome, and how this pressure distribution in the cartilage would link to cartilage health would be an interesting piece of future work.

This study has shown the importance of including SBCs in models where they exist to understand to the truest extent possible the influence of disease on the whole joint, as it was not just a localised effect.

# CHAPTER 6

## FINITE ELEMENT ANALYSIS OF GAIT IN THE HAEMOPHILIC ANKLE MODEL

# CHAPTER 6: FINITE ELEMENT ANALYSIS OF GAIT IN THE HAEMOPHILIC ANKLE MODEL

## 6.1 Introduction

The stance phase of the gait cycle is divided into five main points: heel strike, flat foot, mid stance, heel off and toe off. These points are key to the efficient transfer of energy between the ground and the limb to progress gait. In non-diseased gait, as stance phase progresses, different muscles are activated, with an activation of the dorsi flexor muscles after heel strike, as the gait progresses to mid stance this deactivates and is replaced by an activation of the plantar flexor muscles until toe off (Lee, Lee and Kim 2019).

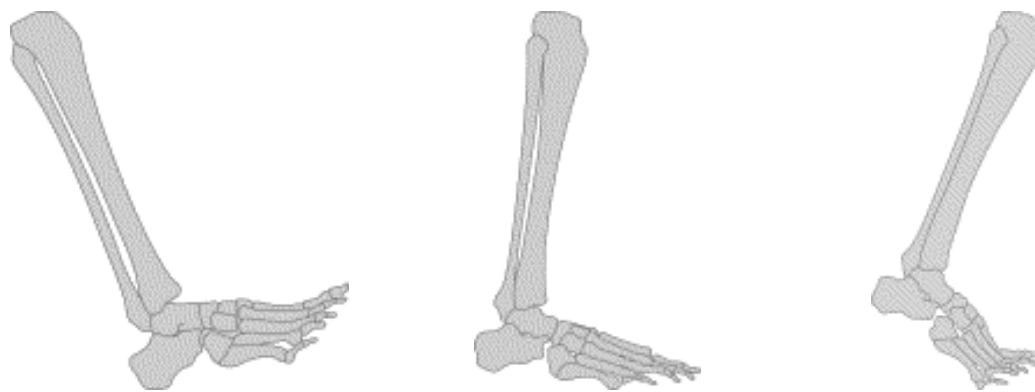


Figure 67 Foot position at heel strike, mid stance and toe off (right leg)

This gait has been seen to be altered in PwH (Lobet *et al.* 2013; Soucie *et al.* 2004), however the cause of this adaptation is still undetermined. Both morphological (Jelbert, Vaidya and Fotiadis 2009; Macnicol and Ludlam 1999) and pain related (Lobet *et al.* 2012) adaptations have previously been suggested.

Previous Finite Element models of the lower limb have incorporated musculoskeletal modelling data before; from individual bones (Altai *et al.* 2021; Seo *et al.* 2014), to joint level models (Anderson *et al.* 2006; Li *et al.* 2008; Park *et al.* 2019). A whole foot model (Akrami *et al.* 2018) has also incorporated gait; this model included soft tissues, to assess the impact on contact pressure in the soft tissues of the lower surface of the foot through the gait cycle.

Incorporating patient specific gait into the finite element models could help in understanding the cause of the adapted gait in PwH. Mechanical stress has previously been linked to pain in

orthopaedics (Buckwalter *et al.* 2013), and in haemophilia has been associated with the onset of joint bleeds (Buckwalter and Saltzman 1999). In order to assess the altered gait in PwH, two studies were carried out on these quasi-dynamic models; the first considered the arbitrary reduction in range of motion, the second utilised patient specific gait inputs. The aim of these studies was to ascertain if the adapted gait in PwH is a physical limitation, or an adaptation, by assessing if there is a potential link between the morphology (findings from Chapter 2), the patient specific gait adaptations, and the FE model outputs.

## 6.2 Methods

To assess the altered gait of PwH, two different comparisons were considered (Figure 68): 1) an arbitrary reduction in range of motion; and 2) patient specific gait. Both of these studies allowed for a contrast with non-diseased gait results.

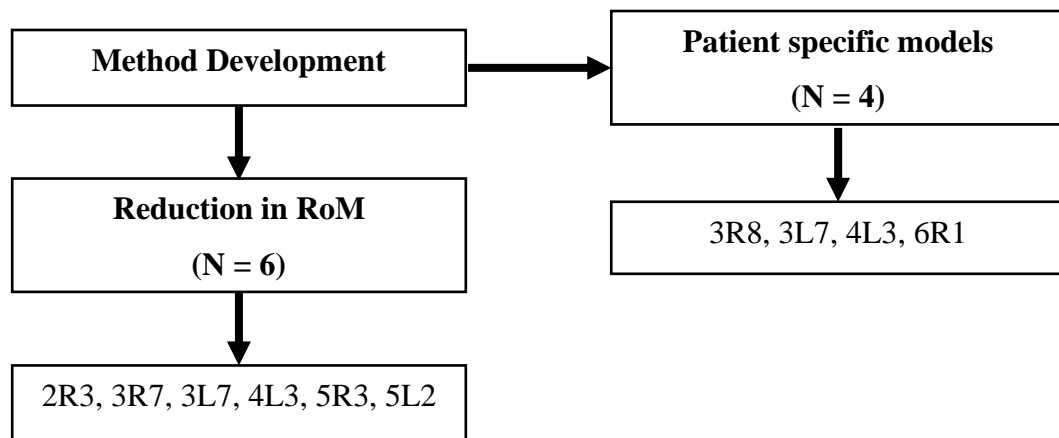


Figure 68 Study design for two gait studies, including models used to generate each

The method development (Section 6.2.1) was carried out with the intention of both studies being carried out on all eight haemophilic ankles. However, between the collection of the most recent MRI sequences, and the gait data capture two of the patient cohort had undergone ankle arthrodesis. The reduction of range of motion study was carried out before the patient gait data was captured, however it was known that gait data would not be available for ankle 1R or 2L as these had undergone arthrodesis – hence these not being modelled in either study.

Arthrodesis is a standard surgical management of end-stage HA; although known to improve joint pain related to HA, it decreases functional mobility and has been associated with secondary hindfoot arthritis as well as subtalar degeneration (Sackstein, Cooper and Kessler 2021). For these reasons, it was decided that the biomechanical data of the patient with a bilateral presentation, with one fused joint, may be influenced by the fusion and not an

appropriate indicator of true joint function, hence gait data was not collected for 2R. This is of most importance when considering if the function is related to a morphological limitation.

In studies that have considered barefoot and in-shoe gait in the same group (Keenan *et al.* 2011; Zhang, Paquette and Zhang 2013) there have been mixed results on the influence of footwear. The two control groups used in this FEA were different cohorts; the in-shoe, and barefoot control groups were both collected for previous studies, meaning the influence of the shoe choice in haemophilic gait data capture could not be ascertained. In-shoe data capture is important in haemophilia, as in local clinical practice, PwH are not recommended to walk barefoot. Barefoot walking has been linked to joint bleeds, hence, collecting data barefoot would be unethical due to this increased risk.

For this reason, it is important to have an in-shoe control group to understand the influence of HA on the joint kinematics. The control group consisted of 36 healthy adult males, who underwent screening prior to inclusion in the study; gait was collected for the left ankle of each participant, and the results were provided for this study as an average of that non-diseased cohort. The gait data for the PwH was originally collected as part of an intervention study (LASERHAEM), investigating the difference between conventional sports shoes and an adapted shoe, to understand if this would reduce the risk of bleeds. The data provided was for the same conventional sports shoe for all participants.

In both the non-diseased control cohort, and patient cohort, each participant carried out self-selected walking speed trials up and down a 12 meter platform (Wilkins 2021), these were repeated until there were five successful trials for postprocessing.

As is standard for in-shoe gait data collection the shoes had holes cut into them so that the biomechanical marker clusters would attach to the skin. The model used for this biomechanical analysis was a single segment model, where the foot is treated as a single rigid segment. This is standard in data collection for ankle biomechanics, however, does limit the knowledge at which joint in the ankle the motion is occurring. For the purpose of these finite element models, it is assumed that all plantar-/dorsi-flexion is occurring at the tibiotalar joint.

The kinematic model is built with the assumption of healthy muscles, as EMG data was not collected during gait, and has not been reported for a haemophilia cohort. The assumption of healthy muscles is known to be incorrect and is a limitation of the models developed, however, the impact will vary depending on the patient and the degree of joint disease.

### 6.2.1 Method development

In order to carry out the two different comparisons (Figure 68), a method was developed to generate an arbitrary simplified gait. This allowed for troubleshooting the applications of complex boundary conditions. The models were generated following the protocol developed in Chapter 3, with one additional step to offset the tibial components from the talar components by 1 mm. This was carried out in ScanIP before the smoothing processes. Without this additional offset the cartilage smoothness was not appropriate for the motion required in these quasi-dynamic models.

These models have been coined quasi-dynamic, as they run through the multiple points of stance phase in one simulation, rather than multiple static models per ankle, meaning any influence of the relative motion between the points in stance phase is accounted for. This is not a dynamic model as it does not take into account inertia. The movement is defined through a series of rotations and loads to rotate and align the tibia at each point in stance phase based on plantar-/dorsi-flexion angles. Each point in stance phase required a movement step and a loading step to be separately defined using a combination of loading and boundary conditions.

Despite the smoothing carried out to improve cartilage motion, it was also necessary to offload the model after the load was applied and before moving to the next point in the gait cycle. This was trialled using two methods in the method development. Loading and offloading in one step, using an amplitude cycling from 0 to 1 to 0 magnitude of the load; and using separate steps for the load and offload, was attempted. This method using separate steps showed more reliable results, hence, for consistency across all models this was used for the main gait studies.

An appropriate coordinate system was required to allow for the conditions in each of these steps to be set up (Figure 69); this coordinate system was defined with the z axis acting vertically through the tibia at the start point of the simulation. The coordinate system was located at the approximate centre of rotation of the tibiotalar joint, and was used to define a reference point for the application of loads and boundary conditions (Figure 69).

The centre of rotation of the talus moves throughout the gait cycle, however, this was simplified to remaining in one point, approximately located where the sinus tarsi would be, for the purpose of this simulation. The sinus tarsi is the approximate location of the centre of rotation of the tibiotalar joint (Baxter *et al.* 2012). As this coordinate system was used to define the rotation, it was aligned so that the rotation would be correctly defined. For each model the x axis was set up across the width of the talus, and the z directly up through the tibia.

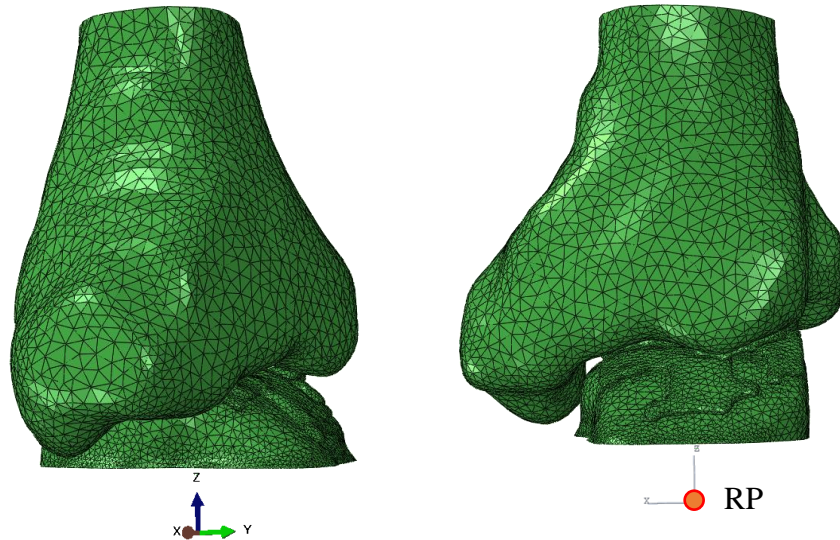


Figure 69 General view (left) and frontal projection (right) with coordinate system and reference point (RP) shown

The reference point at the centre of rotation was kinematically coupled with the top surface of the tibia (Figure 70). This coupling means that any load or boundary condition applied to this reference point was propagated to that top node set, this represents a similar loading condition to the static models, but mitigates the additional modelling complexities the rotation may cause.

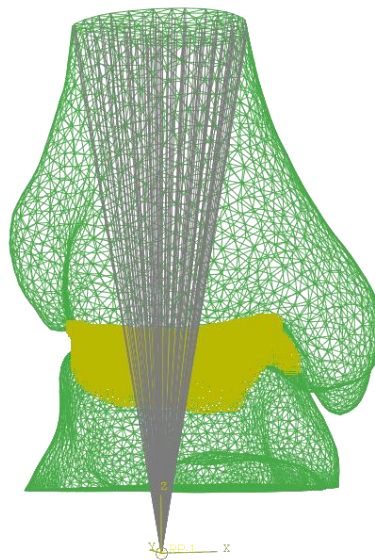


Figure 70 Kinematic coupling between reference point and top surface of tibia

The reference point was utilised for the rotations and loads, examples of the boundary conditions applied to this point in the rotation and loading steps are seen in Table 27, where  $A$  is an arbitrary displacement to initiate contact. This is required, because of the offset applied to these models.



The joint angle,  $\theta$ , varied depending on the gait data inputted, and was defined around the  $x$ -axis, as this was the axis of rotation defined by the coordinate system to represent plantar/dorsiflexion. This motion is where the reduction is thought to occur in HA (Soucie *et al.* 2004).

Table 27 Example boundary and loading condition for the rotation and loading steps, where  $A$  is displacement to make contact  $\theta$  is joint angle, in radians, and  $F$  is force calculated based on patient weight. Loads in tibial axis direction follow the nodal rotation from rotation step

Step	Displacement			Rotation			Load in the tibial axis direction		
	x	y	z	x	y	z	x	y	z
<b>rotation</b>	0	0	-A	$\theta$	0	0	free	free	free
<b>load and offload</b>	0	0	free	Fixed at current position			free	free	load = 0 to F Offload = F to 0

Where the rotation was fixed at current position in the loading step, this ensured that no additional rotation was allowed in the loading step, but that it did not return to the original position. A similarly important consideration was that the loads and boundary conditions follow the nodal rotation, so when the tibia has moved to the new position, the loads are applied based on these new positions.

### 6.2.2 Reduction of Range of Motion

Varying degrees of loss of range of motion (RoM) have been cited in literature, with up to 80% reductions seen (Gamble *et al.* 1991). To investigate this, the first study used maximum plantar- and dorsi-flexion from non-diseased barefoot gait data, and applied two reductions in RoM: 50% and 80% to represent the extremes of RoM reduction in haemophilia. Both maximums were around 14 degrees, giving reduced values of 7 degrees and 2.8 degrees for comparison. The simulations were also run through midstance, however as it was unclear if this was impacted by the altered haemophilic gait, this was kept the same for the three RoMs.

The ground reaction force (GRF) was not used from the non-diseased barefoot biomechanical data, instead the loads applied at the three points were simplified to be kept the same percentage patient bodyweight as the static analysis developed in Chapter 3. This was carried out to ensure this analysis was considering the RoM as an independent variable.

The aim of this RoM reduction study was to determine if there were changes in the contact pressures with reduced RoM that might suggest it is a pain relief mechanism, hence the forces being maintained for the three points.

The six ankles were simulated through the three points, giving 18 RoM reduction comparisons. The peak and mean contact stresses were extracted for the tibial and talar cartilage components separately, and the percentage area in contact was also calculated for the two cartilage surfaces separately.

No statistical analysis was carried out on this data, as it was primarily intended for proof of concept that different gait inputs would influence contact area and contact pressures. The changes in contact areas and pressures were calculated between the non-diseased and the 80% reduced RoM, with checks that the 50% reduced RoM fit within the expected trend. One ankle did not simulate at the non-diseased RoM, hence was excluded from the values reported in the results section.

### 6.2.3 Haemophilic gait

Patient specific gait data was collected for two of the five PwH, covering three of the anticipated five ankles. Static modelling included eight ankles, however three were excluded due to ankle arthrodesis between final MR sequence collection and biomechanical data capture. The final two ankles were not collected due to the patient opting out of research data capture during the Covid-19 pandemic. One additional patient had gait data collected, and appropriate MR images; hence, were included in this study. Therefore, gait data was available for four haemophilic ankles from three PwH, and an average calculated from a non-diseased control group (Figure 71).

The models used in the reduction of range of motion study were repurposed with the patient specific gait data. To give a non-diseased control, one MRI sequence from the control group in Chapter 2 was segmented and built following the protocol in Chapter 3, with the additional offset for smoothing. Due to the cohorts of the two control groups differing, this control gait data was not specific to the ankle in the control MRI.

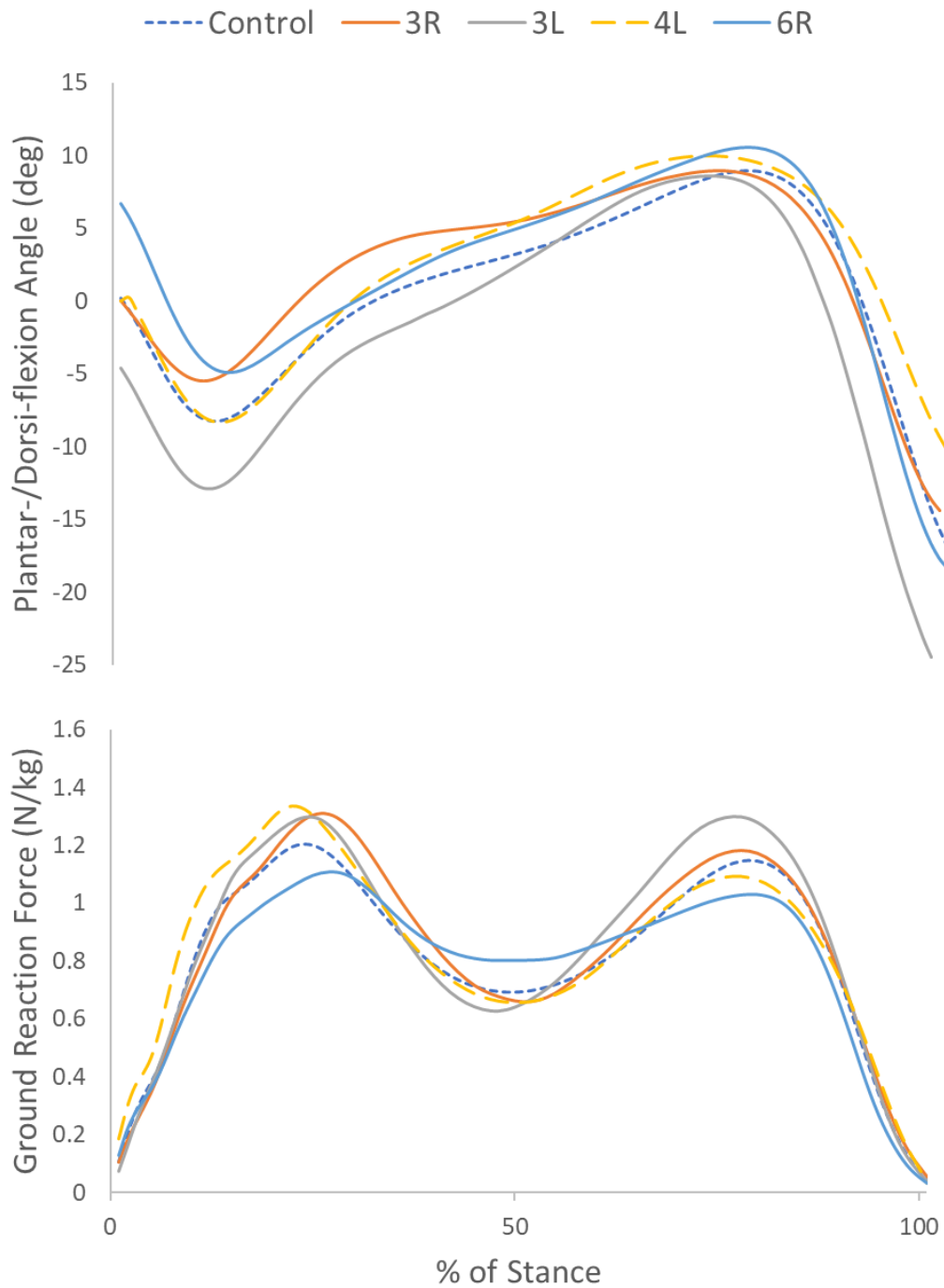


Figure 71 Gait data collected in shoe from haemophilic ankles, and control group average

The ground reaction forces in Figure 71 were used to calculate the load applied to the ankle model in the loading step for each point in the gait cycle. Each model was simulated through the patient specific gait, with joint angles and GRF used to simulate patient specific RoM and loading conditions. The bodyweight of each patient at the time of imaging was used in the calculation of the loads in Table 28.

Table 28 Load (N) applied to gait model for each haemophilic ankle, calculated from GRF

	<b>Heel Strike</b>	<b>Flat Foot</b>	<b>Mid Stance</b>	<b>Heel Off</b>	<b>Toe off</b>
<b>Control</b>	79.27	678.70	510.32	837.83	30.05
<b>3R</b>	73.77	598.12	465.81	813.26	37.68
<b>3L</b>	53.44	658.54	460.76	938.08	28.19
<b>4L</b>	125.68	720.54	441.98	705.20	22.23
<b>6R</b>	117.60	806.02	740.24	946.00	28.44

The control gait data was used on both the control ankle model, and the four haemophilic ankle models. Where the haemophilic ankle models were simulated through the control gait, the loading conditions reflected the control GRF, corrected for patient bodyweight.

The focus of the results in the gait analysis both in the method development and the reduction of RoM studies was on the cartilage contact pressures. For the paired tests in the patient specific gait models, the influence on VMS in the bones was also considered.

Kolmogorov-Smirnov tests were used as non-parametric paired samples tests, to compare each ankle run through non-diseased gait and patient specific gait (3R, 3L and 4L). This test type was used due to the volumes of data extracted for the bone VMS and cartilage contact pressures not being normally distributed. These paired tests were carried out at flat foot, mid stance, and heel off due to these being deemed the most clinically relevant.

Intra-subject analysis was carried out qualitatively, assessing how the contact pressures and areas changed through stance phase progression. The inter-subject analysis followed a similar methodology, to assess the influence of the joint angles and loading conditions at each stage of stance phase.

## 6.3 Results

### 6.3.1 Method Development

As well as the loading using an amplitude being unreliable in some models, it gave different results from loading and offloading in two separate steps (Figure 72 to Figure 78). With the magnitude of the contact pressures differing throughout stance phase; regions in black are above the values in the scale.

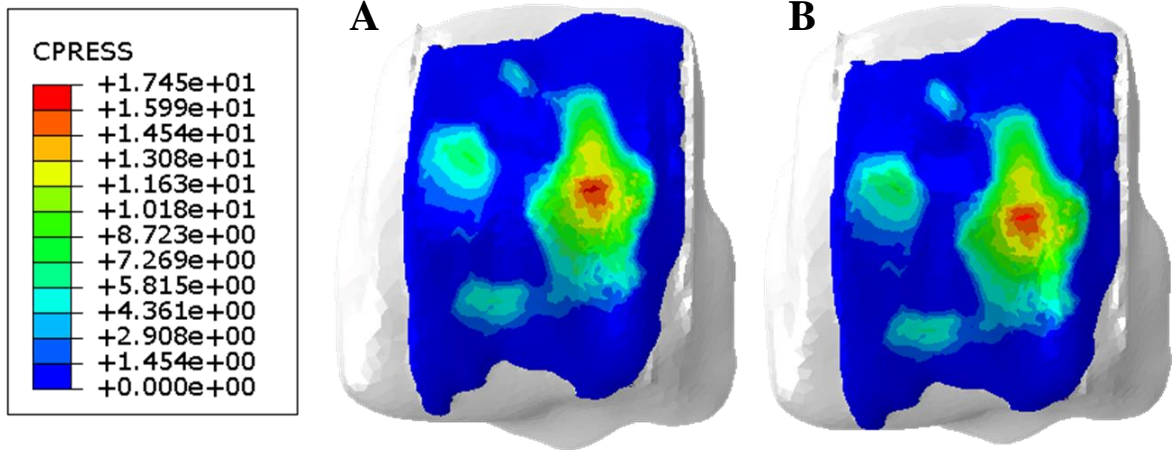


Figure 72 Cartilage Contact Pressure (MPa) distribution before load is applied at maximum dorsiflexion. A) Load and Offload in separate time steps, and B) Ramping load in one time step

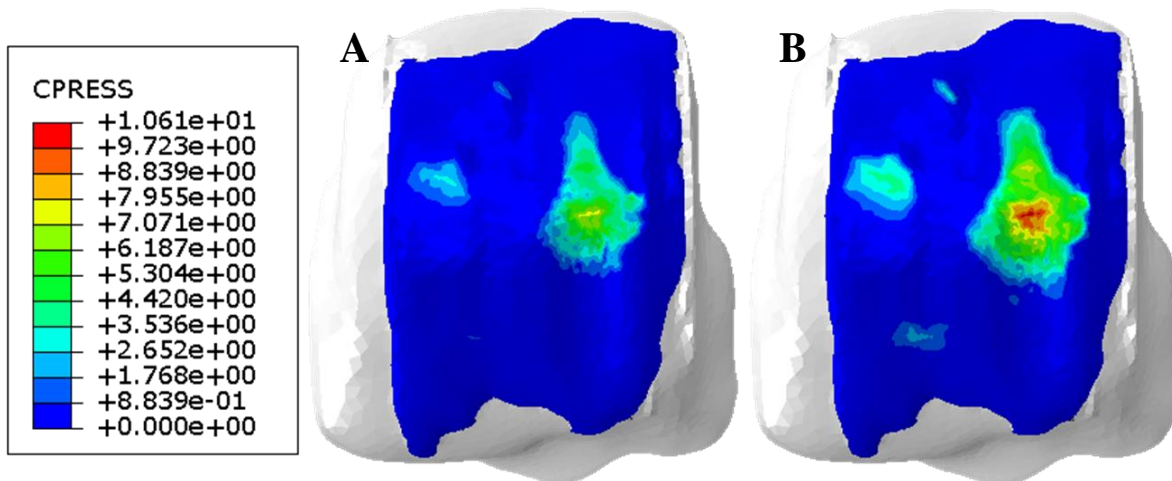


Figure 73 Cartilage Contact Pressure (MPa) distribution at maximum dorsiflexion. A) Load and Offload in separate time steps, and B) Ramping load in one time step

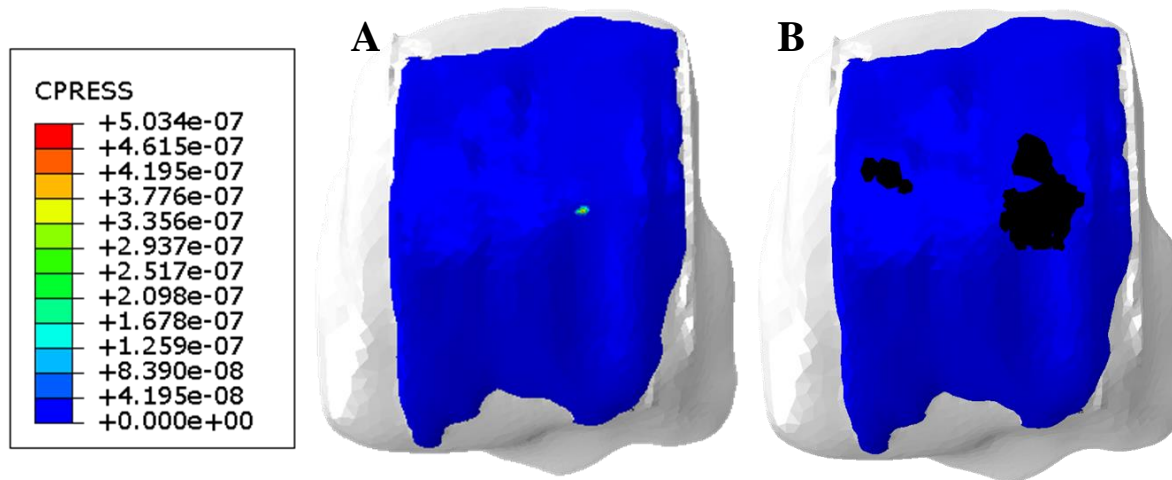


Figure 74 Cartilage Contact Pressure (MPa) distribution after maximum dorsiflexion offload. A) Load and Offload in separate time steps, and B) Ramping load in one time step

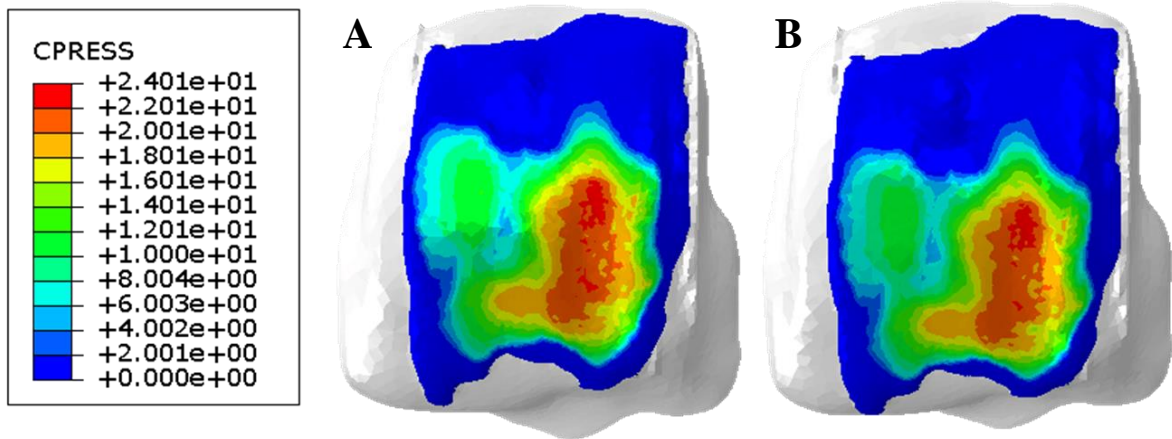


Figure 75 Cartilage Contact Pressure (MPa) distribution before load is applied at mid stance. A) Load and Offload in separate time steps, and B) Ramping load in one time step

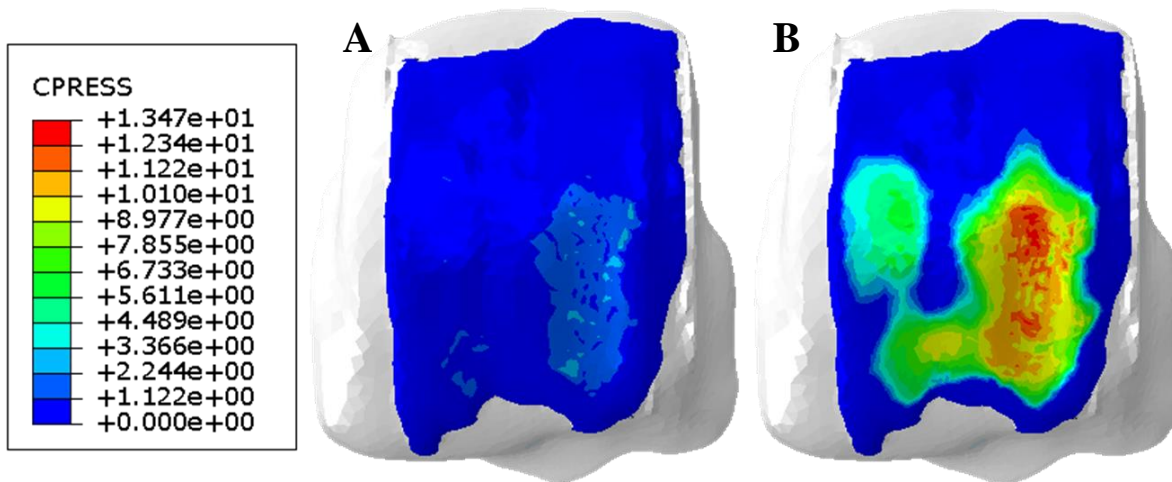


Figure 76 Cartilage Contact Pressure (MPa) distribution at mid stance. A) Load and Offload in separate time steps, and B) Ramping load in one time step

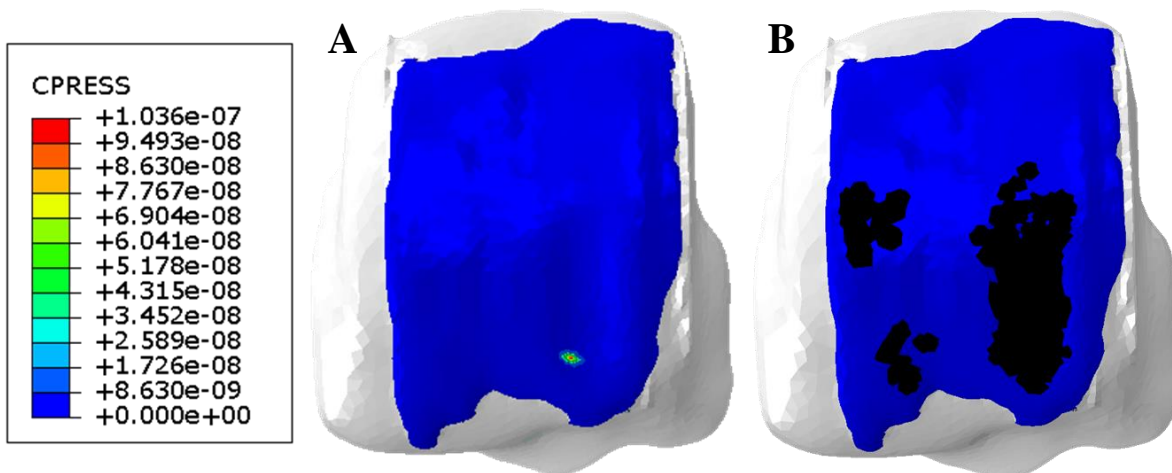


Figure 77 Cartilage Contact Pressure (MPa) distribution after mid stance offload. A) Load and Offload in separate time steps, and B) Ramping load in one time step

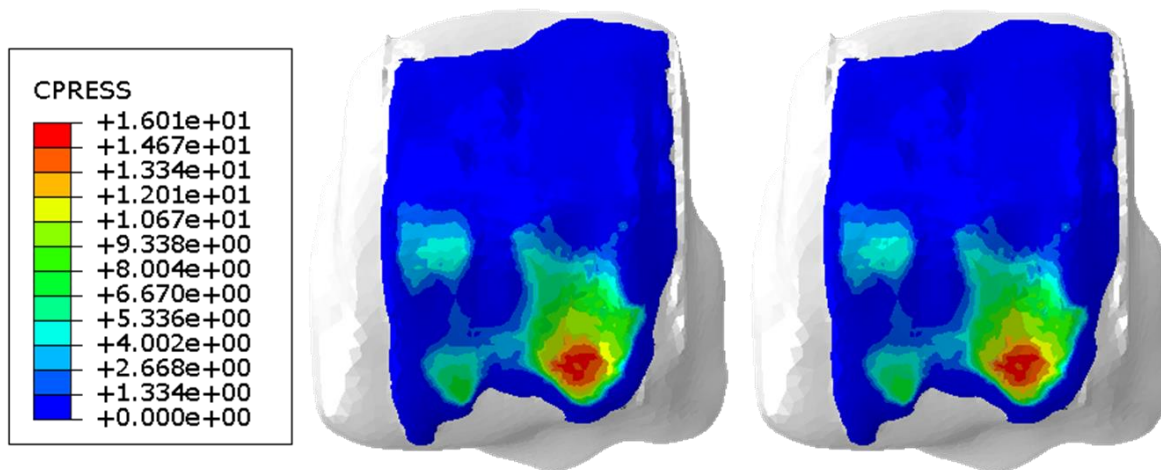


Figure 78 Cartilage Contact Pressure (MPa) distribution before load is applied at maximum plantarflexion. A) Load and Offload in separate time steps, and B) Ramping load in one time step

These differences highlighted that the loading was not being accurately applied using the ramping load in one timestep. The contact pressures were increased with the ramping load, and continued to increase beyond the point in the timestep the maximum load was defined to occur in the model setup. As well as this, the offload (Figure 74 and Figure 77) was clearly not behaving as anticipated; therefore, separate steps were used for the consequent studies.

### 6.3.2 Reduction of Range of Motion

The changes in contact pressures and contact areas were recorded for the individual models between the non-diseased and 80% reduced RoM. Table 29 shows the changes calculated as percentage decrease in contact pressure, and increase in contact area, as these were the anticipated changes with reduced RoM; results that did not behave as anticipated are in red.

The same trends were seen between the non-diseased and 50% reduced RoM results, but to a smaller magnitude. The similarities between the 50% and 80% reductions in RoM can be seen in Figure 79 and Figure 80, where the redistribution of stresses is seen.

Table 29 percentage decreases in contact pressure (peak and mean), and increases in contact area between non-diseased gait and 80% reduced RoM. Including averages calculated for each output. Those that did not behave as expected are highlighted in red

	Tibial Cartilage			Talar Cartilage		
	Peak	Mean	Area	Peak	Mean	Area
	<b>Dorsiflexion</b>					
2R	65.09	124.80	217.02	131.73	190.04	148.35
3R	-15.34	-12.96	-8.50	-0.84	12.47	-10.05
3L	215.39	308.60	236.15	188.74	198.26	288.77
4L	45.98	92.49	117.75	183.34	72.82	58.53
5R	-49.13	-44.15	-40.54	-46.09	-38.81	-51.47
Average	52.40	93.75	104.37	91.38	86.96	86.83
	Tibial Cartilage			Talar Cartilage		
	Peak	Mean	Area	Peak	Mean	Area
	<b>Plantarflexion</b>					
2R	27.12	105.71	68.32	13.41	62.67	131.82
3R	18.72	76.69	81.73	15.12	117.36	67.49
3L	67.58	84.21	172.26	84.23	90.13	212.79
4L	137.45	135.92	137.96	92.13	133.76	160.32
5R	-29.72	-39.55	-35.27	-41.59	-44.63	-44.42
Average	44.23	72.60	85.00	32.66	71.86	105.60

The changes were highly variable between individuals despite the same reductions being applied, and the same loads being used for each ankle. As well as the large changes in contact pressures and areas, there were interesting changes in locations of the areas in contact in both dorsiflexion (Figure 79), and maximum plantarflexion (Figure 80). These changes in contact distribution may explain why some ankles oppose the anticipated trends.

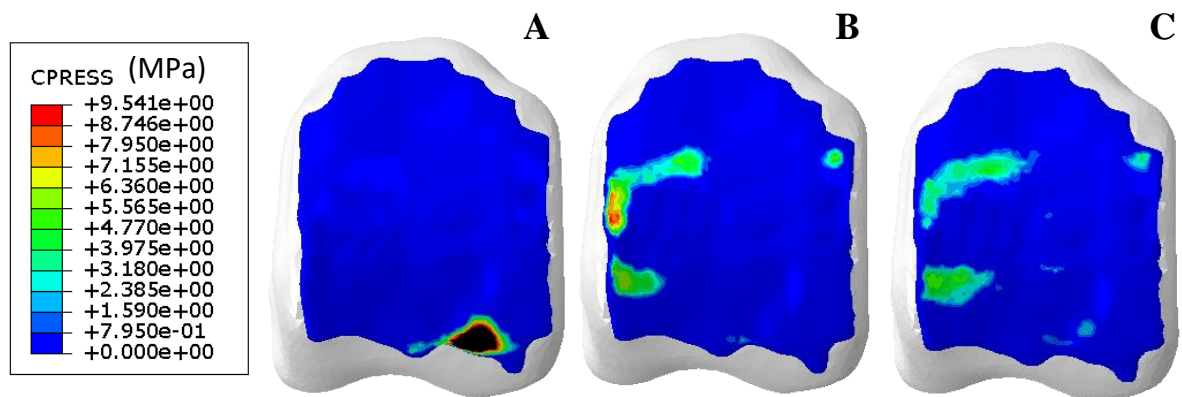


Figure 79 Change in contact distribution at maximum dorsiflexion between (A) non-diseased, (B) 50% reduced RoM and (C) 80% reduced RoM



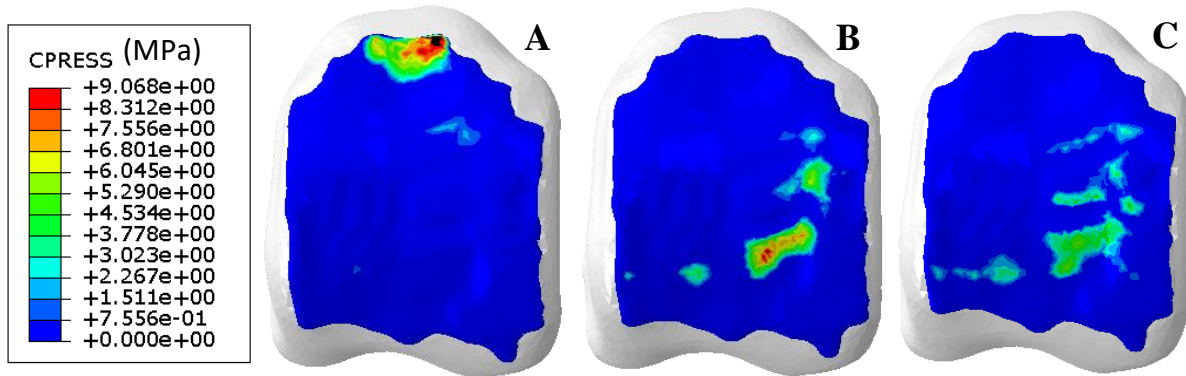


Figure 80 Change in contact distribution at maximum plantarflexion between (A) non-diseased, (B) 50% reduced RoM and (C) 80% reduced RoM

### 6.3.3 Haemophilic gait

The patient specific gait data, shared for use in these studies, showed that the ankle RoM in this patient cohort does not see the same reductions as cited in literature. Table 30 shows the joint angles used as the input data for each patient at the five points in the gait cycle modelled. Each ankle had a slightly adapted walking strategy, however the differences are variable at each point in the gait cycle, with the suggestion that some patients may tend more towards plantarflexion (3L), and others to dorsiflexion (6R).

Table 30 Joint Angles (degrees) at each point simulated in the gait cycle

	Heel Strike	Flat Foot	Mid Stance	Heel Off	Toe Off
<b>Control</b>	0.216	-8.229	3.442	8.975	-16.790
<b>3R</b>	0.658	-5.471	5.602	8.959	-14.370
<b>3L</b>	-3.218	-12.604	1.432	8.579	-24.443
<b>4L</b>	0.246	-8.352	5.960	10.000	-11.044
<b>6R</b>	6.681	-4.923	4.790	10.547	-18.344

The paired non-parametric tests showed that there were significant, not systematic, differences between the control gait and patient specific gait in all talar cartilage contact pressures ( $p < 0.005$ ) and eight of the nine tibial cartilage contact pressures; there was no significant difference between the tibial cartilage outputs at midstance in 3R ( $p = 0.193$ ). The bone results were a little more variable, with significant differences in VMS in seven of the nine tibias, and only two of the tali; the tibial stress in 4L was not significantly different at midstance or when plantarflexed ( $p = 1$ ); the talar stress in 3R at dorsiflexion, and all three points of gait in 3L and 4L, were not significantly different ( $p = 1$ ).

These statistically significant differences in contact pressures depending on gait input data confirmed that this is a valuable output to consider when comparing the patient specific gait. While the non-significant data in the bone stresses may infer these bone outputs are less influenced by the input data. The comparisons between the five models at each point in the gait cycle was a qualitative analysis rather than any further statistical analysis (Figure 81 to Figure 86). 6R did not complete the rotation required to simulate heel off, therefore could not be compared at that point.

The contact distribution was assessed as the ankles progressed through gait (Figure 81), and at each point in the gait cycle with respect to the other ankles (Figure 82 to Figure 86). This comparison at each point in the gait cycle was of interest, due to some ankles having similar joint angles, therefore, any large differences in distribution in these ankles may highlight a relationship with morphology.

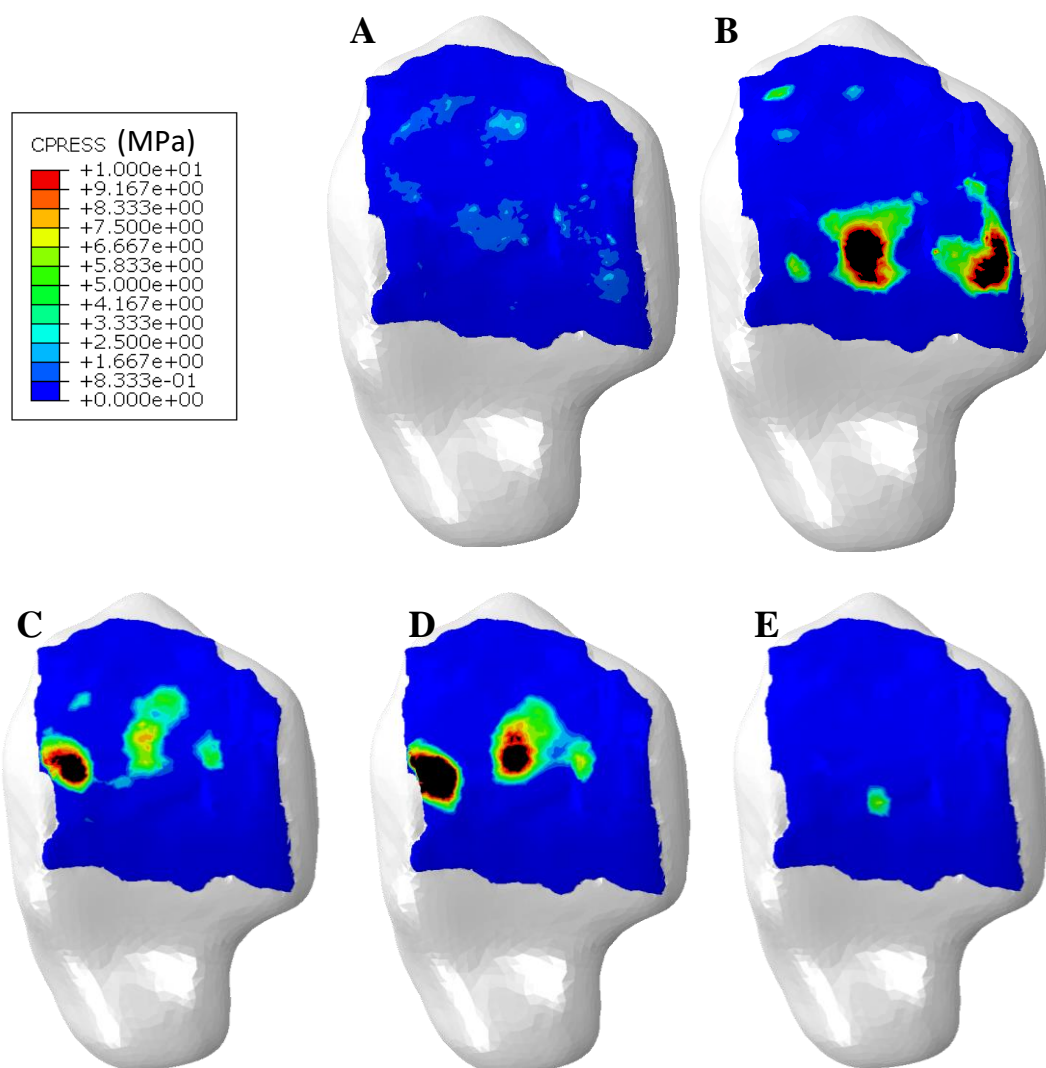


Figure 81 Change in contact distribution between (A) Heel Strike, (B) Flat Foot, (C) Mid Stance, (D) Heel Off and (E) Toe Off in 4L

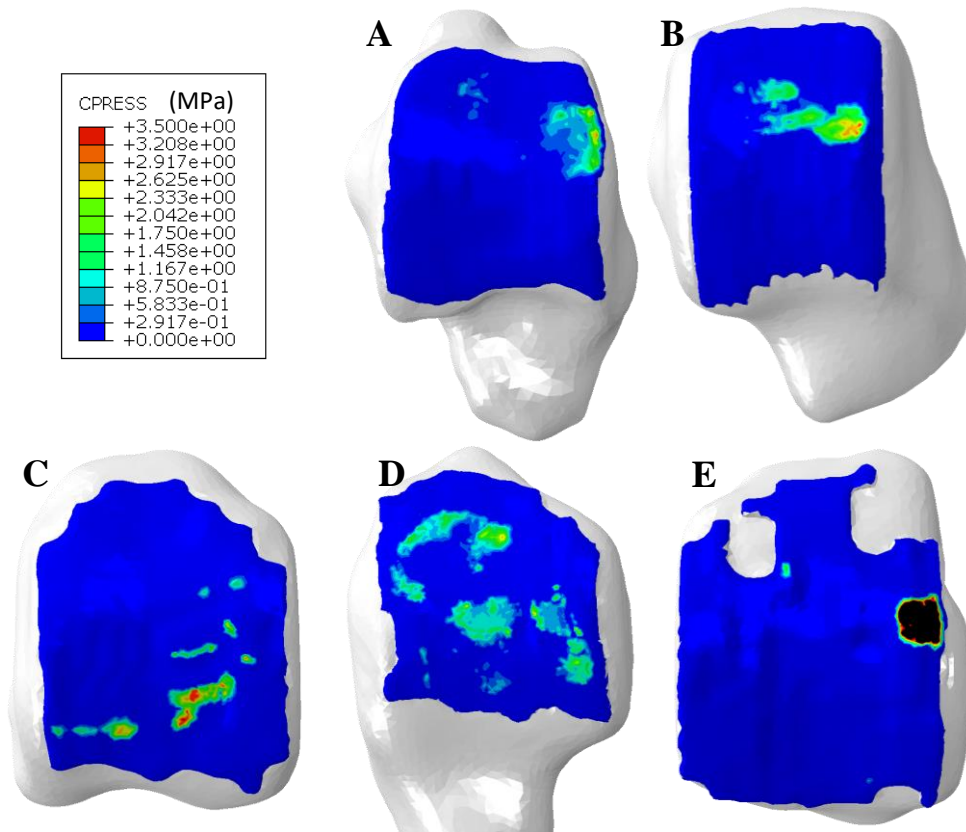


Figure 82 Contact distribution at Heel Strike in (A) Control, (B) 3R, (C) 3L, (D) 4L, and (E) 6R

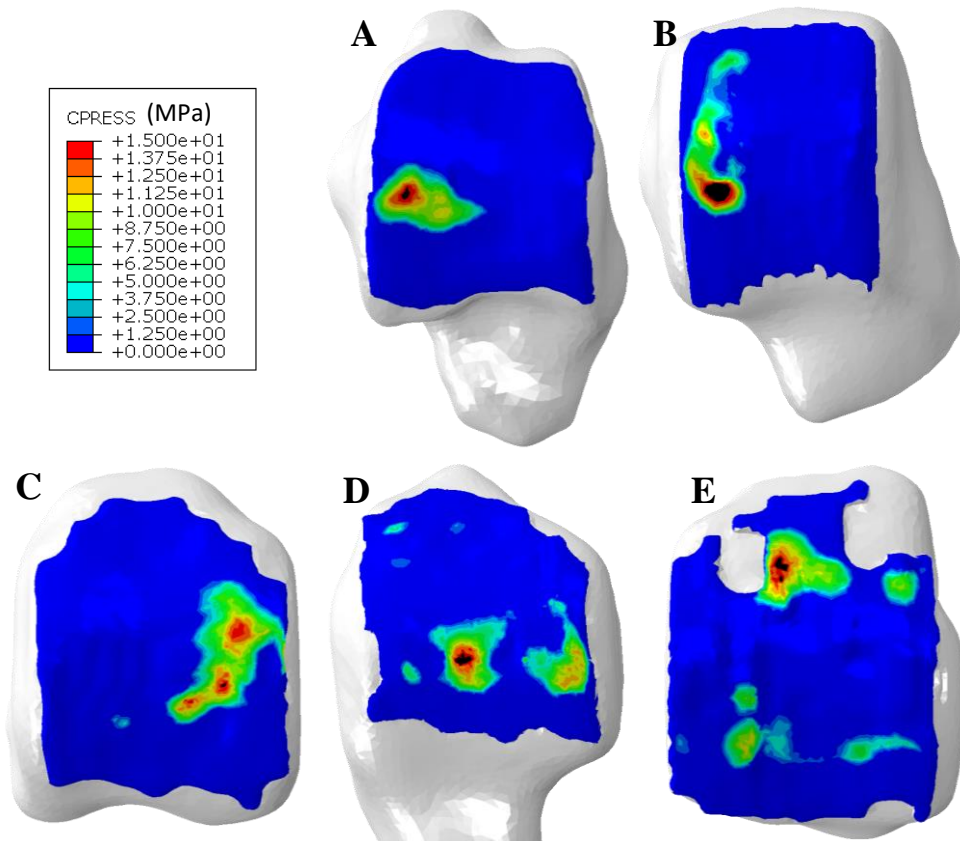


Figure 83 Contact distribution at Flat Foot in (A) Control, (B) 3R, (C) 3L, (D) 4L, and (E) 6R

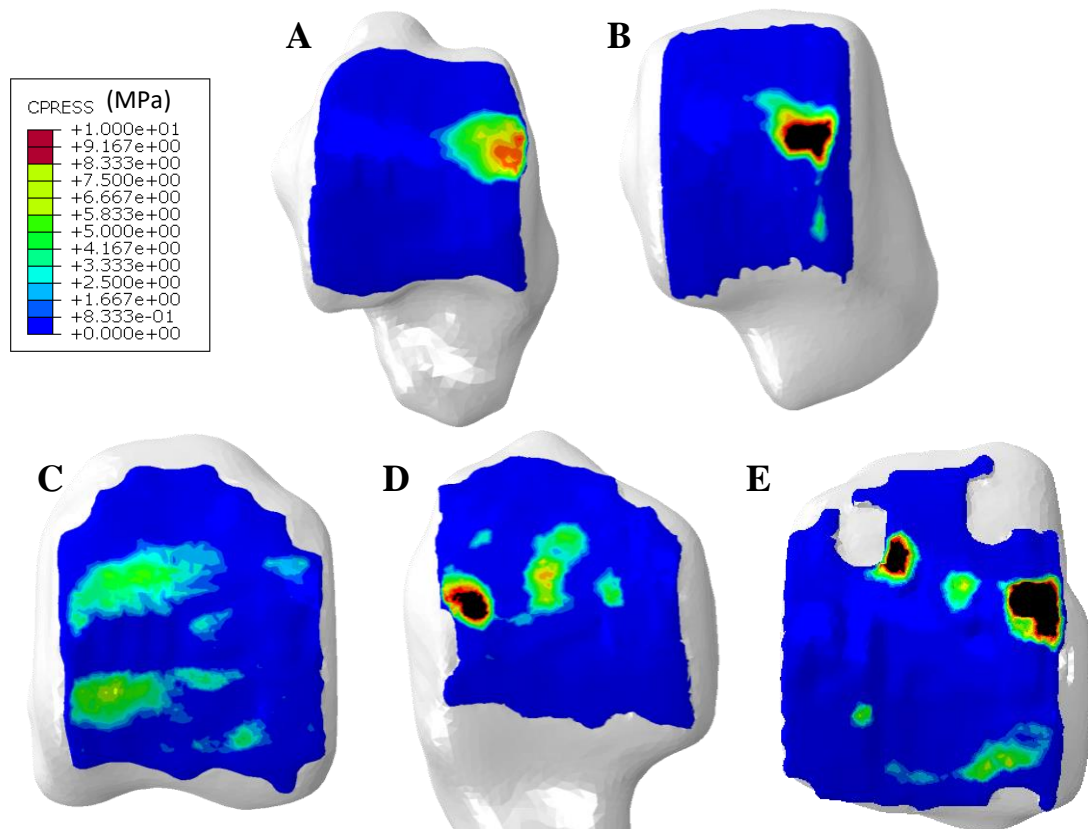


Figure 84 Contact distribution at Mid Stance in (A) Control, (B) 3R, (C) 3L, (D) 4L and (E) 6R

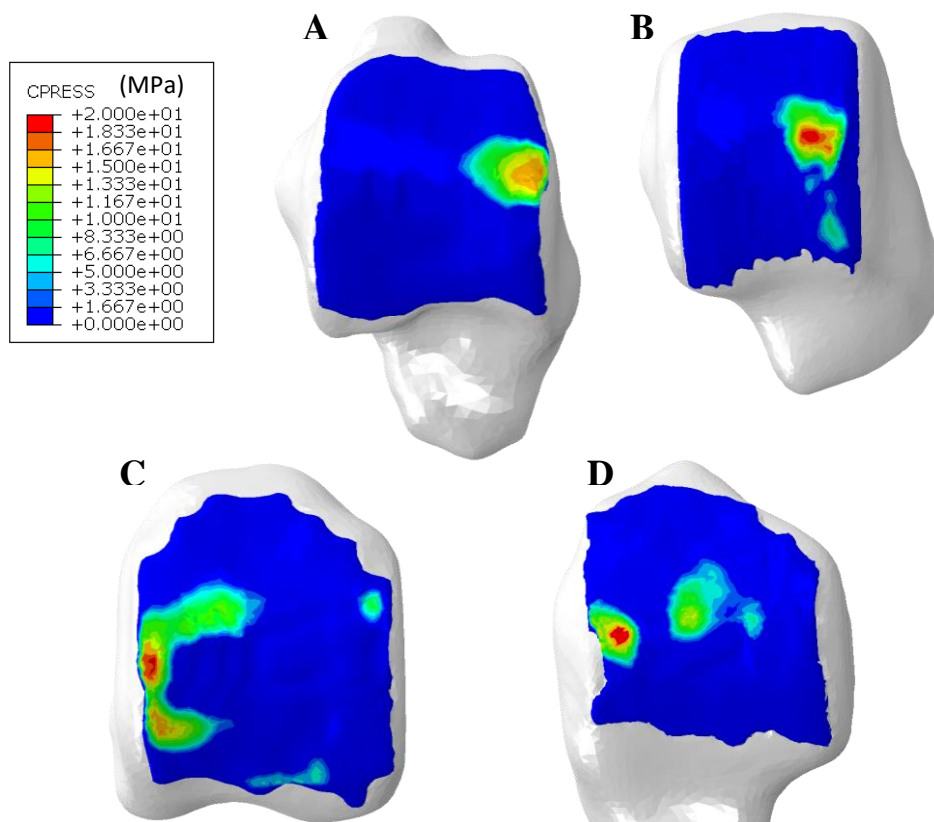


Figure 85 Contact distribution at Heel Off in (A) Control, (B) 3R, (C) 3L, and (D) 4L

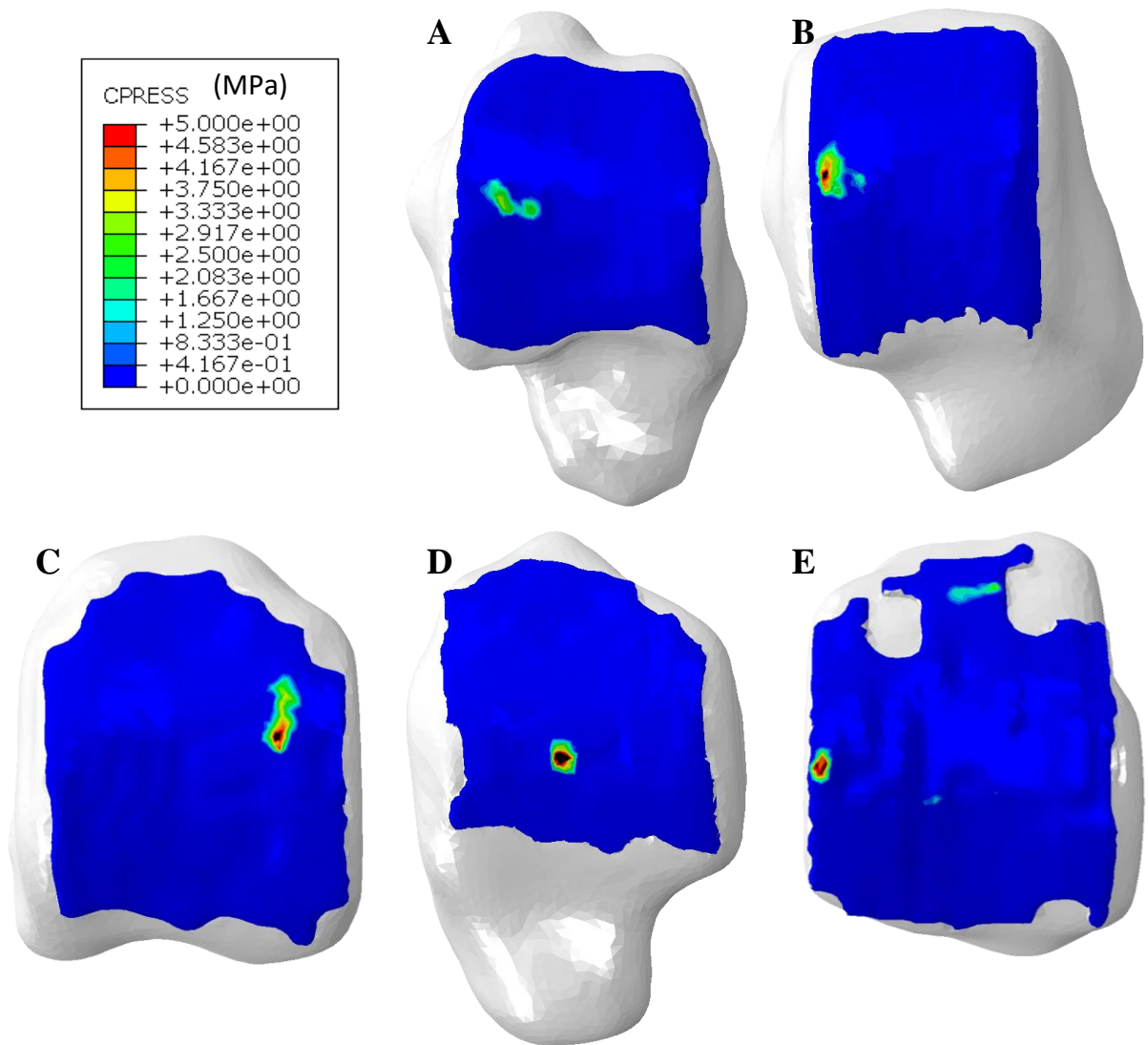


Figure 86 Contact distribution at Toe Off in (A) Control, (B) 3R, (C) 3L, (D) 4L, and (E) 6R

## 6.4 Discussion

The gait analysis carried out on the patient cohort was delayed almost two years due to the Covid-19 pandemic, meaning there were large increments of time between the imaging date and the biomechanical data capture for some patients. This, in turn, makes it more difficult to ascertain a relationship between gait adaptation and joint morphology, as there may have been further morphological changes since the last MRI sequence used to build the model.

Despite this, it was demonstrated that biomechanical data can be successfully incorporated into finite element models, to understand the implication of adapted haemophilic gait on the cartilage contact pressure. It was shown in the paired statistical analysis, comparing haemophilic gait and control gait in the same ankle model, that the model inputs were more likely to give statistically significant outputs in the cartilage contact pressures ( $p < 0.005$  in 17 of the 18 tests) than bone VMS ( $p = 1$  in 9 of the 18 tests).

### 6.4.1 Reduction of Range of Motion

The arbitrary reductions in range of motion showed that the decreased RoM tended to decrease the peak and mean contact stresses in both cartilage components, while the area in contact increased. These findings supported the idea that the decreased RoM might be an adaptation strategy to relieve pain.

One ankle opposed these findings in all outputs, and a second ankle opposed them at dorsiflexion. These unexpected findings may relate to the different pressure distributions that were seen with the reduced RoMs. With the 50% reduction completely different areas of the cartilage were in contact at both dorsi- and plantar-flexion.

With this small sample size, it was not possible to determine if the difference in these two ankles was morphological, as there were not enough other points of comparison, however the findings did show that different joint angles had a large influence on all aspects of contact.

The redistribution of contact pressure due to the presence of SBCs in models was shown in Chapter 5. Two of the five ankles in the reduction of RoM study had SBCs present in the MRI sequence; both of which had both tibial and talar SBCs in the MRI sequence used for the gait model. Of these, one (3R) opposed the trend in dorsiflexion, while the other (2R) followed the trend in both dorsi- and plantar-flexion. The difference between these ankles was the volume of cystic tissue, which was much larger in 3R; however, due to the comparison only being possible between two ankles, it was not possible to ascertain a relationship between SBC volume and the RoM reduction finding.

#### 6.4.2 Haemophilic gait

In the reduction of RoM study, the GRF was kept constant throughout the gait cycle, just to consider the changes due to decreased joint angles. In reality, both the joint angle and GRF change throughout gait. It was seen that the GRF was as variable between ankles as the joint angle, and the two did not directly correlate. Three of the haemophilic ankles had higher GRF than the control at flat foot, of these, two were also higher at heel off. Should the haemophilic gait be an adaptation to relieve pain, it would be expected that PwH would adapt their walking strategy to decrease GRF. The flattened GRF curve in 6R could not be fully understood due to the simulation at heel off not completing the rotation step. This appeared to be due to an area of high stress as the joint reached around 70% of the rotation, which occurred regardless of the efforts to counteract this.

At flat foot, mid stance, and heel off, there were at least two models with similar joint angles, where the influence of morphology could be investigated. At flat foot, the control joint angle was 0.123 degrees less than ankle 4L; despite these similar inputs (with force input difference less than 50N), there were large differences in contact distribution. The same was seen at midstance when comparing 3R and 4L, where the joint angle was 0.358 degrees greater, and force 20N less, in 4L. At heel off, the control could be compared with both 3R and 3L; the differences in inputs were largest between 3L and control. The joint angle was reduced by 0.396 degrees in the haemophilic ankle, however this ankle also had a 100N greater force. This was reflected in higher contact pressures, however the contact distributions in both varied greatly. The results highlighted the role that both joint forces and joint angles play in the changing pressure distributions, but also suggest that there are morphological reasons for these changes in distribution.

Interestingly, as stance phase progressed, the contact pressures appeared to move in a medial-lateral direction, rather than the areas of high pressure being in the anterior/posterior regions of the cartilage. This finding could relate to the morphological findings that the flattening of the haemophilic talus tends to occur in these regions. If areas of high stress are regularly occurring in these regions it may initiate the tendency to collapse.

Conversely, these regions may be experiencing these higher pressures due to the morphological change that has already occurred, as it was seen that talar flattening increased contact pressures

in the static models. Although this would not directly support the limitation theory, but would increase confidence in the finding in the static models that there is a link between structure and joint outcomes in the ankle.

The limitation theory of adapted gait was based off osteophyte formation at the anterior tibiotalar articulation restricting the relative motion between the two (Bauer, Breda and Hardy 2010; Vaseenon and Amendola 2012). However, that is not seen in this particular cohort, as none of the ankles have significantly reduced RoM.

The small sample size limited what was possible to do with demonstrating a relationship between morphology and gait outputs, however, the work done in developing a novel method to implement patient specific gait into finite element models has shown with the right sample size it would be possible to develop a deeper understanding of their relationship.

### 6.4.3 Limitations

There are some limitations to the MSK model used, that lead to assumptions in this FE modelling method. The model assumes normal muscle forces, while in PwH these muscles may be atrophied due to disuse. Despite this, the influence of joint angles could still be investigated. The single segment foot model does however, limits the information regarding the movement of individual bony segments. The use of this model was validated by Richard Wilkins for the original thesis data was captured for (Wilkins 2021). The single segment foot model meant that the FE models assume all plantar-/ dorsi-flexion is occurring in the tibiotalar joint, which is not representative of the true motions of the ankle, and may mean there is some overestimation of joint angles. R Wilkins' (2021) methods also mean there is no barefoot data to ascertain the influence of the conventional sports shoe design of choice on gait in the non-diseased cohort. The analysis is also limited by the postprocessed data provided. There will be intra-subject variability in both the joint angles and ground reaction forces in the five trials per patient due to the self-selected nature of the walking trials, which would be reflected in the average input data used for the models. This data was not provided for all participants, so the influence cannot be commented on, however is available in the appendix for one ankle (Figure 100). This data showed the plantar-/ dorsi-flexion was greater in one trial than the remainder of the trials, which has the potential to skew the average. This average could be especially influential in the non-diseased cohort, where the mean is from 180 walking trials (36 patients, each with 5 repetitions), inter-subject variability in the control group could influence the average, and



misrepresent the non-diseased control gait profile. The original study cited the control sample size was selected to mitigate for this, with 80% confidence in the mean (Wilkins 2021).

## 6.5 Conclusion

This small sample size does not fully answer the question as to whether the adapted gait in haemophilia is a limitation or adaptation, as the two studies have shown both could feasibly be related. The arbitrary reductions in RoM demonstrated that contact pressures were decreased with a restricted RoM, supporting the adaptation hypothesis. While the patient specific quasi-dynamic models have shown there is a feasible connection between structure and function. This was not the anticipated restriction due to osteophyte formation; however, a potential link between increased contact pressures and regions of the talus that tend towards collapse in HA.

# CHAPTER 7

## DISCUSSION AND CONCLUSION

# CHAPTER 7: DISCUSSION AND CONCLUSION

## 7.1 Summary

Findings in this thesis demonstrate there are possible links between the changes in structure and function of the haemophilic ankle, which have potential implications on joint health. The investigations included a morphological analysis, which was uniquely used in conjunction with a longitudinal finite element analysis to assess the impact of the altered talar morphology on joint health over time. These models were then used to assess features of haemarthropathy (HA) such as altered biomechanics and subchondral bone cysts (SBCs), in the aid of further understanding the implication of these features on ankle health in PwH.

The results gathered throughout this thesis highlight the importance of patient specificity in a disease with such variable joint outcomes. Based on these findings, the recommendation is for models to include patient specific geometry and loading conditions as a minimum for understanding consequent joint health. Where disease features such as SBCs exist these must also be included. The models presented in this thesis could further be improved by patient specific material properties, and where data is available this should also be included to provide better insight into bone health.

## 7.2 Implications of Morphology on Ankle Biomechanics

The morphological changes investigated in Chapter 2 demonstrated there was a flattening to the haemophilic talus; talar flattening has been witnessed in other diseases, such as clubfoot, where the implication on patient reported outcome (PROs), joint congruency, and gait have all been considered. The flattening of the talus has been seen to alter the plantar-/dorsiflexion during the stance phase of gait, as well as significantly reduce static range of motion (RoM) (Bach *et al.* 2002; Kolb *et al.* 2017; Shivers *et al.* 2020). Static RoM, also known as passive RoM, is tested by the physical manipulation of the joint, where the dynamic motion does not influence the motion. The reduced ankle plantar flexion during gait appears to reduce the push-off strength of the ankle, resulting in poorer energy economy (Huang *et al.* 2015), this increased energy expenditure could negatively feedback into disease progression if patients consequently decreased physical activity (Timmer *et al.* 2018) which could lead to atrophy of the supporting musculature. Some groups have linked these factors to joint incongruity (Shivers *et al.* 2020). In longitudinal assessment in clubfoot, these changes have been less predictive of PROs such as pain and disability.

For this reason, it was anticipated there would be a link between the morphological changes and biomechanics in the haemophilic gait. The altered gait mechanics (Chapter 6) did not see the extreme reductions of RoM reported in literature; however, the small cohort did allow for some assessment of structure and function.

The morphological measurements of the four haemophilic ankles (3R, 3L, 4L and 6R) were assessed to determine if a link could be drawn between the flatness of the talus, and the change from non-diseased RoM. This was of interest as each of these ankles had a unique morphological response to haemophilic arthropathy; how this influenced biomechanics, and consequent mechanical stresses, was of interest. It was shown in both the morphological analysis (Chapter 2) and chronological FE study (Chapter 4) that extrapolating data within this group was not a reliable method of predicting joint outcomes in the haemophilic group as changes were highly non-linear. Therefore, linking structure and function at individual timepoints may be a better way of expanding knowledge on this subject area.

The neutral standing simulations somewhat showed a relationship between the morphology and magnitude of mechanical stresses, however, did not highlight a significance of the collapse in the medial and lateral regions of the talus. Whereas the patient specific gait models showed there could be a relationship between the morphology and areas of increased stress. As both the morphological changes, and patient gait are unique to each haemophilic ankle, it is likely that the joint health is influenced by both; the degree of which the structure or function dominates this is still unknown, and may be subject specific. Therefore, the analysis cannot yet go as far as to show if the relationship is cause or effect, or both. However, it highlights that there is a relationship between the two warranting further investigation, using higher volumes of patient data, including gait data at multiple timepoints.

### 7.3 Influence of Subchondral Bone Cysts on Joint Health

The finding that the bone outputs were highly influenced by the properties used to represent the SBCs (Chapter 5) meant the relationships discerned between SBCs and bone health could not be deemed significant. However, localised elevated bone stresses have previously been reported in literature (Dürr *et al.* 2004; McErlain *et al.* 2011), and a relationship between SBC presence and altered bone mineral density found (Burnett *et al.* 2019).

The inclusion of segmentation specific SBCs in models assessing joint health is clearly necessary due to the volume, location and shape all influencing model outputs. Previous studies treating size as an independent variable have demonstrated that larger SBCs are more

detrimental to joint health (McErlain *et al.* 2011; Frazer, Santschi and Fischer 2017), while the FE models in Chapter 5 only assessed depth as an independent variable, with volume, shape and location, all changing between the 18 models. SBC depth had significant correlations to bone and cartilage outputs, highlighting the detriment of SBCs closer to the bone surface in the articulating region.

When considering the relationship between SBCs and cartilage health, the complexity lies in the requirement for mechanical loading for cartilage maintenance. Significant changes in cartilage loading can instigate cartilage degeneration (Brand 2005; Andriacchi *et al.* 2004); with abnormal mechanical forces seen to trigger post traumatic cartilage loss through both reduced cartilage thickness (Van Rossom *et al.* 2017) and stiffness (Carter *et al.* 2004). The cartilage thickness could not be quantified in this study due to the resolution of the clinical MRI used; the full thickness of cartilage in the ankle is approximately 1-2 mm (Saltzman *et al.* 2005; Sugimoto *et al.* 2005), therefore changes could be potentially misrepresented when the pixel size is between one quarter to a half of this full thickness, meaning true changes in cartilage thickness may not be accurately represented.

Shape and volume were influential on the contact stresses as the change in contact distribution occurred directly above or below cystic regions, with larger redistribution for larger cysts. Although the statistical analysis showed this was not significant; this is thought to be due to 10 of the 18 models have SBCs present in both bones.

Elevated cartilage pressures are usually associated with cartilage degeneration (Anderson *et al.* 2011b), they have been related to pathological changes at the articular surface found in both human OA and experimental models of joint instability (Li *et al.* 2008; Anderson *et al.* 2011a; Anderson *et al.* 2011b; Buckwalter *et al.* 2013). The non-significant increases in contact pressure when SBCs are present could lead to the conclusion that there is no direct link between SBCs and cartilage degeneration. However, the redistribution of the pressure may have its own detrimental effect, given offloaded regions above and below the location of the SBCs may not have the natural maintenance effect of normal contact pressures.

Within haemophilia, SBCs have the potential to cause damage beyond these degenerative changes, due to the association between elevated stresses and the onset of a joint bleed (Buckwalter and Saltzman 1999). The data from these 18 models does not suggest a direct relationship with either bleed rate or patient reported pain, should these be directly linked with elevated joint stresses. However, could be indirectly linked given the potential for augmented joint health decline, which would in turn elevate patient reported pain.

#### 7.4 Relationship between Altered Biomechanics and Joint Health

In order to fully understand the association between joint health and the altered gait in PwH, more patient information, such as joint health scores, would be required. However, it is seen that both the altered joint angles and ground reaction forces influence the joint contact pressures. When contrasting the stresses experienced by the four ankles simulated through patient specific gait with control gait, the magnitudes varied within the gait cycle; the contact pressure values were much greater at heel off, where the ground reaction forces were the highest, which was reflected in the model loading conditions; this trend was also seen at flat foot and mid stance, which had higher input loads than heel strike and toe off.

When comparing the four ankles, 6R had the highest input value at flat foot, which was reflected in the contact pressure outputs. However, 3R and 4L also had high output values throughout gait, with much lower forces applied to the model.

The joint angle appeared to have an inverse relationship with contact stresses at flat foot, with greater plantarflexion having the lowest contact pressures, while the greater dorsiflexion at mid stance increased the contact pressures. At heel off, where the foot is at maximum dorsiflexion, there was no apparent relationship with the joint angle. The clinical significance of these findings could not be ascertained due to the small sample size available.

The patient specific gait models showed that joints tended to experience high contact pressures moving in a medial-lateral direction, rather than anterior-posterior. This irregular movement of contact could therefore initiate cartilage degeneration through similar mechanisms to the SBCs (Talbot *et al.* 2022) or incongruent joints (Li *et al.* 2008). For this reason, it is hypothesised that the altered gait of the haemophilic patients is linked to the morphological changes the talus experiences, with collapse seen in the medial/lateral regions when contrasted with a healthy control group.

There was not a significant difference in Von Mises stresses (VMS) in the bone, therefore this is potentially a secondary change due to cartilage deterioration in these regions. However, this data is not yet complete enough to draw a definite conclusion. It also could not yet be ascertained if this is a cause and effect relationship, as the change in biomechanics over time, and consequent influence on joint stresses, could not be assessed in the same way the morphology was.

## 7.5 Limitations

The studies carried out in order to draw these conclusions are not without their limitations; these predominantly relate to informational constraints and small sample sizes. The nature of haemophilia as a rare disease means there are relatively low patient numbers within a given haemophilia centre, with approximately 8000 PwH across 56 centres in the UK. This study had access to one haemophilia centre, and included all ankles that met the inclusion criteria or two or more MRI (N=9). The nature of this being patient data also meant only select information was consented for research, and patients could opt out at any time. Due to the Covid-19 pandemic situation one patient opted out of participating in the biomechanical study. A further two were no longer eligible by the time gait data could be captured as they had undergone ankle arthrodesis.

The limited sample size predominantly impacted the methods used for the morphology study in Chapter 2; the method developed to assess the talar flattening only considered 2D morphological measurements, while a 3D analysis would be more detailed. However, 3D analysis such as statistical shape modelling (SSM) require much larger sample sizes ( $N > 50$ ) (Mei *et al.* 2008). This 3D analysis would be able to answer more clearly if there is a redistribution effect as the talus collapses.

Nevertheless, the aim was to make the method relatively quick and easy to repeat for clinical use, which was possible using the 2D method on opensource software.

The sample size also impacted the conclusions that could be drawn from the quasi-dynamic models in Chapter 6. The static finite element models of Chapter 3 to 5 were less influenced by this, but highly influenced by the informational constraints. The quality of clinical MRI is appropriate for diagnostics and disease monitoring, however, is low resolution when comparing to those used for finite element modelling research. It was shown in Chapter 3 that the image resolution can impact the volumes and shapes generated of the bones and cartilages; this is likely to mean the shapes and volumes of the SBCs in Chapter 5 are also not reflections of the true geometry. With slice thicknesses of around 3mm in these MRI scans, with some gaps between slices, there will be missing information in both the morphology and the finite element models. However, the segmentation specific models of SBCs are still less of a simplification that previous studies assuming spherical SBC geometry (Anwar *et al.* 2020; Dürr *et al.* 2004; Frazer, Santschi and Fischer 2017; Sarrafpour *et al.* 2019).

There is also limited information on the properties of bone and cartilage in PwH; there is an improved understanding of the theory behind the disease pathogenesis, however, the

consequent properties of the bone, cartilage and SBC fluid still have not been characterised. The influence of joint disease on material properties is likely to get progressively worse, hence would differ in each of the models, especially in those with SBCs (Burnett *et al.* 2019). Without CT imaging to register patient specific bone properties to each model, it cannot be estimated what the individual properties of the 37 ankle models are. Therefore, simplified properties were used, assuming all ankles have the same bone properties regardless of the disease progression. The quasi-dynamic models were limited by the assumption of healthy muscle function, this would have differed for each patient and the degree of influence on the model outcomes is unknown. In order to overcome this, myography would need to be carried out alongside biomechanical analysis for each individual ankle.

## 7.6 Future work

The work done in Chapters 2 to 6, and the corresponding limitations, leave areas for future work beyond the scope of this thesis. Expanding this work beyond a small sample size and collecting additional data, such as joint scores, would enable this work to progress towards answering clinical questions.

### 7.6.1 Morphological Analysis

It was shown in Chapter 2 that the flattening of the talus can be quantified in the haemophilic population, however this is by no means the end of the morphological analysis needed for this group. The small sample size meant that SSM was not viable. Exploring larger sample sizes would be pertinent in making this 2D analysis more robust, and in undertaking a 3D analysis. Linking the morphological changes to clinical measures, such as treatment type, or HJHS should also be carried out to help clarify the relationship with overall disease progression, as this remained unclear within the small patient sample. Literature suggests weak correlations between HJHS and imaging findings (von Drygalski *et al.* 2019). However these studies have previously been in relation to soft tissue changes, hence an investigation into the relationship between the morphological quantification and clinical scores would be important novel information, and may feed into the understanding of functional outcomes such as gait adaptations.



### 7.6.2 Patient Specific Finite Element Model Generation

The sensitivity analysis used demonstrated the modelling decisions made generated a robust model, however, there were clear limitations to these before this analysis could be transferred to clinical use. Combining the use of CT and MRI data would allow for the most accurate representation of both bone and cartilage; with more clearly defined bone boundaries, and bone properties ascertainable from CT, while MRI allows for the individual cartilage components to be defined. This is particularly important in HA, where the disease is highly influential on cartilage health (Lundin *et al.* 2012).

Either patient specific bone properties, or a clearer understanding of the general effect of haemophilia on the mechanical properties of cortical and trabecular bone would improve the outcomes of these models; enabling meaningful data to be ascertained from the bone as well as the cartilage. Similar information on haemarthritic cartilage would also be valuable, especially relating to different amounts of blood exposure, to use different values for patients with different levels of HA.

These more accurate bone and cartilage properties, relevant to the disease stage, would provide additional information on how the diseased bone responds to forces and improve the understanding of how this may relate to the progressive nature of the disease. This work would involve large amounts of experimental testing, and is much more valuable information now that robust models have been generated in which to implement it.

In order for these models to be used in clinical practice, they would also require validation (Viceconti *et al.* 2005); this would need to be a validation of the modelling process, rather than of a haemophilic ankle, given the nature of the experimental testing required for validation. Validation of FE models gives confidence in the robustness, as a validated model shows that the simulation represents what is happening in the physical model.

There would be two methods of carrying out this validation that can be considered in future work: 1) experimental validation, representing a mechanical test in the FE simulation and contrasting the results; or 2) validation against pre-existing data in the literature. Experimental validation of a patient specific ankle model has previously been reported in the literature (Anderson *et al.* 2007); results from this validation could be contrasted with a model generated using the model generation developed in Chapter 3, and simulated using the loading conditions in literature. Should the results be comparable, it would increase confidence in the model. The previous validation however was generated from CT data, therefore a comparison between

MRI and CT segmentations may also be required to show what may cause any discrepancies between the validated model and that generated from clinical MRI.

The latter of these two options is obviously not the preferred, as it would not be comparing the same ankle joint, and therefore contact distributions are likely to differ. However, this would add confidence in the orders of magnitude of results.

### 7.6.3 Subchondral Bone Cyst Analysis

In order to further the SBC analysis, the shapes of the SBCs should be treated as independent variables. Volume has been investigated as an independent variable in literature (Anwar *et al.* 2020; McErlain *et al.* 2011; Frazer, Santschi and Fischer 2017), however, the distribution of that volume is highly variable between the ankle models and has not yet been considered.

A study into these distributions may show a clearer relationship with volume in these irregular shaped SBCs, as the literature considered only regular shapes changing volume. How the cystic region is distributed may be influential; with SBCs with larger surface area close to cartilage/bone interface potentially behaving differently to SBCs that penetrate deep into the bone. A better understanding of the distribution of volume and shapes could be gained from higher resolution MR images. Acquiring some high resolution MRI of ankles with SBCs, would allow for a general idea of the range of distributions that may be seen in both the tibia and the talus; these distributions, would be scaled to give the same total volume, and modelled in the same ankle geometry, therefore treating shape as an independent variable.

The SBC study was limited by the sensitivity of models to the cystic properties; in order to be able to thoroughly understand the quantitative impact of SBCs, they must be properly characterised, including the influence of blood or haemosiderin on these properties.

The influence of SBCs was also only assessed at neutral standing; to fully understand the contact redistributions and their influence on cartilage health a similar analysis should be considered at multiple points through stance phase. For the models that had SBCs present, these were included in the quasi-dynamic models (Chapter 6), however there was no comparison of the two cystic conditions as was carried out in Chapter 5.

### 7.6.4 Biomechanical Analysis

In order to extend the understanding of the link between structure and function in the haemophilic ankle, with the overarching aim to ascertain which of structure or function drives the relationship, the biomechanical analysis should be carried out on a much larger cohort. The

MRI and biomechanical data should also be collected as close together as possible, as the biomechanical analysis is currently limited by large lead times between MRI data collection and gait analysis.

Extending this work will help in understanding whether the gait in haemophilic arthropathy is a functional adaptation, due to the altered morphology, or if the morphology changes due to regions of high stress due to gait adaptations. Both pathways appeared feasible in the present small sample size; hence, gathering morphology and biomechanical data on a larger range of PwH is key to this. To take this assessment further, these individuals could be monitored over time to see how their gait adapts, in a similar way to the chronological static analysis. However, this would involve much more patient involvement as this is not routinely collected clinical data, and it is not reported in literature what sort of time frame this gait adaptation is expected to occur over.

## 7.7 Conclusion

The generation of patient specific finite element models of the haemophilic ankle has improved understanding of the HA features and their influence on bone stresses and cartilage contact pressures. The models have demonstrated the benefit of including disease manifestations such as SBCs, and highlighted possible routes of assessing the link between structure and function in haemarthritic ankles. The method developed has enabled robust static and quasi-dynamic models of the haemophilic ankle to be built; following appropriate experimental validation, these could be used with confidence in clinical applications surrounding the influence of HA on the ankle.

## 8 Bibliography

- AKRAMI, M., Z. QIAN, Z. ZOU, D. HOWARD, C. J. NESTER and L. REN. 2018. Subject-specific finite element modelling of the human foot complex during walking: sensitivity analysis of material properties, boundary and loading conditions. *Biomechanics and Modeling in Mechanobiology*, **17**(2), pp.559-576.
- ALTAI, Z., E. MONTEFIORI, B. VAN VEEN, A. P. M, E. V. MCCLOSKEY, M. VICECONTI, C. MAZZÀ and X. LI. 2021. Femoral neck strain prediction during level walking using a combined musculoskeletal and finite element model approach. *PLoS One*, **16**(2), pe0245121.
- ANDERSON, A. E., B. J. ELLIS, S. A. MAAS and J. A. WEISS. 2010. Effects of idealized joint geometry on finite element predictions of cartilage contact stresses in the hip. *Journal of biomechanics*, **43**(7), pp.1351-1357.
- ANDERSON, A. E., B. J. ELLIS and J. A. WEISS. 2007. Verification, validation and sensitivity studies in computational biomechanics. *Computer methods in biomechanics & biomedical engineering*, **10**(3), pp.171-184.
- ANDERSON, D. D., S. CHUBINSKAYA, F. GUILAK, J. A. MARTIN, T. R. OEGEMA, S. A. OLSON and J. A. BUCKWALTER. 2011a. Post-traumatic osteoarthritis: Improved understanding and opportunities for early intervention. *Journal of Orthopaedic Research*, **29**(6), pp.802-809.
- ANDERSON, D. D., J. K. GOLDSWORTHY, W. LI, M. JAMES RUDERT, Y. TOCHIGI and T. D. BROWN. 2007. Physical validation of a patient-specific contact finite element model of the ankle. *Journal of Biomechanics*, **40**(8), pp.1662-1669.
- ANDERSON, D. D., J. K. GOLDSWORTHY, K. SHIVANNA, N. M. GROSLAND, D. R. PEDERSEN, T. P. THOMAS, Y. TOCHIGI, J. L. MARSH and T. D. BROWN. 2006. Intra-articular Contact Stress Distributions at the Ankle Throughout Stance Phase—patient-specific Finite Element Analysis as a Metric of Degeneration Propensity. *Biomechanics and Modeling in Mechanobiology*, **5**(2), p82.
- ANDERSON, D. D., C. VAN HOFWEGEN, J. L. MARSH and T. D. BROWN. 2011b. Is elevated contact stress predictive of post-traumatic osteoarthritis for imprecisely reduced tibial plafond fractures? *Journal of Orthopaedic Research*, **29**(1), pp.33-39.
- ANDRIACCHI, T. P., A. MÜNDERMANN, R. L. SMITH, E. J. ALEXANDER, C. O. DYRBY and S. KOO. 2004. A framework for the in vivo pathomechanics of osteoarthritis at the knee. *Ann Biomed Eng*, **32**(3), pp.447-57.
- ANTUNES, P., G. R. DIAS, A. COELHO, F. REBELO and T. PEREIRA. 2011. Nonlinear 3D foot FEA modeling from CT scan medical images.
- ANWAR, A., Z. HU, Y. ZHANG, Y. GAO, C. TIAN, X. WANG, M. U. NAZIR, Y. WANG, Z. ZHAO, D. LV, Z. ZHANG, H. ZHANG and G. LV. 2020. Multiple Subchondral Bone Cysts Cause Deterioration of Articular Cartilage in Medial OA of Knee: A 3D Simulation Study. *Frontiers in Bioengineering and Biotechnology*, **8**(1159).
- ARNOLD, J. B., J. HALSTEAD, A. J. GRAINGER, A. M. KEENAN, C. L. HILL and A. C. REDMOND. 2020. Foot and leg muscle weakness in people with midfoot osteoarthritis. *Arthritis Care Res (Hoboken)*.

- AUDREY, H. X., H. R. B. ABD RAZAK and T. H. C. ANDREW. 2014. The truth behind subchondral cysts in osteoarthritis of the knee. *The open orthopaedics journal*, **8**, pp.7-10.
- BACA, V., Z. HORAK, P. MIKULENKA and V. DZUPA. 2008. Comparison of an inhomogeneous orthotropic and isotropic material models used for FE analyses. *Medical engineering & physics*, **30**(7), pp.924-930.
- BACH, C. M., R. WACHTER, B. STÖCKL, G. GÖBEL, M. NOGLER and B. FRISCHHUT. 2002. Significance of Talar Distortion for Ankle Mobility in Idiopathic Clubfoot. *Clinical Orthopaedics and Related Research®*, **398**, pp.196-202.
- BARTON, T., F. LINTZ and I. WINSON. 2011. Biomechanical changes associated with the osteoarthritic, arthrodesed, and prosthetic ankle joint. *Foot and ankle surgery*, **2**(17), pp.52-57.
- BAUER, T., R. BREDA and P. HARDY. 2010. Anterior ankle bony impingement with joint motion loss: The arthroscopic resection option. *Orthopaedics & Traumatology: Surgery & Research*, **96**(4), pp.462-468.
- BAXTER, J. R., T. A. NOVACK, H. VAN WERKHOVEN, D. R. PENNELL and S. J. PIAZZA. 2012. Ankle joint mechanics and foot proportions differ between human sprinters and non-sprinters. *Proceedings of the Royal Society B: Biological Sciences*, **279**(1735), pp.2018-2024.
- BECK, M., M. KALHOR, M. LEUNIG and R. GANZ. 2005. Hip morphology influences the pattern of damage to the acetabular cartilage: femoroacetabular impingement as a cause of early osteoarthritis of the hip. *The Journal of bone joint surgery. British volume*, **87**(7), pp.1012-1018.
- BEHFOROOTAN, S., P. CHATZISTERGOS, R. NAEMI and N. CHOCKALINGAM. 2017. Finite element modelling of the foot for clinical application: a systematic review. *Medical engineering & physics*, **39**, pp.1-11.
- BING, F., C. WEI, P. LIU, Z. LI, Y. DENG, Z. ZHANG and S. ZHU. 2021. Biomechanical finite element analysis of typical tibiotalar arthrodesis. *Medicine in Novel Technology and Devices*, **11**, p100087.
- BLOBEL, C. P., C. HAXAIRE, G. D. KALLIOLIAS, E. DICARLO, J. SALMON and A. SRIVASTAVA. 2015. Blood-Induced Arthropathy in Hemophilia: Mechanisms and Heterogeneity. *Semin Thromb Hemost*, **41**(08), pp.832-837.
- BOS, C., P. TIEU, J. K. WU, K. STRIKE and A. K. C. CHAN. 2021. Bone mineral density in Canadian children with severe haemophilia A or B: a cross-sectional study. *The Journal of Haemophilia Practice*, **8**(1), pp.111-118.
- BOUGUECHA, A., N. WEIGEL, B.-A. BEHRENS, C. STUKENBORG-COLSMAN and H. WAIZY. 2011. Numerical simulation of strain-adaptive bone remodelling in the ankle joint. *Biomedical engineering online*, **10**(1), pp.1-13.
- BOWES, M. A., G. R. VINCENT, C. B. WOLSTENHOLME and P. G. CONAGHAN. 2015. A novel method for bone area measurement provides new insights into osteoarthritis and its progression. *Annals of the Rheumatic Diseases*, **74**(3), pp.519-525.
- BRAND, R. A. 2005. Joint contact stress: a reasonable surrogate for biological processes? *The Iowa orthopaedic journal*, **25**, pp.82-94.

- BREDBENNER, T. L., T. D. ELIASON, W. L. FRANCIS, J. M. MCFARLAND, A. C. MERKLE and D. P. NICOLELLA. 2014. Development and validation of a statistical shape modeling-based finite element model of the cervical spine under low-level multiple direction loading conditions. *Frontiers in bioengineering & biotechnology*, **2**, p58.
- BROUWER, R. W., M. R. HUIZINGA, T. DUIVENVOORDEN, T. M. VAN RAAIJ, A. P. VERHAGEN, S. M. BIERMA-ZEINSTRAS and J. A. VERHAAR. 2014. Osteotomy for treating knee osteoarthritis. *Cochrane Database of Systematic Reviews*, (12).
- BRYAN, R., P. S. MOHAN, A. HOPKINS, F. GALLOWAY, M. TAYLOR and P. B. NAIR. 2010. Statistical modelling of the whole human femur incorporating geometric and material properties. *Medical engineering & physics*, **32**(1), pp.57-65.
- BUCKLAND, J. 2010. It started with a cyst...or did it? *Nature Reviews Rheumatology*, **6**(6), pp.310-310.
- BUCKWALTER, J. and H. MANKIN. 1998. Articular cartilage repair and transplantation. *Arthritis & Rheumatism: Official Journal of the American College of Rheumatology*, **41**(8), pp.1331-1342.
- BUCKWALTER, J. and C. SALTZMAN. 1999. Ankle osteoarthritis: distinctive characteristics. *Instructional Course Lectures*, **48**, pp.233-241.
- BUCKWALTER, J. A., D. D. ANDERSON, T. D. BROWN, Y. TOCHIGI and J. A. MARTIN. 2013. The Roles of Mechanical Stresses in the Pathogenesis of Osteoarthritis: Implications for Treatment of Joint Injuries. *CARTILAGE*, **4**(4), pp.286-294.
- BURNETT, W. D., S. A. KONTULAINEN, C. E. MCLENNAN, D. HAZEL, C. TALMO, D. R. WILSON, D. J. HUNTER and J. D. JOHNSTON. 2019. Knee osteoarthritis patients with more subchondral cysts have altered tibial subchondral bone mineral density. *BMC Musculoskeletal Disorders*, **20**(1), p14.
- BUTZ, K. D., D. D. CHAN, E. A. NAUMAN and C. P. NEU. 2011. Stress distributions and material properties determined in articular cartilage from MRI-based finite strains. *Journal of Biomechanics*, **44**(15), pp.2667-2672.
- CAMACHO, D. L., W. R. LEDOUX, E. S. ROHR, B. J. SANGEORZAN and R. P. CHING. 2002. A three-dimensional, anatomically detailed foot model: a foundation for a finite element simulation and means of quantifying foot-bone position. *Journal of rehabilitation research & development*, **39**(3), pp.401-410.
- CARTER, D. R., G. S. BEAUPRÉ, M. WONG, R. L. SMITH, T. P. ANDRIACCHI and D. J. SCHURMAN. 2004. The mechanobiology of articular cartilage development and degeneration. *Clin Orthop Relat Res*, (427 Suppl), pp.S69-77.
- CASIER, S. J., R. VAN DEN BROECKE, J. VAN HOUCKE, E. AUDENAERT, L. F. DE WILDE and A. VAN TONGEL. 2018. Morphologic variations of the scapula in 3-dimensions: a statistical shape model approach. *Journal of Shoulder and Elbow Surgery*, **27**(12), pp.2224-2231.
- CAZACU, C.-M. and I. DOROFTEI. 2015. Preliminary Mathematical Model of a New Ankle Rehabilitation Device. *Journal of Engineering Studies and Research*, **21**, pp.78-84.
- CHEUNG, J. and M. ZHANG. 2005. A 3-Dimensional Finite Element Model of the Human Foot and Ankle for Insole Design. *Arch Phys Med Rehabil*, **86**, pp.353-358.

- CHEUNG, J., M. ZHANG, A. LEUNG and Y. FAN. 2005. Three dimensional finite element analysis of the foot during standing- a material sensitivity study. *Journal of Biomechanics*, **38**, pp.1045-1054.
- CHEUNG, J. T.-M. and B. M. NIGG. 2008. Clinical applications of computational simulation of foot and ankle. *Sport-Orthopädie-Sport-Traumatologie-Sports Orthopaedics and Traumatology*, **23**(4), pp.264-271.
- CLAASSEN, L., P. LUEDTKE, D. YAO, S. ETTINGER, K. DANILIDIS, A. M. NOWAKOWSKI, M. MUELLER-GERBL, C. STUKENBORG-COLSMAN and C. PLAASS. 2019. Ankle morphometry based on computerized tomography. *Foot Ankle Surg*, **25**(5), pp.674-678.
- CLIFT, S. 1992. Finite Element Analysis in Cartilage Biomechanics. *Journal of Biomedical Engineering*, **14**, pp.217-221.
- CLOUTHIER, A. L., C. R. SMITH, M. F. VIGNOS, D. G. THELEN, K. J. DELUZIO and M. J. RAINBOW. 2019. The effect of articular geometry features identified using statistical shape modelling on knee biomechanics. *Medical Engineering & Physics*, **66**, pp.47-55.
- COHEN, M. M., N. D. VELA, J. E. LEVINE and E. A. BARNOY. 2015. Validating a new Computed Tomography Atlas for Grading Ankle Osteoarthritis. *The Journal of Foot and Ankle Surgery*, **54**(2), pp.207-213.
- COOPER, R., S. WILLIAMS, M. MENGONI and A. JONES. 2018. Patient specific parameterised cam geometry in finite element models of femoroacetabular impingement of the hip. *Clinical Biomechanics*, **54**, pp.62-70.
- CROSS, S., S. VAIDYA and N. FOTIADIS. 2013. Hemophilic Arthropathy: A Review of Imaging and Staging. *Seminars in ultrasound, CT and MRI*, **34**(6), pp.516-524.
- DAI, X. Q., Y. LI, M. ZHANG and J. T. CHEUNG. 2006. Effect of sock on biomechanical responses of foot during walking. *Clinical Biomechanics*, **21**, pp.314-321.
- DEN UIJL, I. E. M., A. M. A. DE SCHEPPER, M. CAMERLINCK, D. E. GROBBEE and K. FISCHER. 2011. Magnetic resonance imaging in teenagers and young adults with limited haemophilic arthropathy: baseline results from a prospective study. *Haemophilia*, **17**(6), pp.926-930.
- DOHERTY, M., P. COURTNEY, S. DOHERTY, W. JENKINS, R. A. MACIEWICZ, K. MUIR and W. ZHANG. 2008. Nonspherical femoral head shape (pistol grip deformity), neck shaft angle, and risk of hip osteoarthritis: A case-control study. *Arthritis & Rheumatism*, **58**(10), pp.3172-3182.
- DONATELLI, R. A. 1996. *Biomechanics of the Foot and Ankle*. second edition ed. Philadelphia, USA: FA Davis Company.
- DÜRR, H. D., H. MARTIN, C. PELLENGAHR, M. SCHLEMMER, M. MAIER and V. JANSSON. 2004. The cause of subchondral bone cysts in osteoarthrosis: a finite element analysis. *Acta Orthop Scand*, **75**(5), pp.554-8.
- ENGL, W., L. PATRONE and B. ABBUEHL. 2016. Target Joint Status in Patients with Hemophilia A during 18 Consecutive Months of Prophylaxis with a Pegylated Full-Length Recombinant Factor VIII with Extended Half-Life. *Blood*, **128**(22), p2592.
- FELDMAN, B. M., S. M. FUNK, B. M. BERGSTROM, N. ZOURIKIAN, P. HILLIARD, J. VAN DER NET, R. ENGELBERT, P. PETRINI, H. M. VAN DEN BERG, M. J. MANCO-JOHNSON, G. E. RIVARD, A. ABAD and V. S. BLANCHETTE. 2011.

- Validation of a new pediatric joint scoring system from the International Hemophilia Prophylaxis Study Group: validity of the hemophilia joint health score. *Arthritis Care Res (Hoboken)*, **63**(2), pp.223-30.
- FELSON, D. T., A. NAIMARK, J. ANDERSON, L. KAZIS, W. CASTELLI and R. F. MEENAN. 1987. The prevalence of knee osteoarthritis in the elderly. the framingham osteoarthritis study. *Arthritis & Rheumatism*, **30**(8), pp.914-918.
- FESSY, M., J. CARRET and J. BEJUI. 1997. Morphometry of the talocrural joint. *Surgical and Radiologic Anatomy*, **19**(5), pp.299-302.
- FOX, A. J. S., A. BEDI and S. A. RODEO. 2009. The basic science of articular cartilage: structure, composition, and function. *Sports health*, **1**(6), pp.461-468.
- FRAZER, L. L., E. M. SANTSCHI and K. J. FISCHER. 2017. The impact of subchondral bone cysts on local bone stresses in the medial femoral condyle of the equine stifle joint. *Medical Engineering & Physics*, **48**, pp.158-167.
- GAMBLE, J. G., J. BELLAH, L. A. RINSKY and B. GLADER. 1991. Arthropathy of the ankle in hemophilia. *J Bone Joint Surg Am*, **73**(7), pp.1008-15.
- GEFEN, A. 2001. Simulations of foot stability during gait characteristic of ankle dorsiflexor weakness in the elderly. *IEEE Transactions on Neural Systems and Rehabilitation Engineering*, **9**(4), pp.333-337.
- GERAGHTY, S. 2012. Orthopedic Complications and Treatment Related to Chronic Hemarthrosis. *Nursing Working Group – Nurses’ Guide to Bleeding Disorders*. National Hemophilia Foundation.
- GEYSKENS, W., F. M. VANHOENACKER, T. VAN DER ZIJDEN and K. PEERLINCK. 2004. MR imaging of intraosseous haemophilic pseudotumour: case report and review of the literature. *Journal of the Belgian Society of Radiology*, **87**, pp.289-293.
- GOLDSCHNEIDER, G., M. RECHT, P. SOCHACKI, M. MANCO-JOHNSON and J. A. TAYLOR. 2021. Biomarkers of bone disease in persons with haemophilia. *Haemophilia*, **27**(1), pp.149-155.
- GOMPERTS, E. D., J. SCHWARZ, S. M. DONFIELD, A. E. LAIL, J. ASTERMARK, W. K. HOOTS, C. A. WINKLER and E. BERNTORP. 2017. The importance of genetic factors for the development of arthropathy: a longitudinal study of children and adolescents with haemophilia A. *Thrombosis and Haemostasis*, **117**, pp.277-285.
- GONZÁLEZ-CARBONELL, R. A., A. ORTIZ-PRADO, V. H. JACOBO-ARMENDÁRIZ, Y. A. CISNEROS-HIDALGO and A. ALPÍZAR-AGUIRRE. 2015. 3D patient-specific model of the tibia from CT for orthopedic use. *Journal of Orthopaedics*, **12**(1), pp.11-16.
- GREGORY, J. S., J. H. WAARSING, J. DAY, H. A. POLS, M. REIJMAN, H. WEINANS and R. M. ASPDEN. 2007. Early identification of radiographic osteoarthritis of the hip using an active shape model to quantify changes in bone morphometric features - Can hip shape tell us anything about the progression of osteoarthritis? *ARTHRITIS AND RHEUMATISM*, **56**(11), pp.3634-3643.
- GRINGERI, A., B. EWENSTEIN and A. REININGER. 2014. The burden of bleeding in haemophilia: is one bleed too many? *HAEMOPHILIA*, **20**(4), pp.459-463.
- HACKING, C. and A. DIXON. 2018. *Haemophilic Arthropathy* [online]. [Accessed 22/06/2020].



- HAMID, K. S., A. T. SCOTT, B. U. NWACHUKWU and K. A. DANIELSON. 2016. The Role of Fluid Dynamics in Distributing Ankle Stresses in Anatomic and Injured States. *Foot & Ankle International*, **37**(12), pp.1343-1349.
- HAVERKAMP, D. J., D. SCHIPHOF, S. M. BIERMA-ZEINSTRAS, H. WEINANS and J. H. WAARSING. 2011. Variation in joint shape of osteoarthritic knees. *Arthritis & Rheumatism*, **63**(11), pp.3401-3407.
- HAYASHI, D., F. W. ROEMER and A. GUERMAZI. 2016. Imaging for osteoarthritis. *Annals of Physical and Rehabilitation Medicine*, **59**(3), pp.161-169.
- HAYES, A., Y. TOCHIGI and C. SALTZMAN. 2006. Ankle Morphometry on 3D-CT Images. *The Iowa Orthopaedic Journal*, **26**, pp.1-4.
- HELGASON, B., F. TADDEI, H. PÁLSSON, E. SCHILEO, L. CRISTOFOLINI, M. VICECONTI and S. BRYNJÓLFSSON. 2008. A modified method for assigning material properties to FE models of bones. *Medical Engineering & Physics*, **30**(4), pp.444-453.
- HOLLENBECK, J. F. M., C. M. CAIN, J. A. FATTOR, P. J. RULLKOETTER and P. J. LAZ. 2018. Statistical shape modeling characterizes three-dimensional shape and alignment variability in the lumbar spine. *Journal of Biomechanics*, **69**, pp.146-155.
- HOOIVELD, M. J. J., G. ROOSENDAAL, K. M. G. JACOBS, M. E. VIANEN, H. M. VAN DEN BERG, J. W. J. BIJLSMA and F. LAFEBER. 2004. Initiation of degenerative joint damage by experimental bleeding combined with loading of the joint - A possible mechanism of hemophilic arthropathy. *ARTHRITIS AND RHEUMATISM*, **50**(6), pp.2024-2031.
- HOOIVELD, M. J. J., G. ROOSENDAAL, M. E. VIANEN, H. M. VAN DEN BERG, J. W. J. BIJLSMA and F. LAFEBER. 2003. Immature articular cartilage is more susceptible to blood-induced damage than mature articular cartilage - An in vivo animal study. *ARTHRITIS AND RHEUMATISM*, **48**(2), pp.396-403.
- HSU, Y.-C., Y.-W. GUNG, S.-L. SHIH, C.-K. FENG, S.-H. WEI, C.-H. YU and C.-S. CHEN. 2008. Using an optimization approach to design an insole for lowering plantar fascia stress—a finite element study. *Annals of biomedical engineering*, **36**(8), pp.1345-1352.
- HUANG, T.-W. P., K. A. SHORTER, P. G. ADAMCZYK and A. D. KUO. 2015. Mechanical and energetic consequences of reduced ankle plantar-flexion in human walking. *The Journal of experimental biology*, **218**(Pt 22), pp.3541-3550.
- HUISKES, R. and E. Y. S. CHAO. 1983. A survey of finite element analysis in orthopedic biomechanics: The first decade. *Journal of Biomechanics*, **16**(6), pp.385-409.
- IAQUINTO, J. M. and J. S. WAYNE. 2010. Computational Model of the Lower Leg and Foot/Ankle Complex: Application to Arch Stability. *JOURNAL OF BIOMECHANICAL ENGINEERING-TRANSACTIONS OF THE ASME*, **132**(2), p021009.
- IORIO, A., J. S. STONEBRAKER, H. CHAMBOST, M. MAKRIS, D. COFFIN, C. HERR and F. GERMINI. 2019. Establishing the Prevalence and Prevalence at Birth of Hemophilia in Males: A Meta-analytic Approach Using National Registries. *Ann Intern Med*, **171**(8), pp.540-546.
- JAFFE, W. L. and J. T. LAITMAN. 1982. The evolution and anatomy of the human foot. *Disorders of the Foot*. Philadelphia: WB Saunders.

- JAGANATHAN, S. M. D., S. M. D. GAMANAGATTI and A. M. GOYAL. 2011. Musculoskeletal Manifestations of Hemophilia: Imaging Features. *Current Problems in Diagnostic Radiology*, **40**(5), pp.191-197.
- JANSEN, N. W., G. ROOSENDAAL, M. J. WENTING, J. W. BIJLSMA, M. THEOBALD, H. A. HAZEWINKEL and F. P. LAFEBER. 2009. Very rapid clearance after a joint bleed in the canine knee cannot prevent adverse effects on cartilage and synovial tissue. *Osteoarthritis Cartilage*, **17**(4), pp.433-40.
- JANSEN, N. W. D., G. ROOSENDAAL, B. LUNDIN, L. HEIJNEN, M. THEOBALD, J. W. BIJLSMA, F. LAFEBER, U. LUND, L. DIAGNOSTISK RADIOLOGI, U. LUNDS and R. DIAGNOSTIC. 2008. Biomarkers of Cartilage and Bone Damage as a Measure of Joint Damage in Haemophilia. *Blood*, **112**(11), p1214.
- JELBERT, A., S. VAIDYA and N. FOTIADIS. 2009. Imaging and staging of haemophilic arthropathy. *Clinical Radiology*, **64**(11), pp.1119-1128.
- KAHAN, S., A. CUKER, R. F. KUSHNER, J. MAAHS, M. RECHT, T. WADDEN, T. WILLIS, S. MAJUMDAR, D. UNGAR and D. COOPER. 2017. Prevalence and impact of obesity in people with haemophilia: Review of literature and expert discussion around implementing weight management guidelines. *Haemophilia*, **23**(6), pp.812-820.
- KASPER, C. 2008. Treatment of Hemophilia: Hereditary Plasma Clotting Factor Disorders and their Management. In: *World Federation of Haemophilia, Montreal, Canada*.
- KEENAN, G. S., J. R. FRANZ, J. DICHARRY, U. D. CROCE and D. C. KERRIGAN. 2011. Lower limb joint kinetics in walking: The role of industry recommended footwear. *Gait & Posture*, **33**(3), pp.350-355.
- KEMPTON, C. L. 2021. Prophylaxis in hemophilia: how much is enough? *Blood*, **137**(13), pp.1709-1711.
- KEMPTON, C. L., D. M. ANTONIUCCI and E. C. RODRIGUEZ-MERCHAN. 2015. Bone health in persons with haemophilia. *Haemophilia*, **21**(5), pp.568-577.
- KIVIRANTA, P., J. RIEPPO, R. K. KORHONEN, P. JULKUNEN, J. TÖYRÄS and J. S. JURVELIN. 2006. Collagen network primarily controls Poisson's ratio of bovine articular cartilage in compression. *Journal of Orthopaedic Research*, **24**(4), pp.690-699.
- KLEKIEL, T. and R. BĘDZIŃSKI. 2015. Finite element analysis of large deformation of articular cartilage in upper ankle joint of occupant in military vehicles during explosion. *Archives of metallurgy & materials*, **60**(3), pp.2115-2121.
- KNOBE, K. and E. BERNTORP. 2011. Haemophilia and joint disease: pathophysiology, evaluation, and management. *Journal of comorbidity*, **1**(1), pp.51-59.
- KOLB, A., M. WILLEGGER, R. SCHUH, A. KAIDER, C. CHIARI and R. WINDHAGER. 2017. The impact of different types of talus deformation after treatment of clubfeet. *International Orthopaedics*, **41**(1), pp.93-99.
- KOVACS, C. S. 2008. Hemophilia, low bone mass, and osteopenia/osteoporosis. *Transfusion and Apheresis Science*, **38**(1), pp.33-40.
- KUIJLAARS, I. A. R., J. VAN DER NET, B. M. FELDMAN, M. ASPDAHL, M. BLADEN, W. DE BOER, R. CUESTA-BARRIUSO, R. E. D. MATLARY, S. M. FUNK, P. HILLIARD, J. A. JOHN, C. L. KEMPTON, P. DE KLEIJN, M. MANCO-JOHNSON, P. PETRINI, P. POONNOOSE, J. ST-LOUIS, S. THOMAS, M. A. TIMMER, S. S. TRAKYMIENE, L. VAN VLIMMEREN and K. FISCHER. 2020. Evaluating

- international Haemophilia Joint Health Score (HJHS) results combined with expert opinion: Options for a shorter HJHS. *Haemophilia*, **26**(6), pp.1072-1080.
- KUO, C.-C., H.-L. LU, A. LEARDINI, T.-W. LU, M.-Y. KUO and H.-C. HSU. 2014. Three-dimensional computer graphics-based ankle morphometry with computerized tomography for total ankle replacement design and positioning. *Clinical Anatomy*, **27**(4), pp.659-668.
- KWON, D. G., K. H. SUNG, C. Y. CHUNG, M. S. PARK, S. H. LEE, T. W. KIM, J. H. LEE, T. G. KIM and K. M. LEE. 2014. Preliminary findings of morphometric analysis of ankle joint in Korean population. *J Foot Ankle Surg*, **53**(1), pp.3-7.
- LAFEBER, F. P., P. MIOSSEC and L. A. VALENTINO. 2008. Physiopathology of haemophilic arthropathy. *Haemophilia*, **14 Suppl 4**, pp.3-9.
- LAMBERT, T., G. AUERSWALD, G. BENSON, U. HEDNER, V. JIMÉNEZ-YUSTE, R. LJUNG, M. MORFINI, E. REMOR, E. SANTAGOSTINO, S. ZUPANČIĆ ŠALEK, PAEDIATRICS, U. LUND, U. PAEDIATRIC HAEMATOLOGY RESEARCH, H. PEDIATRISK, L. PEDIATRISK, M. INSTITUTIONEN FÖR KLINISKA VETENSKAPER, U. LUNDS and M. DEPARTMENT OF CLINICAL SCIENCES. 2014. Joint disease, the hallmark of haemophilia: What issues and challenges remain despite the development of effective therapies? *Thrombosis Research*, **133**(6), pp.967-971.
- LAU, A. G., J. SUN, W. B. HANNAH, E. W. LIVINGSTON, D. HEYMANN, T. A. BATEMAN and P. E. MONAHAN. 2014. Joint bleeding in factor VIII deficient mice causes an acute loss of trabecular bone and calcification of joint soft tissues which is prevented with aggressive factor replacement. *HAEMOPHILIA*, **20**(5), pp.716-722.
- LEARDINI, A., J. J. O'CONNOR, F. CATANI and S. GIANNINI. 1999. A geometric model of the human ankle joint. *Journal of Biomechanics*, **32**(6), pp.585-591.
- LEE, H. S., J. H. LEE and H. S. KIM. 2019. Activities of ankle muscles during gait analyzed by simulation using the human musculoskeletal model. *J Exerc Rehabil*, **15**(2), pp.229-234.
- LEES, D. and P. PARTINGTON. 2016. Articular cartilage. *Orthopaedics and Trauma*, **30**(3), pp.265-272.
- LENZ, A. L., N. KRÄHENBÜHL, A. C. PETERSON, R. J. LISONBEE, B. HINTERMANN, C. L. SALTZMAN, A. BARG and A. E. ANDERSON. 2021. Statistical shape modeling of the talocrural joint using a hybrid multi-articulation joint approach. *Scientific Reports*, **11**(1), p7314.
- LI, W., D. D. ANDERSON, J. K. GOLDSWORTHY, J. L. MARSH and T. D. BROWN. 2008. Patient-specific finite element analysis of chronic contact stress exposure after intraarticular fracture of the tibial plafond. *Journal of Orthopaedic Research*, **26**(8), pp.1039-1045.
- LI, Z., J.-E. KIM, J. S. DAVIDSON, B. S. ETHERIDGE, J. E. ALONSO and A. W. EBERHARDT. 2007. Biomechanical response of the pubic symphysis in lateral pelvic impacts: A finite element study. *Journal of Biomechanics*, **40**(12), pp.2758-2766.
- LIU, Y., Q. HAN, W. YIN, C. WANG, B. CHEN, N. WU, A. ZHANG and J. WANG. 2020. Sex determination from talus in Chinese population by three-dimensional measurement approach. *Legal Medicine*, **44**, p101647.

- LOBET, S., J. L. CROISIER, A. C. LANTIN, C. HERMANS, K. PEERLINCK, J. VANDESANDE, J. B. PIALAT and K. DESCHAMPS. 2017. Deficits of ankle muscle strength not found in children, adolescents and young adults with haemophilic ankle arthropathy. *Haemophilia*, **23**(5), pp.e409-e418.
- LOBET, S., C. DETREMBLEUR, F. MASSAAD and C. HERMANS. 2013. Three-dimensional gait analysis can shed new light on walking in patients with haemophilia. *ScientificWorldJournal*, **2013**, p284358.
- LOBET, S., C. HERMANS, G. J. BASTIEN, F. MASSAAD and C. DETREMBLEUR. 2012. Impact of ankle osteoarthritis on the energetics and mechanics of gait: The case of hemophilic arthropathy. *Clinical Biomechanics*, **27**(6), pp.625-631.
- LUNDIN, B., M. L. MANCO-JOHNSON, D. M. IGNAS, R. MOINEDDIN, V. S. BLANCHETTE, A. L. DUNN, S. V. GIBIKOTE, S. N. KESHAVA, R. LJUNG, M. J. MANCO-JOHNSON, S. F. MILLER, G. E. RIVARD and A. S. DORIA. 2012. An MRI scale for assessment of haemophilic arthropathy from the International Prophylaxis Study Group. *Haemophilia*, **18**(6), pp.962-970.
- MACNICOL, M. F. and C. A. LUDLAM. 1999. Does avascular necrosis cause collapse of the dome of the talus in severe haemophilia? *HAEMOPHILIA*, **5**(2), pp.139-142.
- MADHOK, R., D. BENNETT, R. D. STURROCK and C. D. FORBES. 1988. Mechanisms of joint damage in an experimental model of hemophilic arthritis. *Arthritis & Rheumatism*, **31**(9), pp.1148-1155.
- MADHOK, R., J. YORK and R. D. STURROCK. 1991. Haemophilic arthritis. *Annals of the Rheumatic Diseases*, **50**(8), pp.588-591.
- MANCO-JOHNSON, M. L., M. J. MANCO-JOHNSON, T. C. ABSHIRE, A. D. SHAPIRO, B. RISKE, M. R. HACKER, R. KILCOYNE, J. D. INGRAM, S. FUNK, L. JACOBSON, L. A. VALENTINO, W. K. HOOTS, G. R. BUCHANAN, D. DIMICHELE, M. RECHT, D. BROWN, C. LEISSINGER, S. BLEAK, A. COHEN, P. MATHEW, A. MATSUNAGA, D. MEDEIROS, D. NUGENT, G. A. THOMAS, A. A. THOMPSON, K. MCREDMOND, J. M. SOUCIE, H. AUSTIN and B. L. EVATT. 2007. Prophylaxis versus Episodic Treatment to Prevent Joint Disease in Boys with Severe Hemophilia. *The New England Journal of Medicine*, **357**(6), pp.535-544.
- MARTIN, R. B. and D. B. BURR. 1989. *Structure, function, and adaptation of compact bone*. Raven Press.
- MCCARTHY, A., A. MOORE, L. REDHEAD, P. MCLAUGHLIN, A. IORIO and P. CHOWDARY. 2015. Development of haemophilic arthropathy of the ankle: results of a Delphi consensus survey on potential contributory factors. *Haemophilia*, **21**(1), pp.116-123.
- MCERLAIN, D. D., J. S. MILNER, T. G. IVANOV, L. JENCIKOVA-CELERIN, S. I. POLLMANN and D. W. HOLDSWORTH. 2011. Subchondral cysts create increased intra-osseous stress in early knee OA: A finite element analysis using simulated lesions. *Bone*, **48**(3), pp.639-646.
- MEI, L., M. FIGL, A. DARZI, D. RUECKERT and P. EDWARDS. 2008. Sample Sufficiency and PCA Dimension for Statistical Shape Models. *In: Computer Vision – ECCV 2008, 2008//*, Berlin, Heidelberg. Springer Berlin Heidelberg, pp.492-503.

- MELINSKA, A. U., P. ROMASZKIEWICZ, J. WAGEL, B. ANTOSIK, M. SASIADEK and D. R. ISKANDER. 2017. Statistical shape models of cuboid, navicular and talus bones. *Journal of Foot and Ankle Research*, **10**(1), p6.
- MELLER, S. and W. A. KALENDER. 2004. Building a statistical shape model of the pelvis. *In: International Congress Series: Elsevier*, pp.561-566.
- MERKELY, G., J. ACKERMANN and C. LATTERMANN. 2018. Articular Cartilage Defects: Incidence, Diagnosis, and Natural History. *Operative Techniques in Sports Medicine*, **26**(3), pp.156-161.
- MIDAS NFX. *Understand Different Mesh Types* [online]. [Accessed 12/11/2018].
- MILLAR, A. 2003. Protecting your joints. *Action Plan for Arthritis*. USA: Human Kinetics, pp.143-158.
- MILLER, M. C., P. SMOLINSKI, S. CONTI and K. GALIK. 2004. Stresses in Polyethylene Liners in a Semiconstrained Ankle Prosthesis. *Journal of Biomechanical Engineering*, **126**(5), pp.636-640.
- MITTAL, S., S. ARORA, S. KHANNA, L. MAINI and V. K. GAUTAM. 2011. An unusual presentation of haemophilia B: pseudotumor of proximal tibia. *American Journal of Orthopaedics*, **40**, pp.E138-E140.
- MONDAL, S. and R. GHOSH. 2017. A numerical study on stress distribution across the ankle joint: Effects of material distribution of bone, muscle force and ligaments. *Journal of Orthopaedics*, **14**(3), pp.329-335.
- MONDAL, S. and R. GHOSH. 2019a. Effects of implant orientation and implant material on tibia bone strain, implant–bone micromotion, contact pressure, and wear depth due to total ankle replacement. *Proceedings of the Institution of Mechanical Engineers, Part H: Journal of Engineering in Medicine*, **233**(3), pp.318-331.
- MONDAL, S. and R. GHOSH. 2019b. The effects of implant orientations and implant–bone interfacial conditions on potential causes of failure of tibial component due to total ankle replacement. *Journal of Medical and Biological Engineering*, **39**(4), pp.541-551.
- MORALES-ORCAJO, E., J. BAYOD and E. BARBOSA DE LAS CASAS. 2016. Computational Foot Modeling: Scope and Applications. *Archives of Computational Methods in Engineering*, **23**(3), pp.389-416.
- MOSHER, T. J. and B. J. DARDZINSKI. 2004. Cartilage MRI T2 relaxation time mapping: overview and applications. *Semin Musculoskelet Radiol*, **8**(4), pp.355-68.
- MUNDERMANN, A., C. O. DYRBY, D. E. HURWITZ, L. SHARMA and T. P. ANDRIACCHI. 2004. Potential strategies to reduce medial compartment loading in patients with knee osteoarthritis of varying severity - Reduced walking speed. *ARTHRITIS AND RHEUMATISM*, **50**(4), pp.1172-1178.
- MYS, K., P. VARGA, F. STOCKMANS, B. GUEORGUIEV, C. E. WYERS, J. P. W. VAN DEN BERGH and G. H. VAN LENTHE. 2021. Quantification of 3D microstructural parameters of trabecular bone is affected by the analysis software. *Bone*, **142**, p115653.
- NAKAI, T., Y. TAKAKURA, Y. TANAKA, K. SUGIMOTO, S. TAMAI and N. KURUMATANI. 2000. Morphologic changes of the ankle in children as assessed by radiography and arthrography. *Journal of Orthopaedic Science*, **5**(2), pp.134-138.
- NAKAMURA, S., R. CROWNINSHIELD and R. COOPER. 1981. An analysis of soft tissue loading in the foot--a preliminary report. *Bulletin of prosthetics research*, **10**, pp.27-34.

- NICOLELLA, D. P. and T. L. BREDBENNER. 2012. Development of a parametric finite element model of the proximal femur using statistical shape and density modelling. *Computer methods in biomechanics & biomedical engineering*, **15**(2), pp.101-110.
- NIU, W. X., L. J. WANG, T. N. FENG, C. H. JIANG, Y. B. FAN and M. ZHANG. 2013. Effects of bone Young's modulus on finite element analysis in the lateral ankle biomechanics. *APPLIED BIONICS AND BIOMECHANICS*, **10**(4), pp.189-195.
- NORTON, N. M., E. SANTSCHI and K. J. FISCHER. 2022. Effects of Internal Fluid Pressure on Stresses in Subchondral Bone Cysts of the Medial Femoral Condyle. *Annals of Biomedical Engineering*, **50**(1), pp.86-93.
- O'BRIEN, M. and E. FREUND. 2002. Anatomy of the Ankle and the Talar Joints. *The Unstable Ankle*. Human Kinetics Publishers, Inc.
- OLOYEDE, A., R. FLACHSMANN and N. D. BROOM. 1992. The dramatic influence of loading velocity on the compressive response of articular cartilage. *Connective tissue research*, **27**(4), pp.211-224.
- OUTERBRIDGE, A. R., E. TREPMAN and L. MICHELI. 2002. Ankle Instability in Children and Adolescents. *The Unstable Ankle*. Human Kinetics Publishers, Inc.
- OZEN, M., O. SAYMAN and H. HAVITCIOGLU. 2013. Modeling and stress analyses of a normal foot-ankle and a prosthetic foot-ankle complex. *Acta of Bioengineering and Biomechanics*, **15**(3).
- PAGET, L. D. A., J. L. TOL, G. M. M. J. KERKHOFFS and G. REURINK. 2021. Health-Related Quality of Life in Ankle Osteoarthritis: A Case-Control Study. *CARTILAGE*, **13**(1\_suppl), pp.1438S-1444S.
- PARK, S., S. LEE, J. YOON and S.-W. CHAE. 2019. Finite element analysis of knee and ankle joint during gait based on motion analysis. *Medical Engineering & Physics*, **63**, pp.33-41.
- PASTA, G., A. FORSYTH, C. R. MERCHAN, S. M. J. MORTAZAVI, M. SILVA, K. MULDER, E. MANCUSO, O. PERFETTO, M. HEIM, H. CAVIGLIA and L. SOLIMENO. 2008. Orthopaedic management of haemophilia arthropathy of the ankle. *Haemophilia*, **14**(s3), pp.170-176.
- PENG, L., J. BAI, X. ZENG and Y. ZHOU. 2006. Comparison of isotropic and orthotropic material property assignments on femoral finite element models under two loading conditions. *Medical Engineering and Physics*, **28**(3), pp.227-233.
- PERRIN, J. M., W. E. MACLEAN JR, R. L. JANCO and S. L. GORTMAKER. 1996. Stress and incidence of bleeding in children and adolescents with hemophilia. *The Journal of pediatrics*, **128**(1), pp.82-88.
- PIERCE, D. M., W. TROBIN, S. TRATTNIG, H. BISCHOF and G. A. HOLZAPFEL. 2009. A Phenomenological Approach Toward Patient-Specific Computational Modeling of Articular Cartilage Including Collagen Fiber Tracking. *Journal of Biomechanical Engineering*, **131**(9).
- POELERT, S., E. VALSTAR, H. WEINANS and A. A. ZADPOOR. 2012. Patient Specific Finite Element Modeling of Bones. *Proceedings of the Institution of Mechanical Engineers, Part H: Journal of Engineering in Medicine.*, **227**(4), pp.464-478.

- POTTIE, P., N. PRESLE, B. TERLAIN, P. NETTER, D. MAINARD and F. BERENBAUM. 2006. Obesity and osteoarthritis: more complex than predicted! *annals of the rheumatic diseases*, **65**(11), pp.1403-1405.
- PULLES, A. E., S. C. MASTBERGEN, R. E. G. SCHUTGENS, F. P. J. G. LAFEBER and L. F. D. VAN VULPEN. 2017. Pathophysiology of hemophilic arthropathy and potential targets for therapy. *Pharmacological Research*, **115**, pp.192-199.
- PURKAIT, R., A. MUKHERJI, T. K. DOLAI and R. BHADRA. 2014. Intraosseous Pseudotumour in a Child with Mild Hemophilia B: Report of a Rare Case and Brief Review of Literature. *Indian Journal of Hematology and Blood Transfusion*, **30**(S1), pp.366-368.
- QIU, T.-X., E.-C. TEO, Y.-B. YAN and W. LEI. 2011. Finite element modeling of a 3D coupled foot–boot model. *Medical Engineering and Physics*, **33**(10), pp.1228-1233.
- QUINTANA, J. M., I. AROSTEGUI, A. ESCOBAR, J. AZKARATE, J. I. GOENAGA and I. LAFUENTE. 2008. Prevalence of knee and hip osteoarthritis and the appropriateness of joint replacement in an older population. *Arch Intern Med*, **168**(14), pp.1576-84.
- RAMLEE, M. H., M. R. A. KADIR and H. HARUN. 2013. Three-dimensional modeling and analysis of a human ankle joint. *In: Student Conference on Research and Development (SCORED)*, 2013: IEEE, pp.74-78.
- RASBAND, W. S. 1997-2018. *ImageJ* [online]. [Accessed]. Available from: <https://imagej.nih.gov/ij/>.
- REILINGH, M. L., L. BLANKEVOORT, I. C. VAN EEKEREN and C. N. VAN DIJK. 2013. Morphological analysis of subchondral talar cysts on microCT. *Knee Surg Sports Traumatol Arthrosc*, **21**(6), pp.1409-17.
- RENNELL, C., F. MAINZER, C. V. MULTZ and H. K. GENANT. 1977. Subchondral pseudocysts in rheumatoid arthritis. *American Journal of Roentgenology*, **129**(6), pp.1069-1072.
- ROBINSON, A. and T. KEITH. 2015. Osteoarthritis of the ankle. *Orthopaedics and Trauma*, **30**(1), pp.59-67.
- RODRIGUEZ-MERCHAN, E. C. 1996. Effects of hemophilia on articulations of children and adults. *CLINICAL ORTHOPAEDICS AND RELATED RESEARCH*, **328**(328), pp.7-13.
- RODRIGUEZ-MERCHAN, E. C. 2010. Musculoskeletal Complications of Hemophilia. *HSS Journal*, **6**(1), pp.37-42.
- RODRIGUEZ-MERCHAN, E. C. 2012. Orthopaedic Problems about the Ankle in Hemophilia. *Journal of Foot and Ankle Surgery, The*, **51**(6), pp.772-776.
- RODRIGUEZ-MERCHAN, E. C. and L. VALENTINO. 2019. Increased bone resorption in haemophilia. *Blood Reviews*, **33**(6-10).
- RODRIGUEZ-MERCHAN, E. C. 2006. The haemophilic ankle. *Haemophilia*, **12**(4), pp.337-344.
- ROEMER, F. W. M. D., F. M. D. ECKSTEIN, D. M. D. P. HAYASHI and A. M. D. P. GUERMAZI. 2014. The role of imaging in osteoarthritis. *Best Practice & Research: Clinical Rheumatology*, **28**(1), pp.31-60.

- ROOSENDAAL, V. RINSUM, VIANEN, V. D. BERG, LAFEBER and BIJLSMA. 1999. Haemophilic arthropathy resembles degenerative rather than inflammatory joint disease. *Histopathology*, **34**(2), pp.144-153.
- ROOSENDAAL, G. and F. P. LAFEBER. 2006. Pathogenesis of haemophilic arthropathy. *Haemophilia*, **12**(s3), pp.117-121.
- RUFFONI, D. and H. VAN LENTHE. 2017. Finite Element Analysis in Bone Research: A Computational Method Relating Structure to Mechanical Function. *Comprehensive Biomaterials II*, **3**.
- SACKSTEIN, P., P. COOPER and C. KESSLER. 2021. The role of total ankle replacement in patients with haemophilia and end-stage ankle arthropathy: A review. *Haemophilia*, **27**(2), pp.184-191.
- SALTZMAN, C., M. L. SALAMON, M. BLANCHARD, T. HUFF, A. HAYES, J. BUCKWALTER and A. AMENDOLA. 2005. Epidemiology of ankle arthritis: report of a consecutive series of 639 patients from a tertiary orthopaedic center. *The Iowa Orthopaedic Journal*, **25**, pp.44-46.
- SARKALKAN, N., H. WEINANS and A. A. ZADPOOR. 2014. Statistical shape and appearance models of bones. *Bone*, **60**, pp.129-140.
- SARRAFPOUR, B., C. EL-BACHA, Q. LI and H. ZOELLNER. 2019. Roles of functional strain and capsule compression on mandibular cyst expansion and cortication. *Archives of Oral Biology*, **98**, pp.1-8.
- SCHNEIDER, C. A., W. S. RASBAND and K. W. ELICEIRI. 2012. NIH Image to ImageJ: 25 years of image analysis. *Nature Methods*, **9**(7), pp.671-675.
- SCHWER, L. E. 2007. An overview of the PTC 60/V&V 10: guide for verification and validation in computational solid mechanics: Transmitted by L. E. Schwer, Chair PTC 60/V&V 10. *Engineering with Computers*, **23**(4), pp.245-252.
- SEO, J. W., D. W. KANG, J. Y. KIM, S. T. YANG, D. H. KIM, J. S. CHOI and G. R. TACK. 2014. Finite element analysis of the femur during stance phase of gait based on musculoskeletal model simulation. *Biomed Mater Eng*, **24**(6), pp.2485-93.
- SERVIER MEDICAL ART. *Ankle Sprain* [online]. [Accessed 03/05/2022]. Available from: [https://smart.servier.com/smart\\_image/sprain-2/](https://smart.servier.com/smart_image/sprain-2/).
- SEUSER, A., P. BOEHM, A. KURME, G. SCHUMPE and K. KURNIK. 2007. Orthopaedic issues in sports for persons with haemophilia. *Haemophilia*, **13**(s2), pp.47-52.
- SHARROCK, M., H. L. FERMOR, A. REDMOND and C. L. BROCKETT. 2022. Characterising The Frictional Properties Of Haemarthritic Articular Cartilage [Poster]. In: *Orthopaedic Research Society Annual Meeting*, Tampa, Florida.
- SHIVERS, C., M. SIEBERT, J. R. ZIDE, K. TULCHIN-FRANCIS, W. STEVENS, J. BORCHARD, A. RICCIO and J. R. ZIDE. 2020. Functional Implications of the Flat-Topped Talus Following Treatment of Idiopathic Clubfoot Deformity. *Foot & Ankle Orthopaedics*, **5**(4), p2473011420S00441.
- SOPHER, R. S., A. A. AMIS, J. D. CALDER and J. R. JEFFERS. 2017. Total ankle replacement design and positioning affect implant-bone micromotion and bone strains. *Medical engineering & physics*, **42**, pp.80-90.



- SØRENSEN, K. R., K. ROEPSTORFF, B. WIINBERG, A. K. HANSEN, M. TRANHOLM, L. N. NIELSEN and M. KJELGAARD-HANSEN. 2016. The F8-/- rat as a model of hemophilic arthropathy. *Journal of thrombosis and haemostasis*, **14**(6), pp.1216-1225.
- SOUCIE, J. M., C. CIANFRINI, R. L. JANCO, R. KULKARNI, J. HAMBLETON, B. EVATT, A. FORSYTH, S. GERAGHTY, K. HOOTS, T. ABSHIRE, R. CURTIS, A. FORSBERG, H. HUSZTI, M. WAGNER and G. C. WHITE. 2004. Joint range-of-motion limitations among young males with hemophilia: prevalence and risk factors. *Blood*, **103**(7), pp.2467-2473.
- STAGNI, R., A. LEARDINI, A. ENSINI and A. CAPPELLO. 2005. Ankle morphometry evaluated using a new semi-automated technique based on X-ray pictures. *Clinical Biomechanics*, **20**(3), pp.307-311.
- STEINHORN, M. and M. VAHLENSIECK. 2000. Ankle and Foot. *MRI of the Musculoskeletal System*. New York: Thieme Stuttgart, pp.213-239.
- STEPHENSON, D., R. C. TAIT, N. BRODIE, P. COLLINS, R. CHEAL, D. KEELING, K. MELTON, G. DOLAN, H. HAYE, E. HAYMAN and M. WINTER. 2009. Changing patterns of bleeding in patients with severe haemophilia A. *HAEMOPHILIA*, **15**(6), pp.1210-1214.
- STONEBRAKER, J. S., P. H. BOLTON-MAGGS, J. M. SOUCIE, I. WALKER and M. BROOKER. 2010. A study of variations in the reported haemophilia A prevalence around the world. *Haemophilia*, **16**(1), pp.20-32.
- STUFKENS, S. A., A. BARG, L. BOLLIGER, J. STUCINSKAS, M. KNUPP and B. HINTERMANN. 2011. Measurement of the Medial Distal Tibial Angle. *Foot & Ankle International*, **32**(3), pp.288-293.
- SUGIMOTO, K., Y. TAKAKURA, Y. TOHNO, T. KUMAI, K. KAWATE and K. KADONO. 2005. Cartilage Thickness of the Talar Dome. *Arthroscopy: The Journal of Arthroscopic and Related Surgery*, **21**(4), pp.401-404.
- TADDEI, F., S. MARTELLI, B. REGGIANI, L. CRISTOFOLINI and M. VICECONTI. 2006. Finite-Element Modeling of Bones From CT Data: Sensitivity to Geometry and Material Uncertainties. *IEEE Transactions on Biomedical Engineering*, **53**(11), pp.2194-2200.
- TAHA, Z., M. S. NORMAN, S. F. S. OMAR and E. SUWARGANDA. 2016. A Finite Element Analysis of a Human Foot Model to Simulate Neutral Standing on Ground. *Procedia Engineering*, **147**, pp.240-245.
- TALBOTT, H. G., R. A. WILKINS, A. C. REDMOND, C. L. BROCKETT and M. MENGONI. 2022. The relationship between subchondral bone cysts and cartilage health in the Tibiotalar joint: A finite element analysis. *Clinical Biomechanics*, **99**, p105745.
- TAO, K., D. WANG, X. WANG, C. WANG, A. LIU, C. J. NESTER and D. HOWARD. 2009. An In Vivo Experimental Validation of a Computational Model of Human Foot. *Journal of Bionic Engineering*, **6**(4), pp.387-397.
- TIMMER, M. A., M. F. PISTERS, P. KLEIJN, R. A. BIE, R. E. G. SCHUTGENS and C. VEENHOF. 2018. Movement behaviour in adults with haemophilia compared to healthy adults. *Haemophilia*, **24**(3), pp.445-451.
- TRABELSI, N., C. MILGROM and Z. YOSIBASH. 2014. Patient-specific FE analyses of metatarsal bones with inhomogeneous isotropic material properties. *Journal of the Mechanical Behavior of Biomedical Materials*, **29**, pp.177-189.

- TSEGAJ, Z. J., M. M. SKINNER, A. H. GEE, D. H. PAHR, G. M. TREECE, J. J. HUBLIN and T. L. KIVELL. 2017. Trabecular and cortical bone structure of the talus and distal tibia in Pan and Homo. *Am J Phys Anthropol*, **163**(4), pp.784-805.
- TÜMER, N., L. BLANKEVOORT, M. VAN DE GIESSEN, M. P. TERRA, P. A. DE JONG, H. WEINANS, G. J. M. TUIJTHOF and A. A. ZADPOOR. 2016. Bone shape difference between control and osteochondral defect groups of the ankle joint. *Osteoarthritis and Cartilage*, **24**(12), pp.2108-2115.
- VALENTINO, L. A. and N. HAKOBYAN. 2006. Histological changes in murine haemophilic synovitis: a quantitative grading system to assess blood-induced synovitis. *Haemophilia*, **12**(6), pp.654-62.
- VALENTINO, L. A., V. MAMONOV, A. HELLMANN, D. V. QUON, A. CHYBICKA, P. SCHROTH, L. PATRONE and W.-Y. WONG. 2012. A randomized comparison of two prophylaxis regimens and a paired comparison of on-demand and prophylaxis treatments in hemophilia A management. *Journal of thrombosis and haemostasis*, **10**(3), pp.359-367.
- VAN DEN BERG, H. M., K. FISCHER, E. P. MAUSER-BUNSCHOTEN, F. J. A. BEEK, G. ROOSENDAAL, J. G. VAN DER BOM and H. K. NIEUWENHUIS. 2001. Long-term outcome of individualized prophylactic treatment of children with severe haemophilia. *British journal of haematology*, **112**(3), pp.561-565.
- VAN MEEGEREN, M. E. R., G. ROOSENDAAL, N. W. D. JANSEN, F. P. J. G. LAFEBER and S. C. MASTBERGEN. 2013. Blood-Induced Joint Damage: The Devastating Effects of Acute Joint Bleeds versus Micro-Bleeds. *Cartilage*, **4**(4), pp.313-320.
- VAN ROSSOM, S., C. R. SMITH, L. ZEVENBERGEN, D. G. THELEN, B. VANWANSEEELE, D. VAN ASSCHE and I. JONKERS. 2017. Knee Cartilage Thickness, T1ρ and T2 Relaxation Time Are Related to Articular Cartilage Loading in Healthy Adults. *PLOS ONE*, **12**(1), pe0170002.
- VAN VALBURG, A., P. VAN ROERMUND, A. MARIJNISSEN, J. VAN MELKEBEEK, J. LAMMENS, A. VERBOUT, F. LAFEBER and J. BIJLSMA. 1999. Joint distraction in treatment of osteoarthritis: a two-year follow-up of the ankle. *Osteoarthritis and Cartilage*, **4**, pp.313-320.
- VAN VULPEN, L. F. D., K. HOLSTEIN and C. MARTINOLI. 2018. Joint disease in haemophilia: Pathophysiology, pain and imaging. *Haemophilia*, **24**(S6), pp.44-49.
- VASEENON, T. and A. AMENDOLA. 2012. Update on anterior ankle impingement. *Current reviews in musculoskeletal medicine*, **5**(2), pp.145-150.
- VICECONTI, M., S. OLSEN, L. P. NOLTE and K. BURTON. 2005. Extracting clinically relevant data from finite element simulations. *Clin Biomech (Bristol, Avon)*, **20**(5), pp.451-4.
- VON DRYGALSKI, A., R. F. W. BARNES, H. JANG, Y. MA, J. H. WONG, Z. BERMAN, J. DU and E. Y. CHANG. 2019. Advanced magnetic resonance imaging of cartilage components in haemophilic joints reveals that cartilage hemosiderin correlates with joint deterioration. *Haemophilia*, **25**(5), pp.851-858.
- WAGNER, D., L. KAMER, P. M. ROMMENS, T. SAWAGUCHI, R. G. RICHARDS and H. NOSER. 2014. 3D statistical modeling techniques to investigate the anatomy of the sacrum, its bone mass distribution, and the trans-sacral corridors. *Journal of Orthopaedic Research*, **32**(11), pp.1543-1548.

- WALLNY, T. A., D. T. SCHOLZ, J. OLDENBURG, C. NICOLAY, S. EZZIDDIN, P. H. PENNEKAMP, B. STOFFEL-WAGNER and C. N. KRAFT. 2007. Osteoporosis in haemophilia – an underestimated comorbidity? *Haemophilia*, **13**(1), pp.79-84.
- WALTERS, R. and S. MULROY. 1999. The energy expenditure of normal and pathologic gait. *Gait Posture*, **9**(3), pp.207-231.
- WANG, Y., Z. LI, D. W.-C. WONG, C.-K. CHENG and M. ZHANG. 2018. Finite element analysis of biomechanical effects of total ankle arthroplasty on the foot. *Journal of orthopaedic translation*, **12**, pp.55-65.
- WHITAKER, J. M., L. ROUSSEAU, T. WILLIAMS, R. A. ROWAN and W. C. HARTWIG. 2002. Scoring system for estimating age in the foot skeleton. *American Journal of Physical Anthropology*, **118**(4), pp.385-392.
- WILKINS, R. A. 2021. *Haemarthrosis of the ankle in haemophilia A and B: prevalence, impact and intervention*. PhD thesis, University of Leeds.
- WITKOP, M., C. GUELCHER, A. FORSYTH, S. HAWK, R. CURTIS, L. KELLEY, N. FRICK, M. RICE, G. ROSU and D. L. COOPER. 2015. Treatment outcomes, quality of life, and impact of hemophilia on young adults (aged 18–30 years) with hemophilia. *American Journal of Hematology*, **90**(S2), pp.S3-S10.
- WONG, T. E. M. D., S. M. D. MAJUMDAR, E. P. R. D. ADAMS, S. M. S. R. D. BERGMAN, M. L. R. N. M. DAMIANO, J. R. N. M. S. DEUTSCHE and M. M. D. P. RECHT. 2011. Overweight and Obesity in Hemophilia. *American Journal of Preventive Medicine*, **41**(6), pp.S369-S375.
- WOODS, C. G. 1961. Subchondral bone cysts. *J Bone Joint Surg Br*, **43-b**, pp.758-66.
- XU, Y., Y. ZHU and X.-Y. XU. 2017. Ankle joint distraction arthroplasty for severe ankle arthritis. *BMC Musculoskeletal Disorders*, **18**(1), p96.
- YU, J., J. T.-M. CHEUNG, Y. FAN, Y. ZHANG, A. K.-L. LEUNG and M. ZHANG. 2007. Development of a finite element model of female foot for high-heeled shoe design. *Clinical Biomechanics*, **23**, pp.S31-S38.
- ZANNONI, C., R. MANTOVANI and M. VICECONTI. 1999. Material properties assignment to finite element models of bone structures: a new method. *Medical Engineering & Physics*, **20**(10), pp.735-740.
- ZHANG, M. and P. GOLLAND. 2016. Statistical shape analysis: From landmarks to diffeomorphisms. *Medical Image Analysis*, **33**, pp.155-158.
- ZHANG, X., M. R. PAQUETTE and S. ZHANG. 2013. A comparison of gait biomechanics of flip-flops, sandals, barefoot and shoes. *Journal of Foot and Ankle Research*, **6**(1), p45.
- ZHOU, Z.-Y., M. A. KOERPER, K. A. JOHNSON, B. RISKE, J. R. BAKER, M. ULLMAN, R. G. CURTIS, J.-L. POON, M. LOU and M. B. NICHOL. 2015. Burden of illness: direct and indirect costs among persons with hemophilia A in the United States. *Journal of Medical Economics*, **18**(6), pp.457-465.
- ZUKOTYNSKI, K., J. JARRIN, P. S. BABYN, M. CARCAO, J. PAZMINO-CANIZARES, A. M. STAIN and A. S. DORIA. 2007. Sonography for assessment of haemophilic arthropathy in children: a systematic protocol. *Haemophilia*, **13**(3), pp.293-304.

## 9 Appendix

### 9.3 Chapter 3: Method Development

#### 9.3.1 Materials Sensitivity

Table 31 Material properties from sensitivity studies carried out on simplified model

<b>Cortical Bone</b>		<b>Trabecular Bone</b>		<b>Cartilage</b>					<b>Reference</b>
$E$ (GPa)	$\nu$	$E$ (GPa)	$\nu$	<i>Linear Elastic</i>		<i>Hyper-elastic</i>			
				$E$ (GPa)	$\nu$	$C_{01}$ (MPa)	$C_{10}$ (MPa)	$C_{20}$ (MPa)	
7.3	0.3	7.3	0.3	0.01	0.3				(Ozen, Sayman and Havitcioglu 2013)
14	0.3	14	0.3	0.01	0.3				
3	0.3	3	0.3	0.01	0.3				
0.6	0.3	0.6	0.3	0.01	0.3				
7.3	0.3	7.3	0.3	0.01	0.49				
7.3	0.3	7.3	0.3			0.41	4.1		(Ramlee, Kadir and Harun 2013)
7.3	0.3	7.3	0.3			0.66	4.5		(Klekiel and Będziński 2015)
7.3	0.3	7.3	0.3				1.25	2.25	(Butz <i>et al.</i> 2011)
7.3	0.3	7.3	0.3				30		(Butz <i>et al.</i> 2011)
7.3	0.3	7.3	0.3				1.25		
7.3	0.3	7.3	0.3			0.66	0.25		
7.3	0.3	7.3	0.3				3		
7.3	0.3	7.3	0.3			1.3	4.5		
7.3	0.3	7.3	0.3				4		
7.3	0.3	7.3	0.3			0.66	9		
7.3	0.3	7.3	0.3			4.5	4.5		(Cheung and Zhang 2005)
17	0.3	0.6	0.3			4.5	4.5		(Miller <i>et al.</i> 2004)
17	0.3	0.6	0.3	0.01	0.49				
21.9	0.3	0.6	0.3			4.5	4.5		(Niu <i>et al.</i> 2013)
29	0.3	0.6	0.3			4.5	4.5		(Niu <i>et al.</i> 2013)

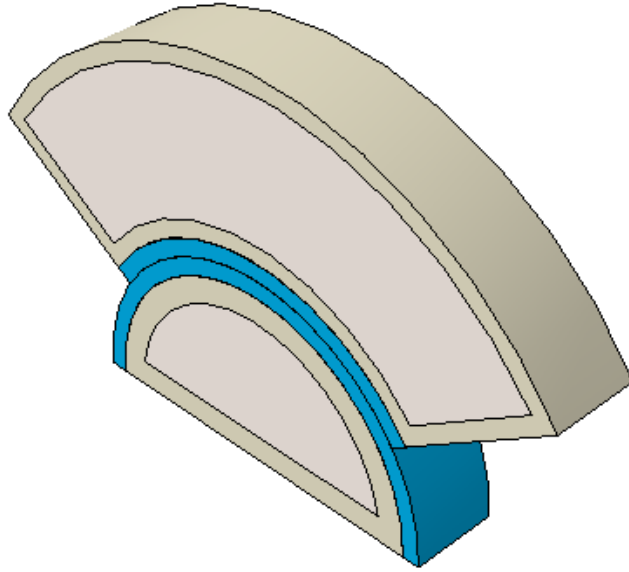


*Figure 87 Geometry used for material sensitivity study before application to whole ankle model*

## 9.4 Chapter 4: Chronological Study

### 9.4.1 Coefficient of Friction Study – No SBCs

Highlight in red (as defined in Chapter 4) shows models where there was a significant difference between 0.1 and 0.5 coefficients of friction. Orange highlights, also defined in Chapter 4, show models that only simulated at coefficient of friction: 0.5.

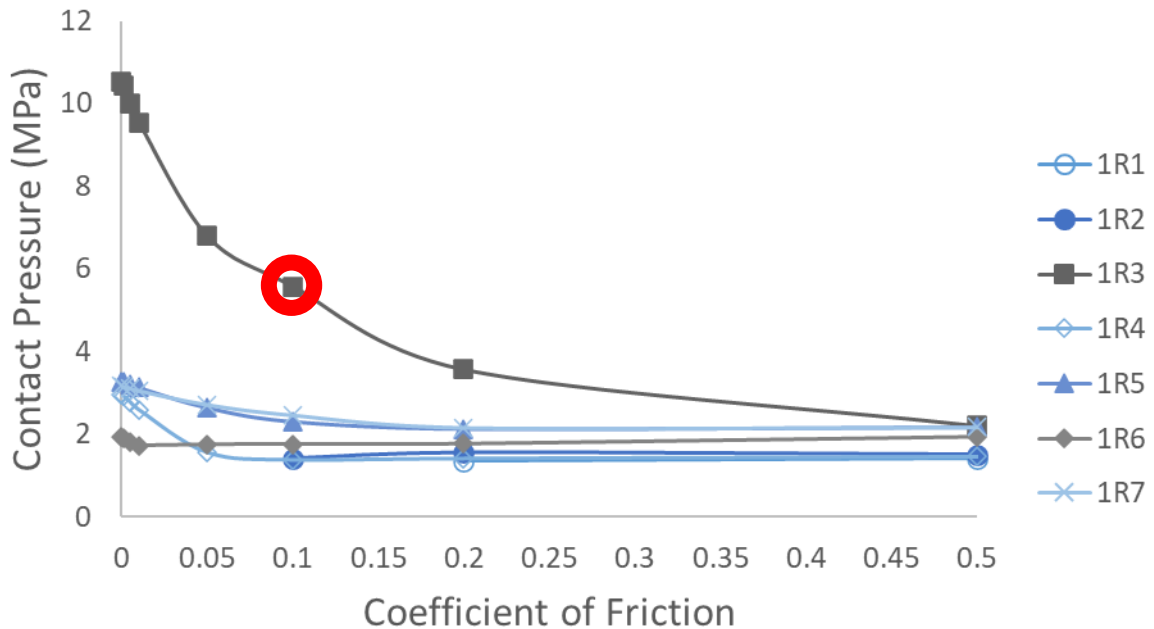


Figure 88 changes in tibial contact pressure (MPa) in Ankle 1R with increasing coefficient of friction

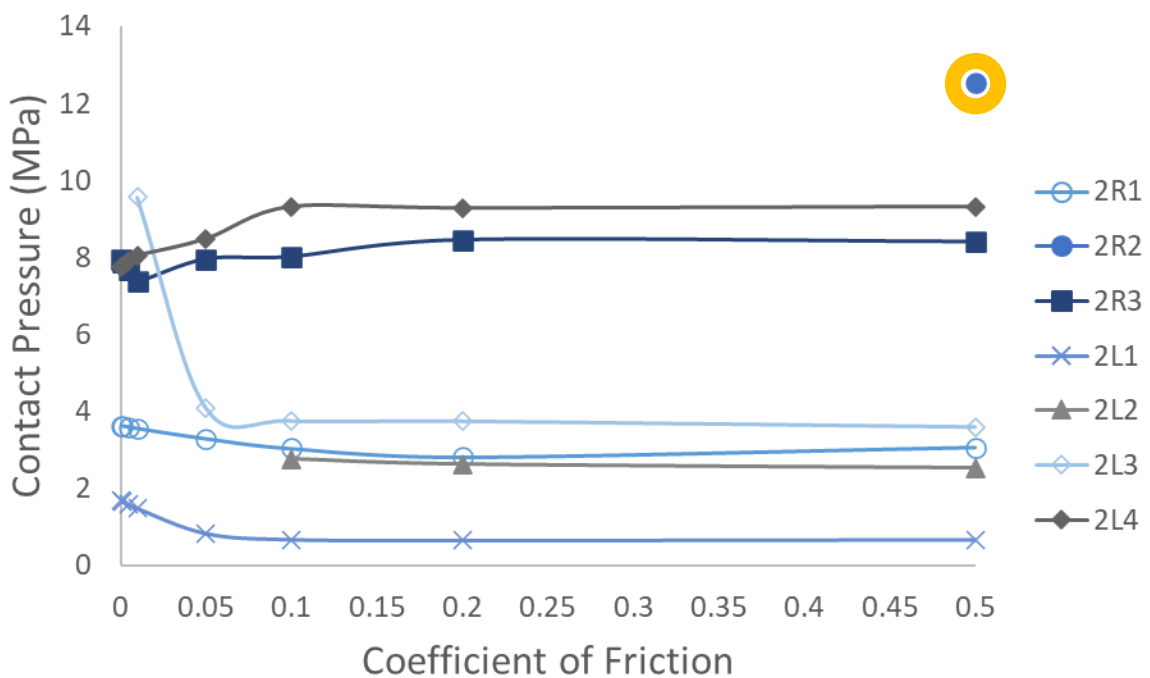


Figure 89 changes in tibial contact pressure (MPa) in Ankle 2R and 2L with increasing coefficient of friction

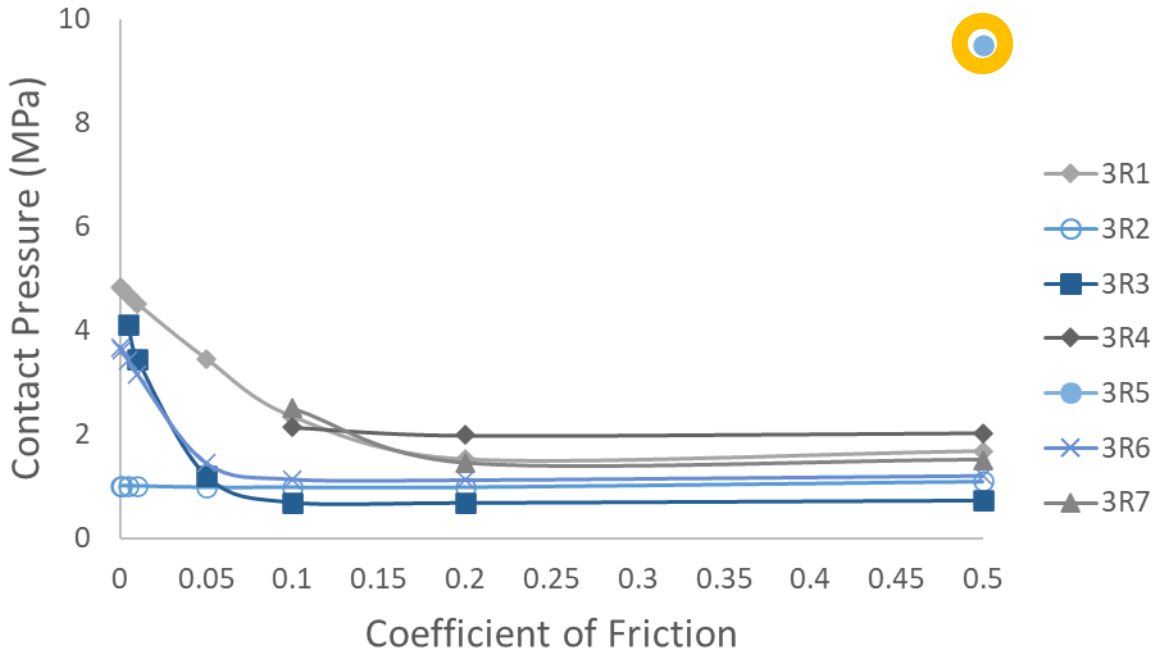


Figure 90 changes in tibial contact pressure (MPa) in Ankle 3R with increasing coefficient of friction

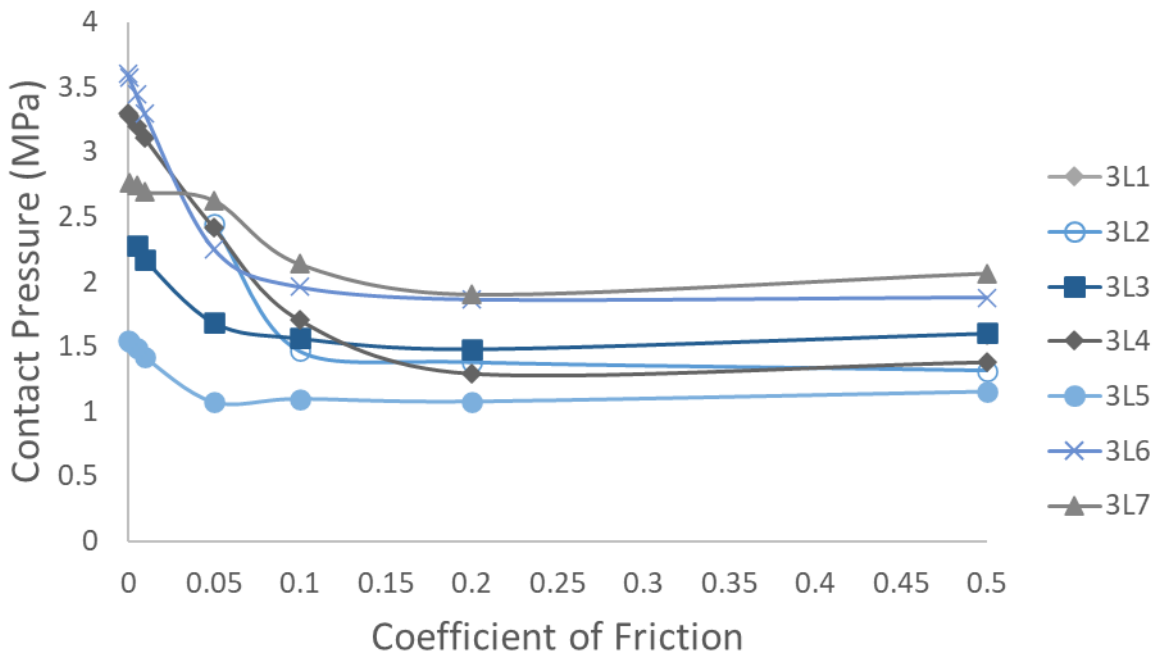


Figure 91 changes in tibial contact pressure (MPa) in Ankle 3L with increasing coefficient of friction

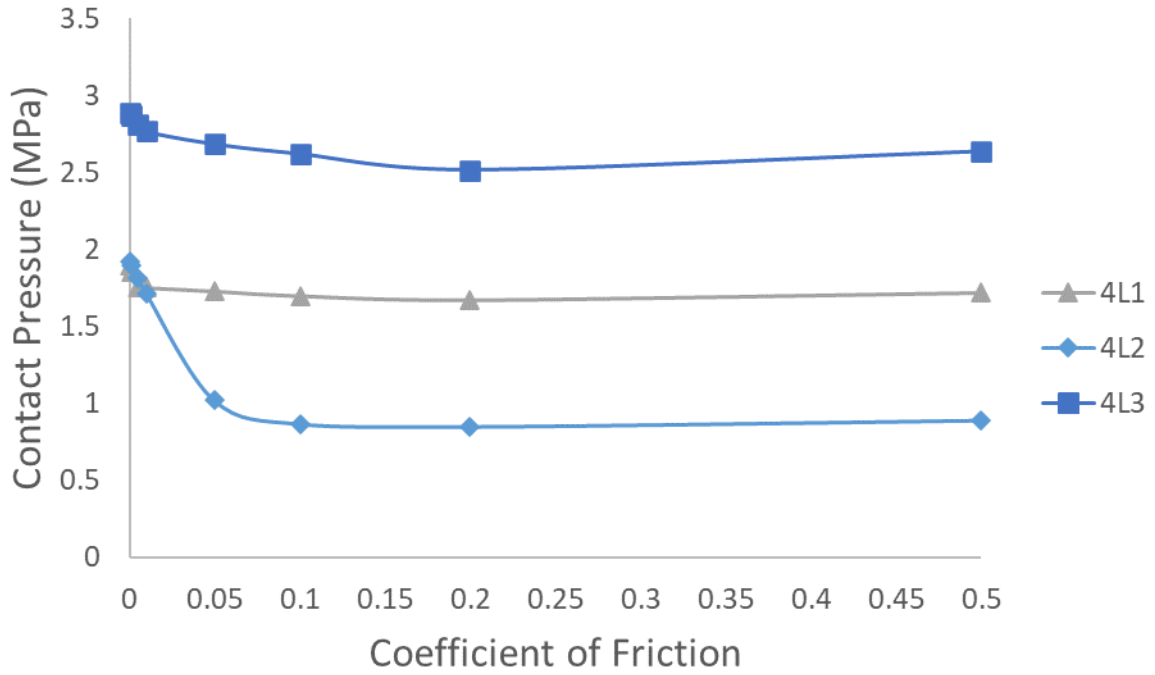


Figure 92 changes in tibial contact pressure (MPa) in Ankle 4L with increasing coefficient of friction

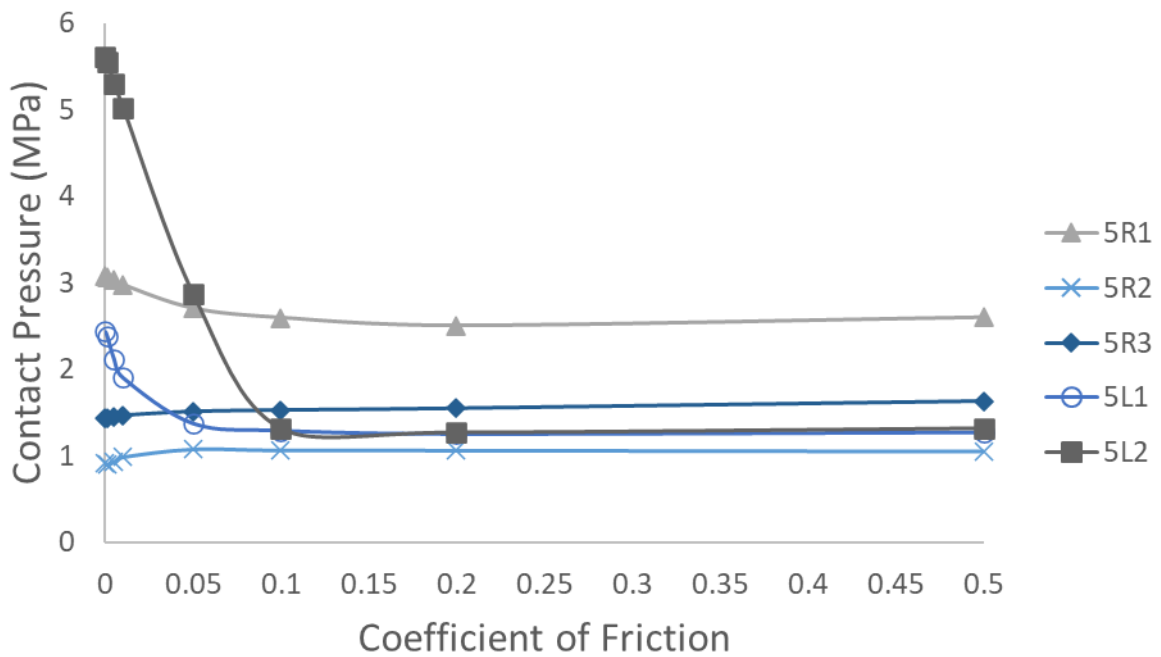


Figure 93 changes in tibial contact pressure (MPa) in Ankle 5R and 5L with increasing coefficient of friction



9.4.2 Coefficient of Friction Study – SBC models

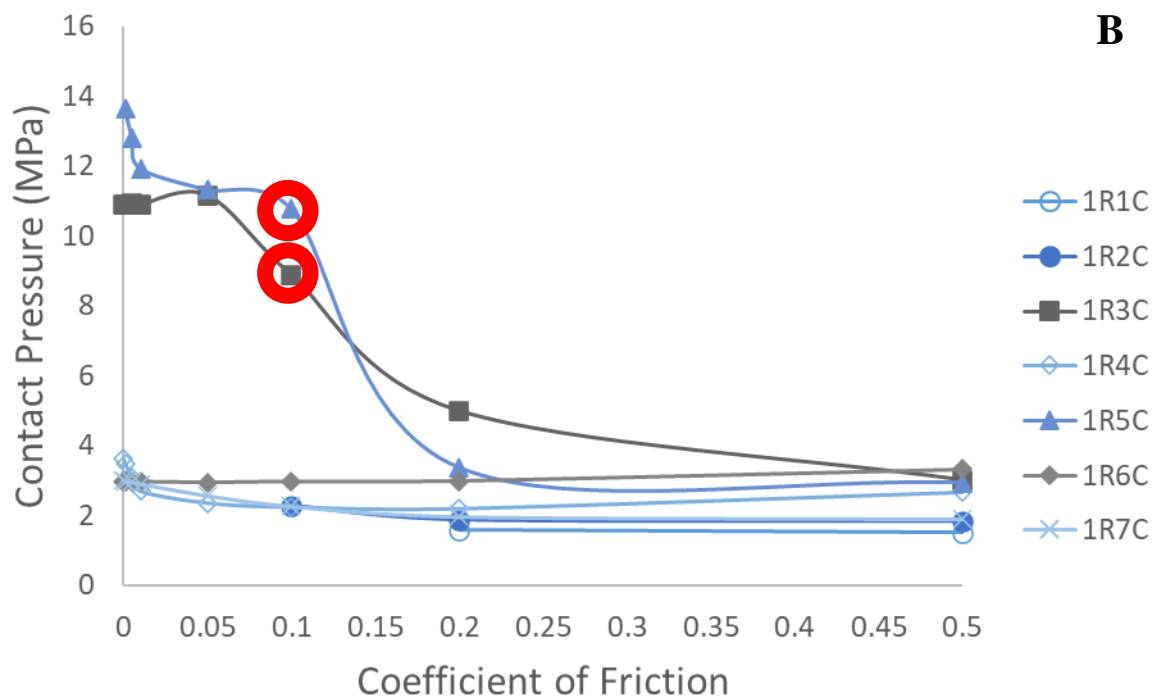
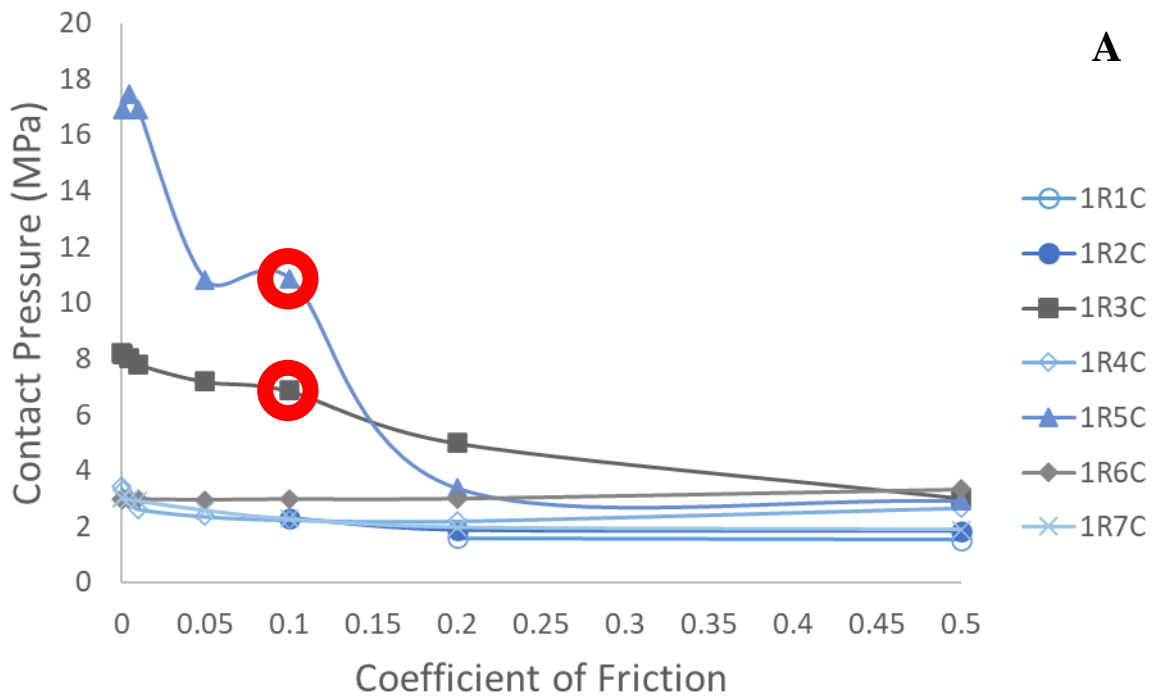


Figure 94 changes in contact pressure (MPa) in A) tibial cartilage, and B) talar cartilage in Ankle IRC with increasing coefficient of friction

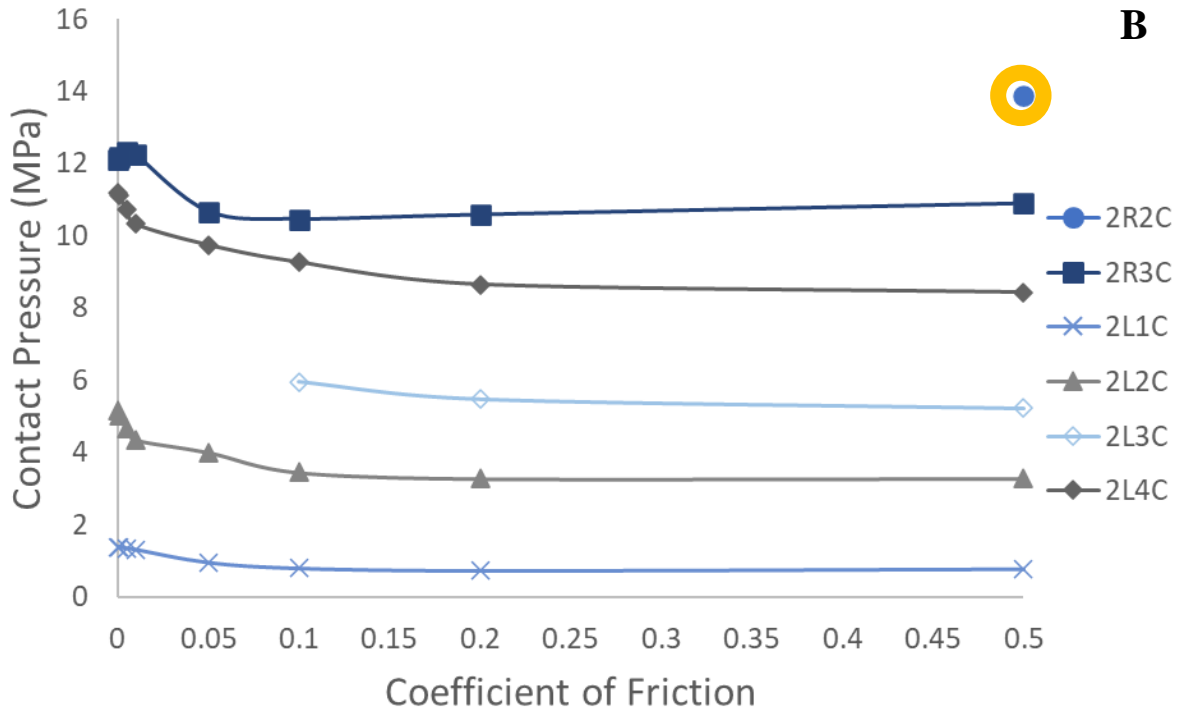
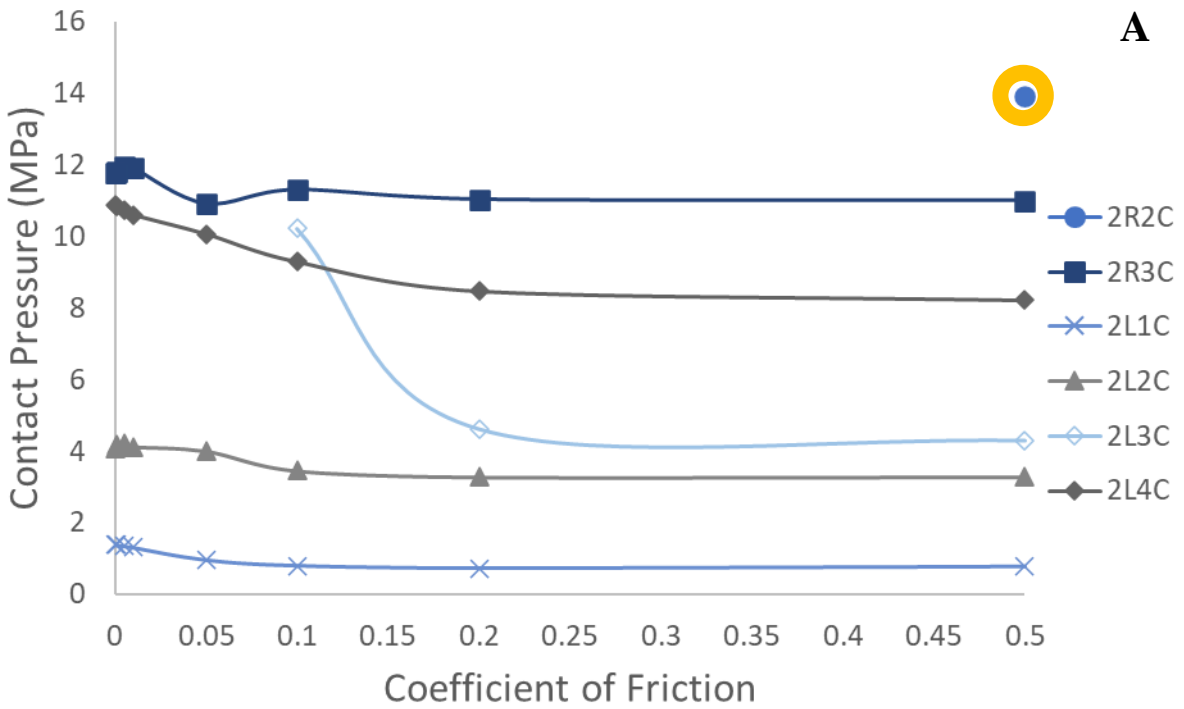


Figure 95 changes in contact pressure (MPa) in A) tibial cartilage, and B) talar cartilage in Ankle 2RC and 2LC with increasing coefficient of friction

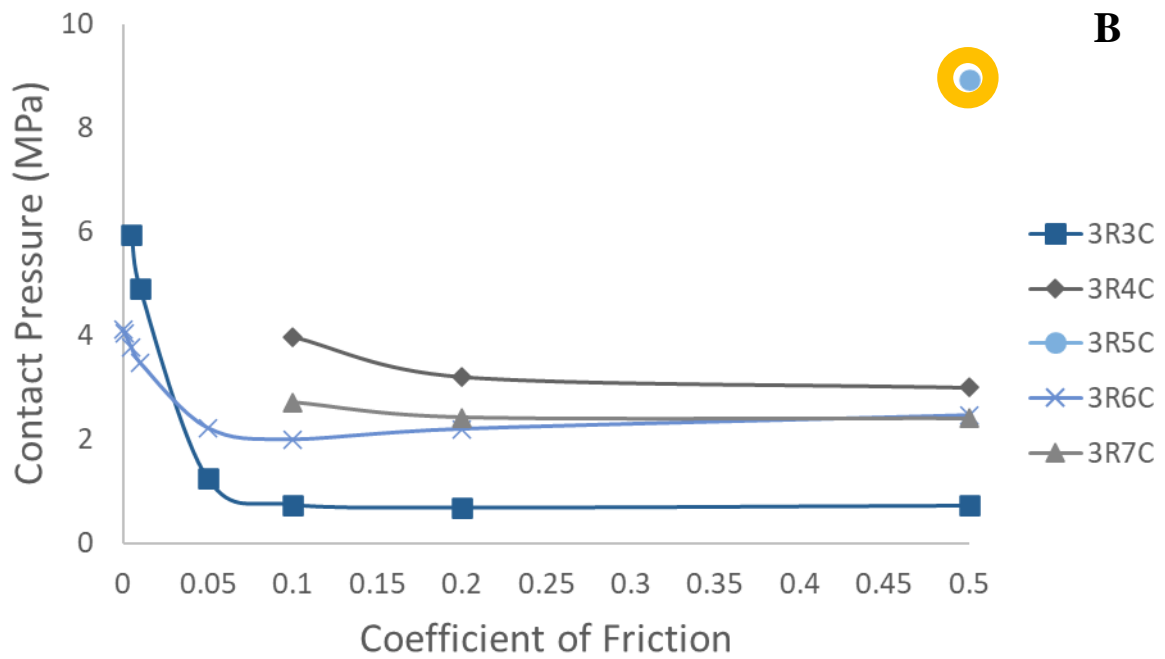
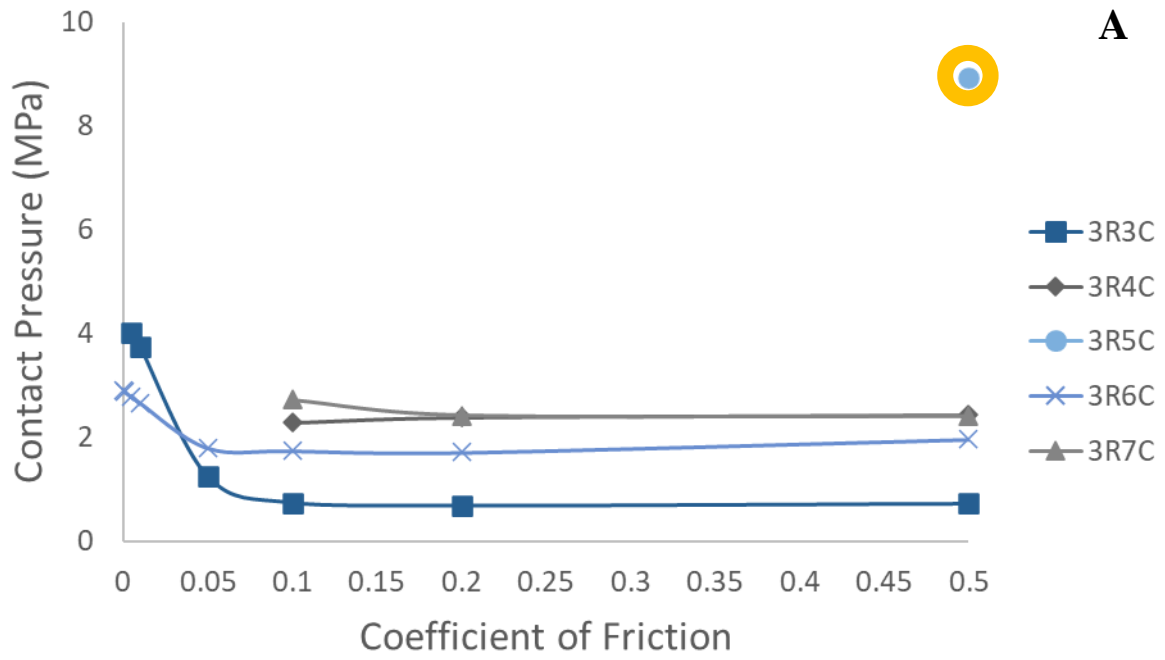


Figure 96 changes in contact pressure (MPa) in A) tibial cartilage, and B) talar cartilage in Ankle 3RC with increasing coefficient of friction

### 9.4.3 Longitudinal Study Outputs

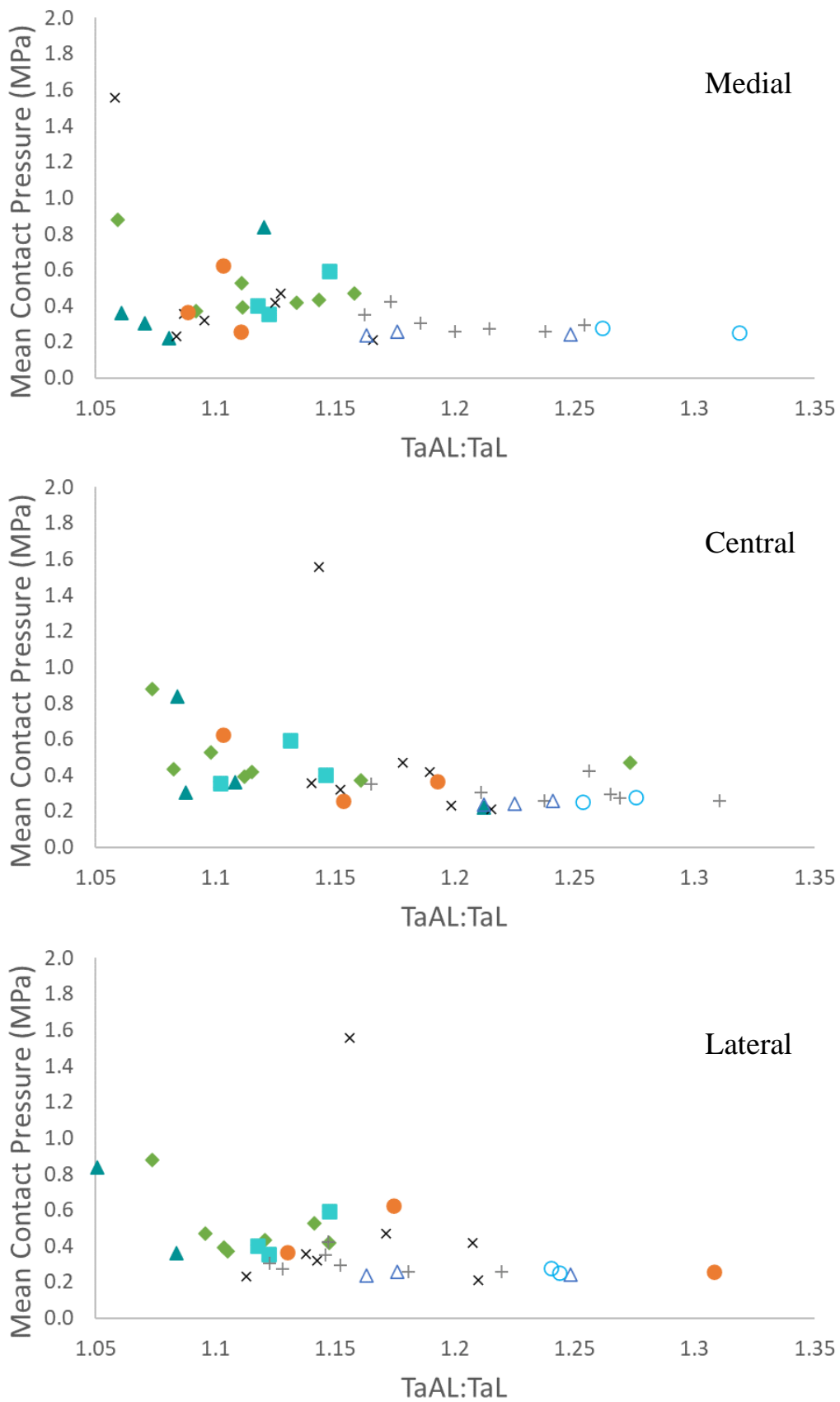


Figure 97 Mean contact pressure (MPa) in the tibial cartilage plotted against morphological measurements

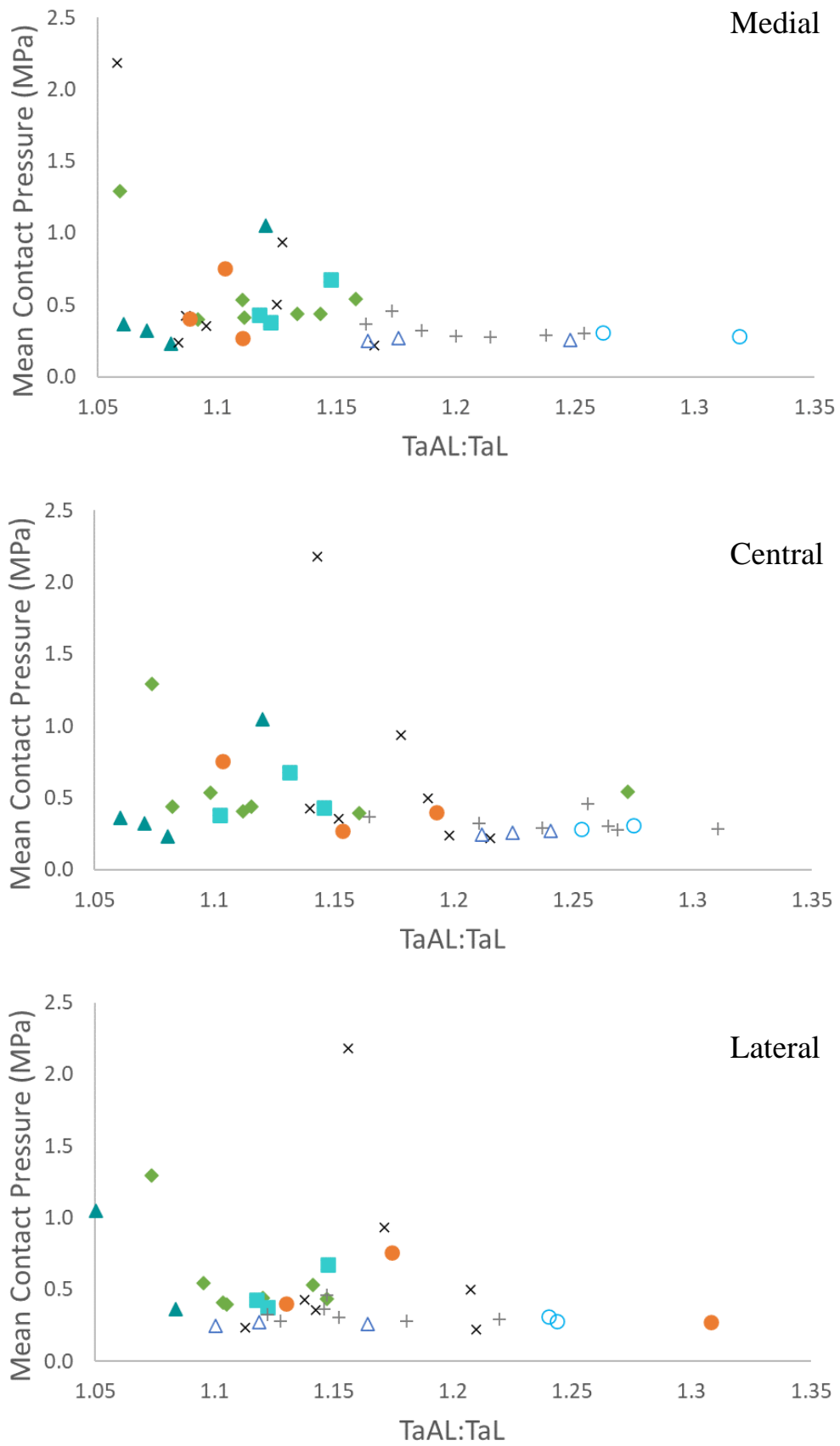


Figure 98 Mean contact pressure (MPa) in the talar cartilage plotted against morphological measurements

## 9.5 Chapter 5: Subchondral Bone Cysts

Table 32 SBC volumes, and respective tibial cartilage contact pressure redistributions

Model	Cyst Volume (mm <sup>3</sup> )			No Cysts	Cysts	
	Total	Tibia	Talus			
1R1	874.082	874.082				
1R2	583.118	583.118				
1R3	1889.07	1889.07				
1R4	2404.31	2404.31				
1R5	1749.49	1749.49				

1R6	1444.09	1444.09		<p>CPRESS</p> <p>+2.955e+00 +2.709e+00 +2.463e+00 +2.217e+00 +1.970e+00 +1.724e+00 +1.478e+00 +1.231e+00 +9.851e-01 +7.388e-01 +4.926e-01 +2.463e-01 +0.000e+00</p>		
1R7	2492.789	2492.79		<p>CPRESS</p> <p>+1.948e+00 +1.786e+00 +1.624e+00 +1.461e+00 +1.299e+00 +1.137e+00 +9.742e-01 +8.118e-01 +6.495e-01 +4.871e-01 +3.247e-01 +1.624e-01 +0.000e+00</p>		
2R2	1968.732	1968.73		<p>CPRESS</p> <p>+1.775e+00 +1.627e+00 +1.480e+00 +1.332e+00 +1.184e+00 +1.036e+00 +8.877e-01 +7.398e-01 +5.918e-01 +4.439e-01 +2.959e-01 +1.480e-01 +0.000e+00</p>		
2R3	460.099	386.077	74.022	<p>CPRESS</p> <p>+1.720e+01 +1.576e+01 +1.433e+01 +1.290e+01 +1.147e+01 +1.003e+01 +8.599e+00 +7.166e+00 +5.733e+00 +4.299e+00 +2.866e+00 +1.433e+00 +0.000e+00</p>		
2L1	109.936	109.936		<p>CPRESS</p> <p>+6.576e-01 +6.028e-01 +5.480e-01 +4.932e-01 +4.384e-01 +3.836e-01 +3.288e-01 +2.740e-01 +2.192e-01 +1.644e-01 +1.096e-01 +5.480e-02 +0.000e+00</p>		

2L2	3870.79	997.661	2873.13	<p>CPRESS</p>		
2L3	4613.25	2095.34	2517.92	<p>CPRESS</p>		
2L4	5088.35	2988.97	2099.38	<p>CPRESS</p>		
3R3	62.08		62.084	<p>CPRESS</p>		
3R4	896.20		896.2	<p>CPRESS</p>		



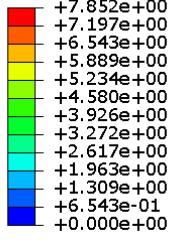
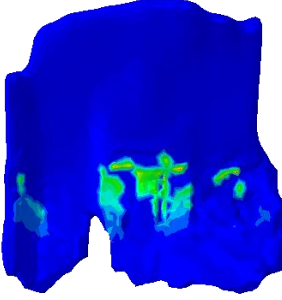
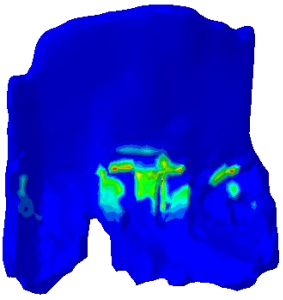
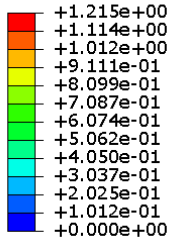
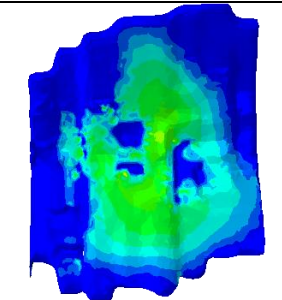
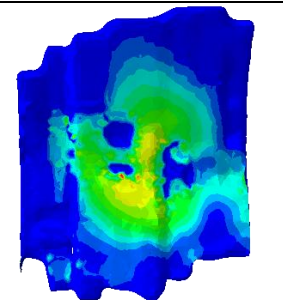
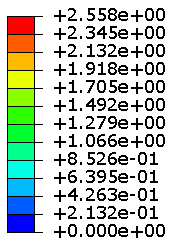
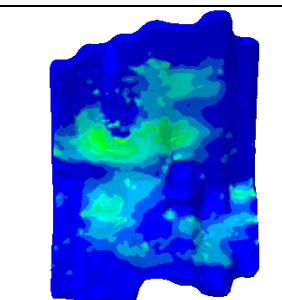
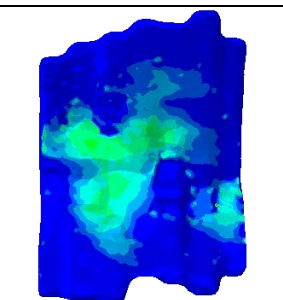
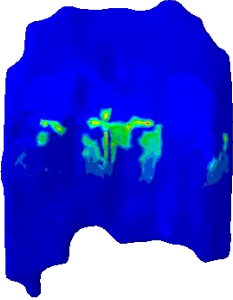
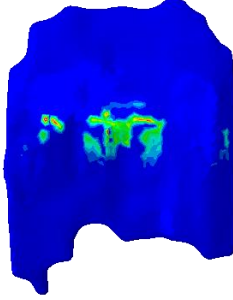
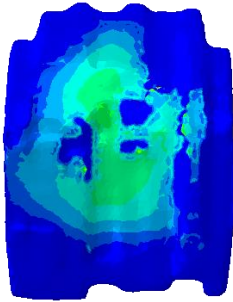
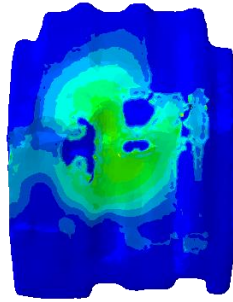
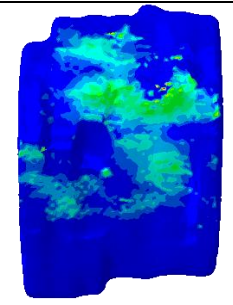
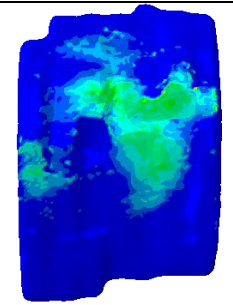
3R5	1632.41		1632.41	<p>CPRESS</p> 		
3R6	2501.68	434.931	2066.75	<p>CPRESS</p> 		
3R7	2345.91	721.173	1624.73	<p>CPRESS</p> 		

Table 33 SBC volumes, and respective talar cartilage contact pressure redistributions

Model	Cyst Volume (mm <sup>3</sup> )			No Cysts	Cysts	
	Total	Tibia	Talus			
1R1	874.082	874.082				
1R2	583.118	583.118				
1R3	1889.07	1889.07				
1R4	2404.31	2404.31				
1R5	1749.49	1749.49				

1R6	1444.09	1444.09		<p>CPRESS</p> <p>+3.423e+00 +3.138e+00 +2.853e+00 +2.567e+00 +2.282e+00 +1.997e+00 +1.712e+00 +1.426e+00 +1.141e+00 +8.558e-01 +5.705e-01 +2.853e-01 +0.000e+00</p>		
1R7	2492.789	2492.79		<p>CPRESS</p> <p>+2.381e+00 +2.182e+00 +1.984e+00 +1.786e+00 +1.587e+00 +1.389e+00 +1.190e+00 +9.920e-01 +7.936e-01 +5.952e-01 +3.968e-01 +1.984e-01 +0.000e+00</p>		
2R2	1968.732	1968.73		<p>CPRESS</p> <p>+2.602e+00 +2.385e+00 +2.168e+00 +1.951e+00 +1.734e+00 +1.518e+00 +1.301e+00 +1.084e+00 +8.672e-01 +6.504e-01 +4.336e-01 +2.168e-01 +0.000e+00</p>		
2R3	460.099	386.077	74.022	<p>CPRESS</p> <p>+1.759e+01 +1.612e+01 +1.466e+01 +1.319e+01 +1.173e+01 +1.026e+01 +8.795e+00 +7.330e+00 +5.864e+00 +4.398e+00 +2.932e+00 +1.466e+00 +0.000e+00</p>		
2L1	109.936	109.936		<p>CPRESS</p> <p>+6.434e-01 +5.898e-01 +5.362e-01 +4.825e-01 +4.289e-01 +3.753e-01 +3.217e-01 +2.681e-01 +2.145e-01 +1.608e-01 +1.072e-01 +5.362e-02 +0.000e+00</p>		

2L2	3870.79	997.661	2873.13	<p>CPRESS</p>		
2L3	4613.25	2095.34	2517.92	<p>CPRESS</p>		
2L4	5088.35	2988.97	2099.38	<p>CPRESS</p>		
3R3	62.08		62.084	<p>CPRESS</p>		
3R4	896.20		896.2	<p>CPRESS</p>		

3R5	1632.41		1632.41	<p>CPRESS</p> <ul style="list-style-type: none"> <li>+9.003e+00</li> <li>+8.253e+00</li> <li>+7.503e+00</li> <li>+6.752e+00</li> <li>+6.002e+00</li> <li>+5.252e+00</li> <li>+4.502e+00</li> <li>+3.751e+00</li> <li>+3.001e+00</li> <li>+2.251e+00</li> <li>+1.501e+00</li> <li>+7.503e-01</li> <li>+0.000e+00</li> </ul>		
3R6	2501.68	434.931	2066.75	<p>CPRESS</p> <ul style="list-style-type: none"> <li>+1.621e+00</li> <li>+1.486e+00</li> <li>+1.351e+00</li> <li>+1.216e+00</li> <li>+1.081e+00</li> <li>+9.458e-01</li> <li>+8.107e-01</li> <li>+6.756e-01</li> <li>+5.405e-01</li> <li>+4.053e-01</li> <li>+2.702e-01</li> <li>+1.351e-01</li> <li>+0.000e+00</li> </ul>		
3R7	2345.91	721.173	1624.73	<p>CPRESS</p> <ul style="list-style-type: none"> <li>+2.541e+00</li> <li>+2.329e+00</li> <li>+2.117e+00</li> <li>+1.906e+00</li> <li>+1.694e+00</li> <li>+1.482e+00</li> <li>+1.270e+00</li> <li>+1.059e+00</li> <li>+8.470e-01</li> <li>+6.352e-01</li> <li>+4.235e-01</li> <li>+2.117e-01</li> <li>+0.000e+00</li> </ul>		

9.6 Chapter 6: Biomechanical Analysis

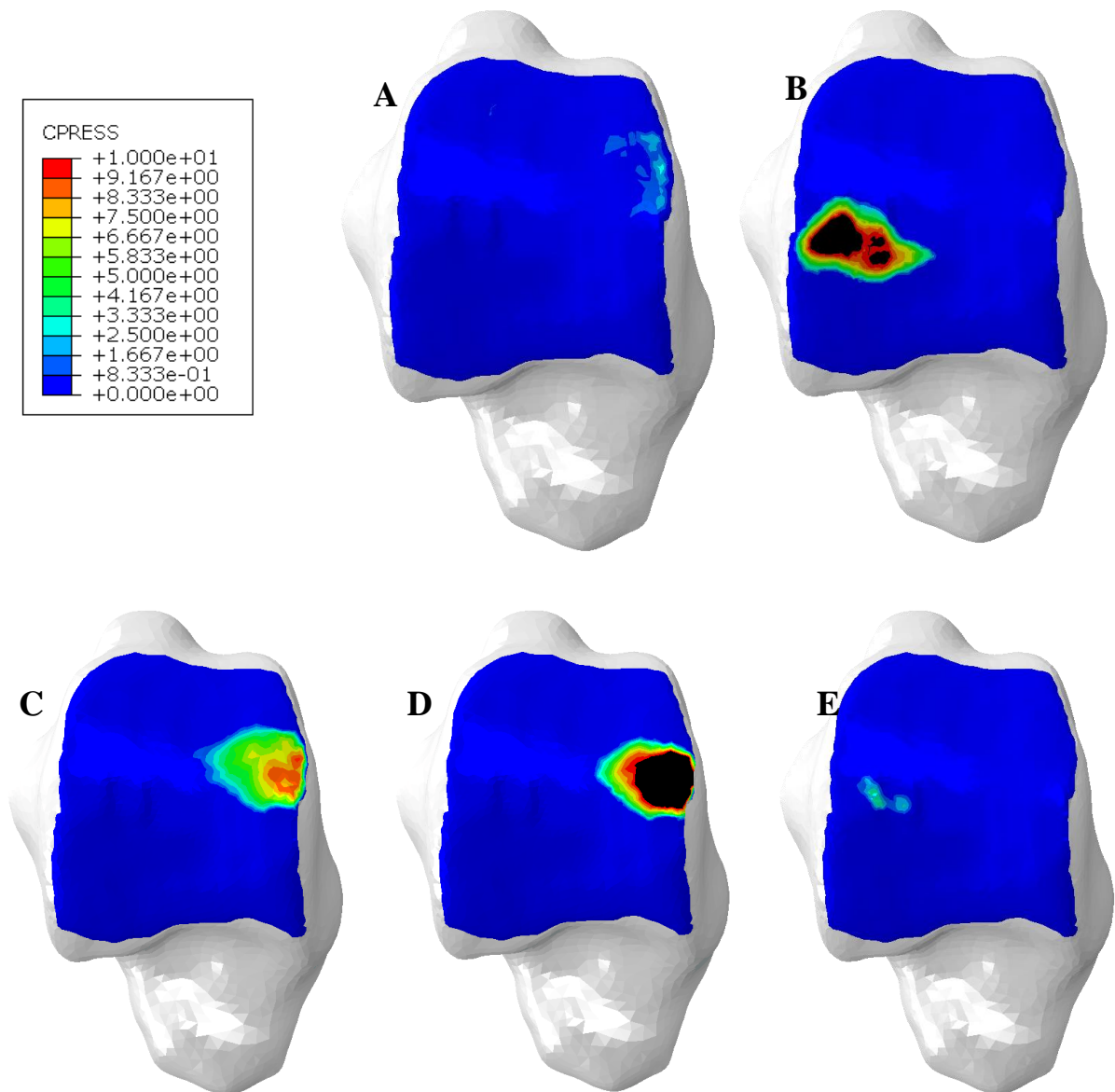


Figure 99 Change in contact distribution between (A) Heel Strike, (B) Flat Foot, (C) Mid Stance, (D) Heel Off and (E) Toe Off in non-diseased control ankle model

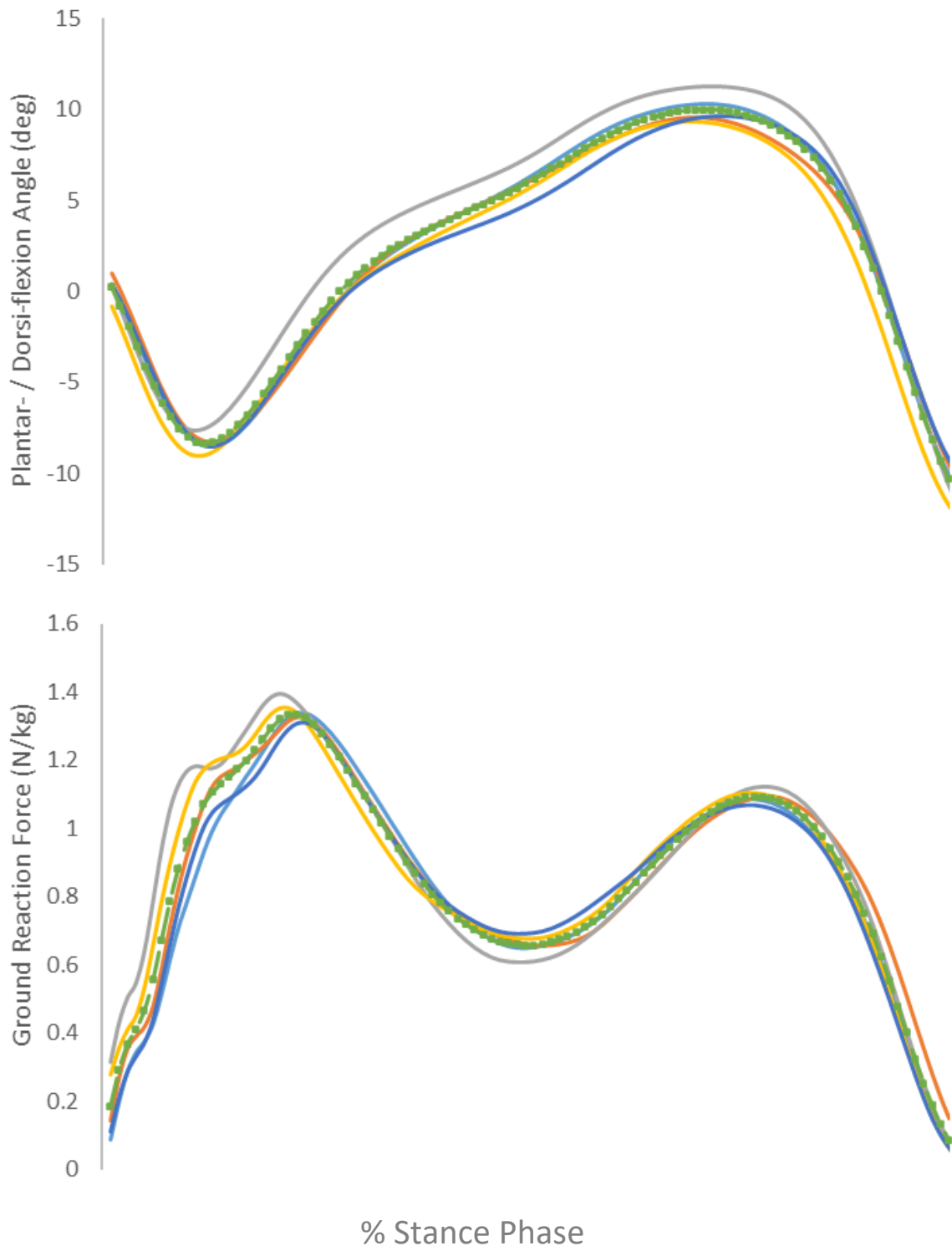


Figure 100 Individual gait data trials for ankle 4L, with grand mean used as input data (green markers)